

Characterization of Solid-Liquid Interfaces with High-Resolution Atomic Force Microscopy

THÈSE N° 6568 (2015)

PRÉSENTÉE LE 2 AVRIL 2015

À LA FACULTÉ DES SCIENCES ET TECHNIQUES DE L'INGÉNIEUR
LABORATOIRE DES NANOMATÉRIAUX SUPRAMOLÉCULAIRES ET INTERFACES - CHAIRE CONSTELLIUM
PROGRAMME DOCTORAL EN SCIENCE ET GÉNIE DES MATÉRIAUX

ÉCOLE POLYTECHNIQUE FÉDÉRALE DE LAUSANNE

POUR L'OBTENTION DU GRADE DE DOCTEUR ÈS SCIENCES

PAR

Maria RICCI

acceptée sur proposition du jury:

Prof. D. Damjanovic, président du jury
Prof. F. Stellacci, Dr K. Voitchovsky, directeurs de thèse
Prof. G. Dietler, rapporteur
Prof. M. Dong, rapporteur
Prof. F. Mugele, rapporteur



ÉCOLE POLYTECHNIQUE
FÉDÉRALE DE LAUSANNE

Suisse
2015

In our work, we are always between Scylla and Charybdis;
we may fail to abstract enough, and miss important physics,
or we may abstract too much and end up with fictitious objects
in our models turning into real monsters that devour us.

– Murray Gell-Mann, *Selected Papers*

Dedico questa tesi alla mia famiglia.

Abstract

Solid-liquid interfaces are ubiquitous. Despite the unquestioned relevance, many scientific research fields rely on simplified or macroscopic descriptions, discarding the molecular nature of the constituents. However, it is the specific molecular interactions and the complex chemistry in the interfacial region that are fundamental in phenomena such as heterogeneous catalysis, electrochemistry, crystal growth, membrane transport and body-antibody recognition. In particular, the models used to describe the so-called electrical double layer of ionic distributions at charged surfaces in liquid, are based on continuum assumptions. For example, the Gouy-Chapman-Stern model assumes that a dense, homogeneously distributed layer with a thickness of a hydrated ion (referred to as the "Stern layer"), is adsorbed onto the charged surface, preceded by an exponentially decaying diffuse ionic cloud, in which ions are point charges in a continuous dielectric media.

In this thesis, I will first illustrate how the assumption of a homogeneous ion lateral density in the Stern Layer fails to describe the actual solid-water interface of several relevant surfaces. Then I will show how the lateral organization of the ions indeed plays a role as important as the vertical modulation of the charge distribution. This is because the molecular nature of the ions, the surface, and the water molecules themselves each contribute to the precise lateral organization of the constituents. As result, the ions can reside on discrete surface sites, defined both laterally and vertically in space. Moreover, the water-mediated interaction can impart a correlation in the reciprocal lateral distribution of the ions.

To achieve this level of description, high-resolution atomic force microscopy (AFM) is used. Unlike most of other experimental techniques, AFM is able to characterize interfaces locally at the atomic/molecular level. In fact, in the AFM small-amplitude regime, detection of even single ions adsorbed at the surface of the solid is possible by measuring the perturbation they induce on the local solvation environment. This capability represents an invaluable tool for the exploration of phenomena occurring at the Stern layer of solid-liquid interfaces. Following, I will investigate the properties of several solid-aqueous interfaces in the presence of different ionic concentrations and species, ranging from hard (mica) to soft systems such as organic self-assembled monolayers, lipid bilayers, and the dynamic surface restructuring of calcite when covered with fatty acid molecules. The experimental study, combined with molecular dynamic simulations, reveals a water-induced ion-ion attractive interaction for some ionic species. These results show that water alone is the driving force to induce order within the Stern layer, creating hydration-correlation effects on mica, self-assembled monolayers and possibly lipid bilayers. The local modulation of the hydration properties of the surface is fundamental to highly dynamic systems such as calcite, where steps act as nucleating points for the processes of dissolution and growth. The specific interaction of foreign ions and fatty acids modify these processes as well as the equilibrium between the crystal and the solution. This thesis provides clear experimental evidence of new mechanisms developing at solid-liquid interfaces paving the way for a deeper and more conscious understanding of the colloidal properties of materials.

Keywords: Solid-Liquid Interface, High-Resolution Atomic Force Microscopy, Solvation Forces, Stern Layer, Single Ion Adsorption, Hydration Correlation Effect, Mica, Self-Assembled Monolayer, Lipid Bilayer, Calcite.

Résumé

Les interfaces solide-liquide se rencontrent partout dans la nature. Malgré leur importance capitale, dans nombreux champs de recherche on ne considère qu'une version simplifiée ou macroscopique du système, négligeant sa nature moléculaire. Cependant, les interactions moléculaires spécifiques dans la région interfaciale sont essentielles pour l'étude de phénomènes tels que la catalyse hétérogène, l'électrochimie, la croissance cristalline, le transport à travers les membranes et la reconnaissance anticorps-antigène. En particulier, les modèles utilisés pour décrire la distribution des ions dans un liquide au voisinage d'une surface chargée (la double couche électrostatique) sont basés sur l'hypothèse des systèmes continus. Le modèle de Gouy-Chapman-Stern considère par exemple l'existence d'une monocouche dense d'ions solvatés (la « couche de Stern ») adsorbée sur une surface chargée. Celle-ci est suivie d'une couche ionique diffuse décroissant exponentiellement, dans laquelle les espèces sont considérées comme des ions ponctuels dans un milieu diélectrique continu.

Dans cette thèse, je montrerai d'abord comment l'hypothèse d'une densité d'ions homogène dans le plan de la couche de Stern ne décrit pas la structure réelle de l'interface solide-liquide. Ensuite, je montrerai comment l'organisation des ions dans le plan de l'interface et la modulation verticale de la distribution de charges jouent un rôle fondamental dans la structure. Cet effet résulte d'une organisation précise de tous les constituants de l'interface induite par la nature moléculaire des ions, de la surface et des molécules d'eau elles-mêmes. Cette organisation favorise l'occupation par les ions de positions latérales et verticales bien définies dans l'espace. En particulier, je montrerai comment les interactions entre les ions à travers les molécules d'eau induisent une corrélation dans la distribution même des ions.

Pour obtenir ce niveau de description microscopique, nous utilisons la microscopie à force atomique à haute résolution. Cette technique permet de caractériser les interfaces solide-liquide au niveau moléculaire et atomique. En régime de faible modulation d'amplitude il est en fait possible détecter des ions isolés par la mesure de leur perturbation sur l'environnement local de solvation. Les propriétés de plusieurs interfaces solide-liquide seront étudiées en présence de différentes espèces ioniques allant des surfaces dures (mica), « moles » telles que des bicouches lipidiques ou des monocouches organiques auto-assemblées, jusqu'à un système dynamique comme la restructuration d'une surface de calcite couverte d'une couche d'acide gras. Cette étude expérimentale, combinée à des simulations de dynamique moléculaire, a révélé l'existence d'une interaction attractive entre les ions induite par les molécules d'eau. Ces résultats indiquent que l'hydratation des espèces adsorbées peut être la force motrice de leur organisation au sein de la couche de Stern, conduisant à un effet de corrélation d'hydratation à la surface du mica, des monocouches organiques auto-assemblées ou des bicouches lipidiques. La modulation locale des propriétés d'hydratation de la surface est également essentielle dans l'étude de systèmes hautement dynamiques, tel que la calcite, où les marches servent de point de départ pour les processus de dissolution et de précipitation. Les interactions spécifiques d'ions extérieurs et de molécules d'acide gras modifient ce processus, ainsi que l'état d'équilibre final du cristal dans l'électrolyte. Cette thèse apporte des preuves expérimentales claires de l'existence de mécanismes nouveaux et de phénomènes se produisant à l'interface d'un solide avec un liquide, et pave le chemin pour une étude plus approfondie et une meilleure compréhension des propriétés colloïdales des matériaux.

Mots-clefs : Interface Solide-Liquide, Microscopie à Force Atomique de Haute-Résolution, Forces de Solvation, Couche de Stern, Adsorption d'Ion Unique, Effet de Corrélation d'Hydratation, Mica, Monocouche Auto-Assemblée, Bicouche Lipidique, Calcite.

Contents

Abstract.....	i
Résumé	iii
Contents	v
Introduction	1
1. Solid-liquid interfaces: from a thermodynamic description to a molecular characterization.....	5
1.1 Solid-liquid interfaces: from a thermodynamic description to a molecular picture	6
1.1.1 Surface energy and work of cohesion	6
1.1.2 Interfacial energy and work of adhesion	7
1.2 Experimental techniques to characterize solid-liquid interfaces	9
1.2.1 X-ray spectroscopy and scattering	9
1.2.2 Neutron scattering and diffraction	12
1.2.1 X- Non-linear optics techniques	12
1.3 Force-based techniques: Surface Force Apparatus and Atomic Force Microscopy ...	14
1.3.1 Forces between two solid surfaces in a liquid medium	14
1.3.2 Surface Force Apparatus	17
1.3.3 Atomic Force Microscopy	17
1.4 AFM to map the solid-liquid interfacial energy with sub-nanometric resolution	18
1.4.1 Solid-liquid work of adhesion and pressure between two approaching surfaces	18
1.4.2 Energy dissipated in the whole oscillation cycle	20
Bibliography Chapter 1	21
2. High resolution AFM at solid-liquid interfaces.....	25
2.1 Working principle of AFM	26
2.2 Historical introduction on AFM: from vacuum to liquid	27

2.3 Concept of resolution in AFM	29
2.3.1 Vertical resolution.....	29
2.3.2 Lateral resolution	30
2.3.3 Ingredients for high resolution	31
2.4 Modeling the dynamic motion of a cantilever in liquid	32
2.4.1 Derivation of the point-mass model from the actual motion of a rectangular lever	32
2.4.2 Point mass model with a sinusoidal driving force	35
2.4.3 Frequency dependence of the hydrodynamic force	36
2.4.4 The effect of the driving mechanism.....	37
2.4.5 Point mass model with an external interaction force	38
2.4.6 Non-linear interaction forces in liquid: higher harmonic and higher eigenmodes ..	42
2.4.7 Phase contrast and energy dissipation in AM-AFM	44
2.5 Interaction forces: conservative and dissipative interactions	45
2.5.1 Conservative forces	46
2.5.2 Dissipative forces.....	47
2.6 High resolution and solvation forces	50
2.6.1 The effect of the “solvation” damping on the cantilever motion	50
2.6.2 Sharp tips and instabilities	52
2.6.3 Conservative part of the hydration force	52
2.6.4 Dissipative part of the hydration force	54
2.6.5 High resolution imaging of solvation structures with AM-AFM	55
Bibliography Chapter 2.....	58
3. High-resolution AFM to characterize the Stern Layer of aqueous-solid interfaces	63
3.1 What do we need and why	64
3.2 Review on the previous works	65
3.3 Physical mechanism behind ion detection with AFM	67
3.4 Imaging monovalent ions at the Stern Layer of mica-water interface with AM-AFM	68
3.4.1 Method to extract the surface coverage of Rb^+ ions from the AFM images	69
3.5 Dynamics of ions in the Stern Layer	71
3.5.1 The effect of the scan speed	73
3.5.2 The effect of scanning drift	74
3.5.3 Confinement effects	75
3.6 Isotherm models	76
3.6.1 Frumkin-Fowler-Guggenheim isotherm model	76

3.7 Perturbation of the system with the AFM tip	78
3.7.1 Correction of the Frumkin model for AFM measurements	78
3.7.2 Extraction of the different energy contributions	79
3.7.3 Results and discussion	80
3.7.4 Experiments with gold-coated tips	82
Bibliography Chapter 3	82
4. Hydration correlation effect at the Stern Layer investigated at the single ion level	87
4.1 Gouy-Chapman-Stern model: theory and limitations	88
4.1.1 Gouy-Chapman-Stern (GCS) model	88
4.1.2 Gouy-Chapman-Stern (GCS) Model: limitations and examples of phenomena not accounted	90
4.2 The example of Mica: the new concept of hydration correlation	95
4.2.1 Statistical analysis of the ionic distribution at the mica surface	95
4.2.2 MD-simulations and the concept of hydration correlation energy	98
4.2.3 Different monovalent ions	102
4.2.4 General discussions on the system	103
4.3 Hydration correlation in other systems	105
4.3.1 Self-Assembled-Monolayer on gold	105
4.3.2 Lipid bilayers	108
4.4 Materials and Methods	111
4.4.1 Atomic Force Microscopy experiments on mica	111
4.4.2 MD-simulations on mica	112
4.4.3 Synthesis of the self-assembled monolayers	113
4.4.4 Lipid bilayer preparation	113
4.4.5 Cleaning procedures	114
Bibliography Chapter 4	114
5. The dynamic interface between calcite and ionic solutions	119
5.1 Interaction of ions with the (10$\bar{1}$4) surface of calcite	120
5.1.1 Surface structure of the (10 $\bar{1}$ 4) cleavage plane of calcite	120
5.1.2 Hydration properties and surface charge of the calcite surface	123
5.1.3 Ion adsorption on the calcite surface	125
5.1.4 General Discussion of the system	131
5.2 Growth and dissolution process of calcite	133
5.2.1 Hydration properties at the calcite's steps	133
5.2.2 Growth and Dissolution process	135
5.2.3 Influence of different ions on the growth-dissolution process	137
5.3 Materials and Methods	139

5.3.1 MD-simulations of ions on calcite	139
5.3.2 Sample preparation for AFM in the experiments of ion adsorption at flat surfaces	139
5.3.3 Sample preparation for AFM in the experiments of growth and dissolution	140
Bibliography Chapter 4.....	141
6. Interaction of organic molecules with the surface of calcite in ionic solutions ...	147
6.1 Interaction of carboxylic acids with the (10$\bar{1}$4) surface of calcite	148
6.1.1 Fatty acids-calcite surface interaction mechanism	149
6.1.2 Structure of the SA patches at the surface of calcite in air and in liquid	150
6.1.3 Dissolution and growth of calcite in the presence of low SA coverage	152
6.1.4 Higher SA coverage on calcite	155
6.1.5 Conclusions on the dynamic restructuring of the calcite in the presence of SA molecules on the surface	157
6.2 Chemical affinity of the carboxyl functional group with the calcite surface in different ionic solutions	158
6.2.1 Tips/surfaces functionalization strategies	159
6.2.2 Control experiments	160
6.2.3 Dilution experiments in Brine1	165
6.2.4 Dilution experiments in Brine1 and acidic Brine1	166
6.2.5 Conclusions on the carboxyl group-calcite surface affinity	167
6.3 Materials and Methods	168
6.3.1 Samples preparation for the experiments of organic patches on calcite surface ...	168
6.3.2 AFM and QNM measurements on the calcite restructuring	168
6.3.3 General procedure for force spectroscopy measurements	169
6.3.4 Protocols for tip functionalization	170
Bibliography Chapter 6.....	171
7. Conclusions and Outlook	175
8. Appendix	179
8.1 Effective ionic concentration at the surface of mica	180
8.2 New fitting coefficients of the isotherm models	183
Bibliography Appendix	185
9. Acknowledgments	187
10. Curriculum Vitae	189

Introduction

In nature the presence of an interface between a liquid and a solid is ubiquitous. Our body is composed by macromolecules immersed in water, the earth crust can be simply described by mineral rocks surrounded by oceans and most industrial processes are performed in conditions that require the presence of solids in contact with liquids. Despite the unquestioned relevance of solid-liquid interfaces, many scientific research fields and industrial applications rely on simplified or macroscopic descriptions of the system. These are continuum descriptions that have been built discarding the molecular nature of the constituents of the interfaces. Thus the resulting macroscopic concepts, such as interfacial free energy, or measurement-related quantities such as effective charge, hide the complexity of the interface under examination. Yet, it is exactly the complex chemistry and the specific molecular interaction forces at the solid-liquid interfaces that are key for phenomena such as heterogeneous catalysis, electrochemistry, crystal growth, membrane transport and body-antibody recognition. In all these cases, the intrinsic heterogeneity of the surface, composed by discrete and diversified molecular groups, creates a modulation in the interaction force between the solid and the liquid molecules in contact with it.

Among all the solid-liquid interfaces, those constituted by a charged surface and aqueous ionic solutions represent an interesting case, particularly in fields such as biology and mineralogy. The built-in electrostatic potential induces a rearrangement of the ionic species in solution. As result, the ionic density distributions deviate significantly from the bulk and an excess of opposite charged ions develop in proximity of the surface, forming the so-called electrical double layer (EDL). Theoretical models, such as the Gouy-Chapman-Stern model (GCS), have been used to describe the vertical density distributions of the ions. In the case of the GCS model, a dense, homogeneously distributed, layer (referred to as ‘Stern layer’) with a thickness of a hydrated ion, is assumed to be adsorbed onto the charged surface. It is followed by an exponentially decaying diffuse ionic cloud, produced by the ions. The GCS model relies on the so-called continuum assumption: ions are considered dimensionless charges immersed in a continuous dielectric environment. Although routinely verified far from the interface, it tends to fall short a few angstroms from the surface, where the discrete size of ions can no longer be ignored. These often oversimplified assumptions, for example, show their limits in the case of highly charged systems. Electrostatic correlation or specific ion adsorptions have been used to close the gap between theory and experimental evidences. These corrections often do not provide a comprehensive physical explanation of the actual system and since the ions are in any case considered as a gas-like cloud, the surface lateral discrete distribution of the charges is neglected.

In this thesis, I first illustrate how the assumption of a homogeneous ion lateral density in the Stern Layer fails to describe the actual solid-water interface of several relevant surfaces. Then I show how the lateral organization of the ions indeed plays a role as important as the vertical modulation of the charge distribution. This is because the molecular nature of the ions, the surface, and the water molecules themselves each contribute to precise lateral organization of the constituents. As result, the ions can reside on discrete surface sites, defined both laterally and vertically in space. Moreover, the water-mediated interaction can impart a correlation in the reciprocal lateral distribution of the ions.

The molecular characterization of solid-liquid interfaces is gaining more and more attention from the scientific community. Unfortunately most of the available experimental techniques cannot provide molecular resolution and/or local nanoscale information. They also tend to miss the intrinsic heterogeneity of the system by averaging out the interfacial properties. For example, techniques such as X-ray or neutron reflectivity and diffraction, can provide information on the

molecular arrangement of the solvent and surface atoms/molecules in the orthogonal and parallel directions, relative to the surface plane. The latter is usually only obtained with crystalline solids and the information is averaged over the lateral dimension of the incident beam (at least several micrometers) missing the local defects specificity.

In the first part of this thesis I show how it is possible to use high-resolution atomic force microscopy (AFM) to characterize solid-liquid interfaces at the atomic/molecular level, with a lateral sensitivity enabling the discrimination of surface heterogeneities and defect-related phenomena. AFM is a force-based technique that detects the vertical and lateral variation of the interaction force between a nanoscopic tip and the surface under examination. If the surface and the tip are immersed in a liquid, forces that are due to the local arrangement, and sometimes confinement, of the liquid/solutes molecules can be detected. The presence of these so-called solvation forces with a vertical and lateral modulation is related to the specific arrangement of the liquid molecules at the interface. It is precisely the existence of these forces that gives the possibility for atomic-scale contrast in dynamic AFM operational modes. In these modes, the AFM tip, at the end of a flexible cantilever, is oscillated. The tip-sample force induces a modification of the lever motion that can be monitored to reconstruct the surface topography reflecting both the arrangement of the surface atoms and that of the liquid molecules around them. The viscous environment in which the AFM cantilever is oscillated introduces some complications in the quantification of the actual interaction forces however, by using appropriate models, this problem can be solved. Moreover, this technique requires the presence of an external object (the AFM tip). The tip can significantly modify the interfacial properties of the liquid by inducing confinement or charge accumulation/depletion. Therefore special care has to be taken if information on the isolated sample-liquid interface is derived from the AFM experiments.

In the second part of this work the attention is focused on ion adsorption at solids' surfaces in liquid environment. In particular, I show how high-resolution AFM in liquid is able to give information about single ions adsorbed at hydrophilic surfaces and therefore can be used to determine the structures that the ions form in Stern Layer. By means of this technique we were able to individuate important mechanisms of lateral interactions of ions adsorbed at the mica surface and other relevant systems like self assembled monolayers (SAMs) and lipid bilayers. At the same time this technique provides an excellent tool for describing the dynamic interface between calcite and ionic solutions both in equilibrium and out-of equilibrium conditions. The latter situation induces the restructuring process of the crystal that can be followed in real time. Finally AFM, providing the tools for both imaging and quantify the mechanical properties of the sample, has been used to characterize the complex interface between fatty acid molecules adsorbed on the calcite surface and aqueous ionic solutions.

The thesis is structured as following:

- Chapter 1 begins with an overview of solid-liquid interfaces. Both thermodynamic and molecular descriptions are provided. The experimental techniques able to characterize solid-liquid interfaces are briefly reviewed. A distinction is made between 'non-perturbative' and 'force-based' techniques with particular emphasis on the latter. The types of forces associated to the properties of the interfacial liquid (solvation forces) are presented. Finally, the approach based on amplitude-modulation atomic force microscopy (AM-AFM), that relates the work of adhesion between a solid and a liquid to the local energy dissipated by AFM tip at the nanoscale, is reviewed.
- In Chapter 2 the technical description of AM-AFM in liquid is provided with special emphasis on the resolution achievable. The relationship between resolution and solid-liquid interfacial properties is discussed. In particular, solvent-related dissipative and conservative interactions are presented. To finish, a critical analysis of the contribution of the solvent in the imaging process depending on the mode of operation and the conditions employed during the image acquisition is conducted.
- The aim of Chapter 3 is to provide the experimental evidence for single ion detection with AM-AFM. In the first part, the progress made by AFM in detection of ionic distributions

at surfaces is reviewed. Subsequently, our experimental results on Rb^+ ions adsorbed on the mica surface in aqueous solution are reported. Finally, the data on the residence time of the ions on the surface and experiments aimed at determining the influence of the AFM tip on the system are presented.

- In Chapter 4 high-resolution AFM is employed to detect interesting phenomena within the Stern Layer. After a summary of the standard GCS model and limitations, the first AFM observation of a new form of correlation energy in the Stern Layer is presented. Using MD-simulations the mechanism behind this correlation energy is discerned in the case of the mica surface: metal monovalent cations can spontaneously form ordered structures on the surface by being stabilised by water molecules. We named this new form of correlation energy ‘hydration correlation energy’. Finally, the possibility to extend this phenomenon to other relevant surfaces like SAMs on gold and lipid bilayers is discussed and some preliminary experimental data presented.
- In Chapter 5 interfacial properties of calcite ($10\bar{1}4$) surface in contact with aqueous ionic solutions are examined. First, a discussion of the hydration landscape of calcite and the development of a surface charge is presented followed by a study on the interaction of specific ions such as Na^+ , Rb^+ , Cl^- and Ca^{2+} with the flat surface. Subsequently, the hydration properties of different step edges are considered showing how they are fundamental in the dynamic restructuring of the crystal. At the end, a series of experiments in which the growth and dissolution processes of the calcite are monitored in real time as a function of the ionic composition and concentration of the solutions are presented.
- Finally in Chapter 6 a more heterogeneous interface composed of fatty acid organic molecules adsorbed on a calcite surface is examined. Here the AFM is used in different ways (imaging and force spectroscopy) to gain insights into the dynamical changes occurring at the surface of calcite in ionic solutions with different composition and concentration. In the last part a study on how the affinity between the carboxylic functional group and the calcite’s surface is influenced by ionic environments and pH is presented.

During my PhD I have been involved also in a different project in collaboration with the group of Prof. Alfredo Alexander-Katz (Laboratory of theoretical Soft Matter, MIT, Massachusetts, USA). A study with AFM and Quartz Crystal Microbalance (QCM) on the interaction between water-soluble gold nanoparticles coated with mixed ligand organic layer and lipid membranes has been performed. Our findings show that the fusogenic pathway of the nano-objects was facilitated at the membrane defects like bilayer edges or membrane high curvature. Dr. Van Lehn with MD-simulations showed that this preferred pathway was due to a higher rate of lipid tail fluctuation in the water media enhancing the hydrophobic contact probability between lipid molecules and hydrophobic residues on the nanoparticles surface. Nevertheless this work has not been presented in this thesis to maintain the homogeneity and consistence of the discussion.

Chapter 1

Solid-liquid interfaces: from a thermodynamic description to a molecular characterization

Solid-liquid interfaces are the central theme of this thesis. In this chapter, I will introduce the concepts that are necessary to the description and modeling of these interfaces - from thermodynamics to molecular characterization (section 1.1). The concepts of surface energy and work of cohesion (subsection 1.1.1), interfacial energy and work of adhesion (subsection 1.1.2) will be derived and put in context with the molecular description of the interfacial region.

The experimental techniques that are able to characterize solid-liquid interfaces will be briefly reviewed with some relevant examples (section 1.2 and 1.3). A distinction will be made between ‘non-perturbative’ (section 1.2) and ‘force-based’ (section 1.3) techniques, exposing advantages and limitations in each case. This thesis is largely focused on force-based measurements, hence a particular attention will be given to the types of forces that are associated to the properties of the interfacial liquid (section 1.3). Finally, I will present an approach based on Amplitude-Modulation Atomic Force Microscopy (AM-AFM) that relates the work of adhesion between a solid and a liquid to the local energy dissipated by an AFM tip at the nanoscale (section 1.4).

1.1 Solid-liquid interfaces: from a thermodynamic description to a molecular picture

To form a solid-liquid interface, the surfaces of a solid and a liquid have to be put in contact. An appropriate description of the interface therefore starts from the definition of isolated surfaces and then extends to the contact between the two dissimilar materials. I will focus specifically on the interface of a solid and a liquid and I will provide both a thermodynamic and a molecular description of the system.

1.1.1 Surface energy and work of cohesion

From a thermodynamic prospective, the free energy γ , that is associated with the formation of a surface unit of area, is related to the Gibbs free energy G through:

$$dG = -S dT + V dP + \sum_i \mu_i dN_i + \gamma dA \quad \Rightarrow \quad \gamma \equiv \left. \frac{\partial G}{\partial A} \right|_{T,P,N_i} \quad (1.1)$$

where T is the temperature, S the entropy, V the volume, P the pressure, μ_i the chemical potential of the species i , N_i is the number of molecules of species i and A the area. The surface (free) energy γ is by definition the energy needed to increase the surface by a unit of area, while keeping constant temperature and pressure of the closed system. Equivalently we can express γ as:

$$\gamma = \frac{1}{2} W_C \quad (1.2)$$

where W_C is the free energy change, or reversible work done (work of cohesion), to separate a unit area of two surfaces or media from contact to infinity in vacuum (Fig. 1.1.A). For solids, γ is denoted by γ_S and expressed as energy per unit area, while for liquids by γ_L and given as tension (force) per unit length. The two options are numerically and dimensionally equivalent.

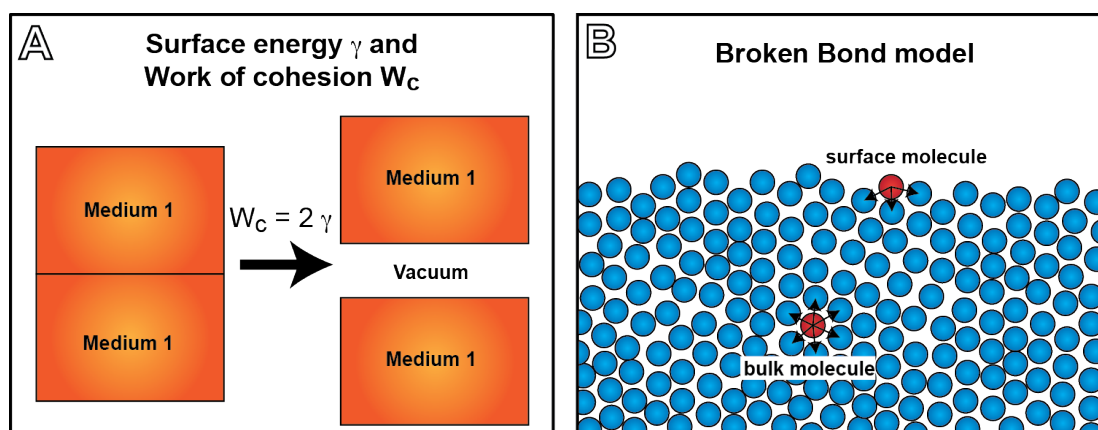


Figure 1.1: Schematic representations of the surface energy. (A) Classical model, where the work of cohesion spent to separate two identical surfaces in vacuum is related to the surface energy γ . (B) Schematic representation of the broken bond model that gives a molecular description of the surface energy.

At the molecular level, the surface energy can be understood by considering the difference in energy between a molecule/atom at the surface and one in the bulk at thermodynamic equilibrium. Each molecule or atom located in the bulk of a medium shares more bonds with nearest neighbors than at the surface (Fig. 1.1.B). If the energy associated with each bond is known, the surface energy can be understood as the excess of energy per unit area at the surface with respect to the bulk due to the under-coordinated atoms (dangling bonds). This way of calculating the surface energy is called broken bond model with nearest neighbor approximation. This model is useful to

provide an intuitive understanding of surface energy at the molecular level. However, it contains several simplifications.

In the case of solids, a typical bond energy per atom ranges between 1 and 10eV. Due to the under-coordination, atoms at the surface tend to be highly reactive and thus are likely to undergo a surface reconstruction. This lowers the surface energy and has to be considered to estimate the effective γ . In liquids, molecules are held together by bond energies typically ranging between 0.1 and 1eV. Although it is still possible to define nearest neighbors, molecular mobility and the absence of long-range order prevent an accurate description of surfaces with the broken bond model. In this case, the surface is not an infinitesimal sharp boundary, but it has a certain thickness in equilibrium with vapor. It is also often necessary to consider the orientation of the molecules at interfaces, particularly in polar liquids. A detailed description of the finite extension of liquid-vapor interface is beyond the scope of the present thesis and can be found in Refs. [1,2].

1.1.2 Interfacial energy and work of adhesion

The concepts defined for surfaces can easily be extended to interfaces. The work of cohesion W_C becomes the work of adhesion W_{12} when two different media (1 and 2) are considered (see Fig.1.2A). Since all media attract each other in vacuum, W_{12} is always positive. This means that energy is always gained by creating an interface as opposed to two single surfaces exposed to vacuum.

In analogy to the surface energy, it is possible to define the interfacial energy γ_{12} as the free energy change associated with the expansion of the interface by a unit area. The energetics associated with this process may be understood by splitting the expansion into two hypothetical steps: first, unit areas of media 1 (solid S) and 2 (liquid L) are created, and then they are brought into contact. The total free energy change γ_{LS} of the process is:

$$\gamma_{SL} = \frac{1}{2} W_{SS} + \frac{1}{2} W_{LL} - W_{SL} = \gamma_s + \gamma_L - W_{SL} \quad (1.3)$$

Eq. 1.3 is often referred to as the Dupré equation (see Fig.1.2A). W_{LL} and W_{SS} are effectively the works of cohesion (denoted as W_C in subsection 1.1.1) of the liquid and the solid, respectively.

Experimentally W_{SL} is typically obtained by measuring the so-called ‘contact angle’ θ_C , the angle formed by a drop of liquid on the surface of a flat solid in ambient atmosphere. The contact angle θ_C (see Fig.1.2B) can be directly related to W_{SL} by the Young-Dupré approximation:

$$W_{SL} = \gamma_L(1 + \cos \theta_C) \quad (1.4)$$

A full derivation of Eq. 1.4 can be found in Ref. [3]. The contact angle has been widely used to describe the affinity of liquids with solid surfaces. To date, it remains the fastest and simplest measurements of the work of adhesion between a solid and a liquid. The technique is by definition macroscopic. It relies on averaging along the macroscopic interface and, thus, cannot provide information about the nanometer scale, i.e. the local distribution of the liquid molecules at the solid’s surface.

The work of adhesion originates from the direct molecular interaction energy between the solvent molecules and the surface of the solid, but not only. The presence of the surface generally modifies the molecular ordering of the solvent molecules. This effect has been found to decay rapidly with distance, extending only a few molecular layers away. We may refer to this region as the solvation zone, wherein the properties of the solvent (density, positional and orientational order, mobility, etc.) are significantly different from the corresponding bulk values. Since the intermolecular bond energy is usually much smaller for liquids than for solids, it is reasonable to assume that most of the molecular restructuring at the interface occurs in the liquid; in other words, the restructuring of the solid surface is in first approximation negligible. Under this approximation the interfacial energy corresponds to the energy involved in the molecular restructuring of the liquid molecules in the solvation zone (see Fig. 1.2C). In specific cases, the

liquid can chemically modify the solid's surface (e.g. oxidation or desorption of ionic species) and the above description of the interface energetics is no longer valid. Such processes can be difficult to describe in the presented framework. It is then often useful to consider a new effective (modified) solid's surface.

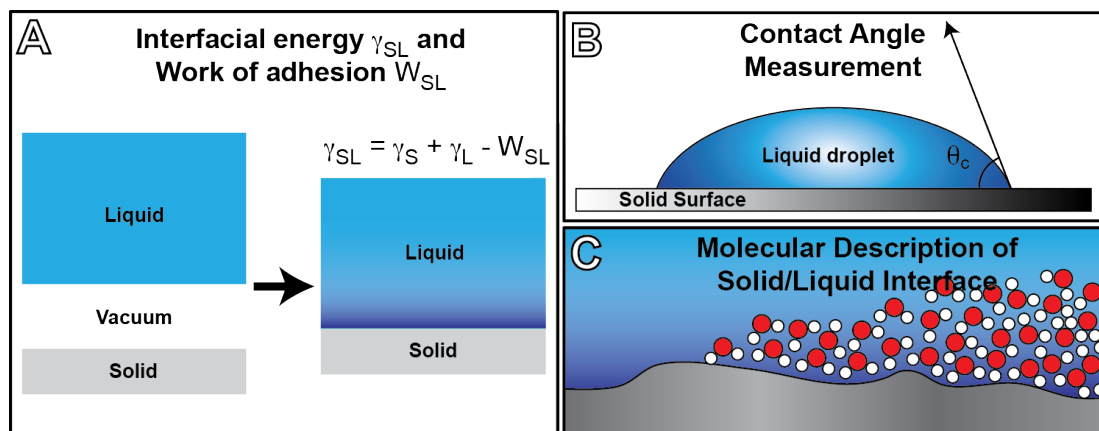


Figure 1.2: Schematic representation of the interfacial energy from a macroscopic/thermodynamic prospective (A). In (B) the representation of the contact angle measurement and in (C) the cartoon that represents the solid-liquid interface from a molecular point of view. The water molecules are schematically represented and do not reflect the actual structure of the interfacial water particularly in terms of hydrogen bonds' network.

From a theoretical perspective, Monte Carlo simulations of the interface based on a Lennard-Jones potential⁴ showed that different configurations for the interface are possible, depending on the mutual interaction between the liquid molecules and the solid surface. An attractive pairwise interaction among the liquid molecules prevents packing against a non-attractive wall, which leads to the formation of a liquid/vapor like interface in contact with the solid. In this case the liquid does not “wet” the solid surface. When an attraction between the liquid and the wall is added, wetting occurs: the liquid molecules form layered structures in proximity to the wall with a significant density variation respect to the homogeneous bulk. This layering is reflected in an oscillatory density profile that extends several molecular diameters into the liquid.⁴ If the surface is idealized to be “mathematically” smooth,⁴ the ordering of the molecules within each layer will be random or disordered, exhibiting only short-range liquid-like order. However, a structured surface, even at the atomic level (for example, a crystalline lattice), will induce epitaxial order within the layers. Such cases exhibit both out-of-plane and in-plane ordering. The former referring to the existence of layers, the latter to the existence of lateral order within the layers themselves.

Water as a solvent

The strong propensity of water molecules to form H-bonds with each other influences the interactions with both nonpolar and polar molecules/surfaces, often leading to unusual effects. The main difference between a dipolar and the H-bond interactions comes from the high directionality of the bonds that tends to locally create tetragonal coordinative states between the water molecules. When a water molecule comes into contact with a non-polar (non H-bond sharing) molecule or surface, it will have to pay an energy cost to reorient in a way to minimize the non-shared H-bonds irrespective to the direction that the water molecule faces. This phenomenon is often referred to as hydrophobic solvation or hydrophobic hydration. The reorientation, or restructuring, of water around hydrophobic solutes or surfaces is entropically unfavorable, as it disrupts the existing water structure imposing a new and more ordered structure on the surrounding water molecules. In contrast, hydrophilic molecules or surfaces have a propensity to contact with water molecules rather than with each other, resulting in a net repulsive force between them. The directional binding of water at hydrophilic surfaces adds an additional steric barrier that increases the range of the repulsive force between two hydrophilic surfaces in water.

At interfaces, at least three different parameters of ordering can be identified for water: (i) positional ordering into layers, which affects the oscillatory forces and manifests itself also in other type of liquids, (ii) orientational ordering, which affects mainly the local electrostatics (local variation of dielectric constant), and (iii) mean density variations near the surfaces, which can give rise to the additional “steric” repulsion between hydrophilic surfaces and a “depletion” attraction between hydrophobic surfaces. Hydrophilic and hydrophobic interactions are interdependent and not additive and thus specific the surface and local physiochemical properties.

The presence of a solid surface in water induces local variation of the liquid properties at the molecular level, both vertically and laterally. ‘Real’ surfaces are usually highly heterogeneous even at the atomic level, where defects like steps, vacancies or specific chemical groups modify the interaction with the liquid molecules and “longer range” distribution/orientation. The contact angle measurements provide a macroscopic reflection of all these effects but also depend on microscopic variations of the surface roughness. Measurements of inhomogeneous interfaces remain particularly challenging, e.g. solid surfaces that are composed of nanoscale domains with different affinities for the liquid. Yet, often these fine lateral inhomogeneities on the nanometer scale produce the most intriguing interfacial phenomena, ranging from the specific function of a protein in the brain to the toxicity of synthetic nanomaterials. In most cases, the interaction of natural or synthetic nanoscale object with the surrounding strongly depends on the local structure of the interfacial water. With the advent of nanomedicine, there is an increasing need for methods able to image and quantify complex solid-liquid interfaces with sufficient lateral resolution.

1.2 Experimental techniques to characterize solid-liquid interfaces

The properties of a solid-liquid interface in terms of liquid densities, orientation variations or chemical information can be experimentally probed by various techniques, such as infrared spectroscopy, Raman spectroscopy, UV-vis spectroscopy, fluorescent emission, ellipsometry, surface plasmon resonance or quartz crystal microbalance.⁵ Here I will review some of the techniques most relevant to this thesis, namely X-ray/neutron scattering and spectroscopy, and non-linear optics. These techniques are usually non-perturbative, but they tend to lack of local information since they rely on averaging over hundreds of micrometer. A more complete review of the subject can be found in Refs. [5,6].

1.2.1 X-ray spectroscopy and scattering

One great advantage of the use of X-rays as probes for solid-liquid interfaces is the fact that they can penetrate deep into the liquid and therefore easily reach the interfaces. Due to short wavelengths, X-rays can measure atomic-scale structures, such as the separation of individual atoms or molecules. However, most X-ray-based techniques are not intrinsically surface sensitive, and special schemes are required to discriminate between the signals originating from interfaces and the much more intense signals originating from the bulk. In most X-ray absorption experiments, this is accomplished either by using high-surface-area solids or by taking advantage of the unique compositions or chemical features at the interface. In diffraction experiments, the beam-surface angular geometry may be used for selective surface probing. In any case, because high-intensity and focused X-ray beams are used, these techniques are difficult to implement: synchrotron sources may be required, and provisions may be needed to avoid sample damage.

X-ray absorption spectroscopy

X-ray absorption spectroscopy is a technique commonly used for the characterization of materials. These spectra are element sensitive being the excitation energy of a specific core level characteristic of the electronic properties of that atom and of its chemical environment. The electronic excitation corresponds to a peak in the absorption spectra. This technique is extremely

useful to investigate the chemical properties or reaction happening at the interface, but usually cannot give information about the 3D spatial distribution of the analyzed chemical species.

A relevant example can be found the work of Peak *et al.*⁷ In this study, they used extended X-ray absorption fine structure (EXAFS) to determine the bonding mechanisms of selenate (SeO_4^{2-}) and selenite (SeO_3^{2-}) on aluminum oxide/water interface over a wide range of pH. EXAFS looks at intensity oscillations in the absorption spectrum near an absorption edge, i.e. the energy at which a specific core level starts to be excited. These oscillations are due to interference of the forward-propagating waves with electron backscattered from neighboring elements. By Fourier-transform analysis, it is possible to obtain information on the local structure around the element being probed in the form of bond distances and average coordination numbers. Peak *et al.*⁷ applied this technique to the Selenium K-edge and found that selenite forms a mixture of outer-sphere and inner-sphere surface complexes (see Chapter 4), while selenate forms primarily outer-sphere surface complexes on aluminum oxide.

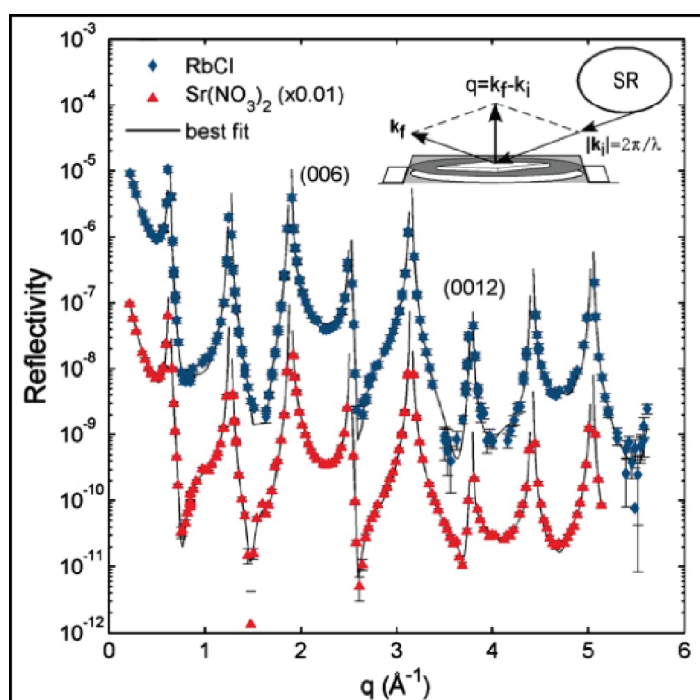


Fig. 1.3: Example of X-ray reflectivity data. The reflectivity is obtained in the specular geometry (inset of the figure) at the mica/water interface in the presence of RbCl and $\text{Sr}(\text{NO}_3)_2$. By varying the incident angle but maintaining the specular geometry, the reflectivity is obtained as a function of different values of q (momentum transfer perpendicular to the interface). From these data is possible to obtain the total interfacial electron density profile perpendicular to the mica surface. Figure adapted with permission from Ref. [8].

X-ray reflectivity

Aside from absorption spectroscopy, X-rays can be used to probe the distribution of the atoms/molecules at the interface by scattering. Grazing-incidence geometry is generally employed to enhance the surface component of the signal. One of the most widely used techniques is X-ray reflectivity.⁶ In this technique a collimated coherent beam of X-rays is shined onto the solid surface (immersed in a liquid) and the reflected beam is monitored by a photo-detector that records the scattered intensity (see Fig.1.3). The efficiency of the scattering is related to the local electron density and so to density of surface/liquid molecules. In the simple case of the mirror-like reflection of X-rays (i.e. specular reflectivity), the structure of the interface is probed only along the surface-normal direction and the incident angle is varied while recording reflected X-ray intensities (see Fig.1.3). These intensities vs. incident angle curves constitute the X-ray reflectivity data and have a similar theoretical foundation as X-ray crystallography. Non-specular reflectivity data can also be obtained by monitoring the intensity in the non-mirror geometry. In this case the momentum transfer has a component parallel to the surface plane and it is possible to

obtain information on the lateral structure of the interfacial liquid.

In recent years, substantial progress has been made in the direct observation of solid-liquid interfaces with non-aqueous fluids. As predicted by theory, liquid density oscillations near solid surfaces have indeed been observed in systems where normal molecular liquids were put in contact with smooth surfaces. Yu *et al.*^{9,10} reported the direct observation of an internal layering in thin liquid films of nearly spherical, nonpolar molecules (tetrakis(2-ethylhexoxy)silane and tetrakis(trimethylsiloxy)silane on a silicon oxide surface using synchrotron x-ray reflectivity. Reflectivity data showed three electron density oscillations near the solid-liquid interface, with a periodicity consistent with the molecular dimensions. Similar results were obtained by Doerr *et al.*¹¹ The direct evidence for such oscillations was obtained for both thin films and macroscopically thick layers, suggesting that the layering was intrinsic to the isolated interface. The silicon-oxide surface, used in these experiments to create the solid-liquid interface, is amorphous and acts as a model system of a “structureless wall” which renders lateral ordering of molecules impossible.

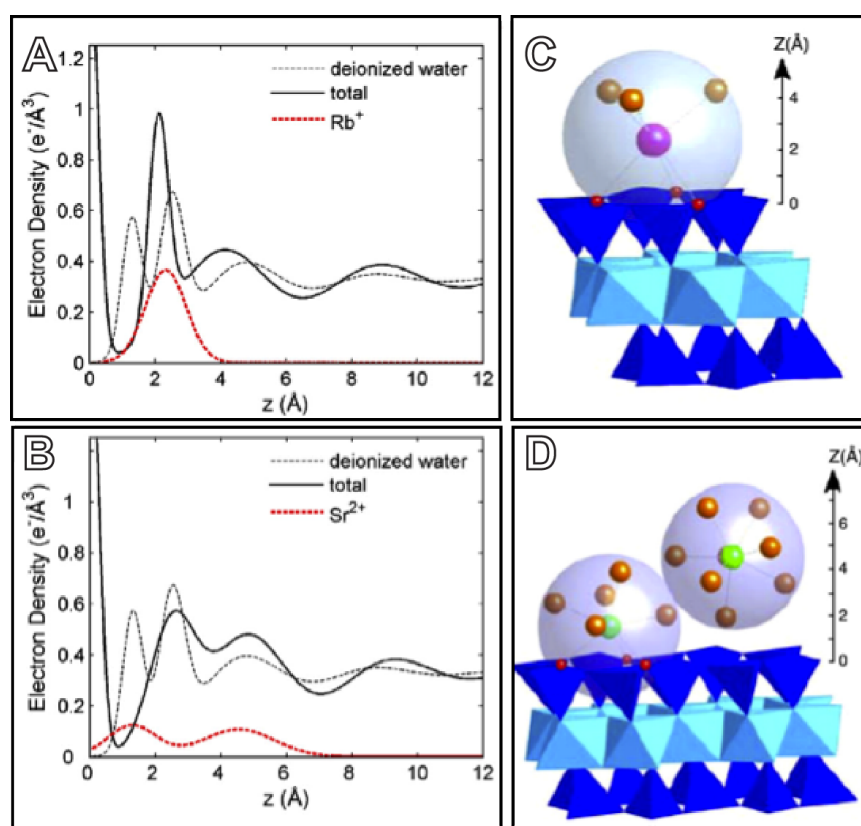


Fig. 1.4: Total (XR) and ion-specific (RAXR) electron density profiles in the direction orthogonal to the mica surface for (A) Rb⁺ and (B) Sr²⁺ solution in water. Schematic representation of (C) Rb⁺ and (D) Sr²⁺ aqueous complexes on the mica surface based on the measured ion adsorption profiles and known ion-hydration structures in bulk solution. Magenta: Rb⁺, green: Sr²⁺, orange: water, red: surface oxygen. Figure adapted with permission from Ref. [12].

A different situation arises for the interaction of water molecules with hydrophilic surfaces. The first direct experimental observations of density oscillations at solid–aqueous interfaces were observed adjacent to conducting substrates under potentiometric control.¹³ Toney *et al.* showed by X-ray scattering that the water density perpendicular to a silver electrode under an applied electric field has an oscillating behavior. The water molecules are ordered in layers extending up to three molecular diameters from the surface of the electrode. The first layer exhibited an increased density and orientation if compared to the bulk water. Later the technique was used to describe water–mineral insulating interfaces, such as mica¹⁴, calcite¹⁵ and barite¹⁶. In all these studies, a vertical layering of the water molecules was consistently found, often in conjunction with a lateral molecular ordering¹⁵. Moreover the possibility to combine X-ray scattering with element sensitive information like resonant anomalous x-ray reflectivity (RAXR), enabled Park *et al.*⁸ to combine

the water density distribution with an information on the specific cationic distributions and the associated changes in the structure of the hydration layers for different ions at the mica-electrolyte solution interface (see Fig.1.4).

X-ray scattering offers an important reference point for the description of isolated solid-liquid interfaces. The possibility to describe an unperturbed interface is giving crucial complementary information to more invasive measurements, such as with AFM, helping to disentangle the actual interfacial properties from measurement-induced modification of the system (see Chapter 3).

1.2.2 Neutron scattering

Neutron scattering uses a monochromatic neutron beam as a probe. The beam is reflected on a large flat surface and the intensity of the specular reflection is measured as a function of either angle or wavelength of the incoming neutrons. Just as the reflection of light on a thin uniform film leads to interference fringes, neutron reflection also gives rise to interference. For both type of experiments, the separation of the fringes is directly related to the film thickness and the amplitude depends on the relative refractive indices (different for light and neutrons) of the three media concerned. Although neutron scattering is not intrinsically sensitive to surfaces, the grazing incidence geometry of neutron reflection and the possibility of varying neutron refractive indices by isotopic substitution make reflection extremely sensitive to selected parts of many interfacial layers. The technique is able to probe the average structure along the surface normal, when the layer is too disordered or complex to be investigated by other methods. This technique has been widely used to characterize the adsorption of surfactant molecules at the air-water interface and more complex interfaces like water/air interface and molecules adsorption at solid-liquid interface.¹⁷

1.2.3 Non-linear optics techniques

Optical second-harmonic generation (SHG) and sum-frequency generation (SFG) have proved to be powerful techniques to study solid-liquid interfaces. These second-order non-linear optical processes are intrinsically surface specific. For a detailed review on these techniques I suggest Refs. [18,19].

Sum-frequency generation

In the SFG technique, two photons are combined at a surface; an infrared (IR) photon from a tunable IR laser is used to excite the vibrational modes of the interface, and a second photon in the visible region, from a second (frequency-fixed) laser is used to energy up-convert the IR photons (see Fig.1.5A). The high-intensity electric field produced by the last incident laser beam induces a coherent nonlinear polarization in the molecules at the interface. This oscillating nonlinear polarization is the source of the collected sum-frequency light. When the infrared source is tuned through the spectral region of interest, coincidence between the photon energy and the energy of the molecular vibrational mode results in a resonant enhancement in the sum-frequency response.¹⁹ Peaks in the sum-frequency collected as a function of the IR photon energy correspond to specific molecular vibrational mode. Vibrationally resonant SFG can be used to measure the coherent vibrational surface spectrum from the interface, which contains information about the molecular composition, order and chirality. The most commonly employed geometry is the reflection geometry from a planar interface, but scattering SHG or SFG, is used even to probe the interfaces of micrometer and nanometer sized particles, droplets and liquid jets.²⁰

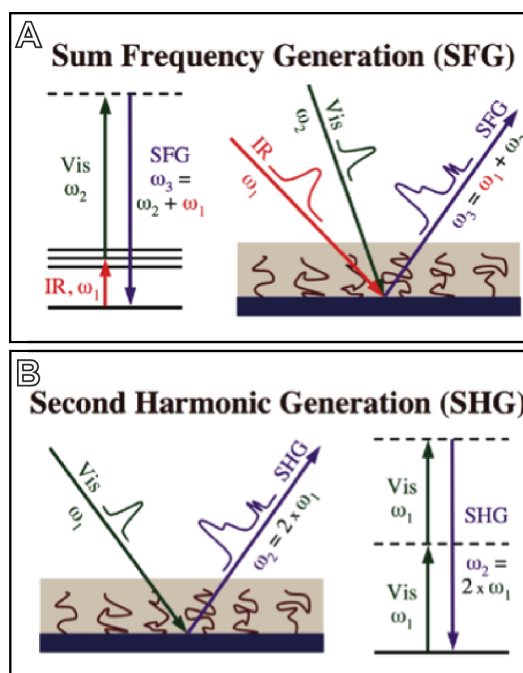


Fig. 1.5: Schematic representation of the two non-linear optics techniques presented in this subsection. (A) Sum frequency generation (SFG) and (B) second harmonic generation (SHG). Figure adapted from Ref. [5].

SFG is particularly useful for the characterization of water-solid interfaces since the water vibrational spectrum provides a sensitive probe for the structure and energetics of a hydrogen-bond network at the interface. However, the interpretation of the results has shown to be sometimes controversial.¹⁹ Generally the vibrational energy spectra of water present complex features that can be divided into three groups: (i) an “ice-like” energy region, corresponding to the typical stretching modes of bulk ice; (ii) a “liquid-like” energy region of the weakly correlated hydrogen-bonded stretching modes of molecular water and (iii) a sharp spectral feature at higher wavenumber that reflects the lack of donor bonding with other water molecules, normally associated to the vapor phase.¹⁹ These features are sometimes simultaneously present in the vibrational spectra of interfacial water, giving rise to a controversial interpretation of the actual water interfacial structure.

As an example, Ostroverkhov *et al.*²¹ were able to study the structure of water at water/quartz interface at different pH and to compare the results with those from the water/silica interface measured under the same experimental conditions. In both cases, they found “ice-like” and “liquid-like” energy peaks, suggesting the presence of more ordered interfacial water layers at the surface of the crystalline oxide. Water adsorbed on a mica surface at room temperature also presents a more ordered hydrogen-bond structure than bulk water.²² An example of a more complex water-based interface can be found in the work of Scheu *et al.*²³ who investigated hydrophobic/water interfaces. One of the most remarkable features of this interface is that it carries a negative charge. This negative charge has been measured on air bubbles, hydrophobic nanoparticles and droplets using mainly electrophoretic techniques. While the sign of the charge at neutral pH is negative, the physicochemical origin has lately been debated. The most intuitive and long-standing explanation is that OH⁻ ions, naturally present in the water, preferentially adsorb at the interface. Scheu *et al.*²³ measured the vibrational sum frequency scattering signal of deuterated water in contact with deuterated n-hexadecane nanodroplets in multiple polarization combinations and as a function of pH. They found that although the electrokinetic mobility increases with pH, the SFG spectra do not change with increasing pH, and do not contain any evidence for the presence of interfacial hydroxyl ions, indicating that the commonly accepted theory of OH⁻ surface enrichment may be incorrect.

Second harmonic generation

Second harmonic generation (SHG) is a two-photon process where both photons are provided by the same laser source (see Fig.1.5B). It may be considered as a simplified version of SFG. However, because the excitation light used in SHG is typically in the visible range, most of the information extracted from the data is related to electronic rather than vibrational properties of the system. SHG can also be used to measure time-dependent phenomena, both on flat surfaces and on the curved surface of nanoparticles or self-assembled layers up to the picosecond time domain.⁵ Subir *et al.*²⁴ successfully used SHG to measure the protonation reaction of the carboxyl (-COOH) functional group fixed at the surface of polystyrene carboxylate microspheres. They measured the SHG of this system as a function of pH. Since the degree of ionization of the surface carboxyl groups is pH dependent, the SHG signal detected as a function of bulk pH provides information about the fraction of carboxyl groups that are ionized (see Chapter 6). They showed that it is possible to determine the pK_a of carboxyl groups at the particle-liquid interface and that it differed significantly from the standard bulk value: the surface pK_a being 5.4 corresponds to a K_a that is four times smaller than that of long chain carboxyl acids in bulk aqueous solution.

1.3 Force-based techniques: Surface Force Apparatus and Atomic Force Microscopy

In the previous section, I have reviewed techniques that are able to characterize an interface by looking at the density or orientational/vibrational distributions of the solvent molecules in proximity to the solid. Surface-sensitive spectroscopic techniques can provide valuable information on solid-liquid interfaces. However the acquired information is averaged over the incident beam spot that generally exceeds in dimensions the micrometer length scale. Even if molecular information is obtained it lacks nanometric lateral resolution.

Alternatively, it is possible to investigate the properties of solid-liquid interfaces through the direct measurement of forces between two solid objects immersed in a liquid as they are brought into contact. Techniques such as surface force apparatus (SFA) or AFM can precisely derive information of force vs. distance between two macroscopic objects (SFA), or between a surface and a nanoscopic tip (AFM). By introducing a solvent between the two solids it is possible to relate the measured force to the properties of the combined solid-liquid interfaces. Moreover, in the case of AFM, extra lateral information can be obtained, often down to the atomic level. In contrast to non-perturbative techniques, where a single interface is investigated, force-base techniques effectively combine two solid-liquid interfaces that coalesce as the two solids come into contact. In an ideal situation, it should be possible to directly relate the measured forces to the actual density distributions and energetic of each single interface, but often the two solid surfaces at close distances introduce complications, such as liquid confinement or other severe perturbations of the single interface as we will see in the following subsections. Furthermore, in AFM measurements, one of the interfaces is often poorly characterized.

1.3.1 Forces between two solid surfaces in a liquid medium

The net force that acts between two macroscopic bodies is the result of all the microscopic interactions between constituents. The system is effectively a many-body problem, where the pair interaction potential $w(r)$ between two molecules or atoms depends on the local environment. This complicated problem is often simplified by assuming that the total interaction potential between the two macroscopic objects is simply the sum over all pair potentials.

If we assume $w(r)$ to be the additive pair potential between two atoms or molecules of the solid, the net force $F(D)$ between two macroscopic solids in vacuum at a the distance D from each other is:

$$F(D) = -\frac{\partial W(D)}{\partial D} \quad (1.5)$$

where $W(D)$ is the net interaction potential obtained by summing all the molecular interactions and taking into account the solid's geometry. The forces experienced by two objects in vacuum are mainly electrostatic forces in the presence of surface charges, attractive van der Waals forces, repulsive contact forces at short range and specific chemical forces due to the formation of new bonds between the two surfaces upon contact.

The different types of forces will be analyzed in the Chapter 2. Here, we focus on the effect that replacing vacuum by liquid has on the force between the two objects. First, the liquid induces a modification of the dielectric constant between the two interacting objects. A corrected constant can be used in first approximation, but the concept itself of dielectric constant is macroscopic. More complex effects related to the molecular nature of the liquid molecules have been shown to play an important role when the gap between the two surfaces is comparable with the typical dimensions of the liquid molecules. For example, the presence of an interface can locally modify the rotational properties of polar liquid molecules, inducing nanoscale variations of the dielectric constant.

Second, forces can arise when solute molecules are present in the liquid between the two surfaces, like ions in water. If these molecules have a non-homogeneous spatial distribution at the interface, like in the case of accumulation of counterions at charges surface, bringing two surfaces in close proximity will induce a local change in the density of the solute molecules in the gap formed between them. This produces a repulsive pressure between the two surfaces that has an entropic origin. The phenomenon, described by the so-called contact value theorem, is at the origin of electrostatic double layer force, examined in Chapter 4.

Third, the solvent interaction with the two objects gives rise to so-called solvation forces between the solids. Although extensive experimental evidences confirm the existence of solvation forces, the actual dependence on the distance between the solids is often ambiguous. This is because solvation forces are usually extrapolated by removal of the other contributions to the total force measured, summing up errors from the different forces' models. Short-range oscillatory solvation forces can arise when spherical liquid molecules are induced to order or "structure" into quasi-discrete layers between two confining surfaces or within any highly restricted space. Oscillatory forces have mainly a geometric origin and they depend critically on the shapes of the liquid molecules. Other solvation forces, normally related to water as a solvent, can decay monotonically with distance. These can be repulsive or attractive, and are less well understood. Solvation forces depend not only on the properties of the intervening liquid, but also on the chemical and physical properties of the surfaces, being hydrophilic or hydrophobic, smooth or rough, amorphous or crystalline (atomically structured), homogeneous or heterogeneous, natural or patterned, rigid or fluid-like. These factors affect the structure that confined liquids adopt between two surfaces, which in turn affects the solvation forces.

Solvation forces

The steric nature of oscillatory solvation forces is generally well accepted. This oscillatory behavior derives from the local density variation of the solvent molecules under confinement. These variations depend on the intrinsic structuring of the molecules at each isolated interface but also from geometrical constraints. When two surfaces approach each other, an excess entropic pressure can rise due to a variation of the density of liquid molecules at each surface and/or at the midplane placed at the mid distance between the two. For two inert surfaces, i.e. without any attractive liquid-liquid or liquid-wall interaction, this is simply due to a change in the liquid molecular packing due to a constrained geometry.²⁵ As the liquid layer is squeezed out there is a variation of local molecular density that gives rise to an oscillatory force/pressure. In first approximation, the entropic solvation contribution to the total interaction energy between two identical surfaces separated by a distance D can be described as follow:³

$$W(D) = W(0)\cos\left(\frac{2\pi D}{\sigma}\right)e^{-\frac{D}{\sigma}} \quad (1.6)$$

where σ is the typical molecular diameter (supposing quasi-spherical molecules) and $W(0)$ is a constant that takes into account the contact energy between the two surfaces. Experimentally, the dependence of the oscillatory decay on the degree of confinement is not trivial and, in the case of the AFM, can be nearly linear due to a lack of symmetry at the tip apex²⁶.

In practice the interaction force between the solids reflects both local density variations induced by the intrinsic distribution of the liquid molecules at the solid-liquid interfaces and the confinement-induced density variation due to the two approaching surfaces. The oscillatory density profile of a single interface and the oscillatory force experience between two surfaces that are confining a liquid are not the same phenomenon, even if related to each other. The more the isolated surface of the solid induces a significant deviation in the liquid density in the proximity, the more, under confinement, the liquid density in the gap will deviate from the bulk values. This is translated into a bigger component in the measured solvation force. If the surface-liquid interaction is much weaker than the liquid-liquid interaction, the oscillatory force tends to be overall more attractive. This complex behavior often exhibits both a short-range oscillatory part and long-ranged monotonic part generally associated to the presence of water as a solvent.

Monotonic long-range solvation forces remain controversial. In the case of water, the short-range forces between surfaces and aqueous salt solutions display some highly unusual properties that are, despite intense experimental and theoretical studies, still poorly understood. These forces can be strongly monotonically repulsive, attractive, oscillatory, or a combination of these.

In the case of two hydrophilic surfaces, two other repulsive hydration contributions can be found in literature, both of them exponentially decaying as a function of the distance: the so called “primary hydration forces”, with a decay length of 2–4 Å²⁷ and the “secondary hydration forces”, with a much bigger decaying length (10–30 Å)²⁸. The first component is normally linked to the enthalpic adsorption or “binding” energy of successive water “layers” to any hydrophilic surface.²⁸ The secondary hydration forces are associated to weaker interactions with a larger decay length. The nature of these interactions is highly debated but seems to be in any case associated to the presence of hydrated solutes in the liquid.²⁷ Parsegian *et al.*²⁸ associated the decay length of these forces to the typical length of solute distribution coming from the “competition” between the amounts of water bound to counterions. It is the distribution of the hydrated solute near the interface that sets the force and the corresponding decay. Parsons *et al.*²⁹ attributed it to the specific hydration properties of the ions at the surface of hydrophilic solids that are not considered in the classical continuum description of interfacial forces. In my opinion, the broad range of models and approximations used to extract information about the hydration forces does not allow for fair and quantitative comparison between different experiments, often leading to confusions and controversies.

In contrast to some hydrophilic surfaces that exhibit enhanced repulsion in water, some hydrophobic surfaces experience an anomalously strong attraction in aqueous solutions, much greater than expected from the London or Lifshitz theories of van der Waals forces. Hydrophobic forces have been described by a full force-law in pure water that follows a double exponential behavior of the type:

$$F = -C_1 e^{-D/D_1} - C_2 e^{-D/D_2} \quad (1.7)$$

where D_1 and D_2 as well C_1 and C_2 are system-specific constants generally obtained experimentally. There is, however, some uncertainty about the values of the four constants, and even a debate on the existence of such a “universal” force-law for the hydrophobic interactions.³ Like in the case of the monotonically repulsive hydration force, the origin of the hydrophobic force is still unknown, and it is not clear whether it should be considered as a solvation force or as some kind of long-range electrostatic or van der Waals-like interaction. It appears, however, to be a surface force rather than a body force. There are currently three main theoretical hypothesis to explain the hydrophobic force, based on one of the following possible mechanisms: (i) vapor bridges, due to the attractive capillary force between bridging nanoscopic bubbles (Laplace pressure); (ii) water structure, as an attractive hydration force associated with changes in the density or ordering of water between two approaching hydrophobic surfaces; (iii) and

electrostatic, as an attractive electrostatic van der Waals–like force between correlated charges or dipoles at the surface. These types of forces are generally easy to identify being associated to the specific chemical composition of the two interaction surfaces.

1.3.2 Surface Force Apparatus

Over the past decades, SFA has enabled to identify and quantify most of the fundamental interactions between surfaces in aqueous solutions, in the presence of ions and in non-aqueous liquids. These include the attractive van der Waals (Chapter 2) and repulsive electrostatic double-layer forces (Chapter 4), oscillatory (solvation) forces, repulsive hydration forces, attractive hydrophobic forces, steric interactions involving polymeric systems, viscous forces, capillary and adhesion forces and friction and lubrication forces.

In a typical SFA experiment two macroscopically curved, atomically flat surfaces of mica are approached with nanometer precision and the interaction force between them is measured using a variety of force-measuring springs. The two surfaces are usually in a precise crossed-cylinder configuration. The separating distance is then measured with a multiple beam interferometry using fringes of equal chromatic order (FECO). From the positions of the colored FECO fringes the thickness of adsorbed layers and the absolute distance between the two surfaces can be derived, as well as the refractive index of the medium between them. The normal and lateral distance resolutions are about 0.1 nm and 1 μm , respectively, and the force sensitivity is about 10^{-8} N. By monitoring the force between the two approaching or retracting surfaces the force-law $F(D)$ can be determined and the energy between surfaces calculated knowing the precise geometry of the system.

Since the SFA's invention about 40 years ago, it has proved to be particularly effective for precise measurements of forces between macroscopic surfaces.³⁰ Further development enabled force measurements in liquids³¹ with precise quantification of repulsive double layer, repulsive hydration forces and the influence of the ionic species in the short range repulsive hydration force³²⁻³⁴. The introduction of organic soft molecules like surfactants and lipid micelles or vesicles extended the SFA's reach to soft and steric interfaces, opening a wider range of possibilities.³⁵ Recently the technique has been used in combination with other techniques, such as X-ray or neutron-scattering and reflectivity for analyzing thin-film structure under confinement.³⁶

The main drawback of the technique is the lack of lateral resolution and the proximity the two macroscopic surfaces, limiting the derivation of information related to isolated interfaces due to the strong confinement of the interfacial liquid. In this respect AFM is more promising as it provides nanometer lateral resolution.

1.3.3 Atomic Force Microscopy

The Atomic Force Microscopy is part of the scanning probe family and largely used to characterize the morphological and mechanical properties of a large variety of samples in environments ranging from high-vacuum to gas and liquid. Measurements are based on the recorded force between a nanometric tip and the sample's surface. The AFM tip is placed at the free end of a flexible cantilever that acts as the transducer of the interaction between the tip and sample. The reflection of a laser beam focused at the backside of the cantilever is then used by most AFMs to detect and amplify the movement of the cantilever through a multi quadrant photodiode.

A detailed description of the technique is presented in Chapter 2, where the different operating modes of the machine are explored and the link between the solid-liquid interface properties and the resolution obtained in the measurement is analyzed. Here, we focus on the molecular mechanisms that dominate the information derived during force measurement. Similarly to the SFA, it is possible to measure down to pN resolution the force dependence between a nanometric tip and a surface as a function of distance, also in liquid. However, unlike for SFA, the small size of the tip allows for a nanometric lateral resolution if a XY-piezoelectric scanner is used.

Moreover, confinement effects between the tip and a sample are reduced to a nanoasperity approaching a flat surface. With AFM, in principle, it is possible to directly measure the force between a small cluster of atoms and a surface in liquid without inducing a strong perturbation to the isolated interface.

1.4 AFM to map the solid-liquid interfacial energy with sub-nanometric resolution

We have seen that, from a thermodynamic point of view, solid-liquid interfaces are characterized by interfacial energy. Using the Dupré equation (Eq. 1.4), it is possible to relate the interfacial energy to the work of adhesion, i.e. the reversible work necessary to separate the two media at the interface. In the cases of a solid-liquid interface and under the approximations examined in section 1.1, the work of adhesion effectively quantifies the gain in free energy of the system obtained by the structural reorganization of the liquid at the interface. This reorganization vanishes typically within a few molecular layers of the liquid (<1-2 nm) when moving away from the interface. AFM can, in principle, directly measure the local work of adhesion between a liquid and a sample, by recording the energy necessary to manipulate the tip-liquid-solid composed interface. However, the measurement contains information about both the tip-liquid and the sample-liquid interfaces, a difficult problem giving the fact that the tip geometry is rarely known. In this last section, the model proposed by Voitchovsky *et al.*³⁷ is analyzed. This model provides a method that deconvolutes information from both interfaces and opens the possibility to map the interfacial energy with sub-nanometric resolution.

It is however important to keep in mind that the concept of work of adhesion is intrinsically macroscopic, even if originating from microscopic molecular properties of the solid and the liquid.³⁸ It is often more appropriate to think in terms of local solvation energy at the atomistic or molecular level, for example when considering nanoscopic domains of the interface.³⁹

1.4.1 Solid-liquid work of adhesion and pressure between two approaching surfaces

Amplitude-Modulation Atomic Force Microscopy (AM-AFM) is an operating mode where the AFM tip is oscillated at the resonance of the cantilever and scanned close to surface while recording variations in the oscillation amplitude as a function of the tip-sample distance (for a technical description of the AM-AFM see Chapter 2).

When operated at small amplitude and in liquid, it is possible to set the parameters so that, during a full oscillation cycle, the tip travels a distance between 1-2 nm from the surface (Fig.1.6A) to almost contact (Fig.1.6B) and then back to the starting position (Fig.1.6C). As a result, during each oscillation, the two solid-liquid interfaces between the tip, the liquid and the sample are partially destroyed. The energy dissipated by the tip during the first part of the oscillation (approach) is the energy necessary to partially destroy both the tip and the sample interface by forming a common interface. Taking into account the geometry of the system and integrating the work accomplished by the tip over the approach part of the oscillation cycle, it is possible to relate the corresponding energy dissipated with W_{SL} (surface-liquid work of adhesion) and W_{TL} (tip-liquid work of adhesion). Assumptions about the spatial dependence of W_{TL} and W_{SL} are however needed.

The work of adhesion represents the energy responsible for interfacial restructuring in the liquid. This restructuring will occur over a finite distance, typically a few molecular diameters. Liquid density variations compared to bulk will tend to vanish rapidly from the interface with a possible oscillatory trend. The exact shape of this decay can be complex with sudden transition between hydration layers and generally depends on both the solid and the liquid (section 1.1 and 1.2). In first approximation Voitchovsky *et al.*³⁷ described this fast local density variation by modeling the gradient of the solid-liquid work of adhesion when moving away from the surface as decaying

exponentially and approached the asymptotic value of zero over a few molecular diameters (see Fig.1.7). In this framework, the effective repulsive force felt by the tip as it approaches the surface comes from the overlap of the two exponentially decaying interfaces.

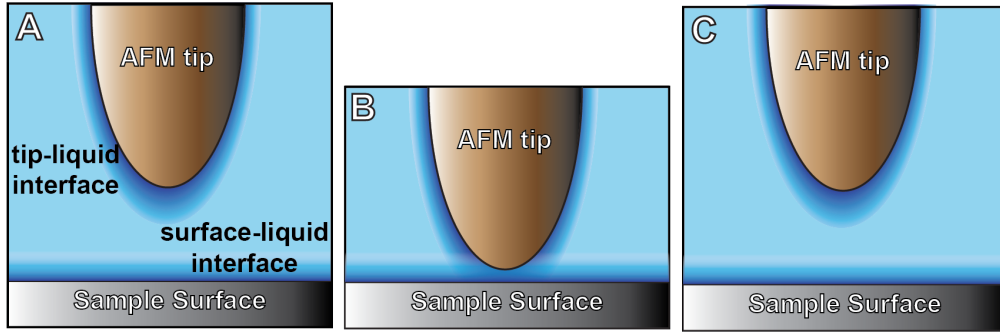


Fig. 1.6: Schematic representation of the oscillation cycle of the AFM tip in liquid close to the surface of the sample. (A) The AFM tip starts at a distance of 1-2 nm from the surface. In this initial configuration the two solid-liquid interfaces of tip-liquid and surface-liquid are completely formed. (B) The AFM tip is at the point of closest approach with the surface. Here the two solid-liquid interfaces are overlapping. (C) The AFM tip comes back to the starting position and the two solid-liquid interfaces are restored.

The reciprocal influence of the tip and the sample on the sample-liquid and tip-liquid interfaces, respectively, are not taken into account and both interfaces are assumed to remain structurally constant while interpenetrating each other. This assumption becomes problematic if there is a large difference in the liquid's affinity for the tip and for the substrate. Under this approximation it is possible to define $P_{SL}(z)$ and $P_{TL}(z)$, the density of work of adhesion (which takes the unit of pressure) as follow (see Fig.1.7):

$$P_{SL}(z) = \frac{\partial W_{SL}(z)}{\partial z} = W_{SL} \alpha e^{-\alpha z} \quad (1.8)$$

$$P_{TL}(z) = \frac{\partial W_{TL}(z)}{\partial z} = W_{TL} \beta e^{-\beta(D-z)} \quad (1.9)$$

where z is the distance from the surface, D is the tip-sample distance and α and β are the exponentially decaying length related to the typical dimension of the solvent molecules. $P_{SL}(z)$ and $P_{TL}(z)$ are normalized so that, when integrated respectively from 0 to ∞ or from $-D$ to $-\infty$, the result is exactly the work of adhesion between the considered liquid and surface. The pressure $P_{SLT}(D)$ met by the tip when approaching the sample at a distance D is then obtained considering the maximum value of pressure among the crossing points z^* between $P_{SL}(z)$ and $P_{TL}(z)$ (see Fig.1.7).

$$P_{SLT}(D) = (W_{SL} \alpha)^{\frac{\beta}{\alpha+\beta}} (W_{TL} \beta)^{\frac{\alpha}{\alpha+\beta}} e^{-\frac{\alpha\beta D}{\alpha+\beta}} \quad (1.10)$$

To obtain the force acting between tip and sample, Voitchovsky *et al.*³⁷ assumed that the solid surface is locally flat and the AFM tip parabolic with local radius of curvature R at the apex. The force acting between tip and sample can then be obtained from the Derjaguin approximation (here assuming $\alpha = \beta$):

$$\begin{aligned} F(D) &= \int_D^\infty 2\pi y P_{SLT} \left(D + \frac{y^2}{2R} \right) dy \\ &= \frac{4\pi R}{\alpha^2} \sqrt{W_{SL} W_{TL}} e^{-\frac{\alpha}{2}(D+D^2/2R)} \end{aligned} \quad (1.11)$$

At each tap, the tip motion is assumed to be purely in the z direction. The lateral scan speed is several orders of magnitude slower and hence neglected. The AFM oscillation amplitude A is relatively small, i.e. comparable to the width of the total surface-liquid-tip interface and the whole system has circular symmetry around the z axis. A quick consideration of the energies involved indicates that the tip never touches the surface, with at least one molecular diameter (σ) of liquid between them. Using these assumptions it is possible to obtain the energy dissipated in the approaching part of the cycle:

$$E_{\frac{1}{2}cycle} = \int_{\sigma}^{A+\sigma} F(D) dD = \frac{4\pi R}{\alpha} \sqrt{W_{SL} W_{TL}} e^{-\frac{\sigma\alpha}{2}} \left(1 - e^{-\frac{\alpha(A+\sigma)}{2}}\right) \quad (1.12)$$

This formula relates the energy dissipated by the tip during the approaching part of the oscillation to the tip-liquid and surface-liquid works of adhesion.

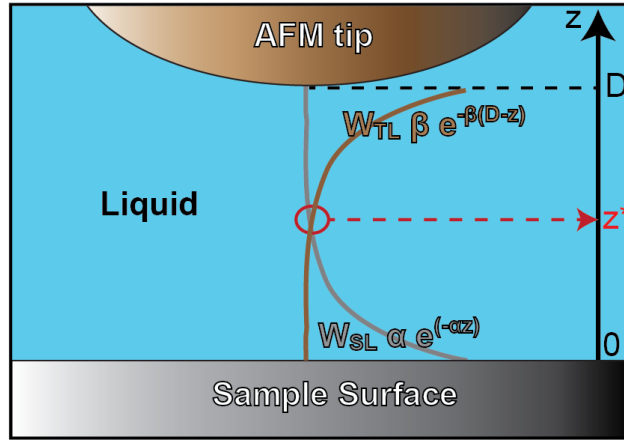


Fig. 1.7: Schematic representation of tip-liquid-sample model used to calculate $P_{SLT}(D)$.

1.4.2 Energy dissipated in the whole oscillation cycle

The work of adhesion is by definition reversible. If the tip oscillation is an adiabatic process no energy should be dissipated during a full oscillation cycle. However, experimental measurements of the energy dissipation are found to scale with W_{SL} ^{39,37}. Voitchovsky *et al.*³⁷ explained this dissipation by a deviation from the adiabatic case induced by the viscoelasticity of the interfacial liquid. This dissipative process creates a hysteresis loop between the approaching and retracting part of the oscillation that causes the observed energy dissipation. A recent work has shown that the molecular mechanism for dissipation is tip-induced liquid slippage at the interface.⁴⁰ Molecular slippage is a dissipative process that scales with the work of adhesion.⁴¹ Practically, Voitchovsky *et al.*³⁷ found that the work of adhesion measured by AFM scales with the W_{SL} obtained with other techniques, such as contact angle, but is not strictly equal. They introduced a proportionality constant λ to quantify the received results:

$$E_{diss} = \lambda E_{TS} = \frac{4\pi R}{\alpha} \sqrt{W_{SL} W_{TL}} e^{-\frac{\sigma\alpha}{2}} \left(1 - e^{-\frac{\alpha(A+\sigma)}{2}}\right) \quad (1.13)$$

Despite the numerous simplifications, this model is able to capture the complex behavior of the work of adhesion of different solid-liquid interfaces as measured by the contact angle technique (see Fig.1.8).

This model provides an intuitive tool for the nanoscale characterization of local wetting properties since under the approximation of single harmonic oscillator model, the energy dissipated in AM-AFM is directly related to the phase contrast (see Chapter 2). By using an oscillation amplitude comparable to the thickness of the interfacial liquid (0.5–1.5 nm) and gentle scanning conditions

to avoid direct tip-sample mechanical interaction, it is possible to probe the interfacial liquid properties. Significantly, the resulting topographic and phase images mostly reflect the properties of the interfacial liquid rather than that of the underlying solid.

In summary, AFM provides a unique method to characterize solid-liquid interfaces with sub-nanometer resolution and can deliver quantitative information about the local work of adhesion between the liquid and the sample surface. Moreover the technique offers an intuitive interpretation of the phase images when operated in AM-AFM (see Chapter 2), reflecting in the phase local variation of the interfacial properties of sample-liquid system.

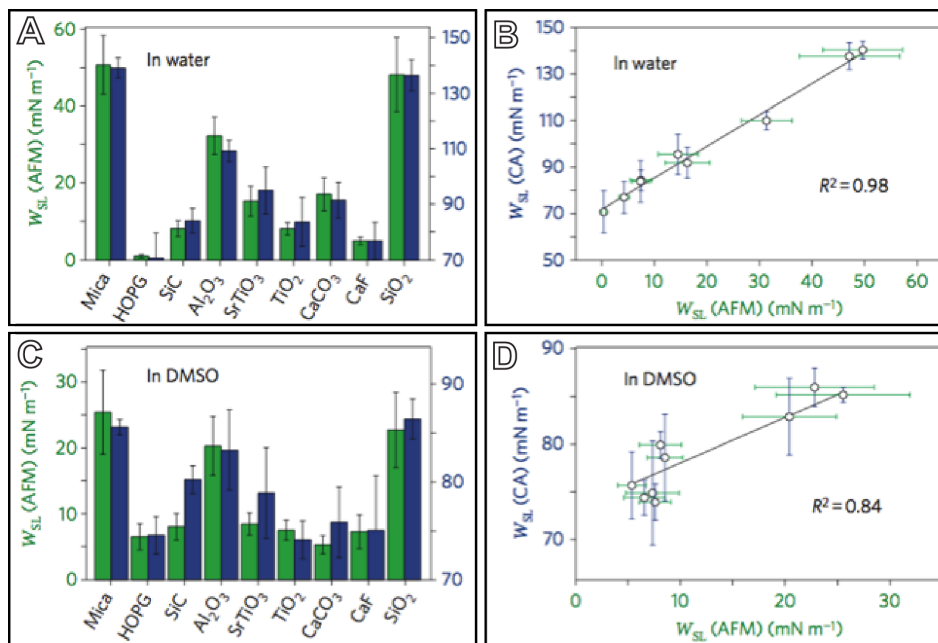


Fig. 1.8: Histograms and scatter plots comparing the measurement of W_{SL} for various substrates. Data were collected in water (A, B) and in DMSO (C, D) using AFM (green) and contact angle (blue). The correlation coefficients for the scatter plots (R^2) are 0.98 (B) and 0.84 (D), both ensuring statistical significance. The error bars represent two standard deviations of the measurements. Systematic errors affecting all the points in the same manner are not represented in the error bars. Figure adapted from Ref. [37].

Bibliography Chapter 1

1. Butt, H.-J., Graf, K. & Kappl, M. *Physics and Chemistry of Interfaces*. Wiley-VCH, 3rd ed., 2003.
2. Cahn, J. W. & Hilliard, J. E. Free Energy of a Nonuniform System. I. Interfacial Free Energy. *J. Chem. Phys.* **28**, 258–267 (1958).
3. Israelachvili, J. N. *Intermolecular and Surface Forces*. Academic Press, 3rd ed., 2011.
4. Abraham, F. F. The interfacial density profile of a Lennard-Jones fluid in contact with a (100) Lennard-Jones wall and its relationship to idealized fluid/wall systems: A Monte Carlo simulation. *J. Chem. Phys.* **68**, 3713–3716. (1978).
5. Zaera, F. Probing Liquid/Solid Interfaces at the Molecular Level. *Chem. Rev.* **112**, 2920–2986 (2012).
6. Fenter, P. & Sturchio, N. C. Mineral–water interfacial structures revealed by synchrotron X-ray scattering. *Progress in Surface Science* **77**, 171–258 (2004).
7. Peak, D. Adsorption mechanisms of selenium oxyanions at the aluminum oxide/water interface. *J. Colloid Interface Sci.* **303**, 337–345 (2006).
8. Park, C., Fenter, P. A., Nagy, K. L. & Sturchio, N. C. Hydration and Distribution of Ions at the Mica-Water Interface. *Phys. Rev. Lett.* **97**, 016101 (2006).
9. Yu, C. J., Richter, A. G., Datta, A., Durbin, M. K. & Dutta, P. Observation of Molecular Layering in Thin Liquid Films Using X-Ray Reflectivity. *Phys. Rev. Lett.* **82**, 2326–2329 (1999).
10. Yu, C. J., Richter, A. G., Kmetko, J., Datta, A. & Dutta, P. X-ray diffraction evidence of ordering in a normal liquid near the solid-liquid interface. *EPL* **50**, 487–493 (2000).
11. Doerr, A. K., Tolan, M., Schlomka, J.-P. & Press, W. Evidence for density anomalies of liquids at

-
- the solid/liquid interface. *EPL* **52**, 330-336 (2000).
12. Fenter, P., Park, C., Nagy, K. L. & Sturchio, N. C. Resonant anomalous X-ray reflectivity as a probe of ion adsorption at solid–liquid interfaces. *Thin Solid Films* **515**, 5654–5659 (2007).
 13. Toney, M. F. *et al.* Voltage-dependent ordering of water molecules at an electrode–electrolyte interface. *Nature* **368**, 444–446 (1994).
 14. Cheng, L. Molecular-Scale Density Oscillations in Water Adjacent to a Mica Surface. *Phys. Rev. Lett.* **87**, 156103 EP (2001).
 15. Geissbühler, P. *et al.* Three-dimensional structure of the calcite–water interface by surface X-ray scattering. *Surface Science* **573**, 191–203 (2004).
 16. Fenter, P., McBride, M. T., Srajer, G., Sturchio, N. C. & Bosbach, D. Structure of Barite (001)– and (210)–Water Interfaces. *J. Phys. Chem. B* **105**, 8112–8119 (2001).
 17. Lu, J. R. & Thomas, R. K. Neutron reflection from wet interfaces. *Faraday Trans.* **94**, 995–1018 (1998).
 18. Shen, Y. R. & Ostroverkhov, V. Sum-frequency vibrational spectroscopy on water interfaces: polar orientation of water molecules at interfaces. *Chem. Rev.* **106**, 1140–1154 (2006).
 19. Richmond, G. L. Molecular bonding and interactions at aqueous surfaces as probed by vibrational sum frequency spectroscopy. *Chem. Rev.* **102**, 2693-724 (2002).
 20. Smolentsev, N., Chen, Y., Jena, K. C., Brown, M. A. & Roke, S. Sum frequency and second harmonic generation from the surface of a liquid microjet. *J. Chem. Phys.* **141**, 18C524 (2014).
 21. Ostroverkhov, V., Waychunas, G. A. & Shen, Y. R. Vibrational spectra of water at water/ α -quartz (0001) interface. *Chem. Phys. Lett.*, **386**, 144-148 (2004).
 22. Miranda, P., Xu, L., Shen, Y. & Salmeron, M. Icelike Water Monolayer Adsorbed on Mica at Room Temperature. *Phys. Rev. Lett.* **81**, 5876–5879 (1998).
 23. Scheu, R., Smolentsev, N., Rick, S. W. & Roke, S. Sum frequency spectroscopy of the hydrophobic nanodroplet/water interface: Absence of hydroxyl ion and dangling OH bond signatures. *Chem. Phys. Lett.*, **615**, 124-131 (2014).
 24. Subir, M., Liu, J. & Eisenthal, K. B. Protonation at the Aqueous Interface of Polymer Nanoparticles with Second Harmonic Generation. *J. Phys. Chem. C* **112**, 15809–15812 (2008).
 25. Evans, R. & Parry, A. O. Liquids at interfaces: what can a theorist contribute? *J. Phys.: Condens. Matter* **2**, SA15 (1990).
 26. O'Shea, S. J. & Welland, M. E. Atomic Force Microscopy at Solid–Liquid Interfaces. *Langmuir* **14**, 4186–4197 (1998).
 27. Kilpatrick, J. I., Loh, S.-H. & Jarvis, S. P. Directly Probing the Effects of Ions on Hydration Forces at Interfaces. *J Am Chem Soc.*, **135**, 2628–2634 (2013).
 28. Parsegian, V. A. & Zemb, T. Hydration forces: Observations, explanations, expectations, questions. *Curr. Opin. Colloid Interface Sci.* **16**, 618–624 (2011).
 29. Parsons, D. F., Bostrom, M., Nostro, Lo, P. & Ninham, B. W. Hofmeister effects: interplay of hydration, nonelectrostatic potentials, and ion size. *PCCP* **13**, 12352–12367 (2011).
 30. Tabor, D. & Winterton, R. H. S. The Direct Measurement of Normal and Retarded van der Waals Forces. *Proceedings of the Royal Society of London A: Mathematical, Physical and Engineering Sciences* **312**, 435–450 (1969).
 31. Israelachvili, J. N. Measurement of forces between surfaces immersed in electrolyte solutions. *Faraday Discuss. Chem. Soc.* **65**, 20–24 (1978).
 32. Pashley, R. M. DLVO and hydration forces between mica surfaces in Li^+ , Na^+ , K^+ , and Cs^+ electrolyte solutions: A correlation of double-layer and hydration forces with surface cation exchange properties. *J. Colloid Interface Sci.* **83**, 531–546 (1981).
 33. Pashley, R. M. Hydration forces between mica surfaces in electrolyte solutions. *Adv. Colloid Interface Sci.* **16**, 57–62 (1982).
 34. Pashley, R. M. & Israelachvili, J. N. Dlvo and hydration forces between mica surfaces in Mg^{2+} , Ca^{2+} , Sr^{2+} , and Ba^{2+} chloride solutions. *J. Colloid Interface Sci.* **97**, 446–455 (1982).
 35. Pashley, R. M. & Israelachvili, J. N. A comparison of surface forces and interfacial properties of mica in purified surfactant solutions. *Colloids and Surfaces* **2**, 169–187 (1981).
 36. Golan, Y., Martin-Herranz, A., Li, Y., Safinya, C. & Israelachvili, J. Direct Observation of Shear-Induced Orientational Phase Coexistence in a Lyotropic System Using a Modified X-Ray Surface Forces Apparatus. *Phys. Rev. Lett.* **86**, 1263–1266 (2001).
 37. Voïtchovsky, K., Kuna, J. J., Contera, S. A., Tosatti, E. & Stellacci, F. Direct mapping of the solid-liquid adhesion energy with subnanometre resolution. *Nature Nanotechnology* **5**, 401–405 (2010).
 38. Zhang, J. & Kwok, D. Y. Combining Rule for Molecular Interactions Derived from Macroscopic Contact Angles and Solid–Liquid Adhesion Patterns. *Langmuir* **19**, 4666–4672 (2003).

-
39. Kuna, J. J. *et al.* The effect of nanometre-scale structure on interfacial energy. *Nature Materials* **8**, 837–842 (2009).
 40. Ortiz-Young, D., Chiu, H.-C., Kim, S., Voitchovsky, K. & Riedo, E. The interplay between apparent viscosity and wettability in nanoconfined water. *Nat. Commun.* **4 SP**, (2013).
 41. Huang, D. M., Sendner, C., Horinek, D., Netz, R. R. & Bocquet, L. Water Slippage versus Contact Angle: A Quasiuniversal Relationship. *Phys. Rev. Lett.* **101**, 226101 (2008).

Chapter 2

High resolution AFM at solid-liquid interfaces

In this chapter, I will describe the different AFM imaging modes suitable for high-resolution measurements in liquid environment. Emphasis will be placed on the resolution achievable and the relationship with the solid-liquid interfacial properties. After a fast introduction on the basic principles of the AFM (section 2.1) I will present some of the historical development of the technique leading to the state of the art experiments performed at the moment (section 2.2). The concepts of lateral and vertical resolution will be discussed (section 2.3) in relation to experimentally measured parameters and the forces acting during the AFM imaging process (section 2.4), in particular solvent-related dissipative and conservative interactions (section 2.5). In the final part of the chapter I will critically analyze the contribution of the solvent in the imaging process depending on the mode of operation and the conditions employed during the image acquisition (section 2.6).

2.1 Working principle of AFM

AFM belongs to the family of Scanning Probe Microscopy (SPM) techniques, along with Scanning Tunneling Microscopy (STM). In SPM the morphology of the surface of the sample under examination is reconstructed by monitoring the distance-dependent interactions between a sharp probe and a sample. In the case of AFM the force existing between the probe and the sample is the interaction parameter used to construct the surface image. AFMs can be operated in a number of modes, depending on the application. In general, operating modes are divided into static and dynamic. In static mode (e.g. *contact-mode*), the cantilever is held static at the base while in dynamic modes (such as amplitude- and frequency-modulation) the cantilever is vibrating, imposing an external but periodic motion to the tip during the measurement. Interactions between tip and sample modify the cantilever dynamic (section 2.4) and variation in the oscillation amplitude, phase and frequency can be detected by the AFM electronics.

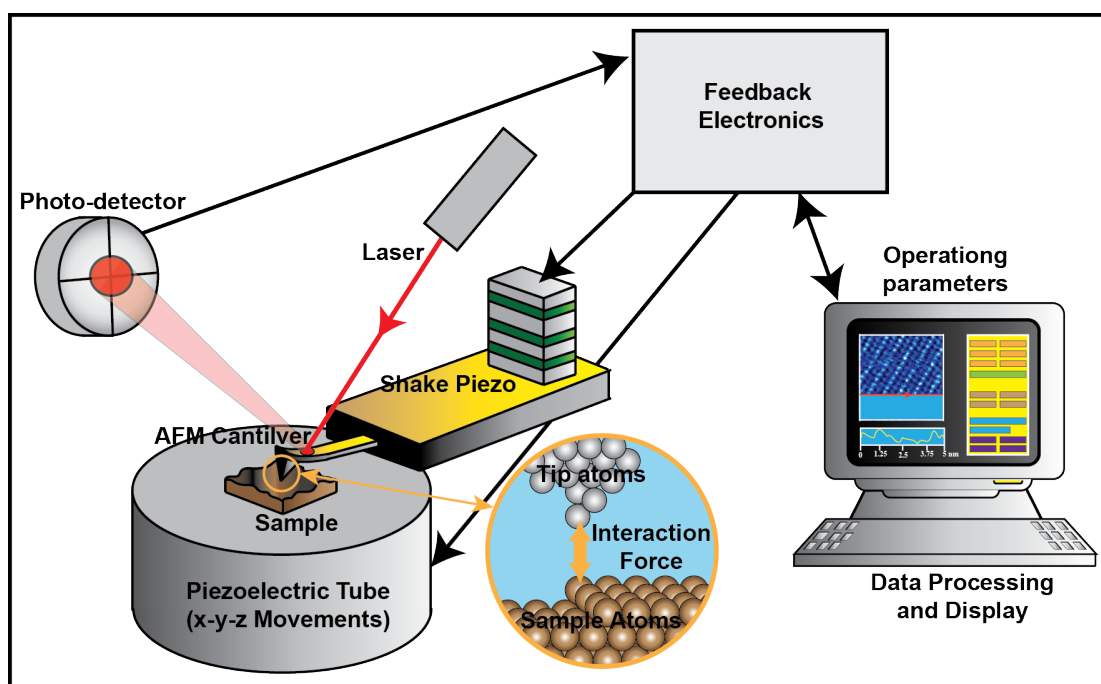


Fig. 2.1: Schematic and simplified representation of an Atomic Force Microscope. The force between tip and sample is monitored by detecting the deflection signal of a cantilever. The deflection is measured by monitoring the displacement of a laser beam on the photo detector. The cantilever can be held statically or oscillated by the shake piezo. The Feedback electronics monitors the deflection signal and adjust the tip-sample distance while changing the lateral relative position of the two by applying a voltage to a piezoelectric tube placed below the sample. The operating parameters can be changed directly on the computer where the image is displayed in real time during the acquisition.

In the case of AM-AFM, the oscillation amplitude and frequency are kept constant during the imaging process while the phase (the dephasing between the driving and tip oscillations) can vary freely. The driving frequency is usually selected to coincide with the first self-resonance ω_0 of the cantilever but this is not a strict requirement and higher harmonics¹ or out of resonance frequencies² can be used. When the tip approaches the sample, elastic and inelastic interactions (see section 2.5) cause changes in both the amplitude and the phase signals. These changes are used by the feedback loop to map the surface morphology by constantly adjusting the tip-sample distance so as to keep the amplitude of oscillation constant.

In frequency-modulation AFM (FM-AFM) the cantilever is subjected to a controlled positive feedback such that it oscillates with constant amplitude, always at the resonance frequency of one of the cantilever oscillation modes. The tip-sample interactions cause frequency shifts of the cantilever resonance. By ensuring to constantly measure the actual resonance of the oscillation (related to the phase signal used sometimes as extra feedback parameter) it is possible to use the shift of the interacting frequency compared to the unperturbed one as the feedback parameter.

In both cases (static or dynamic) it is possible to reconstruct the surface topography from the feedback corrections applied by the piezo actuator to constantly adjust the tip-sample distance while scanning. The output is converted in real-time in a series of images of the different parameters displayed on the computer at which the AFM electronic is connected.

2.2 Historical introduction on AFM: from vacuum to liquid

Presenting a comprehensive history of the AFM development is very challenging. The intention of this section is simply to introduce some of the most important scientific achievements that led to the possibility of obtaining reliable and quantitative measurements of solid-liquid interfaces with the AFM. I will put special emphasis on high resolution.

Since the AFM's invention in 1986 at the IBM laboratory³, it has shown a large potential for surface characterization. Unlike the close cousin, the scanning tunneling microscope (STM), AFM is suitable for the characterization of all types of surfaces (not only conductive materials or semiconductors), in most environments. The first operating mode of the AFM was the standard contact mode. Compared to the STM, the atomic resolution on the first machines seemed to be considerably more challenging due to the presence of additional complications, such as long-range forces, jump into contact and non-monotonic short-range forces.⁴

Part of these problems was successfully addressed by introducing new operating methods able to detect the force between the tip and sample: the dynamic AFM modes. The idea was to prevent the jump into contact of the AFM tip by oscillating the cantilever with amplitude large enough to reach a withdrawing force at the lower tip-sample distance able to overcome the maximal attraction force. In addition, the vertical motion of the cantilever reduces lateral friction force while scanning, thus allowing non-destructive imaging of soft materials. Moreover the intrinsic noise in cantilever deflection measurements has a component that varies in intensity inversely with the frequency of oscillation, making dynamic AFM modes less subject to noise than static operating modes.

Just one year after the invention of the AFM, Martin *et al.*⁵ proposed the use of the oscillation amplitude of a cantilever externally driven at resonance as a feedback parameter for the imaging process. The change in amplitude in AM mode does not occur instantaneously with a change in the tip-sample interaction, but on a time scale of $\tau = Q/2\omega_0$ due to a transient term in the cantilever dynamic. With Q factors reaching 100000 in vacuum, the feedback response in AM mode was very slow.⁶ To overcome this difficulty, in 1991, Albrecht *et al.*⁷ proposed the use of a different feedback signal, the change of the frequency of resonance of the cantilever, paving the way for FM-AFM. In this mode, the response of the instrument to a variation of the tip-sample force occurs within a single oscillation cycle⁶ on a time scale of $\tau = 1/\omega_0$, rendering it more suitable than AM-AFM for measurements in vacuum.

In parallel with the development of new imaging modes, an important effort was done to improve the detection methods of the cantilever deflection and the fabrication process of cantilevers. The optical beam detection method to detect the lever deflection⁸ was firstly proposed in 1988 and the following year, Alexander *et al.*⁹ proved it to be suitable for sub-nanometer resolution. At the same time the microfabrication of cantilever styli¹⁰ contributed to the availability of reliable and more standardized AFM cantilevers. Together, these improvements resulted in the realization of the first commercial instruments (MultiMode, Digital Instruments, Santa Barbara, 1993).

In the same period the possibility of using AFM in liquid was firstly explored, mainly motivated by the growing interest in exploring biologically relevant surface processes in native environment. The first AFM images in liquid were done in contact mode by immersing the AFM cantilever and the surface in water or other solvents¹¹. The idea of liquid environment was initially mainly dictated by the necessity of screening long range attractive forces¹² or to explore evolving systems, like the growth and dissolution of calcite in ionic solutions of different concentrations^{13,14}. Then, with the development of the more gentle imaging condition¹⁵ obtained in AM-AFM (often called "tapping mode") this technique was applied to the characterization of more delicate samples, such as single DNA molecules absorbed on surfaces¹⁶ or enzymes¹⁷. From

that moment on AM-AFM has been largely used to obtain information of different surfaces in liquid environment.

In these early stages of AM-AFM, the possibility to record the phase delay between the forcing sinusoidal signal and the actual tip motion during the imaging process proved to be the main breakthrough¹⁸. This signal was immediately related to the mechanical properties of the sample¹⁹ and subsequently, a new formalism was developed to relate tip energy dissipation with the phase contrast in AM-AFM^{20,21}. This instrumental advance enabled the mapping of compositional variations and changes in material properties of heterogeneous surfaces.

The main problems related to the use of a vibrating cantilever in a liquid environment surfaced, becoming an important motivation for the development of new technologies and theoretical models for the description of the lever dynamic:

1. The cantilever vibration is damped in liquid because of the high viscosity of the media, as compared to that of air or vacuum. The result is a high energy dissipated during the cantilever vibration at resonance. Since the high force sensitivity in dynamic-mode AFM is provided by the resonance effect of a cantilever vibration, an over damped motion leads to lower force sensitivity if compared to less viscous media. This fact drove many technical improvements: new low-noise photodetectors²² with bigger bandwidth and faster electronics²³ appeared first in a few prototypes and were later implemented on commercially available machines. Simultaneously, new microcantilevers with higher Q-factor and resonance frequency were developed²⁴, and soon became commercially available.
2. The standard acoustic driving mechanism, largely employed in all commercially available AFM machines, in liquid, introduces many spurious resonances in the cantilever and sample holders, hindering the identification of the true resonance of the stylus. Moreover the resonances change in time rendering imaging in liquid unstable. To help the identification of the proper resonance, the thermal-noise method was introduced in the standard commercial AFM and helped to develop new calibration methods for the spring constant of the AFM cantilever. At the same time new methods to excite the cantilever motion were proposed, such as the magnetic excitation²⁵ or photothermal excitation^{26,27}, recently available even commercially.
3. The standard simple harmonic oscillator model, used to describe the cantilever motion and the interaction force between tip and sample in low viscosity (air or vacuum) media, is not directly applicable in increased viscosity environments. Large efforts have been dedicated to determining better models or direct simulation of the response of the lever in liquid^{28,29}. This, combined with the new technical improvements in the design of the AFM electronics, lead to the development of new imaging modes based on multi-harmonics detection or second resonance excitation. These new imaging modes are able to give quantitative information on the type of interaction between the AFM tip and the sample.^{28,29}

Before the development of more complex models to describe the cantilever dynamic, most of the big advances made to quantitatively characterize the solid-liquid interface were done starting from the standard harmonic oscillation model. Assuming a parabolic tip-sample interaction potential, this model enables to relate the phase and amplitude of the cantilever oscillation to the distance dependent interaction stiffness and the damping coefficient.³⁰⁻³² The actual measurement of liquid structure with AFM on the surface of graphite was first achieved in 1992 by O'Shea *et al.*³³ using big and bulky molecules. The authors' later work³⁴ showed an oscillatory behavior convoluted with an exponential decay of the measured force and the derived interaction stiffness as the tip approached the surface. In 1995 Cleveland *et al.*³⁵ showed that water layer and/or hydrated ion measurements were possible using static AFM. They discerned different energy minima close to ionic crystals in water by using the thermal noise of the cantilever and related the minima to the density structure of the water hydration layer. These type of measurements stimulated the rinsing of theoretical studies on nano-confinement with special emphasis on the AFM tip case^{36,37}. In the following years, AFM was used to characterize solid-liquid interfaces of different samples and in different liquids, proving the high versatility of the technique.³⁸⁻⁴⁰

The development of FM-AFM in liquid^{41,42} provided a significant improvement for high-resolution studies of hydration forces, enabling measurements in aqueous environment of hydration structures with high lateral resolution. Moreover the possibility of combining the high resolution images with a precise vertical information of the frequency shift helped to understand how the hydration layers were contributing to the contrast formation in FM-AFM.⁴³⁻⁴⁵ The measurements were subsequently extended to ions adsorbed at solid-liquid interfaces⁴⁶⁻⁴⁹. In parallel, new models describing contrast formation at the interface were proposed^{50,51} for AM-AFM relating the dissipative forces that contribute to the formation of the phase contrast to the work of adhesion between the solid-liquid interfaces.

The latest remarkable improvement of the characterization of solid-liquid interfaces was proposed in 2010 by Fukuma *et al.*⁵² and Kimura *et al.*⁵³: they extended three-dimensional AFM⁵⁴ into liquid environments enabling the visualization of the 3D distribution of a liquid at a surface of a solid. In 3D-AFM, a tip is scanned over the surface in the z-direction (orthogonal to the surface) as well as in x-y to cover the whole 3D interfacial space. They applied this technique to FM-AFM: during the scan, the frequency shift is recorded in real time with respect to the 3D tip positions while the averaged tip height is regulated to keep the averaged frequency shift to a constant value. They were able to image the distribution of the water molecules on the surface of mica and subsequently they derived a relationship between the local liquid density and force applied on the AFM tip.⁵⁵ Moreover Kimura *et al.*⁵³ discerned the effect of adsorbed K⁺ ions on mica in the frequency shift of the 3D-AFM map. The new technique was then used to characterize different samples, such as a lipid bilayer⁵⁶, showing how the 3D-hydration structure was important even for biologically relevant surfaces. Finally this technique was also extended to bimodal AM-AFM to reconstruct the force as a function of the distance with sub-nanometer lateral resolution.¹

2.3 Concept of resolution in AFM

Spatial (vertical or lateral) resolution, noise and sensitivity are concepts that are highly correlated in AFM. The relationship that exists between the noise characteristic of a specific detection method, and vertical resolution is rather simple: the noise in the cantilever deflection establishes the upper resolution limit of the microscope but the specific interaction between tip and sample plays a role in the achieved resolution. The sensitivity of the instrument to detect force variations might also control the achievable spatial resolution. The lateral resolution is intrinsically related to the vertical resolution but not in a simple manner and also depends on the surface properties (e.g. when changing the effective contact area between tip and sample). In a heterogeneous surface, features of equal size but different properties might give rise to different values of the lateral resolution. This underlines the role of the sample in the achievable resolution. In this section the concepts of vertical and lateral resolution are presented, focusing on AM-AFM due to the importance in this thesis, and the basic ingredients for a sub-nanometric resolution are briefly described.

2.3.1 Vertical resolution

The vertical resolution in scanning probe is defined by the minimum height variation on the surface that the instrument can detect. This resolution is limited by the noise of the signal used by the feedback-loop system to reconstruct the topographic image. In the case of AM-AFM the signal is the amplitude of oscillation. The vertical noise δh is standardly defined as the ratio between the noise in the amplitude signal δA and the slope of the amplitude with respect to the average tip-surface distance z_c :⁶

$$\delta h = \frac{\delta A}{\left| \frac{dA}{dz_c} \right|} \quad (2.1)$$

The vertical resolution is limited by the noise in the amplitude signal that comes from the deflection noise δd , which has two major components: the thermal noise δd_{th} of the cantilever and the detector noise δd_{det} . Generally the thermal noise determines the ultimate achievable resolution of the instrument, since the detector noise is generally dominating. The thermal noise excites the oscillation of the cantilever, introducing a component in the measured deflection that depends on the frequency. The components that contribute to the noise can be calculated by knowing the amplitude spectral density of the cantilever. If the cantilever is excited at the first resonance frequency f_0 , it is possible to obtain a general expression for the thermal noise²⁸ of the deflection signal as:

$$\delta d_{th} = \sqrt{\frac{4 k_B T Q B}{\pi f_0 k}} \quad (2.2)$$

where T is the absolute temperature, k_B the Boltzmann's constant, Q is the quality factor of the lever, k the spring constant and B the frequency bandwidth²³ of the instrument.

The other noise component is due to the detection mechanism and is typically proportional to the inverse of frequency for low frequencies and merges into a constant noise density (white noise) above the 1/f corner frequency. The 1/f dependence is typical of so-called "Flicker or pink noise" and occurs in almost all electronic devices. At higher frequencies, in the case of optical beam detection (the most commonly used detection method, including for the experiments presented in this thesis) there is a contribution of other kind of white noises such as the shot noise, the excess noise and other electronic noises.⁵⁷ Of course any other noise (mechanical and electrical) not properly shielded contributes to an increase of the noise level detected by the photo-detector.

The noise introduced in the signal by the detection method is not the only factor that affects the vertical resolution. In the denominator of Eq. 2.1 there is the derivative of the feedback signal with respect to the vertical displacement. This component depends on the tip-sample interaction and generally takes into account how strongly the signal depends on the distance between tip and sample. For example, in the case of STM, the feedback signal is the tunneling current that has an exponential dependence with the distance between tip and sample. In this case, even with a relatively blunt tip, a single atom protruding far enough can carry the main part of the tunneling current. The distance dependence of the tip-sample interaction determines the actual interaction volume of the tip, affecting significantly the detected signal and the lateral resolution.⁶

2.3.2 Lateral resolution

The lateral resolution depends on how the image is formed by the AFM tip. Vertical and lateral resolution are tightly related and here we will see how. If we suppose that our AFM tip is imaging a single protrusion on the sample (meaning that the lateral dimension of the feature protruding from the sample is much smaller than the typical dimension of the tip) the resulting topographic image is a protruding feature that has the same dimension of the tip as a result of convolution effects (see Fig. 2.2A). If, instead of a single isolated protrusion on the surface, we consider two protrusions (see Fig. 2.2B) and seek the minimum distance l between them, sufficient to allow the distinction despite convolution effects, we find that l is given by the separation for which the change Δz of the tip deflection is larger than the vertical resolution. Mathematically, this definition states that the lateral separation l between two sharp features imaged by a parabolic tip with end radius R depends on the height difference ΔH that exists between the adjacent features and the vertical noise δh ,⁵⁸ as defined in Eq. 2.1.

$$l = \sqrt{2R}(\sqrt{\delta h} + \sqrt{\delta h + \Delta H}) \quad (2.3)$$

Eq. 2.3 is obtained under the assumption that $l > \sqrt{2R \Delta H}$. The equation clearly shows the nonlinear nature of the image formation in AFM. The lateral resolution depends not only on

intrinsic parameters of the measurement such as the tip radius or the vertical resolution, but also on some properties of the sample: the height difference between adjacent features ΔH . This means that the lateral resolution is not constant in the AFM image but depends on the sample local topographic properties.

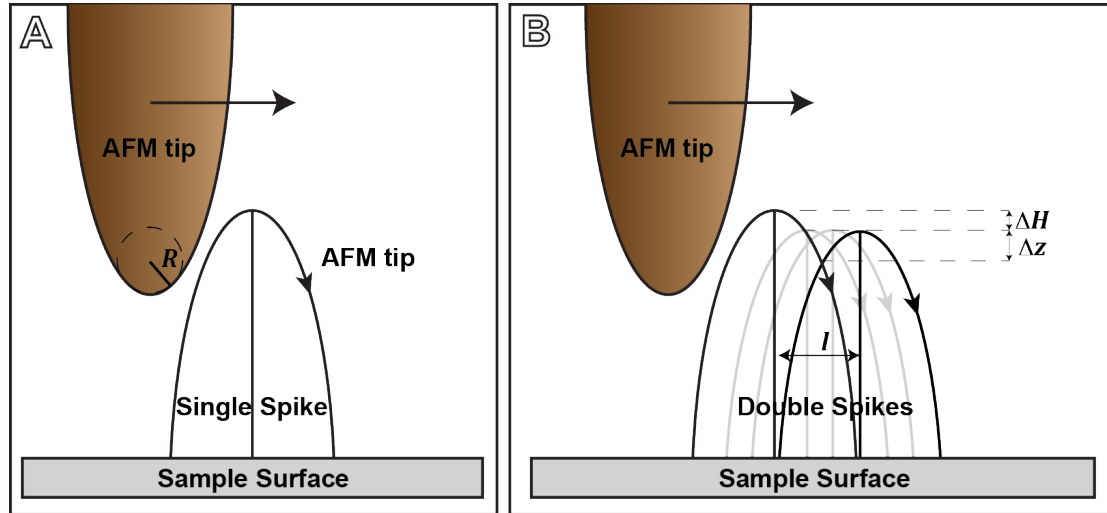


Fig. 2.2: Schematic representation of the convolution effect of the tip with a spike protruding feature on the sample surface (A) and the lateral resolution l obtained for two spike protruding features on the sample surface (B).

A factor that has not been included in the above definition of lateral resolution l is the effective tip-sample contact area. We simply used R as tip radius, while in reality this parameter depends on the sample properties. In the previous formula, we should in fact substitute R with R^* , an effective radius, obtained according to each specific tip-sample interaction.

If we suppose, for example, that the tip is transiently physically in contact with the sample surface we can deduce an analytical expression for the effective tip radius R^* . The force exerted by the tip usually deforms the sample surface. It is accepted that in case of mechanical contact the lateral resolution cannot be better than the real or effective tip-surface contact area. Increasing the applied force increases both the contact area and the deformation. The lateral resolution is then expected to depend on the scanning parameters imposed by the users, not only in terms of proper feedback adjustment but also for changing the interaction parameters in the imaging process. The lateral resolution can in this case be calculated as a function of the applied force using, for example, the Hertz model.⁵⁹ This model provides the effective radius R^* as a function of the tip's radius R , the applied force F , and the effective Young's modulus E^* of the surface:⁵⁹

$$R^* = 2 \left(\frac{3 R F}{4 E^*} \right)^{1/3} \quad (2.4)$$

Eq. 2.4 explains qualitatively why atomic and sub-nanometer resolution is more easily achieved on stiffer materials: the effective Young modulus appears in the denominator, so stiffer materials correspond to a lower effective contact area. Usually, the deformation of the tip is ignored but in some cases, particularly under high-exerted repulsive forces this assumption no longer holds. In particular in the contact mode, the tip, even if initially atomically sharp will also deform plastically, in addition to the elastic deformation, until it reaches a stable apex configuration. This means that in time the resolution of the images will change with the same tip.

2.3.3 Ingredients for high resolution

Atomic resolution is defined as the capability to resolve single or multiple atomic features separated by atomic scale distances. Atomic scale features include atoms, molecules, point

defects, and grain boundaries. Similarly, sub-nanometer resolution is defined as the ability to resolve single or multiple sub-nanometer features.

Obtaining a high-resolution image is a difficult experimental task often requiring expertise from the AFM operator. However, it is possible to specify some minimum requirements⁶⁰ that have to be fulfilled for allowing atomic resolution with a scanning probe microscope:

1. The noise level has to be smaller than the aimed vertical resolution (see Eq. 2.3).
2. A sharp, rigid tip is needed. The tip has to maintain the original shape during the imaging process. First of all, this limit the adhesion between tip and sample and at the same time ensures that the size of the tip apex is small enough to resolve the lateral variation of the imaging parameters.
3. The tip-sample interaction has to decay in the vertical direction fast enough (at least on the atomic length scale) to reduce the averaging of the interaction due to the finite volume of the tip.
4. The interaction responsible of the topographic image formation has to vary measurably on the atomic scale in the lateral direction.
5. The force applied between tip and sample should be as small as possible so as to limit deformations on both components.
6. The distance dependence of the signal used for z -control should behave in a manner that small disturbances of the imaging process which cause a deviation from the chosen setpoint value do not lead to feedback instabilities.

Unfortunately, some of these requirements are poorly controlled by the AFM operator and often the high-resolution imaging reflects more the “feeling” of the operator rather than objective criteria. In my opinion, there are some recursive situations that enable the operator to obtain a good resolution. They are related to the choice of a suitable AFM tip, the scanning conditions but even to some specific ways to prepare and fix the sample or the cantilever chip on the tip holder. This requires the development of good manual skills and experience acquired with time. Unfortunately, some other conditions, like the actual structure of the AFM tip at the atomic level cannot be controlled and are extremely variable in time. “It’s kind of magic”! Often the specific resolution requirements (beyond obvious considerations) can be described a posteriori, once the high resolution is obtained. That is mainly because we do not have access to the actual structure and chemical composition (particularly in liquid) of the tip during the measurement. Practically, once stable high-resolution imaging conditions are obtained we can conclude that the conditions during the measurements were those described in the previous paragraph and learn about the specific interaction probed by the tip and the effect of the liquid molecules in the imaging process.

2.4 Modeling the dynamic motion of a cantilever in liquid

This section presents some simple models describing the oscillatory motion of the cantilever in liquid environment. The results of this modeling part will provide a basis for correct interpretation of the measurements and give some quantitative information on the type of interaction forces between the tip and the sample. In the section, I will follow a semi-quantitative summary of the progresses on this topic. For a more exhaustive treatment I suggest the book of Garcia²⁸ and the book chapter by Kiracofe *et al.*²⁹.

2.4.1 Derivation of the point-mass model from the actual motion of a rectangular lever

The AFM cantilever is an inhomogeneous 3D object that oscillates in a viscous media under the influence of a driving force. This stylus has a tip placed at one end that is subject to some external forces due to the interaction with a close by surface. The aim is to relate some representative parameters of the lever dynamics, such as the amplitude of oscillation, to the interaction forces between the tip and the sample’s surface.

This task is not trivial and there are several approaches to it. Generally, the system is simplified according to a model that retains the important features of the interactions and is verified in real systems. A different approach is to try to maintain as much as possible the complexity of the real situation and simulate with a computer the actual dynamic of the lever. At the moment several free softwares are available online that can simulate the stylus dynamic. One of them is VEDA⁶¹, already available from 2008⁶² and now implemented with more sophisticated features. Another recently released software is the one developed by Garcia and coworkers. In general, comparing experimental results with the simulated experiments provide a more complete picture of the system.

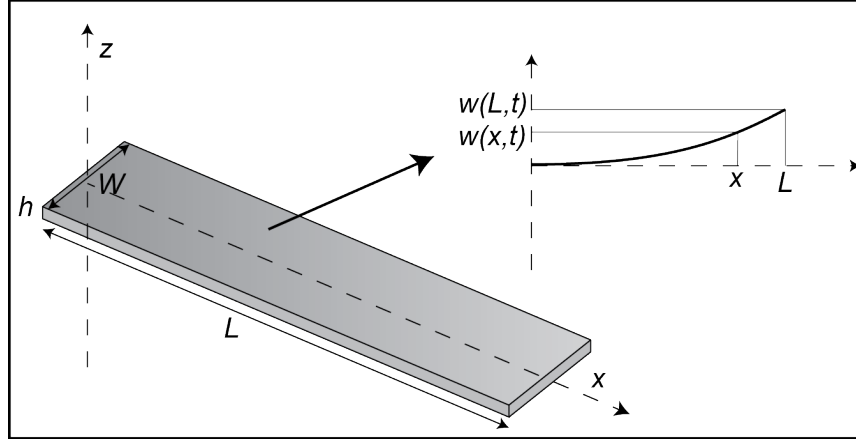


Fig. 2.3: Schematic representation of a rectangular lever and the Bernoulli–Euler beam approximation.

If we consider a rectangular lever, due to some symmetry considerations, we can use the classical Bernoulli–Euler beam theory to describe small deflection of the stylus in the absence of external forces. The theory is based on a partial differential equation that can be modified to introduce some external drive and surface interaction forces:²⁸

$$\begin{aligned}
 E I \frac{\partial^4}{\partial x^4} \left[w(x, t) + a_1 \frac{\partial w(x, t)}{\partial t} \right] + \rho W h \frac{\partial^2 w(x, t)}{\partial t^2} \\
 = a_0 \frac{\partial w(x, t)}{\partial t} + F_{exc}(x, t) + \delta(x - L) F_{ts}(d)
 \end{aligned} \tag{2.5}$$

With $w(x, t)$ being the displacement of the cantilever beam perpendicular to the main axis as a function of the distance x from the clumped end at the time t (see Fig. 2.3). h , W , and L are thickness, width and length of the cantilever, respectively. E , ρ , and I are the Young modulus, linear mass density (integrated on the total length L gives the total mass of the lever), and area moment of inertia of the lever, respectively. a_0 and a_1 are the external and internal damping coefficients of the lever: a_1 takes into account the damping due to internal friction between the atoms/molecules that compose the lever while a_0 takes into account the damping of the lever due to the viscosity of the external media. Often only a_0 is considered being the major component of damping in viscous environment (particularly liquid but even air, see for example a similar equation used by Kiracofe *et al.*⁶³ for the VEDA simulator). $F_{exc}(x, t)$ is the excitation force and depends on both the excitation's position along the cantilever and time. Finally $F_{ts}(d)$ represents all the tip surface interaction forces and depends on d , the instantaneous distance between tip and sample (to be more precise d is a time-dependent variable). The delta function $\delta(x - L)$ indicates that the tip-surface forces are localized only at the tip's apex, situated at the free end of the lever (see Fig. 2.3). This approximation neglects the influence of the tip's shape in the motion of the system across the medium but considers the geometry of the tip for determining the tip-surface forces (hidden in $F_{ts}(d)$). In the above equation, the tip is considered a point object with a mass negligible compared to that of the cantilever. It is anyway possible to include the mass of the tip in the effective mass once the simple harmonic approximation is derived. It has been shown that

when immersed in a liquid, the added mass effect of the surrounding fluid is very large and is uniformly distributed over the beam. As a consequence, the effect of the concentrated tip mass on the lever motion is greatly diminished if compared to the situation in air.⁶⁴ Excluding the tip apex in the theoretical approach is therefore a good approximation in the case of high viscosity media. To solve the differential Eq. 2.5 we have to assign some boundary conditions that are normally clamped and free end. These boundary conditions introduce a discrete number of solutions called eigenmodes. The general solution $w(x, t)$ is simply a linear combination of these. If we make the assumption that it is possible to divide the spatial and temporal components of these eigenmodes we obtain an expression for $w(x, t)$:

$$w(x, t) = \sum_{n=1}^{\infty} X_n(x) Y_n(t) \quad (2.6)$$

$X_n(x)$ determines the shape of the eigenmodes in the x direction (along the long side of the lever), while $Y_n(t)$ is the time dependent function of each mode. These $Y_n(t)$ temporal functions have to follow a second order differential equation that determines the important parameters of the motion of the lever when translated into a point-mass spring model:

$$\frac{d^2 Y_n(t)}{dt^2} + \frac{\omega_n}{Q_n} \frac{d Y_n(t)}{dt} + \omega_n^2 Y_n(t) = \frac{2(-1)^n [F_{exc}(t) + F_{ts}(d)]}{m_n} \quad (2.7)$$

with all the fundamental parameters being:

$$\omega_n^2 = \left(\frac{x_n}{L}\right)^4 \frac{E I}{\rho W h} \quad (2.8)$$

$$m_n = \rho W h L = m_c \quad (2.9)$$

$$Q_n = \frac{\omega_n}{\frac{a_0}{\rho W h} + a_1 \omega_n^2} \quad (2.10)$$

where x_n is the positive real root of $1 + \cos(x_n) \cosh(x_n) = 0$ and m_c is the total mass of the cantilever. We can obtain the tip motion by calculating $w(L, t)$:

$$w(L, t) = \sum_{n=1}^{\infty} X_n(L) Y_n(t) = \sum_{n=1}^{\infty} z_n(t) \quad (2.11)$$

where $z_n(t)$ is the projection of the n^{th} mode at the end of the lever, where the tip is placed, at time t . $z_n(t)$ has to satisfy the following differential equation that derives from the analogous of $Y_n(t)$:

$$\frac{d^2 z_n(t)}{dt^2} + \frac{\omega_n}{Q_n} \frac{d z_n(t)}{dt} + \omega_n^2 z_n(t) = \frac{F_{exc}(t) + F_{ts}(d)}{m} \quad (2.12)$$

with $m = \frac{m_c}{4}$. By expressing the solutions of the Euler-Bernoulli differential equation through the spatial and temporal components of the different eigenmodes, it is possible to obtain a proper interpretation of the widely used point-mass model. In this simple model, a single mode i (generally the first eigenmode) dominates the dynamics of the cantilever beam. If this is a good approximation of the system, it can be assumed that the tip deflection exclusively carries information on this mode, so:

$$w(L, t) = z_1(t) = z(t) \quad (2.13)$$

In this case we have a single second order differential equation that describes the lever deflection:

$$m \frac{d^2 z(t)}{dt^2} = -k_1 z(t) - \frac{m \omega_1}{Q_1} \frac{dz(t)}{dt} + F_{exc}(t) + F_{TS}(d) \quad (2.14)$$

The only new parameter in this equation is k_1 , the force constant of the first eigenmode. It is not the static force constant of the lever (normally indicated with k_S) but it is related to ω_1^2 so that $k_1 = m\omega_1^2$. In practice the values are very similar ($k_1/k_S = 1.03$) so typically they are considered identical.

2.4.2 Point mass model with a sinusoidal driving force

Having derived the point-mass model and related the differential equation's parameters to the actual properties of the rectangular homogeneous cantilever, we can study the response of the lever under an exciting external force sinusoidal in time, $F_{exc}(t) = F_0 \cos(\omega t)$, with frequency ω , and no external forces, $F_{TS}(d) = 0$.

$$m \frac{d^2 z(t)}{dt^2} = -k_1 z(t) - \frac{m \omega_1}{Q_1} \frac{dz(t)}{dt} + F_0 \cos(\omega t) \quad (2.15)$$

The solution of a driven harmonic oscillator with damping has three different regimes but the relevant one for most dynamic AFM experiments is the underdamped regime, when $1/2Q < 1$. The solution in the underdamped regime has a transient term and a steady motion terms:

$$z(t) = B e^{-\frac{\omega_1}{2Q_1} t} \cos(\omega_r t - \beta) + A \cos(\omega t - \varphi) \quad (2.16)$$

$$\omega_r = \omega_1 \sqrt{1 - \frac{1}{4Q_1^2}} \quad (2.17)$$

The transient term, that is the first addendum in Eq. 2.16, oscillates with a frequency ω_r . After a time $2Q_1/\omega_0$ it is reduced by a factor $1/e$, being the sinusoidal component modulated by a negative exponential. We can see that the higher is the quality factor Q_1 , the closer is ω_r to ω_1 and the slower the decay of the transient term. In liquid the two frequencies can differ significantly since Q_1 is rather small. The second addendum is the steady-state term that dominates the motion of the lever after the extinction of the transient. The dependence of the amplitude A of the steady-state term as a function of the excitation frequency has a Lorentzian form (see Fig. 2.4):

$$A = \frac{\frac{F_0}{m}}{\left[(\omega_1^2 - \omega^2)^2 + \left(\omega \frac{\omega_1}{Q_1} \right)^2 \right]^{1/2}} \quad (2.18)$$

while the phase shift φ between the external sinusoidal force and the steady state component of the cantilever deflection can be calculated as:

$$\tan \varphi = \frac{\omega \omega_1 / Q_1}{\omega_1^2 - \omega^2} \quad (2.19)$$

The phase has a sigmoidal shape around ω_1 , where it has the value of $\frac{\pi}{2}$ (see Fig. 2.4).

The maximum amplitude A_{max} is obtained at the frequency ω_{max} , that is different from the resonance frequency ω_1 .

$$A_{max} = \frac{Q_1 F_0}{m \omega_1^2} \frac{1}{\sqrt{1 - \frac{1}{4Q_1^2}}} \quad \omega_{max} = \omega_1 \left(1 - \frac{1}{2Q_1^2}\right)^{1/2} \quad (2.20)$$

In general, the bigger Q_1 (the lower the damping), the closer the two frequencies are, as can be seen in Fig. 2.4. Moreover, by keeping the same drive force F_0 , the maximum amplitude value is diminished. The maximum absorbed energy (or power) occurs at ω_1 . The phase shift is exactly $\frac{\pi}{2}$ at ω_1 and it is independent of Q_1 (see Fig. 2.4). By increasing the damping the transition of the phase becomes smoother.

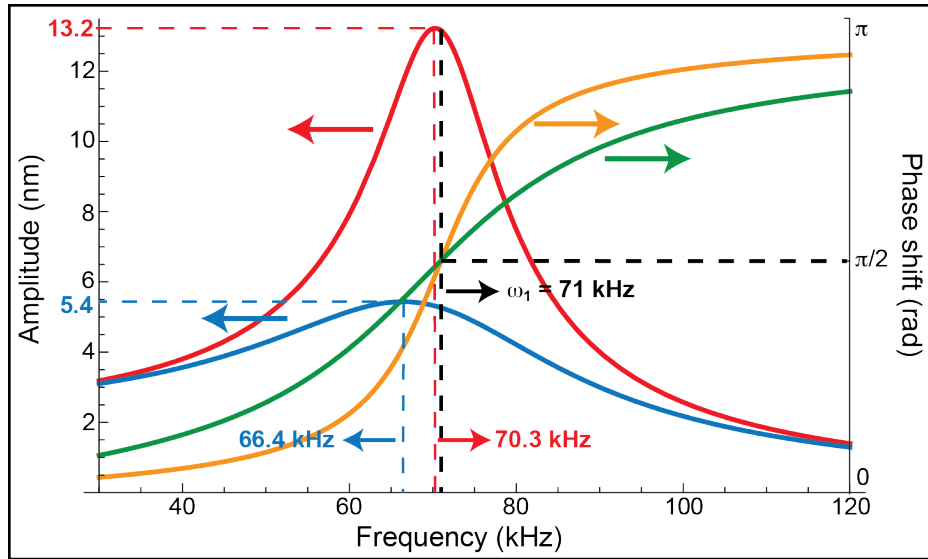


Fig. 2.4: Amplitude and phase steady state response of a damped-forced harmonic oscillator. Two situations are compared: the red/orange curves correspond to an amplitude/phase vs. frequency response in the case of $F_0 = 2 \text{ nN}$, $\omega_1 = 71 \text{ kHz}$, $Q_1 = 5$, while the blue/green curves correspond to an amplitude/phase vs. frequency response in the case of $F_0 = 2 \text{ nN}$, $\omega_1 = 71 \text{ kHz}$, $Q_1 = 2$. ω_1 is marked with the black dotted line, while the frequencies of maximum amplitude for the two damped-forced harmonic oscillator are marked with the colored arrow in the graph.

2.4.3 Frequency dependence of the hydrodynamic force

As an AFM cantilever is immersed in liquid, oscillations couple significantly to the viscous, low-Reynolds number hydrodynamics of the surrounding fluid. The most obvious effect of this coupling is that a cantilever's resonance frequency and quality factor appear significantly reduced in liquid environments compared with ambient conditions. This effect depends on the frequency of oscillation, eigenmode number and on the sample-stylus distance because of the squeeze film that develops between the cantilever's body and the rigid substrate (see subsection 2.5.2). To predict the hydrodynamics of cantilevers near a substrate it is necessary to consider fully coupled fluid-structure interaction calculations using the Navier-Stokes equations. A method to overcome these difficulties has been proposed by Sader.⁶⁵ He expressed the external damping component (represented by a_0 in the differential Eq. 2.5) by a more general term in the frequency domain $F_{hydro}(x, \omega)$.⁶⁵ This hydrodynamic force can find an explicit expression by introducing the so called complex-valued "hydrodynamic function", normally indicated by $\Gamma(\omega) = \Gamma'(\omega) + i\Gamma''(\omega)$.⁶⁵ The actual form of the hydrodynamic function varies depending on the geometry and situation of interest. The most important conclusion of this new development is that the hydrodynamic damping of the lever is actually frequency dependent and not a simple constant, like the previously introduced a_0 . It can sometimes be more useful to show the results in terms of simpler parameters like an effective added mass and added viscosity to the cantilever motion. By following the derivation of Maali *et al.*⁶⁶, then used by de Beer *et al.*⁶⁷, the added mass can be

expressed as:

$$m_{added} = \rho_L \frac{\pi}{4} W^2 L \Gamma'(\omega) = \rho \frac{\pi}{4} W^2 L \left(1.05 + 3.80 \frac{\sqrt{\frac{2\eta_L}{\rho_L \omega}}}{W} \right) \quad (2.21)$$

where the new symbols ρ_L and η_L are respectively the density and viscosity of the liquid. The effective damping is expressed as:

$$\gamma_C = \rho_L \frac{\pi}{4} W^2 L \omega \Gamma''(\omega) = \rho_L \frac{\pi}{4} W^2 L \omega \left(3.80 \frac{\sqrt{\frac{2\eta_L}{\rho_L \omega}}}{W} + 2.74 \left(\frac{\sqrt{\frac{2\eta_L}{\rho_L \omega}}}{W} \right)^2 \right) \quad (2.22)$$

By taking into account these corrections it is possible to use the same differential Eq. 2.15, substituting the mass m with the total mass $m_{TOT} = m + m_{added}$ and the term $\frac{m \omega_1}{Q_1}$ with γ_C . The new differential equation becomes:

$$m_{TOT} \frac{d^2 z(t)}{dt^2} = -k_1 z(t) - \gamma_C \frac{dz(t)}{dt} + F_o \cos(\omega t) \quad (2.23)$$

In this case m_{TOT} and γ_C are frequency dependent. The effect on the amplitude and phase shift responses as a function of the excitation frequency is presented in Fig. 2.5.

All these considerations show that, even for an isolated vibrating lever away from a surface, significant differences in the amplitude response as a function of the excitation frequency can arise due to the complex nature of the hydrodynamic system.

In AM-AFM the excitation frequency is held constant during the imaging process or force-distance curves. This frequency effect is therefore not contributing to the imaging process. However, particular care is needed if the driving frequency is modified, particularly if seeking quantitative information.⁶⁷

2.4.4 The effect of the driving mechanism

The last contribution that has been ignored so far and significantly affects imaging in liquid is the driving mechanism. In Eq. 2.23 the driving force appears as a simple sinusoidal signal with frequency ω . Following the categorization of Kiracofe *et al.*²⁹ we can divide the types of excitation method into three categories. The first category is the “induced displacement methods”. As the name suggests, a displacement is applied to some component, indirectly creating a force that drives the cantilever. An example of this method is the dither piezoelectric/acoustic method largely used in most commercially available AFMs. The second category is the direct forcing methods. In this case, a force, rather than a displacement, is applied to the cantilever. Two relevant examples of these methods are the magnetic/electrostatic excitation and the photothermal method. The final category is the thermal excitation, in which random thermal fluctuations of the cantilever and the surrounding fluid cause a random vibration.

A detailed description of the effect that the different driving mechanisms have on the shape of the amplitude as a function of the excitation frequency curve can be found in Ref. [29]. The full mathematical derivation of the effect of the different excitations is beyond the scope of the present work and would require considering again the entire Bernoulli–Euler differential equation with a frequency dependent hydrodynamic force. Here I focus on simple considerations regarding the acoustic driving mechanism following the steps of de Beer *et al.*⁶⁷.

In the case of the acoustically driven cantilever, we can express the driving mechanism previously indicated as $F_0 \cos(\omega t)$ in the case of simple harmonic oscillator model by introducing an actual sinusoidal displacement of the cantilever base $z_b(t) = A_b \cos(\omega t)$. The resulting exciting force is: $F_{exc} = k_C z_b(t) = k_C A_b \cos(\omega t)$, where k_C is the cantilever spring constant. In the presented model, de Beer *et al.*⁶⁷ distinguish between the actual deflection of the lever, normally indicated as $z(t)$, and the value measured by the optical lever method $d(t)$. The usual deflection detection scheme measures the deflection $d(t)$ of the cantilever relative to base position, which is related to the actual lever deflection $z(t)$ by $d(t) = z(t) - z_b(t)$. If the motion of the base is negligible or absent the two deflection values coincide, but since the quality factor Q is low in a liquid environment, $z_b(t)$ can have a strong effect in the motion that is completely neglected by considering $d(t) = z(t)$. With these considerations it is possible to obtain the dependence of amplitude A and phase ϕ measured with the optical lever detector as a function of the applied exciting frequency (see Fig. 2.5). In Fig. 2.5A and B the experimental amplitude and phase represented by the solid black line are compared with (i) the standard harmonic oscillator model that neglect the base motion of the cantilever (blue dashed lines), (ii) a model that takes into account the base movement (red lines) and (iii) a model taking into account the base movement and the frequency dependence of the total effective mass and the viscous damping (green dashed lines).

Beside the easily modeling considerations just discussed, there are additional factors that affect the final amplitude vs. frequency response of a real, acoustically driven cantilever in liquid. The first is the so-called “forest of peaks”, and the second is “fluid borne loading”. The first consists in the appearance of many peaks in the cantilever frequency response spectrum that are not related directly to the cantilever resonance, but to some combination of fluid cell resonances and mechanical resonances. The solution to this problem is to determine the cantilever’s natural frequency and quality factor based on a thermally driven spectrum. The second effect, the fluid borne loading, consists in the excitation of the fluid in the cell in addition to moving the base of the cantilever up and down. This creates a local fluid flow around the cantilever that serves to excite it. Therefore, for a given base displacement, the actual tip motion will be larger than predicted using the ideal acoustic theory. Generally this effect is rarely considered given the difficulties in deriving a proper model to describe it.

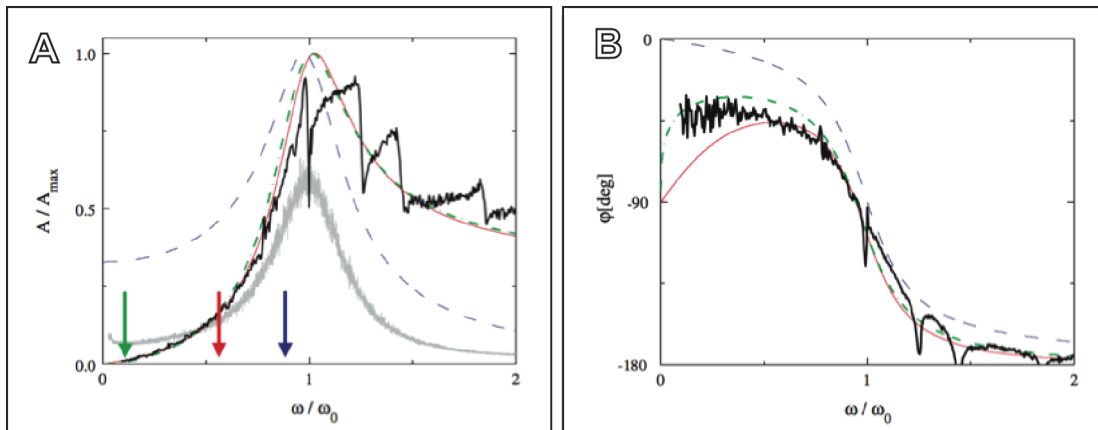


Fig. 2.5: Amplitude and phase responses of an acoustically driven cantilever vs. normalized drive frequency in liquid. The amplitude values are normalized to the maximum amplitude A_{max} . Three models are compared: conventional harmonic oscillator neglecting the base motion (blue dashed lines); the response including the base drive but with constant damping and added mass (red lines); the signal including base drive with frequency-dependent damping and added mass (green dashed line). The black lines are the experimental data while the grey line is the thermal noise spectrum. Taken from Ref. [67].

2.4.5 Point mass model with an external interaction force

It is now possible introduce the effect of the tip-surface interaction forces in the differential Eq.

2.15, in order to extract information about the force measured during AFM experiments. The goal of any theory that describes the motion of the cantilever is to provide a relationship between the tip-surface forces and measured observables. In the case of AM-AFM the observables are the amplitude of the oscillation and phase shift between the driving and the deflection signals. The nonlinear character of the tip-surface forces prevents exact analytical solutions; however, several approximations do provide analytical or semi-analytical solutions. In this section the simplest analytical methods to extract tip-surface force as a function of the amplitude and phase measured in AM-AFM are presented.

The simplest model is a linear approximation based on the simple harmonic oscillator formalism (point-mass model), with the oscillation amplitude, A , induced by the external driving force much smaller than the characteristic length scale of the changes in the interaction force, $F_{TS}(d)$. Under these assumptions, we can linearize (first order Taylor expansion) the tip-sample force around the (quasi-statically moved) average cantilever position that we indicate as z_C :

$$F_{TS}(z_C + z) = F_{TS}(z_C) + \left. \frac{dF_{TS}(z)}{dz} \right|_{z_C} z = F_{TS}(z_C) - k_{int}(z_C) z \quad (2.24)$$

In general z_C is not the tip-sample distance (normally indicated by d) but the mean lever deflection. If we use the point-mass model the two either coincide or are linked by a rigid translation between them given by the tip vertical dimension, so we can consider them equivalent.

In this approximation, the gradient of the force $\left. \frac{dF_{TS}(z)}{dz} \right|_{z_C}$ is the relevant factor that influences the tip motion and the interaction force can be characterized by an effective spring constant k_{int} . Implicitly, in this approximation, we assume that the tip-surface interaction force is only conservative since there is no dependence of F_{TS} on the velocity. Moreover, for small static forces $F_{TS}(z_C)$, the equilibrium force on the cantilever, which appears in the average deflection, can be neglected.

We then obtain the following differential equation (ignoring for a moment the effect of the driving mechanism on the tip motion and the frequency dependence of the hydrodynamic damping):

$$m \frac{d^2 z(t)}{dt^2} = -(k_1 + k_{int})z(t) - \frac{m \omega_1}{Q_1} \frac{dz(t)}{dt} + F_0 \cos(\omega t) \quad (2.25)$$

The result of Eq. 2.25 is exactly the same as that discussed in subsection 2.4.2, with the only difference being that the force constant is increased by k_{int} . This means that the new resonance frequency ω_{eff} , related to the effective spring constant $k_{eff} = k_1 + k_{int}$, is shifted by $\Delta\omega$ from ω_1 , the natural frequency of the first eigenmode:

$$\Delta\omega = \omega_{eff} - \omega_1 = \sqrt{\frac{k_{eff}}{m}} - \sqrt{\frac{k_1}{m}} = \sqrt{\frac{k_1 + k_{int}}{m}} - \sqrt{\frac{k_1}{m}} \quad (2.26)$$

If we suppose that k_{int} is much smaller than k_1 , we can expand the first square root and obtain:

$$\Delta\omega \approx -\frac{\omega_1 k_{int}}{2 k_1} + O(k_{int}^2) \quad (2.27)$$

Eq. 2.26 and 2.27 show that, whenever the interaction force can be approximated by the linear term, the amplitude modulation AFM behaves like a harmonic oscillator with a resonant frequency that depends on the gradient of the interaction.

$$A_{int} = \frac{\frac{F_0}{m}}{\left[((\omega_1 + \Delta\omega)^2 - \omega^2)^2 + \left(\omega \omega_1 / Q_1 \right)^2 \right]^{1/2}} \quad (2.28)$$

$$\tan\varphi_{int} = \frac{\omega \omega_1 / Q_1}{(\omega_1 + \Delta\omega)^2 - \omega^2} \quad (2.29)$$

The dependence of the amplitude on the excitation and effective resonant frequencies provides the first mechanism to explain the dependence of the oscillation amplitude on the strength of the interaction force (related to the tip-surface separation). The shape of the resonance $A_{int}(\omega)$ in the presence of weak conservative forces is preserved and simply shifted in the frequency domain of $\Delta\omega$. The Q -factor is the same as the one in the absence of interaction. Let us assume that the tip is excited at natural frequency in the absence of the interaction. Approaching the tip towards the surface will modify the resonant frequency of the lever to the new ω_{eff} . The oscillation amplitude at the driving frequency will be affected by the tip-sample interfaces with a reduction of the amplitude in both attractive (red-shift) and repulsive (blue-shift) situations (see Fig. 2.6). In this approximation, obtaining the force gradient from the decrease of the oscillation amplitude is straightforward if the free dynamic of the lever (without interaction force) is characterized at the beginning of the experiment. The phase response shifts with the new frequency of resonance so that the maximum dissipated power is always maintained at ω_{eff} . This result is used by FM-AFM to better track the shift of the resonance frequency as a function of the interaction force.

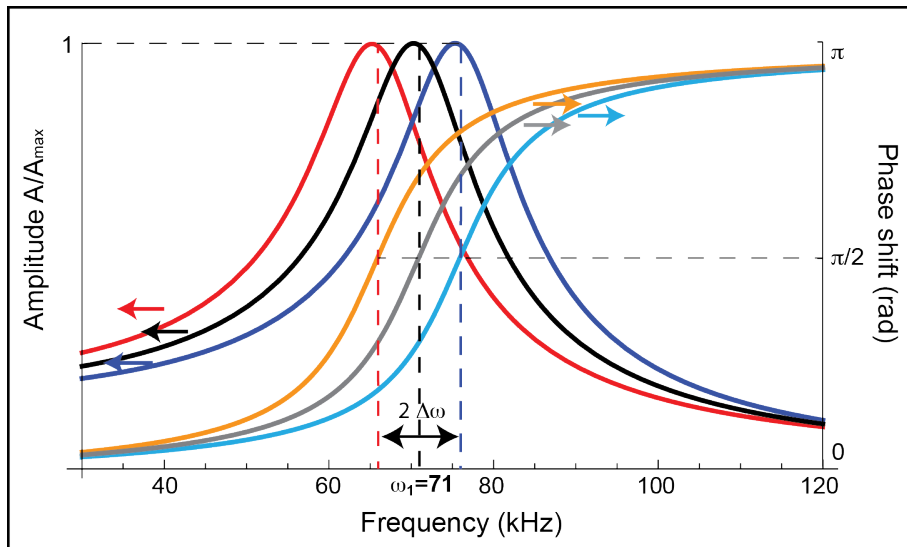


Fig. 2.6: The effect of a small conservative interaction force on the amplitude and phase vs. exciting frequency response. The unperturbed damped-forced harmonic oscillator is presented in black/grey (amplitude/phase) solid line and is characterized by the following parameters: $F_0 = 2 \text{ nN}$, $\omega_1 = 71 \text{ kHz}$, $Q_1 = 5$. The blue/light blue (amplitude/phase) curves represent a small repulsive force that translates into a blue shift of 5kHz (7%) of the resonance curve. The red/orange (amplitude/phase) curves represent a small attractive force that translates into a red shift of 5kHz (7%) of the resonance curve.

The limitations of weakly perturbed harmonic models to describe dynamic AFM can be traced back to the implicit assumption that the tip surface force induces a frequency shift and not an energy transfer or loss. Secondly, the force gradient was assumed independent of the separation in the oscillation cycle.

A first improvement can be done by introducing a dissipative component (proportional to the velocity and not to the displacement) in the differential Eq. 2.25. In this case the interaction force can be expressed as:

$$F_{TS}(z_C + z) = -k_{int}(z_C) z - \gamma_{int}(z_C) \frac{dz}{dt} \quad (2.30)$$

The differential equation of the cantilever motion becomes:

$$m \frac{d^2 z(t)}{dt^2} = -(k_1 + k_{int})z(t) - (\gamma_1 + \gamma_{int}) \frac{dz(t)}{dt} + F_0 \cos(\omega t) \quad (2.31)$$

where $\gamma_1 = \frac{m\omega_1}{Q_1}$. The steady-state solution of the differential equation is identical to that of the free motion, but with the substitution of k_1 with $k_{eff} = k_1 + k_{int}$ and of γ_1 with $\gamma_{eff} = \gamma_1 + \gamma_{int}$. The effect on the new frequency of resonance upon interaction is exactly the same as the one in the absence of tip-surface dissipative interaction force (Eq. 2.32). In addition, an extra damping that induces a broadening of the resonance curve of the amplitude of oscillation is present:

$$\Delta\omega = \omega_{eff} - \omega_1 = \sqrt{\frac{k_{eff}}{m}} - \sqrt{\frac{k_1}{m}} \approx -\frac{\omega_1 k_{int}}{2k_1} \quad (2.32)$$

$$A_{int} = \frac{\frac{F_0}{m}}{\left[(\omega_{eff}^2 - \omega^2)^2 + \left(\omega \frac{\omega_{eff}}{Q_{eff}} \right)^2 \right]^{1/2}} \quad (2.33)$$

$$\tan\varphi_{int} = \frac{\omega \frac{\omega_{eff}}{Q_{eff}}}{\omega_{eff}^2 - \omega^2} \quad (2.34)$$

where $Q_{eff} = \frac{m\omega_{eff}}{\gamma_{eff}} = \frac{m\omega_{eff}}{\gamma_1 + \gamma_{int}}$. The introduction of an extra damping decreases the value of the effective Q -factor. The result is a broader resonance that for the same value of F_0 reaches a lower value of the maximum amplitude. The phase has a smooth dependence on the frequency around the new resonance frequency ω_{eff} (see Fig. 2.7).

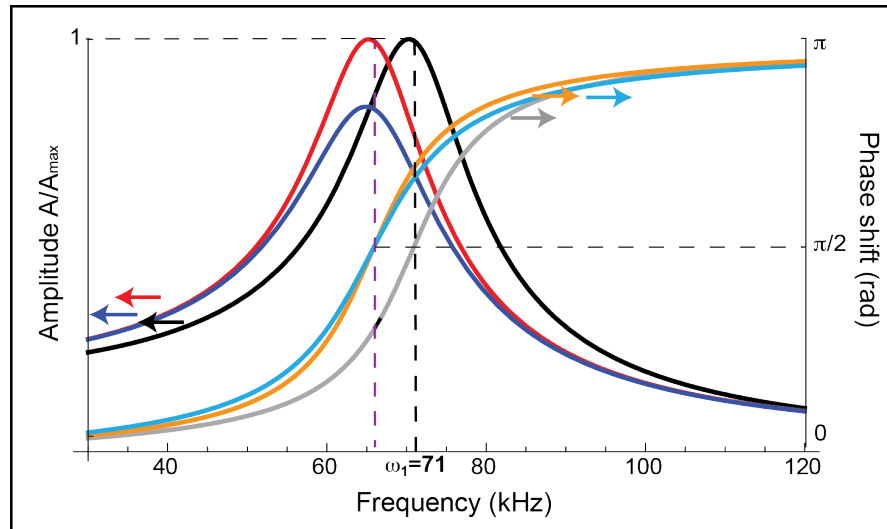


Fig. 2.7: Effect of small conservative and dissipative interactions on the amplitude/phase vs. excitation frequency response. The unperturbed damped-forced harmonic oscillator is presented in black/grey (amplitude/phase) solid line and is characterized by the following parameters: $F_0 = 2 \text{ nN}$, $\omega_1 = 71 \text{ kHz}$, $Q_1 = 5$. The red/orange (amplitude/phase) curves represent a small attractive conservative force that translates into a red shift of 5kHz (7%) of the resonance curve. In the blue/light blue curves we added a small dissipative force to the previous curve that translates into a γ_{int} equal to 20% of γ_1 .

The last simple development was introduced by Schroter *et al.*⁶⁸ who used the Fourier expansion of the force $F_{TS}(z(t))$ in the time domain knowing that the steady state solution $z(t)$ can be expressed as $A \cos(\omega t)$. A similar approach was used previously by Sader *et al.*⁶⁹ in the case of FM-AFM by imposing the self-excitation of the cantilever. Since the distance between tip and sample has a periodic component in time, this same periodicity is expected even in $F_{TS}(z(t))$, supposing the average position z_C of the lever is maintained constant. Under this assumption, $F_{TS}(z(t))$ can be expressed as:

$$F_{TS}(z(t)) = F_{TS}(t) = \frac{a_0}{2} + \sum_{i=1}^{\infty} a_i \cos(i\omega t) + b_i \sin(i\omega t) \quad (2.35)$$

$$a_i = \frac{2}{T} \int_0^T F_{TS}(t) \cos(i\omega t) dt \quad (2.36)$$

$$b_i = \frac{2}{T} \int_0^T F_{TS}(t) \sin(i\omega t) dt \quad (2.37)$$

By keeping only the first Fourier components with $i=1$ the interaction force can be expressed as:

$$F_{TS}(t) = a_1 \cos(\omega t) + b_1 \sin(\omega t) = \frac{a_1}{A} z(t) - \frac{b_1}{A\omega} \frac{dz(t)}{dt} \quad (2.38)$$

and the differential equation becomes:

$$m \frac{d^2 z(t)}{dt^2} = - \left(k_1 - \frac{a_1}{A} \right) z(t) - \left(\gamma_1 + \frac{b_1}{A\omega} \right) \frac{dz(t)}{dt} + F_{ext}(t) + F_{TS}(d) \quad (2.39)$$

In this case it is still possible to solve the differential equation in a similar fashion as previously by introducing again a k_{eff} and a γ_{eff} , defined now as:

$$k_{eff} = k_1 - \frac{a_1}{A} = k_1 + k_{int} \quad (2.40)$$

$$\gamma_{eff} = \gamma_1 + \frac{b_1}{A\omega} = \gamma_1 + \gamma_{int} \quad (2.41)$$

Eq. 2.40 and Eq. 2.41 can be considered identical to those of the harmonic approximation of the interaction force with damping (Eq. 2.31). However, there is a significant difference: the method proposed by Schroter *et al.* establishes that the influence of the interaction force in the tip motion is averaged over the whole oscillation cycle, while in the harmonic oscillator model only the gradient of the force at the mean tip-sample distance position influences the cantilever motion. In all these analytical approaches, the tip motion is considered to be sinusoidal and the derived expressions resemble those of the single harmonic oscillator for the amplitude and phase shift as a function of the frequency. The analytical approaches presented in this section neglect the average deflection of the cantilever and the higher harmonics components of the oscillation. Nevertheless, they have been proven a powerful tool for describing the interaction between tip and sample.

2.4.6 Non-linear interaction forces in liquid: higher harmonic and higher eigenmodes

In the case of a forced harmonic oscillator with damping, the presence of a tip-surface interaction can be described as a sinusoidal wave with a single frequency coinciding with the excitation frequency ω . In the model proposed by Schroter *et al.*⁶⁸, however, the complete form of the tip-surface interaction requires considering even the Fourier terms of higher harmonics (multiple

integer of the excitation frequency, $n\omega$). These non-linear terms would have introduced a higher frequency component in the tip motion $z(t)$. The generation of higher harmonics is therefore related to the presence of a nonlinear interaction force. It is pertinent to remember the distinction between eigenmodes and harmonics. An eigenmode is one of the discrete solutions of the beam model of the cantilever presented in subsection 2.4.1 while a harmonic is a component of the oscillation that vibrates with frequency equal to an integer multiple of the excitation frequency. If we consider nonlinear interaction between tip and sample we can now use the following expression to describe the tip motion:

$$z(t) = z_0 + \sum_{n=1}^{\infty} A_n \cos(n\omega t + \varphi_n) \quad (2.42)$$

In this case we have to consider not only the amplitude A_1 of oscillation of the first harmonic (that normally coincide with the first eigenmode), but even of the higher frequency components of the motion.

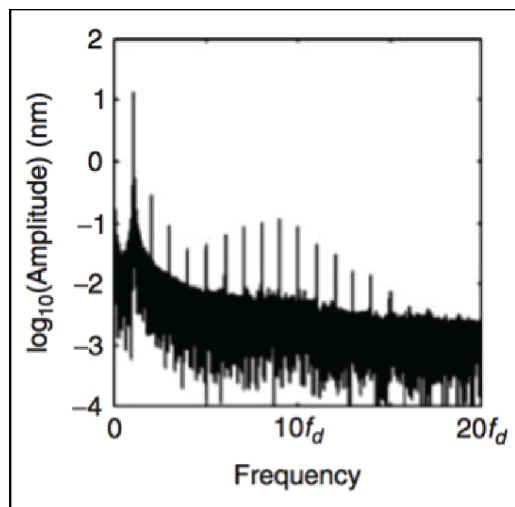


Fig. 2.8: Experimental amplitude vs. frequency spectrum (obtained from the Fourier transform of the actual oscillation motion) of a soft cantilever mechanically interacting with the surface of mica in buffer solution. The appearance of higher harmonics is modulated by the first and second eigenmode of oscillation and in fact around $9-10f_d$ (fundamental excitation frequency) there is an enhanced oscillation amplitude. Figure adapted from Ref. [29].

Although the presence of higher harmonic components is a common feature, their relevance in experiments performed in air is diminished by the observation that under gentle imaging conditions, the amplitude of the fundamental component is two to three orders of magnitude higher than any of the amplitudes of the other harmonics.²⁸ Higher harmonic components are enhanced by operating the microscope in liquid because of the low quality factor of the resonance that often include part of the second or higher harmonics in the resonance-enhanced frequency region.

Basak *et al.*⁷⁰ noticed that, beside the excitation of higher harmonics during the tip-sample nonlinear interaction, even the second eigenmode of the cantilever is momentarily excited around moments of tip-sample contact. They noticed, by monitoring the tip motion in time, high-frequency components that locally distort the perfect sinusoidal oscillation and are caused by the physical contact between the tip and the sample. The lever motion after the sudden interaction with the surface was exhibiting the signature of an impulse or “ring down” response with a typical frequency corresponding to the resonance of the second eigenmode.⁷⁰ We will see that this phenomenon can affect the energy dissipated by the tip during the oscillation.

In a realistic situation the two effects of higher harmonic and second (or higher) eigenmode excitation are related. The evidence of multimodal cantilever dynamics in liquids is even more compelling in frequency domain. When the dynamics of the cantilever are captured by a single eigenmode, the higher harmonics decay monotonically with frequency following the envelope of the resonance of the first eigenmode. If the second eigenmode is excited, the experimental

amplitude vs. excitation frequency spectrum reveals a cluster of enhanced harmonics surrounding the second resonance. Higher harmonics that are enhanced around a certain natural frequency indicate the presence of the corresponding eigenmode in the response (see Fig. 2.8).²⁹

2.4.7 Phase contrast and energy dissipation in AM-AFM

In the AM-AFM the phase lag φ between the external excitation and the vibrating probe is not maintained constant but can vary freely during the imaging process. Usually the phase lag is recorded in a separate channel during the measurement and referred to as the phase image of the sample. In the previous sections we have seen how from the amplitude and phase response of the lever, we could derive information about the force acting between the tip and the sample. Here I present a more general framework for interpreting the phase images, which can provide some important information on the energy dissipated by the oscillator in the presence of dissipative tip-surface forces.

Let's start by supposing the steady state oscillation of the AFM tip can be expressed as:

$$z(t) = z_0 + \sum_{n=1}^{\infty} A_n \cos(n\omega t + \varphi_n) \quad (2.43)$$

To keep the cantilever oscillating in the presence of hydrodynamic damping and tip-surface dissipative processes, the energy per cycle supplied by the external excitation E_{exc} must be equal to the energy per cycle dissipated by the tip-surface forces E_{diss} and the hydrodynamic damping in the medium E_{med} .

$$E_{exc} = E_{med} + E_{diss} \quad (2.44)$$

We can find an expression for the these terms:

$$E_{exc} = \oint F_{exc}(t) \frac{dz(t)}{dt} dt = \oint F_0 \cos(\omega t) \frac{dz(t)}{dt} dt \quad (2.45)$$

$$E_{med} = \oint F_{hydro}(t) \frac{dz(t)}{dt} dt = \oint \left(\frac{m\omega_1}{Q} \frac{dz(t)}{dt} \right) \frac{dz(t)}{dt} dt \quad (2.46)$$

$$E_{diss} = \oint F_{TS}(d(t)) \frac{dz(t)}{dt} dt \quad (2.47)$$

By substituting the explicit expression for $z(t)$ and its derivatives in Eq. 2.47 we obtain the following result:⁷¹

$$\sin\varphi_1 = \sum_{n=1}^{\infty} \frac{n^2 A_n^2 \omega}{A_0 A_1 \omega_1} \left(1 + \frac{E_{diss}}{E_{med}} \right) \quad (2.48)$$

where A_0 is the free amplitude of oscillation at the frequency ω . Eq. 2.48 determines the relationship between the phase shift of the oscillation at the excitation frequency ω , the amplitude of the higher harmonics A_n and the ratio between the energy dissipated per cycle due to non-conservative tip-surface forces E_{diss} and the energy dissipated by the viscosity of the surrounding media E_{med} .

In particular, if the higher harmonic contributions are neglected we obtain:

$$\sin\varphi_1 = \frac{\omega A_1}{A_0 \omega_1} \left(1 + \frac{E_{diss}}{E_{med}} \right) \quad (2.49)$$

This is the same expression as obtained by Martínez *et al.*⁷² The sine of the phase shift φ_1 is

related to the amplitude A_1 and to the energy per cycle dissipated in the sample by the non-conservative tip-surface forces. This formula is particularly interesting in the case of AM-AFM. In this case, the microscope operates under the condition of constant A_1 so the prefactor in Eq. 2.49 remains unchanged while imaging. Consequently, any of the recorded phase shift variations in the image reflect local changes in the energy irreversibly transferred from the cantilever/tip system to the surface (of course assuming the feedback system to be ideal).

Eq. 2.49 can be easily adapted to determine either the average power transferred from the tip to the sample surface or the interfacial media as was originally done by Cleveland *et al.*^{20,21}:

$$\langle P_{diss} \rangle = \frac{k_1 A_1^2 \omega}{2Q} \left(\frac{A_0}{A_1} \sin \varphi_1 - \frac{\omega}{\omega_1} \right) \quad (2.50)$$

Eq. 2.50 provides a direct method to measure dissipation at the nanoscale. The value of the mean dissipated power $\langle P_{diss} \rangle$ due to the interaction between tip and sample can be calculated by simply recording the experimental parameters: free and set point amplitudes, cantilever force constant, Q -factor, resonance and excitation frequencies and phase shift. The interesting part of this approach is that no assumption has been done on the interaction force. This implies that this formula is generally valid even when the dissipative part of the forces is hysteretical. The only requirement is a sinusoidal motion of the tip. In AM-AFM the amplitude of oscillation, as well as the exciting frequency, is constant, so the phase contrast is related to the power dissipated. The only exception, where phase contrast is not due to dissipation, arises because symmetric phase changes of $\pi/2$ are allowed even if there are no losses in the tip-sample interaction.^{20,21}

In liquid media, the presence of higher harmonic distortions render the energy dissipation developed assuming a single harmonic not entirely accurate and Eq. 2.48 is generally preferred. However, the full implications of the energy losses in higher harmonic distortions to energy dissipation have recently been shown to include even the energy transfer between different eigenmodes of the lever.⁷³ When the second eigenmode is excited during interaction with the sample, a relatively large amount of energy is transferred from the first to the second eigenmode. This energy is subsequently dissipated into the surrounding media during the “ring down” of the second eigenmode. This contribution has been added by Melcher *et al.*⁷³ in the energy balance of the dissipated power of the driving force:

$$E_{exc} = E_{med} + E_{diss} + E_{1-2} \quad (2.51)$$

where E_{1-2} is the energy transferred from the first eigenmode to the second eigenmode as a result of the nonlinear interaction with the sample. These interactions can be conservative, so the phase shift may simply be the result of a transfer of energy between different eigenmodes for highly non-linear interactions. Unfortunately, to the best of my knowledge, there are to date no simple and intuitive descriptions of these phenomena. Most of the related descriptions tend to rely on computer simulation^{61,74}

2.5 Interaction forces: conservative and dissipative interactions

In this section an explicit expression of the type of forces between tip and sample in a liquid media is provided. For an extensive treatment of the topic I suggest the book of J. N. Israelachvili⁷⁵ and the summary proposed by Kiracofe *et al.*⁶³ The aim of this section is to isolate and quantify properties related to the solid-liquid interface from all measurable forces. Initially, we can divide the forces between conservative and dissipative as already done in the previous section. This is important because these two types of forces have a different effect on the cantilever motion.

2.5.1 Conservative forces

Van der Waals forces

The van der Waals interaction forces originate from the electric dipole interaction between atoms or molecules. This dipole can be either permanent or induced by another permanent dipole or arise from thermal and/or zero point quantum fluctuations. In all cases, the interaction potential $w(r)$ between molecules or atoms, scales as $-\frac{1}{r^6}$, where r is the distance between the two atoms/molecules.⁷⁶ The total net van der Waals force between the AFM tip and the surface is the result of adding all the individual dipole interactions between tip and surface atoms. Assuming the atom/atom interaction is additive and disregarding the discrete nature of matter, we can replace the sum over individual atoms by an integration over a volume with a fixed number density of atoms. Moreover we can disregard retardation effects due to the finite speed of light (usually appropriate for distances up to several hundred angstroms). This approach, used to obtain the van der Waals interaction between macroscopic bodies, was proposed by Hamaker already in 1937.⁷⁷ For a spherical tip with radius R next to a flat surface (r is the distance between the plane connecting the centers of the surface atoms and the center of the closest tip atom, so the tip-sample distance) the van der Waals potential and force is given by:⁷⁵

$$V_{vdW} = -\frac{A_H R}{6r} \quad \text{and} \quad F_{vdW} = -\frac{A_H R}{6r^2} \quad (2.52)$$

The Hamaker constant A_H depends on the type of materials (atomic polarizability and density) of the tip and sample. The van der Waals force between two surfaces is usually attractive but there are some exceptions. The van der Waals force between two identical materials in a medium is always attractive, as is the van der Waals force between two different materials in air or in vacuum. The van der Waals force between two different materials in liquids could be either attractive or repulsive depending on the values of the dielectric constants and the refractive indexes of the media in which they are immersed.⁷⁵

Stearic repulsion, contact mechanics and chemical forces

The stearic repulsion force between two atoms/molecules is characterized by a very short range, steep increase as a function of the mutual distance. It originates from an overlap of the electron clouds of both molecules/atoms resulting in a strong repulsive force (Pauli repulsion). This force determines how close two atoms or molecules can approach each other. Unfortunately there is no general equation for describing the distance dependence but instead, a number of empirical potential functions have been introduced over the years.⁷⁵

In the case of AFM experiments, a net repulsive force originates from the interaction involving hundreds or thousands of atoms/molecules repelling each other. The description of the effective repulsive force is provided by contact mechanics models.^{63,76} These models take into account the deformation of two elastic bodies that are brought into mechanical contact. The deformation depends on the applied force and the mechanical properties of both sample and tip. Continuum elasticity theories describe the contact and adhesion between real bodies under an external load, providing analytical relationships between the deformation or the contact area of the two bodies and the applied force in the presence of adhesion forces. For detailed descriptions of the contact mechanic models I suggest the work of Cappella *et al.*⁷⁶

Other important contributions are coming from the so-called “chemical forces”. These forces are short-ranged and arise from the actual formation of chemical and/or specific bonds between the atoms of the tip and the ones of the surface. Generally the effect is a difference in the force measured before and after contact of the tip with the surface. This contribution is thus often hidden in the concept of adhesion hysteresis, as we will see in the part of dissipative forces.

Solvation forces

These forces are discussed in details in Chapter 1, including the effect at the tip-liquid and surface-liquid interfaces. Solvation forces, together with the Electrostatic Double Layer (EDL) forces, will be extensively discussed with the results presented in Chapter 4. They often are the dominating solid-liquid forces in the presence of a liquid media between the tip and the sample.

Electrostatic Double Layer (EDL)

This type of forces plays a fundamental role in situations where a charged surface is immersed into a liquid that contains dissolved ionic species. The density distribution of the ions close to surface is spatially dependent and deviate significantly from the constant value of the bulk liquid. When similarly charged surfaces are brought together from infinity to a certain distance D , the pressure between them can be calculated using the Poisson-Boltzmann equation (see Chapter 4 for a full derivation of the formulae). This pressure has two contributions: the first one, always attractive, is due to the electrostatic field energy contribution, while the second term is repulsive and derives from the entropic contribution to the energy. In general the second term is larger making the overall force repulsive.⁷⁵

2.5.2 Dissipative forces

The mechanisms responsible for energy dissipation in AFM experiments constitute an important and complex field of research. Energy dissipation arises from a variety of processes that depend on both the material properties and the environment. For example, dissipation is involved in force-induced atomic or molecular reorientations, interdigitation, and whenever there is an exchange of atoms and molecules between the tip and the sample. Some of the mechanisms involve the direct mechanical interaction between the tip and a sample with viscous properties: adhesion hysteresis and sample viscosity. Physically, the two mechanisms differentiate between velocity-dependent dissipation processes and hysteresis-dependent processes where dissipation depends on a difference magnitude between the attractive interactions during approach and retraction of the tip from the surface. The other types of dissipative mechanisms are related to the variation of the viscous properties of the liquid close to the solid surfaces and are important for the characterization of solid-liquid interfaces.

Viscosity of the sample

In general, materials are not purely elastic. They often exhibit a viscous component that contributes to dissipate the energy during the mechanical contact of the tip with the surface.

The most widely used model describing the viscosity contribution to the tip-surface force is the Voigt model. According to it, elastic and damping components of the interaction force are connected in parallel (in the Maxwell model they are connected in series). Moreover the viscous component has the following stress (σ)-strain (ε) relationship:

$$\sigma = \mu \frac{d\varepsilon}{dt} \quad (2.53)$$

The stress σ has the dimensions of pressure, μ is the viscosity of the material composing the sample and ε is the strain, that corresponds to a displacement and so it has the dimension of length. Eq. 2.53 is actually the definition of Newtonian fluid. Using the Hertz model of contact mechanic,⁷⁶ it is possible to translate the stress into a force by considering the contact area a , the indentation rate $\frac{d\delta}{dt}$ and the radius of curvature R of the tip:

$$\delta = \frac{a^2}{R} \quad \text{so} \quad F_{visc} = \sigma a = \mu \sqrt{\delta} R \frac{d\delta}{dt} \quad (2.54)$$

This expression has been used, for example, by Garcia *et al.*⁷⁸, Gómez *et al.*⁷⁹, Melcher *et al.*⁷³ and Schirmeisen *et al.*⁸⁰. It provides a suitable model for the dissipative contact force when added to the contact hysteresis contribution. The total force F_{TS} according to the Voigt model is simply obtained by summing this contribution in the contact region to the conservative elastic response.

Surface adhesion hysteresis

This process of energy dissipation is present every time the work needed to separate two surfaces is greater than the energy initially gained by bringing the surfaces together. As a consequence, the surface energy γ of the system shows two different values, one during the approach half period γ_a and the other in the retraction half period γ_r . Garcia *et al.*⁷⁸ use the Derjaguin-Muller-Toporov (DMT) model⁷⁶ to calculate the energy dissipated in the surface energy hysteresis. The adhesion component to the DMT force is:

$$F_{DMT}^{adh} = -4\pi R\gamma \quad (2.55)$$

The total energy dissipated in the oscillation is hence related to the variation of the surface energy:

$$E_{DMT}^{adh} = \oint F_{DMT}^{adh} dz = 4\pi R\delta(\gamma_r - \gamma_a) \quad (2.56)$$

The energy dissipation can be obtained using the fact that the adhesion force is acting only in the part of the motion in which the tip is in contact with the surface where the vertical motion of the tip is simply δ . Surface adhesion hysteresis can have two contributions: one coming from long-range interactions and the other coming from short-range atomic and molecular interactions. The important point is that such a hysteresis should take place at a time scale much faster than the tip velocity. Therefore, it can be assumed that energy dissipation caused by a hysteresis is nearly independent of the tip velocity.⁸⁰

Non-contact region dissipative forces in liquid

Some dissipative processes occur in the non-contact region and are related to the properties of the solid-liquid interface. The nature and the form of these dissipative processes are still a matter of debate. In general the dissipation arises from the fact that, during the approach part of the oscillation, the liquid (with a certain viscoelastic response) is confined in a nanometric gap between the tip and the sample. By progressively approaching the solids, the liquid is expelled from the gap in a non-conservative process due to the intrinsic friction between the layers of liquid molecules or a viscosity change of the fluid at the interface.

At close distances between sample and tip, an increased energy dissipation that translates into an increased damping term in the cantilever dynamic, is experimentally measured. There are several components to this increased damping.³⁰ The first component is normally called “squeeze-damping” and arises from the hydrodynamic squeezing of the liquid between the two approaching surfaces. Squeeze films’ damping depends strongly on the geometry. For a spherical tip approaching a flat surface, the squeeze term can be obtained from the Reynolds equation for squeeze films.^{30,81}

$$\gamma_s = 6\pi\eta \frac{R^2}{D} \quad (2.57)$$

where R is the tip radius, D the tip sample distance and η the viscosity of the fluid. Another squeeze damping term is often considered and it is due to the squeezing of the liquid by the actual cantilever body.^{29,30} If the oscillation of the lever or the distances covered in the spectroscopic measurements are in the order of tens of nanometers, this term can be neglected, being slowly distance-dependent. These dampings are added to the hydrodynamic damping of the cantilever, so multiplied to the velocity term in the differential Eq. 2.31.

The squeezing effect often does not fully describe the measured energy dissipation. In particular, there is the necessity to introduce a spatial dependent “effective viscosity” $\eta_{eff}(d)$ in Eq. 2.57 to match the experimental data.³⁰ Although it has been widely accepted that nanoconfined liquids are different from the bulk, the often surprising viscoelastic behavior is not completely understood and it is still debated.⁸²⁻⁸⁵ O’Shea *et al.*³⁰, for example, found a monotonic increase of $\eta_{eff}(d)$ at small tip-sample separation. They concluded that even for small contact radii, like the ones in the case of sharp AFM tips, confinement causes the liquid nearest the surfaces to become more viscoelastic. Klein *et al.*⁸⁶ detected with SFA an abrupt transition from liquid-like to solid-like behavior of a liquid under confinement. Khan *et al.*⁸¹ found a bulk-like viscosity in a nanoconfined, weakly interacting liquid similarly to what previously found by Becker *et al.*⁸⁷. Khan *et al.*⁸¹ observed even a further decrease in viscosity at confinement sizes of just few molecular layers that they addressed to shear thinning and/or boundary slip, while Becker *et al.*⁸⁷ found an increase of the effective viscosity that was attributed mainly to the increasing weight of the frictional component of the liquid-wall contact compared to the liquid-liquid friction.

Kan *et al.*⁸³ showed that the complete picture is more complex and that a variation in the viscoelastic response can be obtained by changing the approach speed. They noticed that increasing the approach speed from 6 Å/s to 8 Å/s induces a decrease of the damping with a simultaneous increase of the stiffness when the tip-sample gap is an integer multiple of the molecular size (water in this specific case). Above a certain threshold rate, the liquid behaves solid-like with low viscosity and high elasticity when the gap is commensurate with molecular size, while retaining a liquid-like, high viscosity state when the gap is incommensurate with the molecular size.⁸³ Li *et al.*⁸⁸ studied the viscoelastic dynamics of nanoconfined wetting liquids (water and OMCTS) with lateral AFM by varying shear amplitude and rate. They observed a nonlinear viscoelastic behavior remarkably similar to that widely observed in metastable complex fluids like supercooled water. Moreover, by measuring the viscoelastic modulus at different frequencies and strains, they found that the intrinsic relaxation time of nanoconfined water is orders of magnitude longer than that of bulk water. Zhu *et al.*⁸⁹ found a frequency-dependence in the shear viscosity of water containing monovalent or divalent ions, confined between mica crystals. They found that by changing the twist angle between the two mica sheets the effective viscosity varied by orders of magnitude. They concluded that confinement appeared to imprint lateral spatial correlation on the ultrathin liquid; the more so, the better the confining lattices were aligned.

One of the main debated phenomena in literature is the non-monotonic damping variation upon liquid confinement.^{45,67,81-83,90} Confined liquids self-assemble into an equilibrium structure with discrete molecular layers (see Chapter 1). These results into oscillatory solvation forces measured with both AFM and SFA. To expel one layer of liquid molecules a collective sliding movements of those is required to further decrease the tip-sample distance. Such a thermodynamically irreversible process costs a large amount of energy and leads to a large oscillatory damping and solid-like behavior in certain dynamical conditions. A plausible model for the nonmonotonic dissipation curve assumes two alternating dissipation mechanisms in the small-amplitude regime. In one case, the modulation of mechanical stress exerted by the vibrating tip leads to periodic compression and decompression of the underlying molecular lattice. As the molecular order is maintained and no large-scale molecular movement is involved (constant number of molecular layers between tip and sample), this process is dominated by the elastic, low-dissipation response characteristic of a crystalline solid. At a certain point the compression is increased to the point where layer penetration occurs. At this point the vibrating tip repeatedly expels and reincorporates molecules within a solvation layer in every oscillation cycle. This squeeze-out process relaxes the mechanical stress and lowers the effective sample stiffness sensed by the tip, but results in an increased dissipation.⁴⁵ Interestingly, the existence of non-monotonic variations of the damping with decreasing film thickness has sometimes been questioned and attributed to experimental artifacts.⁸⁴ This oscillatory behavior of the energy dissipated, as a function of the confining distance, seems to be related to roughness, shape and asymmetry of the tip. Hofbauer *et al.*⁴⁵ found that sharp non-monotonic dissipation features were related to individual tips. For most tips, the dissipation peaks were either not really pronounced or not noticeable at all. They also found that the dissipation peaks could be induced by deliberately blunting the tip by scanning in contact

mode.⁴⁵ Similarly Labuda *et al.*⁹¹ attributed to the different parts of the tip two different contributions: the oscillatory behavior of the force (in the presented experiment the oscillatory part is related only to the conservative part of the force) due to mesoscopic tip and the monotonic damping due to nano-asperities.

In the work of Young *et al.*⁸⁵, the specific interaction between the solid surface and the liquid is analyzed in terms of dissipative loss in lateral and standard AFM. They studied water interfacial viscosity on substrates with different wettability and showed that boundary viscous forces are related to slippage processes, which in turn can depend on the wettability of the surface. They use a modified form of the Newtonian definition of viscosity, which takes into account the fluid slip, to explain the decrease of the interfacial viscous forces with increasing hydrophobicity (corresponding to an increase of the water slip length on the surface). To do so they suppose that the intrinsic dependence of the viscosity of water on the confinement gap remains the same for all the surfaces from mica to HOPG. The only varying parameter is the slip length. The same model is used to give an interpretation of the correlation between surface wettability and energy dissipation in small amplitude AM-AFM experiments at solid-liquid interfaces. The average energy costs associated with the subsequent approach and retraction of a tip vertically oscillating at the interface is directly correlated to the shear force and can be explained by water slippage at the surface. In this last example, a reference ‘effective viscosity’ profile of the interfacial water was obtained for mica from the experimental data and subsequently applied to the other surfaces.

An alternative approach is to look for a simpler model that will directly match the experimental data. Normally it is assumed that the damping coefficient is proportional to the conservative portion of the solvation (plus eventual hydration) force (see Chapter 1). This approach was proposed initially by Jeffery *et al.*³¹ and then used by Kiracofe *et al.*⁷⁴ to model the dynamic of the lever oscillation in liquid (see section 1.6) and implemented in the VEDA simulator⁶³. In the last two cases though, the hydration force is simply modeled as an exponentially decaying function without an oscillatory behavior. The result is a spatial dependent dumping coefficient to be added directly to the equation of motion. Even if a simplified model, this approach has been found to be in agreement with the experimental data.⁷⁴

One more possible dissipative mechanism was discerned by Wu *et al.*⁹² and Ebeling *et al.*⁹³ by showing that the dissipation measured with the AM-AFM in ionic solutions is related to the ionic strength and so to the Debye length of the solution. This observation was attributed to the so-called electroviscous effect, which causes excess damping upon overlap of the Debye layers. For the highest salt concentrations, this effect is screened due to the shortness of the Debye layer. The interdependence of the ionic distribution and hydration forces at the water-hydrophilic surfaces render the disentanglement of the two contributions difficult.

2.6 High resolution and solvation forces

Section 2.3 details some of the necessary requirements for obtaining high-resolution images by AFM. Here I show how these requirements can be applied to the specific solid-liquid interfaces systems. In this section I first analyze how the presence of the interfacial liquid affect the dynamic of the cantilever, showing that this external damping force helps to maintain an harmonic motion even in the presence of non linear forces. In the second part I report the suspected main mechanisms behind high resolution. Finally, I present examples where the solvation structures of various liquid/solid systems affect the achievable resolution.

2.6.1 The effect of the “solvation” damping on the cantilever motion

The presence of liquid between the AFM tip and the sample appears to be a determining factor in AFM measurements. Firstly, it modifies the cantilever dynamic because of the added mass to the lever and hydrodynamic damping, as described in section 2.4. This effect can be incorporated in the simple harmonic oscillator model by introducing an effective mass and effective viscosity. A

strongly non-linear tip-surface interaction, for example due to mechanical contact between tip and sample, can seriously perturb the system rendering the harmonic oscillator model no more applicable. However, when using the working conditions for AM-AFM as defined in Chapter 1, these effects are negligible, since the actual mechanical contact between tip and sample is avoided during the oscillation. Non-linearities due to a tip impact of the surface are also limited by the presence of the extra “solvation” damping mechanism discussed in the previous section⁷⁴.

Kiracofe *et al.*⁷⁴ presented a study on the effect that hydration forces have on the dynamic of the cantilever in liquid with both experiments and simulation. In the simulations they propose a viscous drag where the damping coefficient decays exponentially away from the wall. They first show that the experimental results cannot be reproduced by the VEDA simulator⁷⁴ without the introduction of the hydration force (both conservative and dissipative part). Secondly, by analyzing the separate contributions of the hydration force and a Hertz contact force they conclude that depending on the relative contribution of the two, the dynamic of the cantilever could go from a more linear behavior to a strongly non-linear response (see Fig. 2.9). Additionally, the nonlinear response depends on the dominating type of forces. Larger cantilever stiffness and larger free amplitudes tend to decrease the effect of the hydration forces, and therefore lead to stronger nonlinearities. This conclusion is particularly relevant for this thesis’ experimental results, where softer cantilevers and small amplitudes were found to provide a better sensitivity while probing the solid-liquid interface.

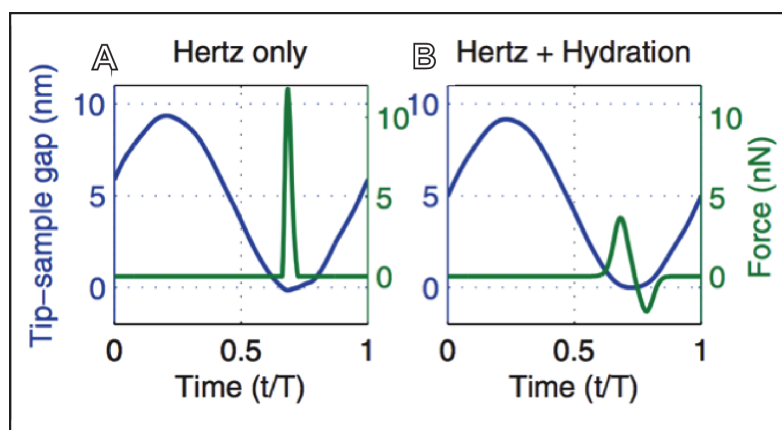


Fig. 2.9: Time histories of tip-sample distance (or oscillation amplitude). Depending on the model used for the tip-sample force we can see how the force (green line) between tip and sample translates into the cantilever motion (blue solid line). By adding the hydration forces (B) to the Hertz contact mechanic model (A) we can see that the interaction force from a short impulsive spike becomes a smoother, broader pulse. Figure adapted from Ref. [74].

The reason for the strong influence of hydration forces on the dynamic of the lever is the additional damping/energy dissipation imposed to the system. Nonlinear behaviors tend to be suppressed by damping. Further, hydration forces smooth out the abrupt transition from noncontact to Hertz contact. Fig. 2.9 presents two simulations of the cantilever dynamic in the presence of external forces in which one includes Hertz contact only (Fig. 2.9A) and the other hydration forces and Hertz contact (Fig. 2.9B). The time history of tip-sample force is clearly different. For the Hertz contact model, the force is a short, impulsive spike, whereas for the hydration forces model, the force is much lower and broader. In both cases, higher harmonics of the force excite higher harmonics of the cantilever deflection when the tip taps on the sample. However, the hydration forces smooth out the contact force such that, in the second case, the higher harmonics of the cantilever oscillation are suppressed.

A similar result was obtained by Voïtchovsky⁹⁴, who systematically studied the anharmonicity of the cantilever dynamic as a result of the non-linear interaction between tip and sample. He found that the appearance of higher harmonics in the cantilever motion was related to the actual mechanical contact between the tip and the sample as seen in the previous paragraph. Generally while imaging softer materials like a lipid bilayer, a lower degree of anharmonicity was obtained from the experimental data. Moreover, by tuning the free amplitude to make it comparable with

the vertical extension of the hydration force (modeled in this case as an exponentially decay function in space for both the conservative and dissipative part of the interaction), the anharmonicity of the motion was decreased even for stiffer samples. In these conditions the tip motion was much more harmonic and the actual interfacial layer was probed. These conditions of free amplitude and setpoint were previously associated to an improvement of lateral resolution. In this study he concluded that the resolution is again related to the interfacial properties of the solid-liquid interface and that the motion shows a lower degree of anharmonicity related to a dominant hydration component of the force on the mechanical contact.

2.6.2 Sharp tips and instabilities

One of the fundamental requirements for high resolution listed in section 2.3 is the use of a sharp nanoscopic tip. This condition has shown to be experimentally achievable even with a probe with a nominal radius of curvature of tens of nanometers. Hiasa *et al.*⁹⁵ showed that they were able to obtain images in liquid with atomic resolution regardless of the nominal radius of the tips. They conclude that minitips, smaller than the nominal radius and present on the tip body, are acting as the effective force probe. The presence of minitips is largely mentioned in AFM experimental papers^{43,45,91} and always postulated as a consequence of the high-resolution results. To obtain the experimental proof of their presence, a systematic imaging of the tip after the AFM experiments, with high resolution SEM, should be conducted. This is however a challenging task, hindered by the fact that the tip's morphological preservation after the imaging process is not guaranteed. Not a lot can be done with respect to 'ideal tips' showing no time variance and prevent instabilities during the imaging process; just deal with it! Structural instability of the tip apex is one of the most commonly cited mechanisms to explain instabilities in the imaging process⁹¹ and has recently been observed by molecular dynamic (MD-) Simulations.⁹⁶

2.6.3 Conservative part of the hydration force

The fact that a minitip is determining the actual contrast of the AFM image implies that the force decay in the vertical direction is fast enough to reduce the averaging of the interaction due to the finite volume of the rest of the tip. Only in this case the interaction of the minitip would dominate over the other long-range forces always present between two microscopic objects. The process is however more complicated. It is now widely accepted that the hydration or generally solvation forces play a fundamental role for achieving high resolution in liquid. The main confusion and controversies arise from which aspects of these forces are dominant in the enhanced contrast of the high-resolution images. Special care has to be taken by considering the often differing imaging conditions used in the several experiments reported.

MD-simulations have provided valuable information on the interaction energy between tip and sample in liquid.^{37,96-99} Liquid and in particular water molecules can strongly modify this interaction and generate the lateral contrast. However, the presence of an atomically sharp tip has a drastic effect on the liquid molecules between the outmost atoms of the tip and the surface, implying that the mechanisms supporting the water-mediated contrast are related to specific tip/liquid molecules/surface interactions.

In MD-simulations studies, Watkins *et al.*^{96,97} explored the effect that water molecules, located between tip and sample, have on the force profiles experienced by an AFM tip modeled as a small cluster of the material composing the surface (CaF₂). This approach breaks down the energy contributions into direct tip-surface interaction and water-mediated interactions. They concluded that unless the tip was very sharp, a net repulsive interaction, due to the cost of removing bound water from tip and surface, occurred before direct tip-surface interactions become significant. As in vacuum, a sharp tip is needed to sample direct tip-surface interactions. However, in solution, the lateral contrast due to the adsorbed water structure may be measurable with blunter tips.⁹⁶ Watkins *et al.*⁹⁶ also found that the water is always in a dynamic equilibrium (even on the time-scales accessible to simulation so nanoseconds). However, water molecules directly interacting

with both tip and surface could slow down this dynamic by orders of magnitude. Watkins *et al.*⁹⁶ stated that this slower dynamic could lead to sampling fewer water configurations during the time that the tip spends at the closest approach to the surface. The experimental manifestation of this phenomenon could be an irreversible contribution to a dissipation signal during the tip approach-retraction cycle.⁹⁶

Experimentally, high-resolution measurements in liquid are often performed with FM-AFM. In this mode the cantilever is oscillated at natural resonance frequency. The interaction force is inducing a modification of the resonance amplitude vs. frequency response and the frequency shift of the resonance curve is maintained constant during the imaging process. In the framework of the simple harmonic oscillator model, the frequency shift is associated to the gradient of the conservative part of the force (see section 2.4). When imaging at constant $\Delta\omega$, we obtain a map of constant force gradient of the surface. Any variation of the amplitude of oscillation is compensated by the external feedback loop that changes the intensity of the driving force. The difficulty related to the achievement of high resolution in liquid with this operational mode derives from the low Q -factor of the cantilever since the force sensitivity in FM-AFM improves with increasing Q -factor.⁴¹ To generally improve the sensitivity of the measurements a low noise deflection sensor was introduced by Fukuma *et al.*²², enabling true atomic resolution in liquid.⁴² Beside the technical improvement of the deflection sensors, as was previously observed for measurements in vacuum,¹⁰⁰ the frequency shift decreases as the oscillation amplitude increases. This is expected, since the cantilever tip experiences the short-range force over a smaller fraction of oscillation cycle as the amplitude increases, hence decreasing the change in effective stiffness of the cantilever.⁶⁹ In this case, small amplitudes (0.5 nm or less) are used while keeping high cantilever spring constants (generally bigger than 10 N/m), in order to increase the sensitivity and avoid instability during the measurements. Using these requirements, high resolution with FM-AFM has been possible on different samples ranging from mica⁴² to lipid bilayers⁴⁴ and biologically relevant molecules¹⁰¹ to self-assembled monolayers^{102,103}. Recently, a substantial effort has been dedicated to the study of ionic distribution on surfaces in solution^{46-48,104,105}. This topic constitutes the core of Chapters 3 and 4.

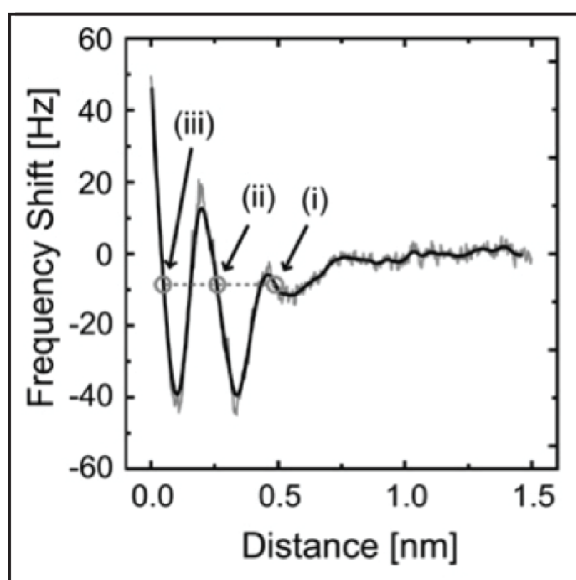


Fig. 2.10: Example of frequency shift versus distance curve measured on a DPPC bilayer in phosphate buffer solution, showing an oscillatory profile with two peaks. The smoothed line (solid) is obtained by averaging the raw data (shaded). Figure adapted from Ref. [43].

Usually FM-AFM in liquid shows a non-monotonic frequency shift as a function of the approaching distance between tip and sample^{42,43}, reflecting the non-linear conservative solvation force at the solid-liquid interface (see Fig. 2.10). Experimentally, as the tip approaches the sample surface, the frequency shift shows a steep increase due to the short-range repulsive interaction

potential. The standard tip-sample distance feedback regulation is based on the assumption that $\Delta\omega$ increases with decreasing tip-sample separation.⁴³ This allows keeping stable imaging on different interfacial regions, as indicated by the arrows in Fig. 2.10. These equivalent positions will be stable, provided that the tip does not pass into a region where the frequency shift decreases with decreasing separation. If it does, it will move continuously until it reaches the next equivalent position till the setpoint value is restored. Thus, the tip can spontaneously jump between iso-setpoint positions (indicated by the circles in Fig. 2.10.) that correspond to different tip-sample distances. These jumps can be interpreted as the tip passing from one hydration layer to the following, as possible to see in Fig. 2.11 on a DPPC bilayer.⁴³

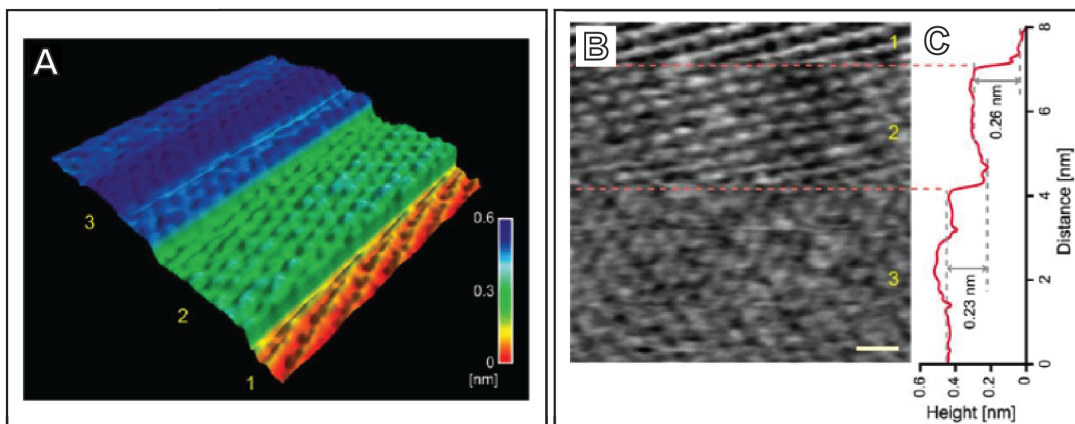


Fig. 2.11: (A) Example of an FM-AFM image ($8 \times 8 \text{ nm}^2$) of the DPPC bilayer in phosphate buffer solution. Spontaneous jumps between different hydration layers are detected during the imaging process. (B) Line-by-line flattened image of (A). (C) Line profile obtained vertically from image (B) before the flattening procedure. Scale bar, 1 nm. Height range: 0.1 nm. The regions indicated by the numbers 1, 2, and 3 correspond to the terraces 1, 2, and 3 in (A). Images adapted from Ref. [43].

As is clear from Fig. 2.11, the hydration force gradient not only renders possible the vertical detection of individual hydration layers, but also the lateral resolution of single molecules as the tip is scanned over the surface. This implies that the hydration force has to vary significantly parallel to the surface at the atomic-molecular level. Recent advances on FM-AFM made it possible to obtain a 3D- frequency shift map of the interface. In 3D-AFM, the tip is scanned in the vertical direction as well as in plane (standard imaging mode), to cover the whole 3D interfacial space.⁵² This method has been used to characterize mica-water^{1,52,105}, lipid bilayer-water⁵⁶ and other interfaces. In all the cases a frequency shift that can be attributed to a water-mediated interaction force is shown to significantly vary laterally, in the planes parallel to the surface. Kimura *et al.*⁵³ compared the force profile, obtained from the measured frequency shift in the 3D-AFM “images” of water on mica (in the presence of ions), with the gradient of the 3D-water density distribution obtained from a molecular simulation of the isolated surface. As we have seen in Chapter 1, even the isolated surface has a 3D-modulation of the density distribution of the liquid molecules at the interface. This has been demonstrated for the mica-water interface with both x-ray scattering¹⁰⁶, and by MD-simulation¹⁰⁷. Kimura *et al.*⁵³ found an excellent agreement between the shape of the measured force and the gradient of the density distribution even though comparing the two is not formally correct. A more complete approach has been proposed by Amano *et al.*⁵⁵ who considered the AFM probe as a sphere with the diameter comparable to the solvent’s molecules size. This “ideal probe” approach, even if far from the real case, correlates well with the experimental data. This implies that, in this case, the molecular density distribution of a single interface is enough to qualitatively explain the results obtained with a perturbative measurement like AFM.

2.6.4 Dissipative part of the hydration force

The interpretation of AM-AFM measurements is more complicated since the feedback is operating on the oscillating amplitude of the lever that, in the framework of the simple harmonic oscillator, is affected at the same time by the conservative and dissipative part of the force (see section 2.4). Experimentally, we found that the amplitude providing a high resolution in this imaging mode⁵⁰ is typically higher than for FM-AFM measurements (0.5 nm to 1.5 nm). Moreover the cantilever force constant used in our AM-AFM experiment is typically an order of magnitude lower than for FM-AFM. Under these conditions, the oscillating structure of the hydration force exploited in FM-AFM to image different hydration layers cannot be detected since the tip probes all the interfacial liquid layers during a single oscillation cycle (see section 1.4). These imaging conditions tend to yield an enhanced phase contrast that is associated to an enhancement of the local variation of the energy dissipated experienced by the tip during the imaging process (see section 2.4). This experimental observation suggests that high resolution in AM-AFM can be attributed mainly to the dissipative part of the interaction force. The main confusion in this situation derives from the controversial results regarding the specific mechanisms of energy dissipation at the solid-liquid interface (see section 2.5), which are related to each specific system, tip geometry, degree of confinement, etc. These forces are difficult to be simulated at the molecular level in a reasonable timescale because it requires monitoring the entire tip trajectory during the motion in the interfacial layer.

In the model of Voitchovsky *et al.*⁵⁰ presented in the Chapter 1, the main mechanism of energy dissipation was associated to the energy spent to destroy the interface between the sample and the liquid, and the tip and the liquid. This mechanism was associated to an enhancement of the lateral resolution particularly in the phase channel. If the solvation forces are at the origin of the enhanced resolution, since these forces depend on the specific vertical and lateral interaction of the solvent molecules with the surface and the tip, the resolution will depend on the specifics of the system considered (combination of solid and liquid). In particular, the lateral structuring of the interfacial liquid at the solid surface should be the main limiting parameter for resolution. This was the idea behind the work presented in details in the next subsection¹⁰⁸.

2.6.5 High resolution imaging of solvation structures with AM-AFM

In order to evidence the role of solvation forces in the resolution achieved by AM-AFM, we compare sub-nanometer resolution images of crystalline solids obtained in different liquids and discuss the differences in the resolution achieved in phase and topography, depending on the liquid. We selected three liquids for ease of use, relatively low vapor pressure and molecular size: ultrapure water, dimethylsulfoxide and 1-hexanol. Considering the fact that the solvation structure formed by a liquid generally reflects that of the solid surface, the results presented here demonstrate how an appropriate choice of liquid can enhance imaging resolution. It is important to note that the images presented in this work provide a direct comparison between systems when only the liquid varies, showing how the liquid can influence the imaging.

High-resolution images (10 nm × 10 nm) of several solids in water and in dimethylsulfoxide are presented in Fig. 2.12. In each case both the topographic (brown scale) and the phase image (orange scale) are given and atomic-level features are often distinguishable. In order to allow unambiguous interpretation of the images, all the samples imaged are single crystals with a known crystallographic structure and well-defined orientation of the surface: calcium fluoride (111), silicon carbide (0001), silicon dioxide (β -quartz, x-cut), titanium oxide (001), sodium chloride (001) and aluminum oxide (0001) in ultrapure water and in dimethylsulfoxide. From Fig. 2.12 it is immediately apparent that for a given substrate, the resolution achieved strongly depends on the imaging liquid. In several cases such as for silicon, aluminum and titanium oxides, high-resolution features can only be distinguished clearly in one of the liquids (dimethylsulfoxide). In most cases, however, it is possible to identify the expected crystallographic symmetry of a surface in both liquids (e.g. hexagonal symmetry for silicon carbide and calcium fluoride), although

surface reconstruction effects of the crystals cannot be excluded. Interestingly, when atomic-level details can be resolved in both liquids, features generally tend to appear significantly larger in dimethylsulfoxide than in water, as visible for calcium fluoride and mica (Fig. 2.12 and 2.13).

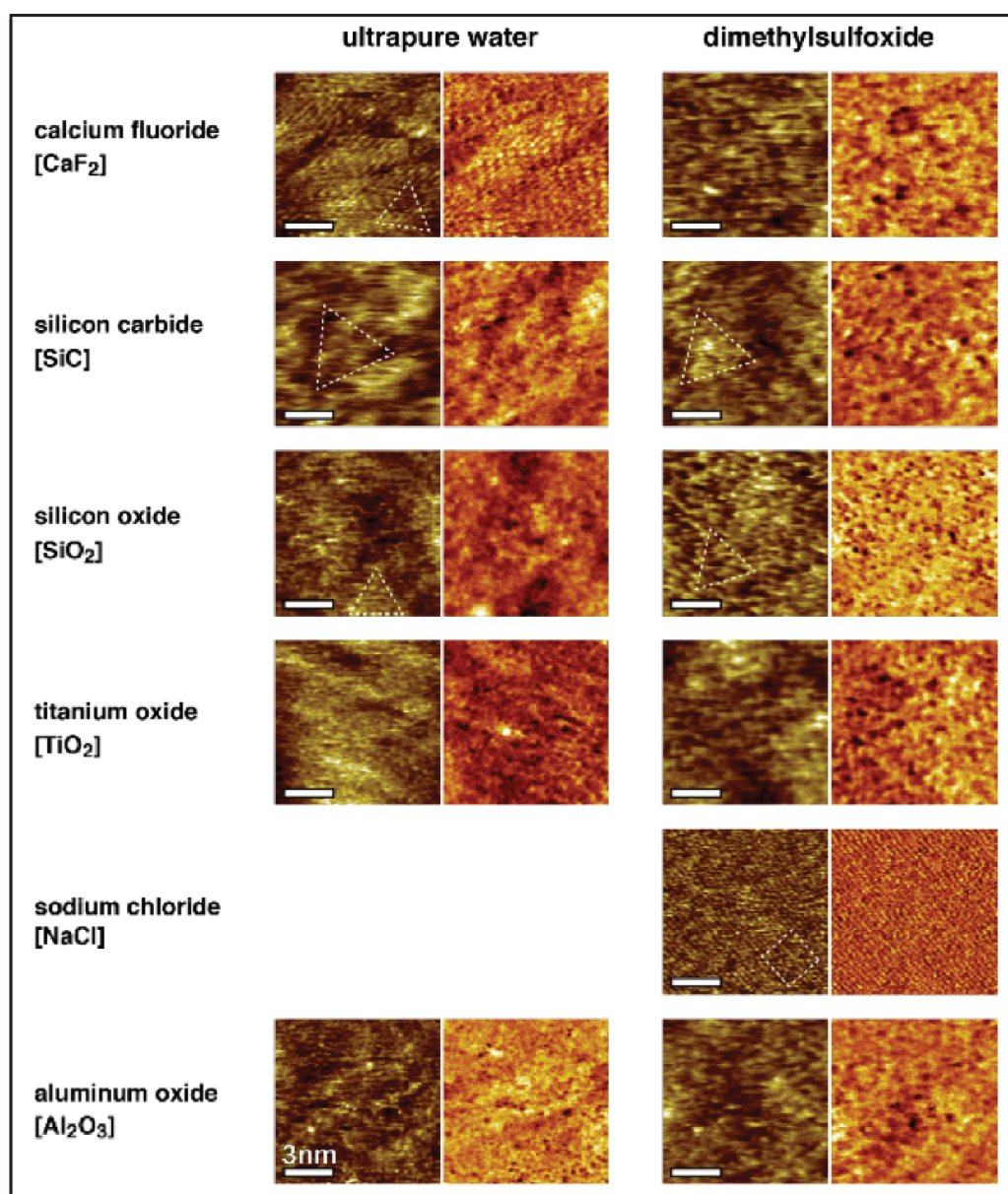


Fig. 2.12: High-resolution images of single crystals in water and dimethylsulfoxide. In each case, the topography (brown color scale) and the phase (orange color scale) are given. Every image is 10 nm by 10 nm. When visible, the symmetry of the crystal lattice is indicated with dotted line aligned with surface features (triangle for hexagonal symmetry and square for cubic symmetry). The size of the dotted polygon is not related to the size of the unit cell and has only the purpose of indicating the main crystal symmetry axis of the surface.

Dimethylsulfoxide does, however, not necessarily prevent true atomic-level resolution, as illustrated by the image achieved on sodium chloride where the square lattice formed by the surface atoms is clearly visible and with sub-nanometer precision. Unfortunately no equivalent image could be obtained in water for practical reasons (dissolution of the sample). These observations suggest that the image does not necessarily reflex the actual atomic structure of the surface despite the presence of atomic-level details and the correct symmetry, but rather that of the solvation layer formed by the liquid at the surface of the solid images. In terms of imaging process, this implies that when operated in the regime described above, the vibrating AFM tip probably maintains liquid molecules between apex and the sample at all time, without physically

touching the surface. As the tip oscillates close to the surface of the sample, the solvation layers formed by the liquid at the surface of the sample and of the tip are coalesced and re-created for each vibration cycle. Since the same tip is used for scanning the whole surface of the sample, solvation structure can be assumed constant throughout the scanning and lateral variations visible in the topographic and phase images mostly reflect the spatial arrangement of the sample's solvation structure. Information about the structural organization of the liquid molecules at the tip's surface is consequently implicit in the images.

In order to further investigate the role played by the liquid in high-resolution AM-AFM imaging, we carried out measurements in 1-hexanol for calcite, mica and strontium titanate (Fig. 2.13). Images of calcite and mica exhibit atomic-level details in each solvent, making these crystals particularly interesting for studying the imaging differences between solvents. In water, calcite exhibit atomistic details, both in topography and phase images. In dimethylsulfoxide, the image appears less regular with only part of the image revealing details with a resolution comparable to water where the orientation of the crystal is visible. Interestingly, higher resolution was achieved in 1-hexanol than in dimethylsulfoxide: in 1-hexanol, the lines formed by the rows of oxygen atoms are clearly visible in topography. The atomic structure of mica is particularly well resolved in water. In dimethylsulfoxide, only larger details are visible and the atomic lattice cannot be directly identified. Overall the surface appears rougher with irregular rows loosely following the underlying lattice. Comparison with the image in water suggests that the molecules of dimethylsulfoxide can form global solvation structures at the surface of mica with several cohesive layers. This could explain the apparent roughness as due to local removal of the distal layers by the scanning AFM tip. This is further supported by the fact that several rows have a width similar to the diameter of the surface hexagons visible in water and a direction coinciding with the crystalline symmetry of the surface. Similar observations can be made in 1-hexanol where it is also possible to identify distinct protrusions within a row. Contrary to calcite and mica, strontium titanate provided poor images in water, with only the crystal symmetry (cubic) recognizable. Substantially more details are visible in dimethylsulfoxide, similarly to aluminum and titanium oxides. The size of the visible protrusion is however too large to be induced by individual atoms and more likely to correspond to groups of atoms. Images obtained in 1-hexanol are comparable to those in water and only the crystal symmetry can be identified.

In the case of solids with a well-defined lattice of surface charges such as mica, calcium fluoride or calcite (Fig. 2.12 and 2.13), the solvation structure can be particularly well defined in water, since water molecules are small enough to form individual hydration shells around the charged surface atoms. As a result, AM-AFM images of these samples in water directly reflect the atomic structure of the surface charges atoms. Dimethylsulfoxide molecules, although polar, are larger than water molecules and possess two hydrophobic tails that affect arrangement in solvation structure around solids. This amphiphilic nature also tends to impose further orientation constraints when compared with water. As a result, the dimethylsulfoxide solvation structure likely follows the arrangement of the surface atoms more loosely, with lateral variations that may comprise several atoms. This is reflected in AM-AFM images by the protrusions often larger in dimethylsulfoxide than for images in water. This disadvantage is balanced by the fact that dimethylsulfoxide, being an amphiphile, is able to interact more efficiently with most surfaces, thus creating solvation structures more readily. This is clearly reflected by the percentage of substrates allowing high-resolution images in dimethylsulfoxide. 1-hexanol molecules also exhibit amphiphilic properties, but are substantially larger than both water and dimethylsulfoxide molecules. Interestingly, for samples exhibiting a large density of surface charges (calcite and mica), images acquired in 1-hexanol are comparable or better than images in dimethylsulfoxide. This could be explained by an ordered packing of the hexanol molecules with the alcohol group contacting the surface, although many defects are visible on mica, possibly due to a mismatch between the mica lattice and ideal hexanol packing. Finally, the resolution achieved on strontium titanate is comparable to that obtained in water, suggesting that no ideal solvation structure for AM-AFM imaging could be formed. Overall, the results in 1-hexanol are consistent with our interpretation that AM-AFM images reflect the solvation structure of the sample rather than the surface atomic arrangement.

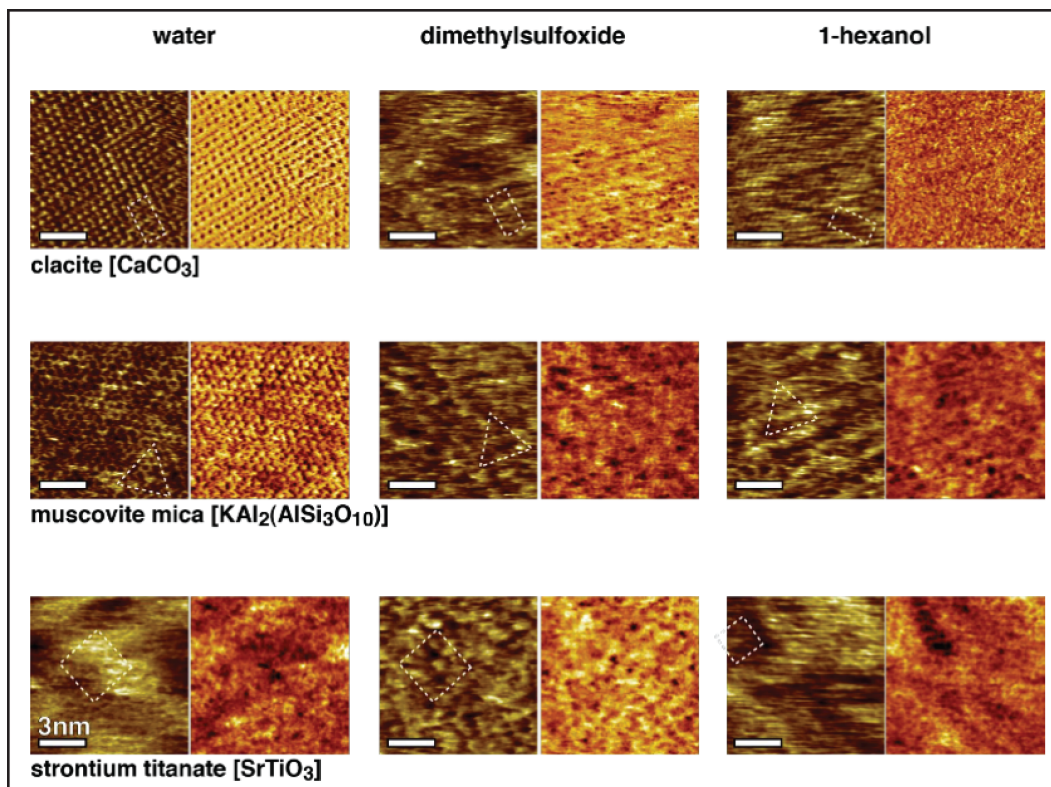


Fig. 2.13: High-resolution images of single crystals of calcite, mica and strontium titanate in water, dimethylsulfoxide and 1-hexanol. As in Fig. 2.12, the topography (brown color scale) and the phase (orange color scale) are given in each case. Every image is 10 nm by 10 nm. As for Fig. 2.12, the surface symmetry of the crystal deduced from the images is indicated with dotted lines. In the case of strontium titanate in hexanol, the image appears “compressed” vertically due to thermal drift.

We conclude that, even though the presence of a liquid with a different dielectric constant can in principle influence the direct interaction between the tip and the solid, it is the solvent mediated interaction that dominated the resolution achievable with the AM-AFM. This interaction is reflected in the energy dissipated during the oscillation cycle of the AFM cantilever and is experimentally proven to be spatially varying at the atomic level. Liquids forming spatially well defined interfaces will allow higher resolution, but the imaged solvation structure, although correlated with the surface of the underlying solid does not necessarily directly coincide with the atomic arrangement of the solid’s surface.

Bibliography Chapter 2

- Herruzo, E. T., Asakawa, H., Fukuma, T. & García, R. Three-dimensional quantitative force maps in liquid with 10 piconewton, angstrom and sub-minute resolutions. *Nanoscale* **5**, 2678 (2013).
- Hoffmann, P., Jeffery, S., Pethica, J., Özgür Özer, H. & Oral, A. Energy Dissipation in Atomic Force Microscopy and Atomic Loss Processes. *Phys. Rev. Lett.* **87**, 265502 (2001).
- Binnig, G., Quate, C. F. & Gerber, C. H. Atomic Force Microscope. *Phys. Rev. Lett.* **56**, 930–933 (1986).
- Giessibl, F. J. AFM's path to atomic resolution. *Materials Today* **8**, 32–41 (2005).
- Martin, Y., Williams, C. C. & Wickramasinghe, H. K. Atomic force microscope-force mapping and profiling on a sub 100-Å scale. *J. Appl. Phys.* **61**, 4723–4729 (1987).
- Giessibl, F. J. Advances in atomic force microscopy. *Rev. Sci* **75**, 949–983 (2003).
- Albrecht, T. R., Grütter, P., Horne, D. & Rugar, D. Frequency modulation detection using high-Q cantilevers for enhanced force microscope sensitivity. *J. Appl. Phys.* **69**, 668–673 (1991).
- Meyer, G. & Amer, N. M. Novel optical approach to atomic force microscopy. *Appl. Phys. Lett.* **53**, 1045–1047 (1988).
- Alexander, S. *et al.* An atomic-resolution atomic-force microscope implemented using an optical

- lever. *J. Appl. Phys.* **65**, 164–167 (1989).
10. Albrecht, T. R., Akamine, S., Carver, T. E. & Quate, C. F. Microfabrication of cantilever styli for the atomic force microscope. *Journal of Vacuum Science & Technology A* **8**, 3386–3396 (1990).
 11. Drake, B. *et al.* Imaging crystals, polymers, and processes in water with the atomic force microscope. *Science* **243**, 1586–1589 (1989).
 12. Ohnesorge, F. & Binnig, G. True Atomic Resolution by Atomic Force Microscopy Through Repulsive and Attractive Forces. *Science* **260**, 1451–1456 (1993).
 13. Hillner, P. E., Manne, S., Gratz, A. J. & Hansma, P. K. AFM images of dissolution and growth on a calcite crystal. *Ultramicroscopy* **42**, 1387–1393 (1992).
 14. Hillner, P. E., Gratz, A. J., Manne, S. & Hansma, P. K. Atomic-scale imaging of calcite growth and dissolution in real time. *Geology* **20**, 359–362 (1992).
 15. Putman, C. A. J., Van der Werf, K. O., De Grooth, B. G., Van Hulst, N. F. & Greve, J. Tapping mode atomic force microscopy in liquid. *Appl. Phys. Lett.* **64**, 2454–2456 (1994).
 16. Hansma, P. K. *et al.* Tapping mode atomic force microscopy in liquids. *Appl. Phys. Lett.* **64**, 1738–1740 (1994).
 17. Kasas, S. *et al.* Escherichia coliRNA Polymerase Activity Observed Using Atomic Force Microscopy †. *Biochemistry* **36**, 461–468 (1997).
 18. Babcock, L. K. & Prater, C. B. *Phase imaging: beyond topography*. (Digital Instruments, 1995). at <<http://www.veeco.com>>
 19. Magonov, S. N., Elings, V. & Whangbo, M. H. Phase imaging and stiffness in tapping-mode atomic force microscopy. *Surface Science* (1997).
 20. Cleveland, J. P., Anczykowski, B., Schmid, A. E. & Elings, V. B. Energy dissipation in tapping-mode atomic force microscopy. *Appl. Phys. Lett.* **72**, 2613–2615 (1998).
 21. Anczykowski, B., Gotsmann, B., Fuchs, H., Cleveland, J. P. & Elings, V. B. How to measure energy dissipation in dynamic mode atomic force microscopy. *Applied Surface Science* **140**, 376–382 (1999).
 22. Fukuma, T., Kimura, M. & Kobayashi, K. Development of low noise cantilever deflection sensor for multienvironment frequency-modulation atomic force microscopy. *Rev. Sci. Instrum.* **76**, 053704 (2005).
 23. Ando, T. *et al.* in *Atomic Force Microscopy in Liquid* (Wiley-VCH Verlag GmbH & Co. KGaA, 2012).
 24. Viani, M. B. *et al.* Probing protein–protein interactions in real time. *Nature Structural & Molecular Biology* **7**, 644–647 (2000).
 25. Han, W., Lindsay, S. M. & Jing, T. A magnetically driven oscillating probe microscope for operation in liquids. *Appl. Phys. Lett.* **69**, 4111 (1996).
 26. Ratcliff, G. C., Erie, D. A. & Superfine, R. Photothermal modulation for oscillating mode atomic force microscopy in solution. *Appl. Phys. Lett.* **72**, 1911–1913 (1998).
 27. Labuda, A., Kobayashi, K., Miyahara, Y. & Grütter, P. Retrofitting an atomic force microscope with photothermal excitation for a clean cantilever response in low Q environments. *Rev. Sci. Instrum.* **83**, 053703 (2012).
 28. García, R. *Amplitude Modulation Atomic Force Microscopy*. (John Wiley & Sons, 2011).
 29. Kiracofe, D., Melcher, J. & Raman, A. in *Atomic Force Microscopy in Liquid* 121–155 (Wiley-VCH Verlag GmbH & Co. KGaA, 2012). doi:10.1002/9783527649808.ch5
 30. O'Shea, S. J. & Welland, M. E. Atomic Force Microscopy at Solid–Liquid Interfaces. *Langmuir* **14**, 4186–4197 (1998).
 31. Jeffery, S. *et al.* Direct measurement of molecular stiffness and damping in confined water layers. *Phys. Rev. B* **70**, 054114 (2004).
 32. Patil, S. V. & Hoffmann, P. M. Small-Amplitude Atomic Force Microscopy. *Adv. Eng. Mater.* **7**, 707–712 (2005).
 33. O'Shea, S. J., Welland, M. E. & Rayment, T. Solvation forces near a graphite surface measured with an atomic force microscope. *Appl. Phys. Lett.* **60**, 2356–2358 (1992).
 34. O'Shea, S. J., Welland, M. E. & Pethica, J. B. Atomic force microscopy of local compliance at solid–liquid interfaces. *Chemical Physics Letters* **223**, 336–340 (1994).
 35. Cleveland, J. P., Schaffer, T. E. & Hansma, P. K. Probing oscillatory hydration potentials using thermal-mechanical noise in an atomic-force microscope. *Phys. Rev. B* **52**, R8692 (1995).
 36. Gelb, L. D. & Lynden-Bell, R. M. Effects of atomic-force-microscope tip characteristics on measurement of solvation-force oscillations. *Phys. Rev. B* **49**, 2058–2066 (1994).
 37. Patrick, D. L. & Lynden-Bell, R. M. Atomistic simulations of fluid structure and solvation forces in atomic force microscopy. *Surface Science* **380**, 224–244 (1997).

-
38. Jarvis, S. P., Uchihashi, T., Ishida, T., Tokumoto, H. & Nakayama, Y. Local Solvation Shell Measurement in Water Using a Carbon Nanotube Probe. *The Journal of Physical Chemistry B* **104**, 6091–6094 (2000).
 39. Jarvis, S. P., Ishida, T., Uchihashi, T., Nakayama, Y. & Tokumoto, H. Frequency modulation detection atomic force microscopy in the liquid environment. *Appl Phys A* **72**, S129–S132 (2001).
 40. Higgins, M. J. *et al.* Structured Water Layers Adjacent to Biological Membranes. *Biophysical Journal* **91**, 2532–2542 (2006).
 41. Fukuma, T., Ichii, T., Kobayashi, K., Yamada, H. & Matsushige, K. True-molecular resolution imaging by frequency modulation atomic force microscopy in various environments. *Appl. Phys. Lett.* **86**, 034103 (2005).
 42. Fukuma, T., Kobayashi, K., Matsushige, K. & Yamada, H. True atomic resolution in liquid by frequency-modulation atomic force microscopy. *Appl. Phys. Lett.* **87**, 034101 (2005).
 43. Fukuma, T., Higgins, M. J. & Jarvis, S. P. Direct Imaging of Individual Intrinsic Hydration Layers on Lipid Bilayers at Ångstrom Resolution. *Biophysical Journal* **92**, 3603–3609 (2007).
 44. Sheikh, K. H. & Jarvis, S. P. Crystalline Hydration Structure at the Membrane–Fluid Interface of Model Lipid Rafts Indicates a Highly Reactive Boundary Region. *J. Am. Chem. Soc.* **133**, 18296–18303 (2011).
 45. Hofbauer, W., Ho, R. J., R, H., Gosvami, N. N. & O'Shea, S. J. Crystalline structure and squeeze-out dissipation of liquid solvation layers observed by small-amplitude dynamic AFM. *Phys. Rev. B* **80**, 134104 (2009).
 46. Fukuma, T., Higgins, M. & Jarvis, S. Direct Imaging of Lipid-Ion Network Formation under Physiological Conditions by Frequency Modulation Atomic Force Microscopy. *Phys. Rev. Lett.* **98**, 3603–3609 (2007).
 47. Loh, S.-H. & Jarvis, S. P. Visualization of Ion Distribution at the Mica–Electrolyte Interface. *Langmuir* **26**, 9176–9178 (2010).
 48. Rode, S., Oyabu, N., Kobayashi, K., Yamada, H. & Kühnle, A. True Atomic-Resolution Imaging of (10 $\bar{1}$ 4) Calcite in Aqueous Solution by Frequency Modulation Atomic Force Microscopy. *Langmuir* **25**, 2850–2853 (2009).
 49. Contera, S. A., Voitchovsky, K. & Ryan, J. F. Controlled ionic condensation at the surface of a native extremophile membrane. *Nanoscale* **2**, 222 (2010).
 50. Voitchovsky, K., Kuna, J. J., Contera, S. A., Tosatti, E. & Stellacci, F. Direct mapping of the solid-liquid adhesion energy with subnanometre resolution. *Nature Nanotechnology* **5**, 401–405 (2010).
 51. Kuna, J. J. *et al.* The effect of nanometre-scale structure on interfacial energy. *Nature Materials* **8**, 837–842 (2009).
 52. Fukuma, T., Ueda, Y., Yoshioka, S. & Asakawa, H. Atomic-Scale Distribution of Water Molecules at the Mica-Water Interface Visualized by Three-Dimensional Scanning Force Microscopy. *Phys. Rev. Lett.* **104**, 016101 (2010).
 53. Kimura, K. *et al.* Visualizing water molecule distribution by atomic force microscopy. *J. Chem. Phys.* **132**, 194705 (2010).
 54. Hölscher, H., Langkat, S. M., Schwarz, A. & Wiesendanger, R. Measurement of three-dimensional force fields with atomic resolution using dynamic force spectroscopy. *Appl. Phys. Lett.* **81**, 4428–4430 (2002).
 55. Amano, K.-I., Suzuki, K., Fukuma, T., Takahashi, O. & Onishi, H. The relationship between local liquid density and force applied on a tip of atomic force microscope: A theoretical analysis for simple liquids. *J. Chem. Phys.* **139**, 224710 (2013).
 56. Asakawa, H., Yoshioka, S., Nishimura, K.-I. & Fukuma, T. Spatial distribution of lipid headgroups and water molecules at membrane/water interfaces visualized by three-dimensional scanning force microscopy. *ACS Nano* **6**, 9013–9020 (2012).
 57. Labuda, A. Adventures in atomic force microscopy: towards the study of the solid-liquid interface. *PhD thesis* (2012).
 58. Bustamante, C. & Keller, D. Scanning Force Microscopy in Biology. *Phys. Today* **48**, 32 (1995).
 59. Weihs, T. P., Nawaz, Z., Jarvis, S. P. & Pethica, J. B. Limits of imaging resolution for atomic force microscopy of molecules. *Appl. Phys. Lett.* **59**, 3536–3538 (1991).
 60. Schwarz, U. D., Hölscher, H. & Wiesendanger, R. Atomic resolution in scanning force microscopy: Concepts, requirements, contrast mechanisms, and image interpretation. *Phys. Rev. B* **62**, 13089–13097 (2000).
 61. Kiracofe, D. *et al.* VEDA: Virtual Environment for Dynamic AFM. (2012).
 62. Melcher, J., Hu, S. & Raman, A. VEDA: a web-based virtual environment for dynamic atomic

-
- force microscopy. *Rev. Sci. Instrum.* **79**, 061301 (2008).
63. Kiracofe, D., Melcher, J. & Raman, A. Gaining insight into the physics of dynamic atomic force microscopy in complex environments using the VEDA simulator. *Rev. Sci. Instrum.* **83**, 013702 (2012).
 64. Kiracofe, D. & Raman, A. On eigenmodes, stiffness, and sensitivity of atomic force microscope cantilevers in air versus liquids. *J. Appl. Phys.* **107**, 033506 (2010).
 65. Sader, J. E. Frequency response of cantilever beams immersed in viscous fluids with applications to the atomic force microscope. *J. Appl. Phys.* **84**, 64–76 (1998).
 66. Maali, A. *et al.* Hydrodynamics of oscillating atomic force microscopy cantilevers in viscous fluids. *J. Appl. Phys.* **97**, 074907 (2005).
 67. de Beer, S., van den Ende, D. & Mugele, F. Dissipation and oscillatory solvation forces in confined liquids studied by small-amplitude atomic force spectroscopy. *Nanotechnology* **21**, 325703 (2010).
 68. Schröter, K., Petzold, A., Henze, T. & Thurn-Albrecht, T. Quantitative Analysis of Scanning Force Microscopy Data Using Harmonic Models. *Macromolecules* **42**, 1114–1124 (2009).
 69. Sader, J. E. *et al.* Quantitative force measurements using frequency modulation atomic force microscopy-theoretical foundations. *Nanotechnology* **16**, S94–S101 (2005).
 70. Basak, S. & Raman, A. Dynamics of tapping mode atomic force microscopy in liquids: Theory and experiments. *Appl. Phys. Lett.* **91**, 064107 (2007).
 71. Tamayo, J. Energy dissipation in tapping-mode scanning force microscopy with low quality factors. *Appl. Phys. Lett.* **75**, 3569–3571 (1999).
 72. Martínez, N. F. & García, R. Measuring phase shifts and energy dissipation with amplitude modulation atomic force microscopy. *Nanotechnology* **17**, S167 (2006).
 73. Melcher, J. *et al.* Origins of phase contrast in the atomic force microscope in liquids. *PNAS* 1–6 (2009). at <<http://www.pnas.org/cgi/doi/10.1073/pnas.0902240106>>
 74. Kiracofe, D. & Raman, A. Nonlinear dynamics of the atomic force microscope at the liquid-solid interface. *Phys. Rev. B* **86**, 205405 (2012).
 75. Israelachvili, J. N. *Intermolecular and Surface Forces*. 1–706 (ELSEVIER, 2011).
 76. Cappella, B. & Dietler, G. Force-distance curves by atomic force microscopy. *Surface Science Reports* **34**, 1–104 (1999).
 77. Hamaker, H. C. The London—van der Waals attraction between spherical particles. *Physica* **4**, 1058–1072 (1937).
 78. García, R. *et al.* Identification of Nanoscale Dissipation Processes by Dynamic Atomic Force Microscopy. *Phys. Rev. Lett.* **97**, 016103 (2006).
 79. Gómez, C. J. & García, R. Determination and simulation of nanoscale energy dissipation processes in amplitude modulation AFM. *Ultramicroscopy* **110**, 626–633 (2010).
 80. Schirmeisen, A. & Hölscher, H. Velocity dependence of energy dissipation in dynamic force microscopy: Hysteresis versus viscous damping. *Phys. Rev. B* **72**, 045431 (2005).
 81. Khan, S. H., Kramkowski, E. L. & Ochs, P. J. Viscosity of a nanoconfined liquid during compression. *Applied Physics Letters* **104**, 023110 (2014).
 82. Beer, S. de, Otter, W. K. D., Ende, D. V. D., Briels, W. J. & Mugele, F. Non-monotonic variation of viscous dissipation in confined liquid films: A reconciliation. *EPL* **97**, 46001 (2012).
 83. Khan, S. H., Matei, G., Patil, S. & Hoffmann, P. M. Dynamic Solidification in Nanoconfined Water Films. *Phys. Rev. Lett.* (2010).
 84. Kaggwa, G. B., Kilpatrick, J. I., Sader, J. E. & Jarvis, S. P. Artifact-free dynamic atomic force microscopy reveals monotonic dissipation for a simple confined liquid. *Applied Physics Letter* **93**, 011909 (2008).
 85. Ortiz-Young, D., Chiu, H.-C., Kim, S., Voitchovsky, K. & Riedo, E. The interplay between apparent viscosity and wettability in nanoconfined water. *Nat Commun* **4 SP**, (2013).
 86. Klein, J. & Kumacheva, E. Simple liquids confined to molecularly thin layers. I. Confinement-induced liquid-to-solid phase transitions. *J. Chem. Phys.* **108**, 6996–7009 (1998).
 87. Becker, T. & Mugele, F. Nanofluidics: Viscous Dissipation in Layered Liquid Films. *Phys. Rev. Lett.* **91**, 166104 (2003).
 88. Li, T.-D. & Elisa, R. Nonlinear Viscoelastic Dynamics of Nanoconfined Wetting Liquids. *Phys. Rev. Lett.* **100**, 106102 (2008).
 89. Zhu, Y. & Granick, S. Reassessment of Solidification in Fluids Confined between Mica Sheets. *Langmuir* **19**, 8148–8151 (2003).
 90. Li, T.-D. *et al.* Structured and viscous water in subnanometer gaps. *Phys. Rev. B* **75**, 115415 (2007).

-
91. Labuda, A., Kobayashi, K., Suzuki, K., Yamada, H. & Grütter, P. Monotonic Damping in Nanoscopic Hydration Experiments. *Phys. Rev. Lett.* **110**, 066102 (2013).
 92. Wu, Y., Gupta, C. & Shannon, M. A. Effect of Solution Concentration, Surface Bias and Protonation on the Dynamic Response of Amplitude-Modulated Atomic Force Microscopy in Water. *Langmuir* **24**, 10817-10824 (2008).
 93. Ebeling, D., van der Ende, D. & Mugele, F. Electrostatic interaction forces in aqueous salt solutions of variable concentration and valency. *Nanotechnology* **22**, 305706 (2011).
 94. Voitchovsky, K. Anharmonicity, solvation forces, and resolution in atomic force microscopy at the solid-liquid interface. *Phys. Rev. E* **88**, 022407 (2013).
 95. Hiasa, T., Kimura, K. & Onishi, H. Minitips in Frequency-Modulation Atomic Force Microscopy at Liquid-Solid Interfaces. *Jpn. J. Appl. Phys.* **51**, 025703 (2012).
 96. Watkins, M., Berkowitz, M. L. & Shluger, A. L. Role of water in atomic resolution AFM in solutions. *Phys. Chem. Chem. Phys.* **13**, 12584 (2011).
 97. Watkins, M. & Shluger, A. L. Mechanism of Contrast Formation in Atomic Force Microscopy in Water. *Phys. Rev. Lett.* **105**, 196101 (2010).
 98. Watkins, M. & Reischl, B. A simple approximation for forces exerted on an AFM tip in liquid. *J. Chem. Phys.* **138**, 154703 (2013).
 99. Reischl, B., Watkins, M. & Foster, A. S. Free Energy Approaches for Modeling Atomic Force Microscopy in Liquids. *J. Chem. Theory Comput.* **9**, 600–608 (2012).
 100. Giessibl, F. J. Forces and frequency shifts in atomic-resolution dynamic-force microscopy. *Phys. Rev. B* **56**, 16010 (1997).
 101. Fukuma, T., Mostaert, A. S., Serpell, L. C. & Jarvis, S. P. Revealing molecular-level surface structure of amyloid fibrils in liquid by means of frequency modulation atomic force microscopy. *Nanotechnology* **19**, 384010 (2008).
 102. Hiasa, T., Kimura, K. & Onishi, H. Hydration of hydrophilic thiolate monolayers visualized by atomic force microscopy. *Phys. Chem. Chem. Phys.* **14**, 8419 (2012).
 103. Hiasa, T. & Onishi, H. Mercaptohexanol assembled on gold: FM-AFM imaging in water. *Colloids Surf., A* **441**, 149–154 (2014).
 104. Kilpatrick, J. I., Loh, S.-H. & Jarvis, S. P. Directly Probing the Effects of Ions on Hydration Forces at Interfaces. *Multiple values selected* **135**, 2628–2634 (2013).
 105. Kobayashi, K. *et al.* Visualization of hydration layers on muscovite mica in aqueous solution by frequency-modulation atomic force microscopy. *J. Chem. Phys.* **138**, 184704 (2013).
 106. Cheng, L. Molecular-Scale Density Oscillations in Water Adjacent to a Mica Surface. *Phys. Rev. Lett.* **87**, 156103 (2001).
 107. Park, S.-H. & Sposito, G. Structure of Water Adsorbed on a Mica Surface. *Phys. Rev. Lett.* **89**, 085501 (2002).
 108. Voitchovsky, K. & Ricci, M. High-resolution imaging of solvation structures with amplitude-modulation atomic force microscopy. in (Parak, W. J., Yamamoto, K. & Osinski, M.) **8232**, 82320O–8 (SPIE, 2012).

Chapter 3

High-resolution AFM to characterize the Stern Layer of aqueous-solid interfaces

Interfaces between solids and aqueous ionic solutions are among the most common and important in nature, playing a central role in biological processes, mineralogy, electrochemistry and colloidal science. In this chapter, I will present high-resolution AFM measurements of single ions adsorbed at mica surface. The aim of the chapter is to provide the experimental evidences for single ion detection. The technique will subsequently be used to obtain quantitative information on the arrangement of ions adsorbed at the surface of solid.

In the first part, I will motivate the necessity to characterize the distributions of ions at the Stern layer level (section 3.1) and I will present the progresses made by AFM in this field (section 3.2). It will follow an analysis on the requirements to achieve single ion resolution in light of the possible physical mechanisms behind ion detection with AFM (section 3.3).

Subsequently, I will present our experimental results on Rb^+ ions adsorbed on the mica surface in aqueous solution (section 3.4). The ion-related topographical features, visible in the AFM images, will enable a quantification of the surface coverage (subsection 3.4.1). This value, being comparable to X-Ray reflectivity data¹, will validate the single-ion resolution in our AFM measurements. The residence time of the ions will be evaluated (section 3.5) and experiments aimed at determining the influence of the AFM tip on the system will be presented (section 3.6 and 3.7).

3.1 What do we need and why?

One of the effects of the creation of a solid-liquid interface, as already mentioned in Chapter 1 and 2, is the development of a charge at the solid's surface. In order to maintain electroneutrality, the counterions dissolved in the liquid tend to accumulate close to the solid, forming an electrical double layer (EDL) that counterbalances the solid's surface charge. The precise structure and spatial distribution of ions in the EDL has been the subject of intense experimental and theoretical research over the last century. At the present time, the most widely used EDL model, the Gouy-Chapman-Stern model (GCS) (see e.g., Bard & Faulkner²) relies on the so-called continuum assumption: ions are modelled as point charges in a continuous dielectric environment. Although routinely verified far from the interface, these models tend to fall short in the so-called Stern layer region³ few angstroms from the surface, where the discrete size of ions can no longer be ignored. The phenomenon is similar to the discrete distribution of the solvent molecules that give rise to the largely discussed solvation forces in liquid. These difficulties are particularly obvious in highly charged systems^{4,5} and corrections have been proposed to better account for the complex interactions linking ions, liquid molecules and the surface structure of the solid⁶⁻⁹. Moreover, continuum models usually make the implicit assumption that the Stern layer is homogenous, with a uniform ion distribution. This assumption becomes often oversimplified at the nanoscale where most solids exhibit some structure with localised charges and a well-defined hydration landscape that can determine the position and organisation of single ions at the interface. Such a complexity is key to many processes such as the folding and function of biomolecules¹⁰⁻¹³, the accumulation and transfer of charges at the surface of extremophiles^{14,15} or at the electrodes of solar cells¹⁶, electro-friction¹⁷, the nucleation of nanoparticles on surfaces¹⁸ or the preferential adsorption of a particular type of ion onto minerals^{19,22}. Even at the macroscopic level, intense research is currently dedicated to the synthesis of colloid particles exhibiting non-homogenous charge distributions at the surface for better controlling the stability or ordering of colloidal solutions²³. The GCS model and specific phenomena that go behind the classical description will be analysed in Chapter 4. Here I will focus on the experimental challenges of single ion detection with high-resolution AFM.

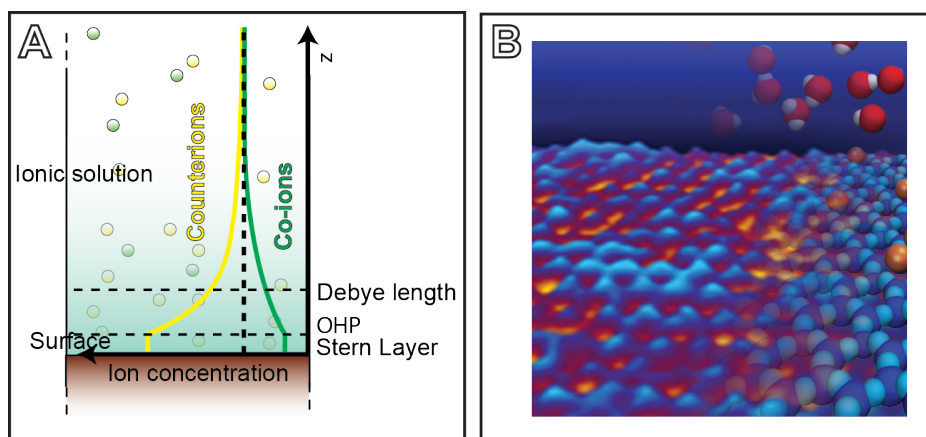


Figure 3.1 Schematic (A) and more realistic (B) representations of the EDL at a surface of a charged solid. In (A) the standard Gouy-Chapman-Stern model is presented while in (B) an artistic representation of a more realistic surface in liquid obtain combining an AFM image (left) and the MD-simulations (right).

Part of the difficulties in developing suitable models for the description of the ionic distributions at the interface comes from the lack of experimental results, particularly in the close vicinity of the surface where the continuum assumption brakes down. The finite size and specificity of the solvent molecules and the ions, together with the inhomogeneous lateral distribution of the surface charge can induce misinterpretation of the experimental results. One of the most challenging tasks is the determination of the lateral organisation of ions within Stern layers. The results available to date stem either from computer simulations¹⁷ or theoretical developments^{6,7}. When available, experimental data are typically obtained indirectly²⁴ or through techniques that

require averaging over a large area of the interface²⁵, hence implicitly relying on the assumption of a homogeneous Stern layer in order to provide a precise picture of the position of the ions and the liquid molecules.

To obtain information about the actual lateral distribution of the ions that are ‘bound’ to the surface of the solid, it is necessary to use a technique that:

- (i) is able to have a sub-nanometric spatial resolution, since the typical size of a hydrated ion is of the order of few Angstroms;
- (ii) is measuring a signal that is significantly affected by the presence of a single ion;
- (iii) is surface sensitive to discriminate the contribution of surface ions from all the others;
- (iv) is local so that the obtained information is localized at the sub-nanometric level in space, non-mediated over the surface;
- (v) is fast enough so that the residence time of the ions on a point on the surface is bigger than the time required for the acquisition of the data at that position;
- (vi) is non-perturbative to obtain, or at list deduce, the information of the actual system that is in the focus of the study.

These difficulties can in principle be overcome by AFM. When operated in liquid, AFM is able to investigate solid-liquid interfaces locally, often with atomic- or molecular-level resolution (see Chapter 2) and in the presence of ions. Studies allowing a clear and unequivocal identification of single ions within a Stern layer are however still sparse, with little information about the formation, stability and dynamics of adsorbed ions at the nanoscale.

3.2 Review on the previous works

To the best of my knowledge, the first paper that explicitly analyzed the effect of the ions on a high resolution AFM image was published by Fukuma *et al.*²⁶ They were able to image the headgroups of the phosphocholine-terminated lipid membrane in gel phase (DPPC). The FM-AFM study was performed in phosphate buffer solution (PBS) containing monovalent ions and the phosphate-buffering agent. They noticed a local variation of the AFM contrast at the level of the lipid headgroups and attributed it to the presence of mobile ions on the surface. The hypothesis proposed was that the ions, moving much faster than the time scale of the AFM image acquisition, were producing an effective charge distribution on the surface. Therefore, the height contrast observed in the images was reflecting the averaged positions of mobile ions or, in other words, spatial distribution of ion occupancy.²⁶ The ion-induced contrast variation was detected only in specific area of the sample as possible to see in Fig. 3.2B while other regions were unaffected (Fig. 3.2A).²⁶

The lipid bilayer system is complex and the dynamic interaction between the fluctuating headgroups and the ions in solution that can physically modify the actual structure of the surface (see Chapter 4). In the work of Ferber *et al.*²⁷, for example, a variation of the lattice constant of the hexagonal unit cell of the DPPC lipid bilayer is measured upon exchange of ionic solution. In this situation the ions are not simply moving at the Stern layer level but can even interact specifically with the different parts of the lipid headgroups with an affinity that depends on the type and charge of ion.²⁷ This implies that, at the ‘electrically neutral’ surface of the zwitterionic lipids, there is a condensation of both cations and anions. The relative ratio and complexation sites of the two (or more) species depend on the specific ions considered (see Chapter 4). The interpretation of the effect of a single ion on the bilayer surface becomes thus complicated to disentangle from other surface effects. Nevertheless the studies performed by Ferber *et al.*²⁷ and Fukuma *et al.*²⁶ demonstrated that FM-AFM was able to characterize the structural properties of the lipid bilayer headgroups at the molecular lever showing how ion specific effects can be important both in the lateral organization of the bilayer and image contrast formation.

In order to directly detect adsorbed ions, it is easier to consider a more rigid surface with a constant surface charge. Mica, an alumino-silicate mineral, has a negatively charged surface with hexagonal structure (see Fig. 3.3A). The surface charge is constant providing a stable model system where the effect of ions could be, in principle, easily detected on the atomically flat

surface. Loh *et al.*²⁸ studied the effects of different monovalent and divalent ions on the topographic images of the mica surface with FM-AFM. They noticed a modulation of the standard contrast of the hexagonal unit cell with the appearance of 50 pm protrusions above the location of an apparently random number of the oxygen triads of the mica lattice. Even in this case, these protrusions were assigned to the mobile cations considered as a diffuse cloud of charge. The preferential locations of the mobile cations were consistently identified as the oxygen triad sites (Fig. 3.3A). Although the adsorption location of the cations found with X-ray reflectivity²⁹⁻³¹ does not coincide with the positions individuated in the AFM measurements, this work opened the field of ion imaging at mineral surfaces. Later, Kimura *et al.*³² identified single potassium ions between the mica surface and the first water hydration layer. The ions appeared as elliptical structures (white contrasts in Fig. 3.3D) observed in the modulation of the frequency shift in both the vertical and lateral directions (see Fig. 3.3D). These repulsive “blobs” were located in the center of the ditrigrinal cavity as expected for the monovalent ions adsorbed on the surface. Interestingly the dark contrast, associated in this work to the first hydration layer, is surrounding the ions without disrupting the periodicity of the hydration layer in the lateral direction. This is the first time in which the effect of single ions has been reported in literature even if not explicitly stated by the authors. In this case the ions are not a homogenously distributed surface charge but a precise spatially located entity, able to induce a specific contrast in the AFM image in the time scale of the measurement.

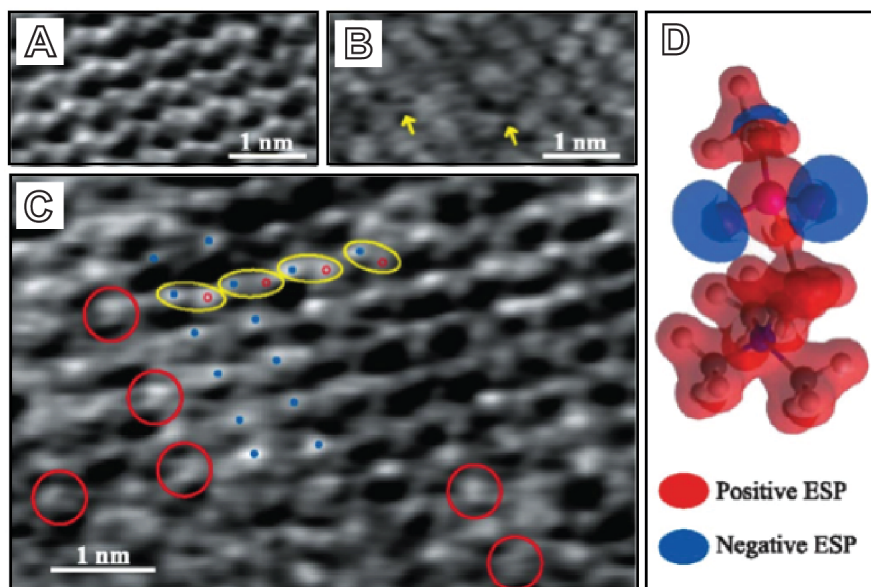


Fig. 3.2: FM-AFM images of the DPPC bilayer in PBS solution. Height scale: 0.12 nm. (A) Structure identified by the authors as PC headgroups not associated with ions or water molecules except for the possible bridging below the headgroups. (B) Structure identified by the authors as the contrast obtained in the case of ion-mediated tip-surface interaction. (C) Transient region between the two structures. (D) Electrostatic potential distribution (ESP) of a methyl-terminated PC headgroup. Figure adapted from Ref. [26].

Siretanu *et al.*³³ were able to detect the adsorption of divalent cations at the surface of gibbsite. Using force spectroscopy technique, high resolution AM-AFM, and numerical simulations they showed that these cations were adsorbing specifically on the surface forming an ordered array. This ordering was promoted by the water molecules bridging the ions. At higher concentration an effect of the anions was observed as well. Interestingly these results show that the Stern layer is a complex system that can form ordered structures when there is a strong affinity between the ions, the surface and the water molecules. They also showed how the contrast obtained in the AM-AFM images could be directly related to the presence of the ions, suggesting that, in specific conditions, the interaction between these adsorbates and the surface is strong enough to not be perturbed by the imaging AFM tip.

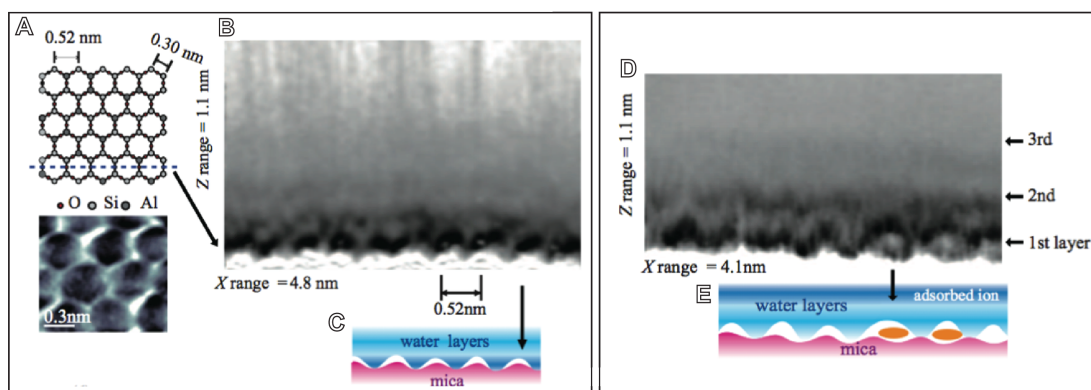


Fig. 3.3: (A) Schematic illustration and FM-AFM image (frequency shift) of muscovite mica (001) surface structure. (B) 2D hydration structure measured by FM-AFM. A periodicity of ~ 0.5 nm in the signal is found at both the mica surface and the first water molecule layers. In this layer the water molecules penetrate into the center of the hexagon as schematically illustrated in (C) therefore showing the same periodicity dictated by the surface. In the upper layers, fluid water molecule layers are observed. They show a vertically decaying correlation with the surface structure. (D) 2D hydration structure measured by FM-AFM in which some white elliptical white contrasts surrounded by dark contrasts appears in the center of the ditrigonal cavities as schematically illustrated in (E). The contrast is likely to be a K^+ ion or a hydrated K^+ ion complex adsorbed on the surface. Figure adapted from Ref. [32].

3.3 Physical mechanism behind ion detection with AFM

To detect an ion or an ionic distribution at solid-liquid interface with the AFM, the force acting between the tip and the sample must be affected by the ion's presence. This implies that the substrate-hydrated ion interaction has to be strong enough to survive the perturbation exerted by the AFM tip. This aspect will be analyzed in detail in section 3.2.5 where I will treat the effect of the tip in the imaging process.

Fukuma *et al.*²⁶ attributed the contrast obtained in the high-resolution FM-AFM images in the presence of the ions to the short-range electrical interaction force between the tip front atom and the charge distribution of the surface. The idea was that, similarly to Hembacher *et al.*³⁴ where a small carbon atom is able to image the charge distribution of a tungsten atom at the end of the tip, in the AFM images in ionic solutions, the contrast reflected the charge distribution of the surface affected by the mobile ions.²⁶ Therefore, the contrasts they observed in the AFM images (see Fig. 3.2) is likely to represent averaged positions of mobile ions or, in other words, spatial distribution of ion occupancy.²⁶

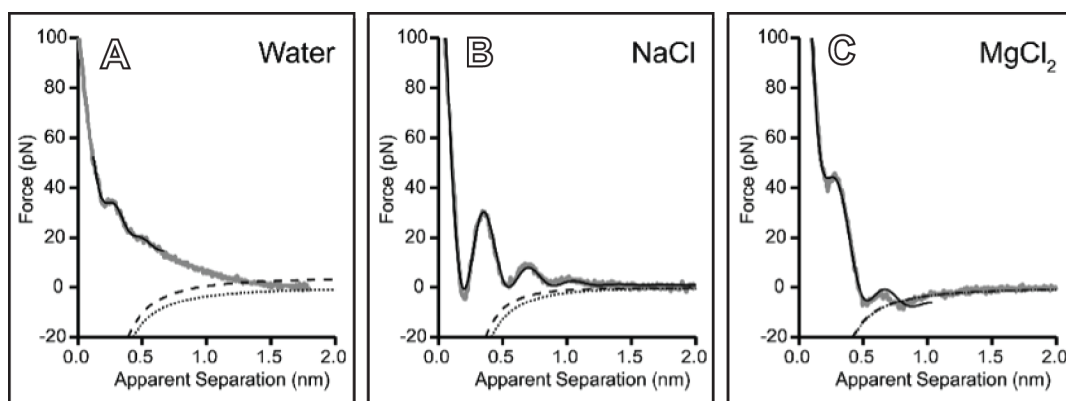


Fig. 3.4: Averaged force versus distance curves measured in pure water (A), 150mM NaCl (B), and 150mM $MgCl_2$ (C). Gray curves are the averaged data; black solid curves are the results of the fit to data taking into account only primary and structural hydration force; DLVO forces are calculated for constant charge (---) and constant potential (···) boundary conditions for a tip with a radius of 1 nm. Figure adapted from Ref. [35].

In the FM-AFM high resolution images both Fukuma *et al.*²⁶ and Loh *et al.*²⁸ used amplitude of oscillation of the order of 1-2 Å interacting directly with the solid surface, as explicitly stated by

the authors. They could, in fact, discriminate the surface level from the first hydration layer as a discrete jump of ~ 3 Å done by the tip in the vertical direction. In this imaging conditions the oscillating amplitude and the mean tip-sample distance is comparable with the size of a hydrated ion on the surface^{21,30}. Therefore the steric effect of the ions is more likely to be missed since the tip is ‘pushing’ them aside rather than ‘surfing’ over them. The average effect of ionic charge distribution is likely to be the true mechanism of the contrast variation recorded in the FM-AFM images as a function of ionic species and concentrations.

In Chapters 1 and 2 I have shown that AM-AFM could derive quantitative information about the local free solvation energy of a solid fully immersed into a liquid, with sub-nanometre resolution³⁶. This is possible when the vibrating AFM tip dissipates most of the energy within the interfacial liquid, without significantly interacting with the solid’s surface^{36,37}. Interestingly, this technique has shown to be sensitive to the local variation of the solvation structure of the liquid on the solid.³⁸ An ion that adsorbs on the surface induces a substantial perturbation of the local solvation environment and should hence be detectable.

The influence on the surface hydration structure of the ions adsorbed on mica has been investigated by X-ray reflectivity^{39,40} and MD-simulations⁴⁰. In all these works the ions has shown to have specific effects at the interface. They have different possible complexation sites³¹ and induce a significant modification of the water molecules around them. Particularly interesting is the work of Kilpatrick *et al.*³⁵ where they analysed the effect of several ions and concentrations on primary and structural hydration forces at the surface of mica (see Chapter 1). Using a sharp tip, where the lateral confinement is in principle extremely reduced, they showed that the introduction of the ions caused a serious modification of the hydration forces. Increasing ion valence and concentration induced an increase in the magnitude and a decrease of the decay length of the primary hydration force. Moreover, the structural hydration force showed ion specificity (Fig. 3.4). By comparing the relative contributions of the two hydration forces, they were able to observe conditions that maximize the observation of structural hydration adjacent to the charged interface. In the same work, the maximization of this structural force was associated to the achievement of atomic-resolution images of mica in aqueous environments.³⁵

3.4 Imaging monovalent ions at the Stern Layer of mica-water interface with AM-AFM

All the considerations made in sections 3.1 and 3.3 suggest that the small amplitude AM-AFM is a suitable technique to image the effects of the ions at the solid-liquid interface. To test this idea, we decided to use a simple, well-characterized system for which spectroscopic measurement of the isolated unperturbed interface were available. We choose the mica-water interface in the presence of symmetrical monovalent ions. In particular we focused our attention on RbCl, already characterized by Park *et al.*^{1,25} with resonant anomalous X-ray reflectivity.

Fig. 3.5A presents an AM-AFM of the mica surface obtained in 3mM RbCl solution with a commercial RC800-PSA tip (Olympus, Tokyo; see Materials and Methods section 4.6). What we consider as single Rb⁺ ions can be clearly identified in the topographic image of muscovite mica. The adsorbed Rb⁺ ions appeared as distinct protrusions on the sites normally occupied by K⁺ ions in bulk mica that correspond to the ditrigonal cavity (Fig. 3.5B). In the associated phase image the ions induced a sharp dark contrast, indicating an increase of the local tip energy dissipation (see also Fig. 3.6). The adsorbed Rb⁺ ions appeared surprisingly stable, with the same protrusion often visible in several consecutive line-scans (see section 3.5 for the residence time analysis). Nonetheless, the protrusions unambiguously indicate the presence of Rb⁺ ions at the corresponding sites, as evidenced when varying bulk ionic concentration (Fig. 3.6). In this experiments we imaged the mica-water interface increasing the concentration of the ions in solution. We noticed a progressively increasing number of protrusions appearing at the surface always associated to a darker contrast in the corresponding phase images.

Throughout this study, the phase contrast associated with a particular type of ion has always remained a clear signature of its presence. This is visible in Fig. 3.6, where the phase images,

associated with the corresponding topographic ones, are presented as a function of the bulk concentration. The phase contrast induced by the presence of ions is always consistent regardless of the surface coverage. Different types of ions provided different magnitude of phase contrast (see Chapter 4) that though appeared always darker (lower phase) than the mica. For each concentration, the measurements were repeated with several cantilevers to allow meaningful statistical results. The presence of ions could also be detected in amplitude spectroscopy where a distinctive step was visible as the tip expelled ions while approaching the mica surface (Fig. 3.6). Consistently, the fraction of curves exhibiting this step increases with the bulk ionic concentration.

The obvious way to proceed is to compare the ionic coverage measured with AFM for Rb^+ ions with the values obtained by Park *et al.*¹ with resonant anomalous X-ray reflectivity.

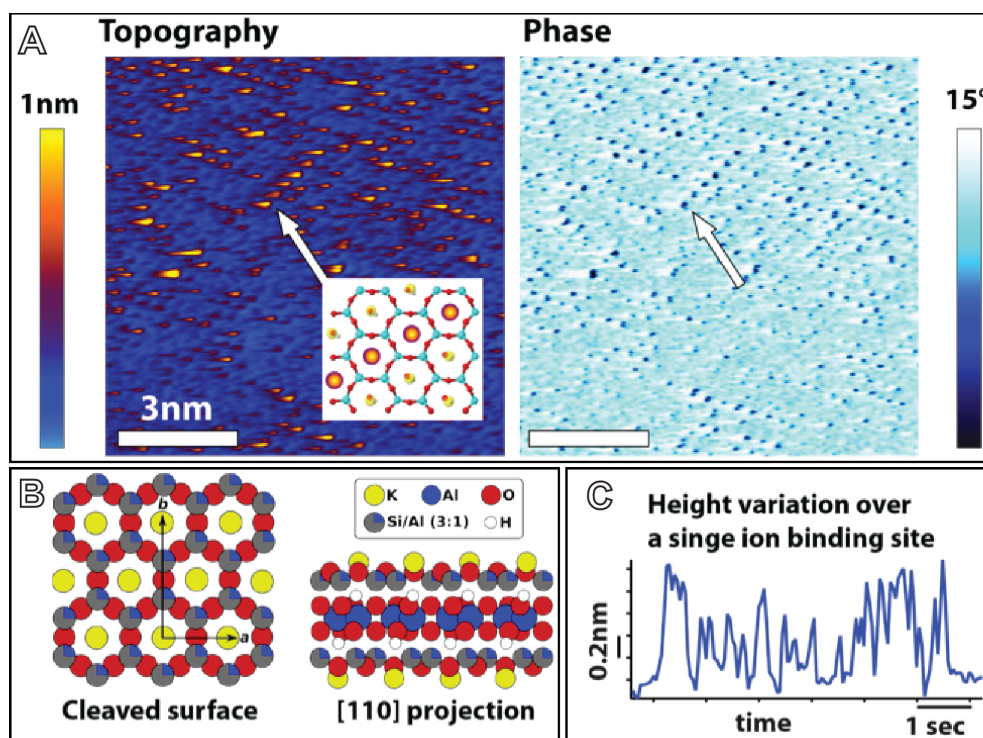


Fig. 3.5: AFM imaging of Rb^+ ions adsorbed at the surface of mica in an aqueous solution. The solution contains 3 mM RbCl (A). Individual ions can be distinguished both in topography and in phase (arrow), often forming geometrical domains or rows. Occasionally, a bright 'tail' is visible adjacent to the dark spots attributed to adsorbed ions. This tail is induced by a momentary increase of the tip vibration amplitude as the feedback loop completes the tip-sample distance correction, and is due to the particularly gentle imaging conditions. The atomic structure of mica evidences the position of the ion binding sites, which are occupied by K^+ ions in the bulk crystal (B). Repeatedly scanning over a same binding site (C), yields substantial height variations in time as single Rb^+ ions adsorb and desorb from the site. The scale bar is 3 nm (A) and the colour bars represent 1 nm (topography) and 15° (phase).

3.4.1 Method to extract the surface coverage of Rb^+ ions from the AFM images

Quantification of the surface coverage was performed using a thresholding procedure as illustrated in Fig. 3.7 for a series of AFM images obtained at different RbCl concentrations. A first order global background was subtracted from all the height images. Subsequently, from each image, a histogram (Fig. 3.7E) was generated. In the cases of zero and full surface coverage (respectively in Fig. 3.7A and D) the histograms were fitted with Gaussian curves.

At 2mM RbCl (Fig. 3.7B) the histogram showed a single peak with a pronounced asymmetry towards events with larger height. The alignment with the other histograms was done by fitting the main peak with a Gaussian centred at zero coverage.

At 4mM RbCl (Fig. 3.7C) the histogram showed two distinct peaks; the peak at smaller height values is due to the mica while the other is induced by the adsorbed ions. The histogram curve could therefore be aligned and decomposed into two Gaussians which centres are determined by the data at zero and full coverage respectively.

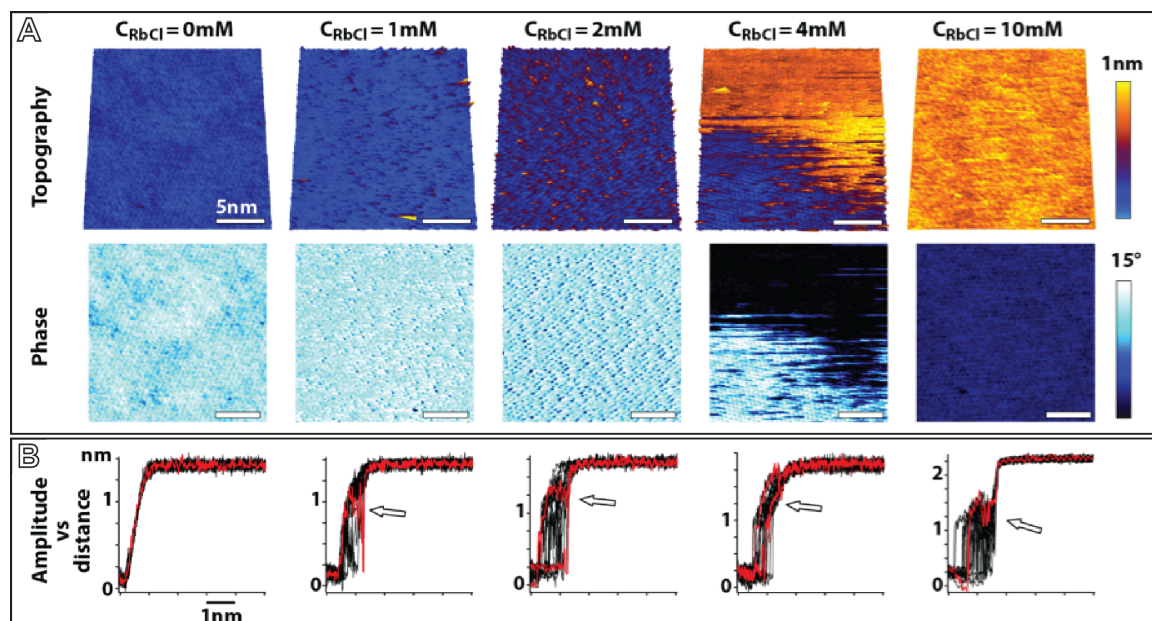


Fig. 3.6: Evolution of the Stern layer at the surface of mica as a function of the RbCl bulk concentration. For each concentration, the topographic image (top), the corresponding phase image (middle) and 20 representative amplitude vs. distance spectroscopic curves (bottom) are presented. The underlying mica lattice is visible in each image and single ions appear as bright protrusions in topography and a dark contrast in the phase. For each set of spectroscopic curves, two curves are highlighted in red. The presence of ions tends to induce a characteristic step in the curves (indicated by the arrow) as the tip expels the ions from the surface. At 10mM, the surface is fully covered and average height/phase were arbitrarily set with respect to the colour scale.

Based on this analysis, all the images/histogram curves were shifted in the same way together with all related data (i.e. the shift of the histogram curves are reported in the images as height alignment). It was then possible to objectively decide a threshold value, chosen between the centres of the two histogram's peaks (mica and adsorbed ions layer). This threshold value provided a mask in the image, selecting all the pixels with a height value larger than the threshold (Fig. 3.7F) and so providing direct access to the actual coverage value (see table in Fig. 3.7).

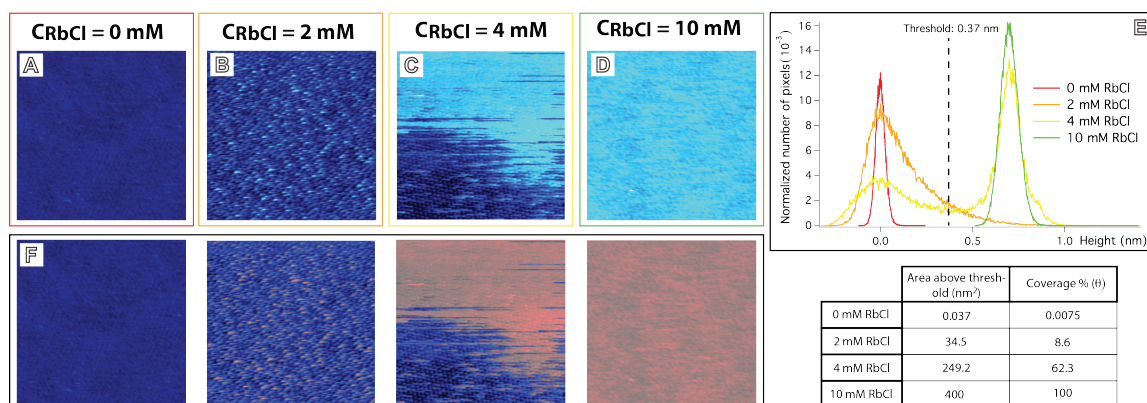


Fig. 3.7: Example of surface coverage analysis. From the four images on the top-left we obtained the histograms presented on the top-right. According to the histograms a specific threshold was chosen (in this example it is 0.37 nm). In (E), regions with a height larger than the threshold value are selected with a mask (reddish areas) and the total area covered by the mask is subsequently calculated. The final data are summarized in the table on the bottom-right.

A similar threshold value could generally be obtained by visual thresholding after flattening the image. In some cases, particularly at low surface coverage, phase images could be used in a

similar manner due to the clear binary behaviour where darker areas indicated ion adsorption. Using the phase images was particularly effective if the height images were noisy or when many isolated ions were present. In such cases, the number of ions could be directly counted and compared to the number of available sites in the image considered.

For each concentration of RbCl we typically selected 15-20 representative images with a scan size sufficient to resolve single ions (between $10 \times 10 \text{ nm}^2$ and $20 \times 20 \text{ nm}^2$). We then determined the ionic coverage. The statistical variance between the coverage values obtained for different images acquired at a same concentration was by far the largest source of errors. All the other sources of errors were comparatively small or negligible.

3.5 Dynamics of ions in the Stern Layer

The timescale of the phenomena we are investigating constitute a fundamental aspect of the observation. In the present case, the ion has to reside in a specific position for a sufficient amount of time in order to obtain a significant local perturbation of the hydration structure at the surface of the solid. From a theoretical point of view a variation of the mobility of the ions adsorbed at the surface is expected to depend on several parameters such as local viscosity, surface roughness, electrostatic energy between surface and ions and eventual external electric field.¹⁷

Theoretical approaches such as MD-simulations have focused mainly on the specific mobility of the ions under confinement⁴¹⁻⁴³ sometimes analysing the effect of the surface properties like charge and water affinity⁴⁴. In all cases a significant variation of the ionic mobility has been found but the confinement effect seems to play an important role in the obtained diffusion coefficient.⁴² MD-simulations studies showed that the decrease of diffusivity of Na^+ and Ca^{2+} ions in close proximity to mica surface (first few Ångströms) was at maximum 2 order of magnitude lower than the bulk diffusivity of the same ions⁴⁵. Bourg *et al.*⁴⁵ distinguished two diffusion constants parallel and normal to the mica surface. From the simulations they concluded that no significant difference exists between the two directions. In contrast, other simulations studies⁴⁶ concluded from the water dynamics that the average velocity of water molecules is higher parallel to the surface plane than perpendicular. This last finding may be important for explaining AFM measurements since interfacial water is expected to play an important role in the behaviour of ions under confinement^{36,41}.

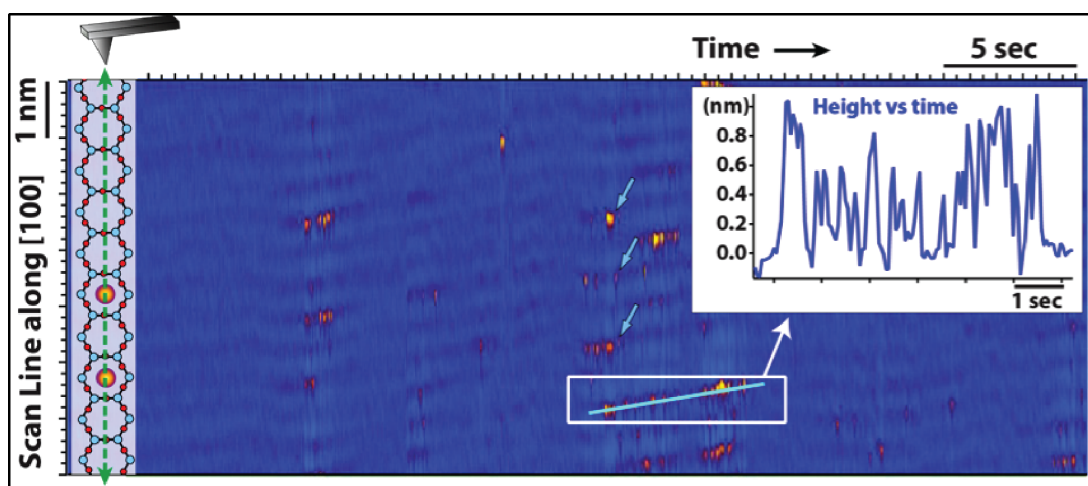


Fig. 3.8: Example of image obtained with the slow scan direction disabled. The yellow protrusions are Rb^+ ions on the mica surface. The inset presents an example of height profile (y-axis) varying with time (x-axis). The cartoon representation of the mica lattice (left) is to scale and correctly aligned with the actual data. The blue arrows point to Rb^+ ions binding simultaneously to adjacent sites, presumably stabilized by correlation effects.

The few available experimental measurements of ions mobility at surfaces in different relative humidity are obtained for example with polarization force measurement.⁴⁷⁻⁵⁰ Kendall *et al.*⁵⁰ found a relaxation times τ between 20 and 30 ms for ions at the calcite-water interface in controlled

humidity environment (95% humidity). The relaxation time is directly linked to the ionic mobility μ_i and densities σ_i of the different ionic species, and the overall capacitance C through:

$$\tau = C / \sum \mu_i \sigma_i \quad (3.1)$$

In the case of mica Xu *et al.*⁴⁸ found a relaxation time in the order of milliseconds for a relative humidity around 85%. Generally, a higher humidity tended to increase the ions' mobility. It is however complicated to extract from this type of experiment the actual diffusion coefficient of the ions at the surface immersed in the liquid.

Our AFM measurements, on the contrary, showed that, interpreting a single protrusion as an ion adsorbed at the surface, the residence time exceeded the time resolution capability of the technique (~50 ms). Our MD-simulations results indicate that, within the full duration of a simulations run (1 ns), Rb⁺ and K⁺ ions rarely moved once forming inner-sphere surface complexes. In contrast, Na⁺ ions were diffusing substantially in the plane parallel to the surface. Although the results are consistent with AFM observations, the large differences in the timescales do not allow for direct comparison. We have therefore decided to examine in details the dynamics of adsorbed ions and the influence of the AFM measurements in order to give the best possible interpretation of our experimental data. We do not distinguish between lateral and normal ion mobility but rather concentrate on deriving an estimate of the apparent residence time of a single ion at given adsorption sites.

In the experiment presented in Fig. 3.8, the slow scan motion of the AFM was disabled and the tip repeatedly scanned over the same adsorption sites along a selected crystallographic direction on the mica's surface. The study was conducted at a bulk salt concentration of 2.5mM RbCl, ensuring a low apparent surface coverage (see Fig. 3.8). Before starting an actual experiment we determined an appropriate scanning direction (in registry with the mica lattice) by varying the scanning angle. A typical experiment is presented in Fig. 3.8. The y-axis corresponds to the position of the lattice sites in space along the [100] direction.

In order to test for possible effects of the measurement dynamics, the experiment was conducted at different scan speed: 15Hz, 20Hz and 25Hz (1Hz is equivalent to 1 line scan/sec). At these scanning speeds, the tip typically takes 150-250 μ s per imaged pixel.

Similarly to standard AFM measurements, it was always possible to detect the consecutive appearance/disappearance of higher protrusion at the specific ion-binding sites of the lattice. These protrusions, which we attribute to the presence of one or more ions, often presented different height values and time durations. To objectively investigate the phenomenon we conducted a careful statistical analysis of these events. Taking multiple line profiles, similar to that shown in the inset of Fig. 3.8, we analysed the time distribution and eventual dependence on scan speed of the events. The analysis can be done in an automatized way once a specific height threshold has been selected (Fig. 3.9B). A single event is characterized by a duration: the time lapse between the instant when the height profile exceeds the threshold value and the instant in which it returns below the threshold line. The choice of an appropriate threshold value is not trivial since it is likely to affect the results of the analysis. We therefore repeated the statistical analysis of the residence times with several thresholds, each chosen as a multiple of q , where q is the height RMS value obtained over ion-free images (e.g. Fig. S8). A typical experimental value for q in our experimental conditions is $q \sim 0.12$ nm.

In Fig. 3.9 the results of the analysis for different threshold values are presented. As expected, the distributions of residence times depend on the selected threshold (Fig. 3.9A) with a larger number of events and slower overall dynamics for the lower thresholds. The results obtained at $4 \times q$ and $10 \times q$ can therefore be seen as respectively higher and lower estimates of the measured Rb⁺ residence times.

It is possible to extract quantitative information about ions' dynamics at the interfaces from the distributions presented in Fig. 3.9A. Such a task is however far from trivial because the AFM data may only present part of the residence time distributions (the tail) and appropriate model for fitting the distributions hence is needed.

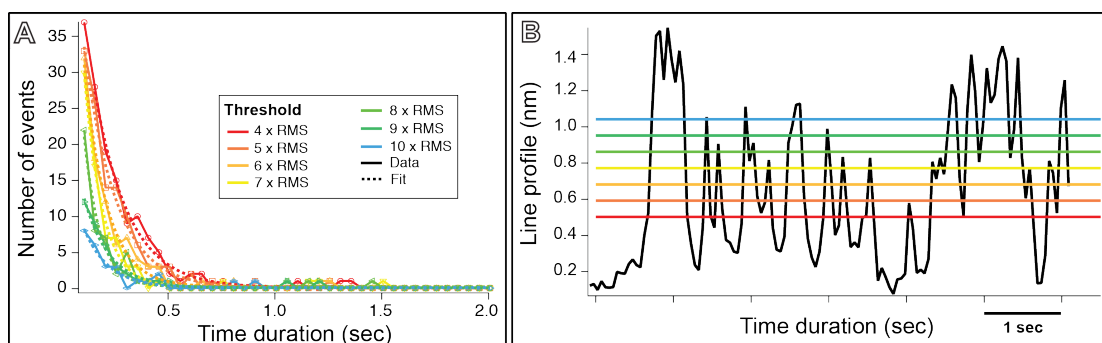


Fig. 3.9: Example of residence time analysis. Line profiles obtained from the AFM images are analysed according to a specific threshold values chosen as a multiple of the height RMS of a clean (ion free) surface (B). The residence time distributions (A) have been obtained through statistical analysis of multiple time profile over ion binding sites (see text for details). A characteristic decay time was obtained for each distribution by fitting with an exponential decay. The corresponding results are presented in Table 3.1.

Experimentally, since ions can diffuse on the surface and desorb at the same time (lateral and normal diffusion) we generalized the procedure used by Impey *et al.*⁵¹ to analyse the simulations' results. Impey *et al.*⁵¹ described the time evolution of water molecules lying in the first coordination shell of a specific ion using an exponentially decaying function, $n_{ion}(t) = n_{ion}(0)e^{-t/\tau}$, with a characteristic time τ . In this case, τ provides a simple definition of the residence time of water molecules in the ion's first solvation shell. Most of the diffusing processes tend to present a similar behaviour and our results are no exception (Fig. 3.9A). In our case, however, τ would refer to an apparent mean residence time. The values obtained by fitting the data are presented in the Table 3.1.

Scan rate of 20 Hz	Residence time τ of ions (s)
threshold of $4 \times$ RMS value	0.12 ± 0.01
threshold of $5 \times$ RMS value	0.12 ± 0.01
threshold of $6 \times$ RMS value	0.073 ± 0.006
threshold of $7 \times$ RMS value	0.084 ± 0.003
threshold of $8 \times$ RMS value	0.106 ± 0.004
threshold of $9 \times$ RMS value	0.148 ± 0.006
threshold of $10 \times$ RMS value	0.162 ± 0.005

Table 3.1: Mean residence times as a function of the threshold value used for the analysis. The mean residence times τ were obtained from the decay factor obtained by fitting the distributions in Fig. 3.9A with a decaying exponential. The uncertainties were obtained from the fits but are likely to underestimate the actual errors of the measurements. The average residence time obtained over all the threshold values is $\tau = 115 \pm 32$ ms (the error is the standard deviation).

From the results obtained it is possible to conclude that the typical residence time obtained is on the order of 100ms.

3.5.1 The effect of the scan speed

The apparent residence times derived from the experiments described above are rather slow when compared to the available literature. Confinement effects, induced by the AFM tip, could in principle be responsible for the slow dynamics⁵² and ion specificity⁴³ observed in the results. The acquisition time of the AFM is however invariably a limiting factor with an effective time resolution corresponding to the inverse of the scan rate (i.e. the time τ_t , necessary for the tip to come back to the same binding site). The typical residence time obtained in the previous subsection is however very similar to the value of τ_t . It is hence possible that the time resolution of the AFM measurement constitute the ultimate limit of the value τ values derived here. To test this hypothesis, we repeated the experiment presented in Fig. 3.9 at different scan speeds. We consistently used a threshold of $4 \times$ for the analysis so as to allow direct comparison of the

results. In Fig. 3.10 the residence time distributions as well as the derived mean residence time decay τ obtained by fitting the results are presented.

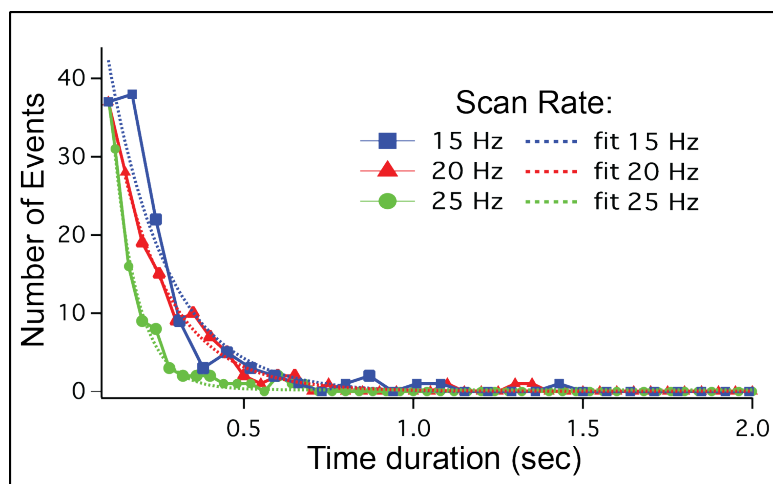


Fig. 3.10: The residence time distribution functions are presented for three different scan rates (15, 20 and 25 Hz). The chosen threshold value is 4 times the reference RMS. These distributions have been fitted with a decaying exponential and the characteristic decay times are presented in the Table 3.2.

	Residence time of ions (s)
Scan rate of 15 Hz	0.18 ± 0.02
Scan rate of 20 Hz	0.12 ± 0.01
Scan rate of 25 Hz	0.071 ± 0.003

Table 3.2: Residence times derived by fitting for the distributions in Fig.3.10 with a decaying exponential. The procedure is the same as for Fig. 3.9.

The apparent residence times τ for the different scan rates have the same order of magnitude as those obtained in the previous experiment. They seem to correlate with the effective AFM time resolution (40ms@25Hz, 50ms@20Hz, and 65ms@15Hz), suggesting that the temporal resolution of the AFM is the final limiting factor. It is however not clear from these data if the AFM tip was able to slow down the ion's dynamics or whether faster measurements were simply capable of better capturing the true (and AFM independent) ions dynamics. Furthermore, the residence times obtained from AFM measurements are always slower than the AFM time limitation. Ultimately, AFM alone is not sufficient to answer this question, which will require complementary measurements from other experimental techniques.

3.5.2 The effect of scanning drift

Due to the high imaging resolution needed to estimate the residence time of ions, scanning drift can be a major cause of error during the measurement. In order to obtain a precise idea of the typical magnitude and direction of the drift in our experiments, we conducted a calibration using the mica lattice as a reference. An example of this calibration is illustrated in Fig. 3.11. The drift contribution can be decomposed into two components; one parallel and one orthogonal to the fast scan direction. The drift parallel to the scan direction induces the lattice sites to form oblique lines in time (not perfectly horizontal). Practically, this contribution can be compensated by taking line profiles along the timeline of the site considered (as shown in Fig. 3.11).

The drift component orthogonal to the fast scan direction can be estimated from the periodic discontinuity visible when following the timeline of a given mica site. Every ~ 10 seconds (in the case of Fig. 3.11A) a vertical offset of half a lattice site is visible (white dotted lines in Fig. 3.11A). This phenomenon was due to the tip drifting onto a row of sites adjacent to the row

initially scanned, as illustrated in Fig. 3.11B. According to this interpretation, we could estimate a drift vector with a component of $\sim 0.8 \text{ \AA/s}$ parallel to the fast scan direction and a component of $\sim 0.5 \text{ \AA/s}$ in the orthogonal direction. The time error resulting from such a drift is negligible in our measurements. Moreover line profiles compensate for the drift parallel to the fast scan direction, and are taken in regions without ‘drift transition’.

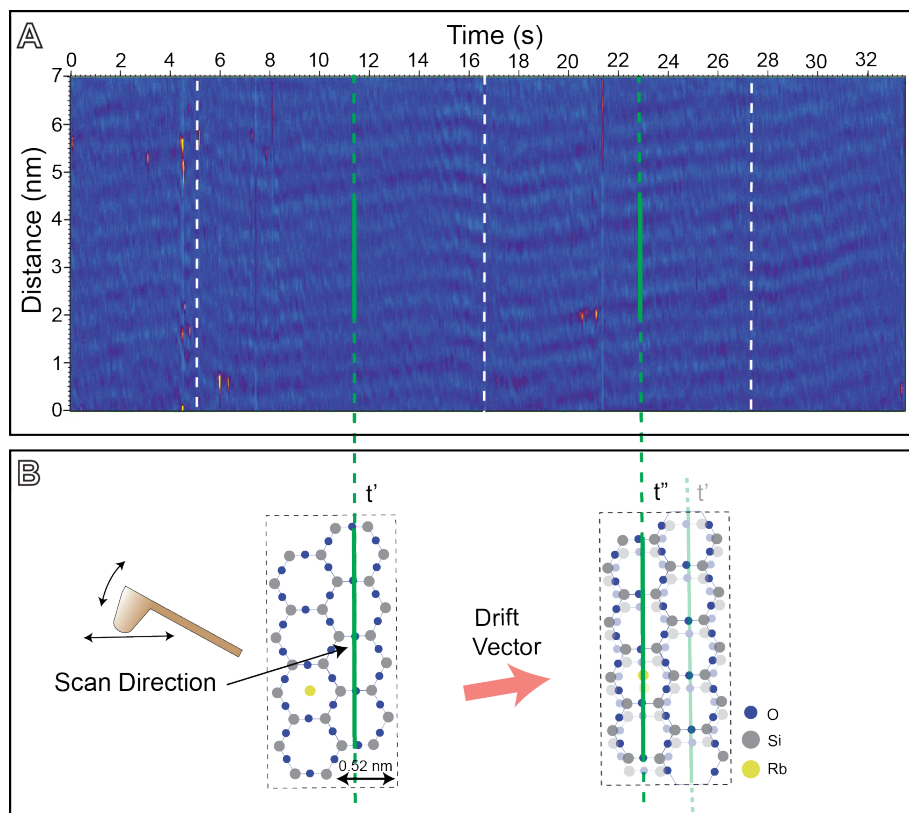


Fig. 3.11: Example of drift calibration. The tip repeatedly scans over the same line. In first approximation, the drift vector (supposed nearly constant in time and space) has two components: one parallel and one orthogonal to the fast scan direction (the red arrow in the figure). The drift component parallel to the fast scan direction results in the formation of oblique lines in time, as opposed to horizontal lines. The component perpendicular to the fast scan direction produces an abrupt vertical offset (i.e. an offset parallel to the scanning direction) every ~ 10 seconds. The magnitude to this offset corresponds to half a lattice site, indicating that the tip has drifted to an adjacent lattice row from the initial position (B).

3.5.3 Confinement effects

The results and control experiments presented here indicate a discrepancy between the residence time of ions at the surface of mica measured with AFM and the values hinted in the literature. The confinement effect of the interfacial liquid between the sample and the tip provides one possible explanation for this discrepancy. Studies have shown that, in this geometry, the dynamics of the confined water molecules can slow down several orders of magnitude^{39,52,53} (between 3 and 4, depending on the confinement). The effect of confinement on the dynamics of ions is still a matter of debate in the literature, but growing evidence indicates that the specific hydration structure of a particular ion often dominates the interfacial behaviour^{1,25,39-41,53-56}. Differences between measured ions are therefore likely to be enhanced in AFM measurements due to the confinement of the interface by the AFM tip. The sharpness of the AFM tip combined with the relatively slow approaching speed is unlikely to create a degree of confinement comparable to the one in a nanochannel or in the SFA. Moreover, the results show ion-dependent effects, which are intrinsic to the system, as shown in the simulations of the ‘free’ interface.

The dynamics of the ions under confinement may be system-dependant. MD-simulations of Na-montmorillonite interlayers in stacked lamellae showed a Na^+ diffusivity more than three orders

of magnitude slower than the bulk value⁵⁷. In contrast, Alcantar and co-workers with SFA obtained a reduction in ions diffusivity of, at most, two orders of magnitude between two mica sheets.⁴⁷ Considering a typical diffusion coefficient value of 10^{-9} m²/s for most anions and cations in bulk water, a reduction of two orders of magnitude would not be sufficient to explain our results. A definitive answer will come from complementary techniques such as MD-simulations^{20,58,59}.

3.6 Isotherm models

The results of coverage vs. bulk concentrations presented in Fig. 3.12 clearly indicate the existence of an adsorption isotherm for the Rb⁺ ions at the surface of mica. For a given bulk concentration, the observed coverage depended on the tip/cantilever employed for imaging, therefore providing an ideal system for quantifying the influence of the tip on the measurement. RAXR results available for the same system can be used as a reference for the ‘unperturbed’ system. Practically, the procedure relies on a systematic quantification of the isotherm using a model described in the section 3.6.1.

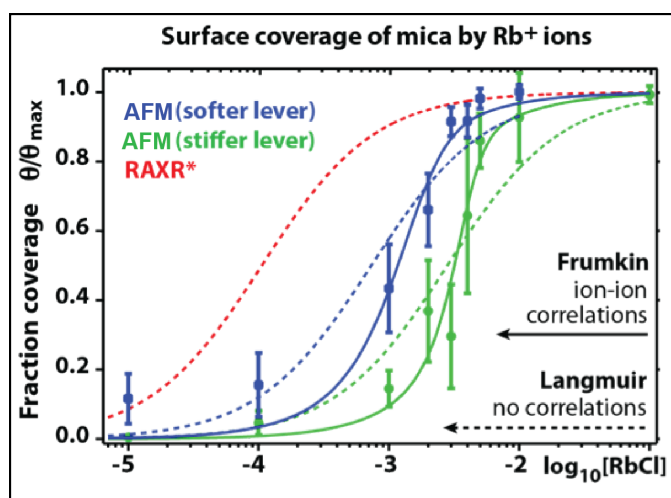


Fig. 3.12: Adsorption isotherm of Rb⁺ at the surface of mica measured by AFM and RAXR. The AFM measurements were conducted with two types of cantilevers exhibiting different spring constant $k_s \sim 0.1\text{N/m}$ (softer lever) and $k_s \sim 0.5\text{N/m}$ (stiffer lever) but a same tip design. The solid lines represent data fits with the corrected Frumkin isotherm, which allow for ion-ion correlations. The dashed lines show fit results in the case of the Langmuir isotherm. *The Langmuir isotherm fitted to the RAXR data is reproduced from Refs. [1].

3.6.1 Frumkin-Fowler-Guggenheim isotherm model

The Langmuir isotherm adsorption model has been used to describe the results presented in Fig. 3.12, similarly to the approach followed by Park *et al.*¹. This is a phenomenological reaction model, largely used to describe the adsorption of ions or more complex molecules at the solid-liquid interfaces.^{1,61,62} The basic assumptions of the model proposed by Langmuir are:

1. A fixed number of binding sites per units of area ultimately determined by the surface structure.
2. The adsorption rate proportional to the number of vacant binding sites and the pressure/concentration of the solution (in reality the concentration at the surface should be used, that can be obtained by coupling the EDL model with the Langmuir isotherm to derive the concentration of the ions at the OHP⁶², see the corrections in the Appendix).
3. The desorption rate proportional to the number of adsorbed molecules.
4. Equivalence of all the binding sites.

In the specific case of the Rb^+ ions at the surface of mica we assumed even that the large majority of the ions are adsorbed in the inner-sphere hydration state as shown by Park *et al.*¹. If this is not the case, two different types of binding sites with different binding energy should be considered. In an equilibrium situation, the mean number of adsorbates on the surface is constant (desorption and adsorption rate are equal). This simple consideration enables the derivation of the classical Langmuir isotherm:

$$\theta_{\text{Rb}^+} = \frac{K_{\text{Rb}^+} \cdot C_{\text{Rb}^+}}{1 + K_{\text{Rb}^+} \cdot C_{\text{Rb}^+}} \quad (3.2)$$

θ_{Rb^+} is the surface coverage of the Rb^+ ions, K_{Rb^+} is the binding constant of Rb^+ (ratio between the adsorption and desorption rates) with the dimension of the inverse of the concentration and C_{Rb^+} is the bulk concentration of the Rb^+ ions.⁶³ In our case we had to consider the competitive adsorption of Rb^+ cations and hydronium (H_3O^+) on the charged surface so Eq. 3.2 has to be modified to:^{1,62}

$$\theta_{\text{Rb}^+} = \frac{K_{\text{Rb}^+} \cdot C_{\text{Rb}^+}}{1 + K_{\text{Rb}^+} \cdot C_{\text{Rb}^+} + K_{\text{H}_3\text{O}^+} \cdot C_{\text{H}_3\text{O}^+}} \quad (3.3)$$

where now $K_{\text{H}_3\text{O}^+}$ and $C_{\text{H}_3\text{O}^+}$ are respectively the binding constant and concentration of the hydronium ion. Some extra modifications to the Eq. 3.3 have been proposed to better describe the interactions between adsorbates on the surface. The classical example is the Frumkin-Fowler-Guggenheim (hereafter Frumkin) isotherm model^{1,64}. The variation of the coverage expected in the Langmuir case, is expressed through the introduction of an ion-ion correlations energy E_c . The new expression for the rubidium coverage is given by:

$$\theta_{\text{Rb}^+} = \frac{K_{\text{Rb}^+} \cdot e^{\frac{E_c \theta_{\text{Rb}^+}}{RT}} \cdot C_{\text{Rb}^+}}{1 + K_{\text{Rb}^+} \cdot e^{\frac{E_c \theta_{\text{Rb}^+}}{RT}} \cdot C_{\text{Rb}^+} + K_{\text{H}_3\text{O}^+} \cdot C_{\text{H}_3\text{O}^+}} \quad (3.4)$$

Attraction between Rb^+ ions occurs if $E_c < 0$ and repulsion if $E_c > 0$. If $E_c \equiv 0$ the Frumkin isotherm simplifies back to the Langmuir isotherm.

The change of free energy ΔG_{Rb^+} upon Rb^+ adsorption is given by:

$$\Delta G_{\text{Rb}^+} = \Delta G_{\text{Rb}^+}^0 + E_c \cdot \theta_{\text{Rb}^+} \quad (3.5)$$

where $\Delta G_{\text{Rb}^+}^0 = -RT \ln(K_{\text{Rb}^+})$ is smaller than zero if adsorption occurs.

The experimental data presented in Fig. 3.12 were fitted with both the Frumkin (full line) and Langmuir (dashed line) isotherm models. In both cases, a modification was implemented to take into account the perturbation induced by the measuring tip. Electrostatic and mechanical perturbations were supposed to be the major sources of tip-induced effects on the isolated interface (see section 3.7).

As possible to see in Fig. 3.12 the Frumkin isotherm model (with the tip perturbation contributions), provides a substantially better fit to the data. The possibility to treat the protruding features on the surface as a parameters to determine the effective coverage of the ions with a surprisingly good match with the RAXR data¹, is again a strong indication that single ions are detected. The maximum coverage observed by AFM (10mM, Fig. 3.6) corresponds to all the available binding sites being occupied and the isotherm is modeled accordingly. In reality, only half the binding sites should, on average, be occupied to ensure electro-neutrality at equilibrium.¹ This suggests that at 10mM, the AFM images show predominantly Rb^+ patches with empty area outside the imaging region. The existence of patches is consistent with correlations effects.

The isotherm analysis indicates the presence of a clear correlation between Rb^+ ions during the adsorption process. The associated correlation energy was found to be always attractive and

similar, within uncertainty, for different types of cantilever: $E_c = -7 \pm 3 \text{ kJ mol}^{-1}$. This value is consistent with the observed formation of Rb^+ rows and small domains at low salt concentration in the AFM images (Fig. 3.5).

Since this chapters focus on the details of the measurement process, a systematic analysis of the correlation effect on the distribution of the ions in AFM images and the origin of this attractive component will be discussed in the Chapter 4 where the physical properties of the Stern Layer of different solid-aqueous interfaces are analyzed.

3.7 Perturbation of the system with the AFM tip

We have already mentioned the effect that the tip can have on the dynamic of the ions, in terms of confinement, during the imaging process. However, this is not the only effect that can affect the AFM measurement. In this section I will present a correction to the Frumkin model that can take into account the mechanical and electrostatic perturbation of the tip during the AFM measurement. Finally I will show some experimental data obtained with a tip composed by a different material (gold) to show the effect that the electrostatic component can have on the measurement.

3.7.1 Correction of the Frumkin model for AFM measurements

The AFM tip probing a Stern layer in solution will invariably perturb the adsorbed ions, hence affecting the apparent surface coverage observed in the images and the resulting data.

We propose two main perturbation mechanisms:

- i. A mechanical perturbation: as the tip vibrates at the interface, it can expel from the tip-surface gap adsorbed ions inducing a lower apparent coverage. It is reasonable to assume that the energy E_m^{AFM} associated with this perturbation is directly proportional to the energy dissipated by the vibrating tip into the interface³⁶.
- ii. An electrostatic perturbation: when immersed into the solution, the silicon nitride tip becomes charged⁶⁵ and develops around a Stern and double layers. In AFM measurements, the tip is likely to affect the apparent surface coverage, either increasing it if attracting more ions locally (lensing effect), or decreasing it if repelling them. A perturbation energy E_e^{AFM} can be associated with this effect.

Taking into account these two contributions from the AFM measurements, Eq. 3.5 can be re-written as:

$$\Delta G_{\text{Rb}^+} = \Delta G_{\text{Rb}^+}^0 + E_c \cdot \theta_{\text{Rb}^+} + E_m^{AFM} + E_e^{AFM} \quad (3.6)$$

It is important to realise that written as in Eq. 3.6, ΔG_{Rb^+} represent an effective or ‘apparent’ change of free energy of the Rb^+ ion when adsorption occurs under AFM perturbation:

- If the mechanical perturbation effectively makes the adsorption less favourable, then $E_m^{AFM} > 0$,
- If the tip artificially increases the number of ions present by ‘lensing’ effect, then $E_e^{AFM} < 0$, otherwise $E_e^{AFM} > 0$ if the effective electrostatic interaction between the tip and the ions is repulsive and decreases the apparent surface coverage.

The corrected-perturbed adsorption isotherm therefore becomes:

$$\theta_{\text{Rb}^+} = \frac{K_{\text{Rb}^+} \cdot e^{-\frac{E_c \theta_{\text{Rb}^+} + E_m^{AFM} + E_e^{AFM}}{RT}} \cdot C_{\text{Rb}^+}}{1 + K_{\text{Rb}^+} \cdot e^{-\frac{E_c \theta_{\text{Rb}^+} + E_m^{AFM} + E_e^{AFM}}{RT}} \cdot C_{\text{Rb}^+} + K_{\text{H}_3\text{O}^+} \cdot C_{\text{H}_3\text{O}^+}} \quad (3.7)$$

3.7.2 Extraction of the different energy contributions

The correlation energy E_c can be directly obtained by fitting with Eq. 3.7 the isotherms derived experimentally from AFM results (Fig. 3.12). It is however more challenging to separate $\Delta G_{Rb^+}^0$ from the two perturbation energies E_m^{AFM} and E_e^{AFM} since a fit with Eq. 3.7 will only provide a value for the total contribution $\Delta G_{Rb^+}^0 + E_m^{AFM} + E_e^{AFM}$. The value for $\Delta G_{Rb^+}^0$ (or K_{Rb^+}) and $K_{H_3O^+}$ can be taken from RAXR results¹ which then act as a reference of ‘non-perturbed’ Stern layer.

The two energies E_m^{AFM} and E_e^{AFM} can then be separated by carrying out the experiment with two different types of cantilever which exhibit different spring constants (resulting in different E_m^{AFM} values) but an identical tip design (and hence a same E_e^{AFM}). Practically, since two tips are never perfectly identical at the atomic level, we used several cantilevers (at least 5) to statistically limit the impact of tip morphology variations between the two types of cantilevers and between cantilevers of the same type.

The mechanical perturbation energy E_m^{AFM} is proportional to the energy E_{dissip}^{AFM} locally dissipated by the vibrating AFM tip at the interface. The later can be calculated from experimental parameters:⁶⁶

$$E_m^{AFM} \propto E_{dissip}^{AFM} = \frac{k \nu}{Q} f(A, \varphi) \quad (3.8)$$

where k , ν and Q are respectively the spring constant the resonance frequency and the Q -factor of the cantilever vibrating close to resonance. $f(A, \varphi)$ is a function of the cantilever vibration amplitude A and phase φ . The higher harmonics can in principle contribute to the energy dissipation but we decided to neglect them accordingly to the imaging conditions used in these experiments (see discussion in subsection 2.6.1). Experimentally, both types of cantilevers were operated at comparable amplitudes and provided similar phase shifts. Using Eq. 3.8 on both cantilevers, we can therefore write:

$$\alpha = \frac{E_{m,stiff}^{AFM}}{E_{m,soft}^{AFM}} = \frac{\frac{k_{stiff} \nu_{stiff}}{Q_{stiff}} f(A_{stiff}, \varphi_{stiff})}{\frac{k_{soft} \nu_{soft}}{Q_{soft}} f(A_{soft}, \varphi_{soft})} \cong \frac{k_{stiff} \nu_{stiff} Q_{soft}}{k_{soft} \nu_{soft} Q_{stiff}} \quad (3.9)$$

where α is a constant and the indexes ‘soft’ and ‘stiff’ refer to the softer and the stiffer lever respectively. Experimentally, average values of k , ν and Q can be measured for each type of cantilever and the constant α is therefore easily accessible.

The Rb^+ ions surface coverage $\theta_{Rb^+,soft}$ and $\theta_{Rb^+,stiff}$ obtained experimentally for the softer and stiffer levers can now be used to determine the mechanical and electrostatic contributions to the adsorption free energy. Using Eq. 3.7 for both cantilevers, taking the logarithm and combining the expressions, we obtain:

$$RT \ln \left[\frac{\frac{1}{\theta_{Rb^+,soft}} - 1}{\frac{1}{\theta_{Rb^+,stiff}} - 1} \right] = E_{c,soft} \cdot \theta_{Rb^+,soft} - E_{c,stiff} \cdot \theta_{Rb^+,stiff} + E_{m,soft}^{AFM} - E_{m,stiff}^{AFM} \quad (3.10)$$

where we have used the fact that $E_{e,soft}^{AFM} = E_{e,stiff}^{AFM}$. Furthermore, Eq. 3.10 holds, provided that the values of $\theta_{Rb^+,soft}$ and $\theta_{Rb^+,stiff}$ are taken at a same $RbCl$ concentration C_{Rb^+} . Combining Eq. 3.9 and Eq. 3.10 we can now write:

$$\begin{cases} E_{m,\text{soft}}^{AFM} = \frac{\beta - \gamma}{1 - \alpha} \\ E_{m,\text{stiff}}^{AFM} = \frac{\alpha(\beta - \gamma)}{1 - \alpha} \end{cases} \text{ with } \begin{cases} \beta = RT \ln \left[\frac{\frac{1}{\theta_{Rb^+, \text{soft}}} - 1}{\frac{1}{\theta_{Rb^+, \text{stiff}}} - 1} \right] \\ \gamma = E_{c,\text{soft}} \cdot \theta_{Rb^+, \text{soft}} - E_{c,\text{stiff}} \cdot \theta_{Rb^+, \text{stiff}} \end{cases} \quad (3.11)$$

we can then also obtain an expression for the energy corresponding to the electrostatic perturbation:

$$E_{e,\delta}^{AFM} = RT \ln \left[\frac{C_{Rb^+, \delta}(1 - \theta_{Rb^+, \delta})}{\theta_{Rb^+, \delta}(1 + K_{H_3O^+} \cdot C_{H_3O^+})} \right] - E_{c,\delta} \cdot \theta_{Rb^+, \delta} - E_{m,\delta}^{AFM} - \Delta G_{Rb^+}^0 \quad (3.12)$$

with $\delta = \text{soft, stiff}$ and $\Delta G_{Rb^+}^0 = -RT \ln(K_{Rb^+})$.

β and γ both depend on $\theta_{Rb^+, \text{soft}}$ and $\theta_{Rb^+, \text{stiff}}$ but not explicitly on C_{Rb^+} . This is implicit in our model where the values of $E_{m,\text{soft}}^{AFM}$ and $E_{m,\text{stiff}}^{AFM}$ should remain constant throughout all the salt concentrations C_{Rb^+} . Evaluating $E_{m,\text{soft}}^{AFM}$ and $E_{m,\text{stiff}}^{AFM}$ from Eq. 3.12 for each set of values ($\theta_{Rb^+, \text{soft}}(C_{Rb^+}); \theta_{Rb^+, \text{stiff}}(C_{Rb^+})$) obtained experimentally, provides a good opportunity to prove the consistency of the derivation: if the perturbations induced by the AFM tip can indeed be modelled as proposed here, the values obtained for $E_{m,\text{soft}}^{AFM}$ and $E_{m,\text{stiff}}^{AFM}$ should remain constant for each C_{Rb^+} . This is indeed verified, as visible in Fig. 3.13.

3.7.3 Results and discussion

The correlation energies obtained by fitting the experimental data with Eq. 3.7 are summarized in Table 3.3. The values obtained for both cantilevers are similar (within uncertainty) and both values are negative indicating an attractive correlation between adsorbed ions. The correlation energies are typically 2-3 times bigger than the thermal energy ($RT = 2.5$ kJ/mol at 25°C).

	Corrected Frumkin isotherm			Langmuir isotherm	
	E_c	E_m^{AFM}	E_e^{AFM}	K_{Rb^+}	$\Delta G_{Rb^+}^0$
Softer lever	-6 ± 2.5	0.3 ± 0.1	$7 \pm 6^*$	1.9 ± 0.4	-18.7 ± 0.5
Stiffer lever	-7.5 ± 1	4 ± 1	$7 \pm 6^*$	0.5 ± 0.1	-15.5 ± 0.5

Table 3.3: All the values (except for K_{Rb^+}) are given in kJ/mol and have been calculated using the binding constant for H_3O^+ ions from Ref. [1] ($K_{H_3O^+} = 126000 \pm 10000$ L·mol⁻¹). The K_{Rb^+} is expressed as L·mol⁻¹. *From the AFM data it is only possible to deduce $E_e^{AFM} + \Delta G_{Rb^+}^0$ directly. The values presented have therefore been calculated using the $\Delta G_{Rb^+}^0$ value given in Ref. [1] ($\Delta G_{Rb^+}^0 = -23.5 \pm 4.5$ kJ/mol).

The values of $K_{H_3O^+}$ and K_{Rb^+} used in this calculation and obtained from Ref. [1] can be compared to the experimental values obtained by Pashley²² with SFA measurements in the case of two mica sheets brought together in different ionic solutions. Compared to this data, the binding constants are defined as the inverse of the one we used in our treatment. Moreover Pashley is normally reporting the values of $p(K_{H_3O^+}^{-1})$ or $p(K_{M^+}^{-1})$ where M^+ is a general monovalent cation. Converting explicitly our data to the values used by Pashley²² we obtain a $p(K_{H_3O^+}^{-1})$ of 5.1 while he reported a value of 6.0 and a $p(K_{Rb^+}^{-1})$ of 4.1 while the reported ranges for different monovalent cations are from 3.0 to 3.5. Apparently we have an order of magnitude of difference between the values of $K_{H_3O^+}$ and K_{Rb^+} . Even taking into account the corrections for the cations concentrations at the surface (see Appendix) we cannot reconcile our data with the ones obtained by Pashley. In general we believe that this discrepancy is due to the higher degree

of confinement that induces an increase of the ions adsorbed at the surface of mica. This phenomenon, also known as charge regulation⁶⁰, is present, in principle even in the case of the AFM but the importance in SFA experiments is undoubtedly stronger.

The mechanical perturbation energies E_m^{AFM} were calculated using a value of $\alpha \approx 12$. This average value was obtained from the experimental measurements of k , ν and Q for the two types of cantilever in solution (see Eq. 3.9). We then calculated $E_{m,soft}^{AFM}$ using Eq. 3.12 for each bulk RbCl concentration studied. The results are presented in the Fig. 3.13 ($E_{m,stiff}^{AFM}$ is simply the same as $E_{m,soft}^{AFM}$ but multiplied by α and is hence not shown). The values obtained are statistically independent of the salt concentration, as expected. They are however less reliable at high (> 90%) and low (< 10%) where terms in the equations start to diverge. These terms would normally compensate each other in a perfect set of data. The $E_{m,soft}^{AFM}$ value given in Table 3.3 was obtained by averaging the results at each salt concentration (dashed line) in Fig. 3.13. These values are surprisingly small and only correspond to a fraction of the thermal energy for the softer cantilever. We note that, as for the Rb^+-Rb^+ correlation energy E_c , it is not necessary to know the unperturbed free adsorption energy $\Delta G_{Rb^+}^0$ of the ion to the mica in order to derive E_m^{AFM} .

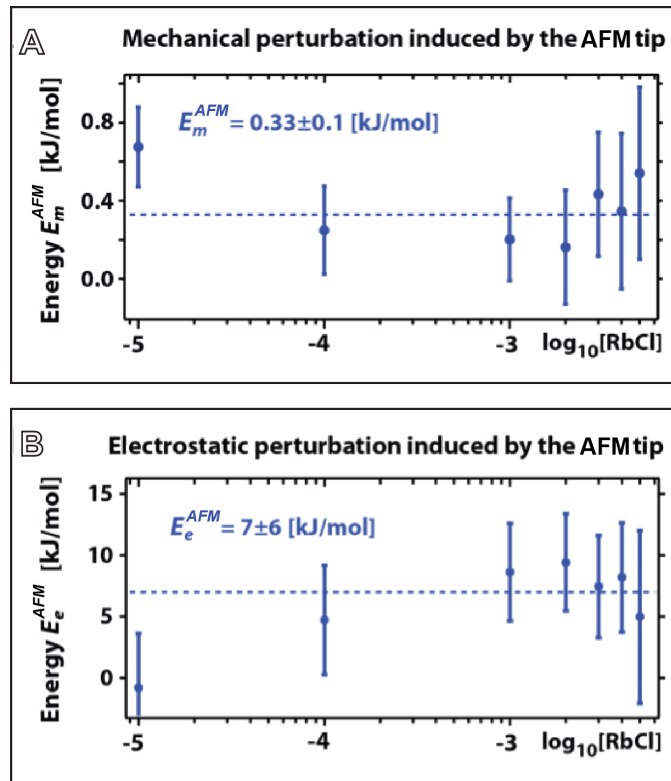


Fig. 3.13: Derivation of the mechanical E_m^{AFM} (A) and electrostatic E_e^{AFM} (B) perturbation energies for the soft cantilever at different RbCl salt concentrations. The values should be independent of the RbCl concentration and the average (dotted line) is therefore taken (Table 3.3). Since the convergence of the equations used to extract E_m^{AFM} and E_e^{AFM} is relatively poor away from the surface coverage transition ($\theta < 10\%$ and $\theta > 90\%$), the corresponding RbCl concentrations have not been taken into account in the averaging process. The E_m^{AFM} and E_e^{AFM} values for the stiffer lever are by definition 12 times larger.

The electrostatic perturbation energies E_e^{AFM} , presented in Fig. 3.13, were calculated from Eq. 3.12. In this case, it is necessary to know $\Delta G_{Rb^+}^0$, which appears explicitly in Eq. 3.12. We used the $\Delta G_{Rb^+}^0$ value derived from published RAXR experiments¹. As for the E_m^{AFM} calculations E_e^{AFM} was obtained separately for each salt concentration and averaged by putting more emphasis on the values corresponding to $0.1 < \theta_{Rb^+} < 0.9$. The resulting values (by definition identical for the softer and the harder cantilever) are given in Table 3.3. Despite the large uncertainty, the values

are clearly larger than the mechanical perturbation energies of the AFM tip and appear similar in magnitude to the correlation energies.

Perhaps the most interesting observation is the sign of the electrostatic perturbation energy, which indicates a repulsive interaction between tip and adsorbed ions. The opposite can be expected given the negative surface charge of the tip at the experimental pH^{58,59,65}. This suggests that it is not the actual tip dominating the imaging process, but rather the counterionic cloud around it.

Finally, for comparison, we calculated the Rb⁺ binding constant to mica using the uncorrected Langmuir isotherm (that is, imposing $E_c \equiv E_m^{AFM} \equiv E_e^{AFM} \equiv 0$). The binding free energy $\Delta G_{Rb^+}^0$ obtained are given in Table 3.3. The values substantially differ from that derived with RAXR, but the effect of the scanning tip has not been taken into consideration here. This last consideration further supports the validity of the correction procedure described in this section. It should however be pointed out that Langmuir fit does not capture satisfactorily the AFM data (Fig. 3.12) even when introducing E_m^{AFM} and E_e^{AFM} , and the introduction of a correlation energy provides a substantial improvement. Confinement effects may indeed render possible the AFM observations of correlations effect that would otherwise be difficult to capture; RAXR measurements did not detect any measurable correlation energy between Rb⁺ ions within experimental uncertainty¹.

3.7.4 Experiments with gold-coated tips

The effects of electrostatic and mechanical perturbations induced by the AFM tip were precisely quantified from the isotherm data. It is possible to vary the mechanical perturbation by changing the cantilever stiffness. Alternatively, the electrostatic perturbation can be modified by using tips composed by different material like for example metal-coated tip. Imaging with a metal-coated tip (here gold) is however far from trivial, first because the coating tend to get rapidly contaminated in ambient conditions, and secondly because the tip radius is considerably larger than for a standard silicon nitride tip (typically >20 nm radius). We used gold-coated Olympus RC800-PB (Olympus RC800 PB, Olympus, Tokyo) tips to ensure comparability with previous results. The tips/cantilever are identical to those used for the isotherm, apart for the gold coating. As expected, high-resolution imaging proved to be considerably more difficult to achieve than with the standard silicon nitride tips. Nevertheless, images such as those presented in Fig. 3.14 could be obtained.

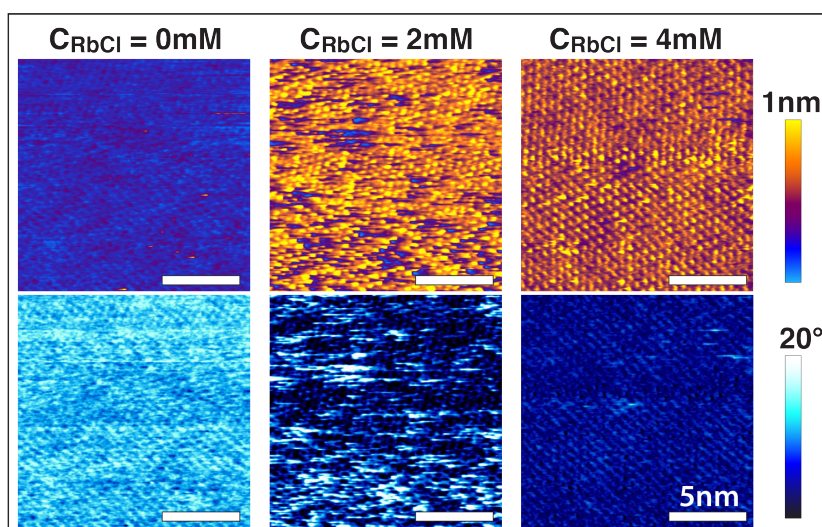


Fig. 3.14: AFM imaging of mica in RbCl solution obtained with a gold-coated tip. Correlation effects are visible at 2mM. At 4mM, the Stern layer appears fully formed.

The results confirm the build-up of an Rb⁺ layer on mica and provide a phase contrast consistent with our previous results obtained with silicon nitride tips. There is however one important difference: an almost complete Sayer layer can already be observed at 2mM. This is to be

expected due to the smaller electrostatic perturbation induced by the gold-coated tip; the tip has an overall negative surface charge⁶⁷⁻⁶⁹, but this charge is less important than for the silicon nitride tips and is delocalized in the metal. As a result, AFM results obtained with the gold-coated tip are less perturbative and hence closer to the X-ray reflectivity results^{1,22}. Interestingly, the effect of Rb⁺-Rb⁺ correlations is still visible at 2mM where vacancies tend to form rows or small islands.

Bibliography Chapter 3

1. Park, C., Fenter, P. A., Sturchio, N. C. & Nagy, K. L. Thermodynamics, Interfacial Structure, and pH Hysteresis of Rb⁺ and Sr²⁺ Adsorption at the Muscovite (001)–Solution Interface. *Langmuir* **24**, 13993–14004 (2008).
2. Bard, A. J. & Faulkner, L. R. *Electrochemical Methods*. (Wiley, 2000).
3. Wang, J. & Bard, A. J. Direct Atomic Force Microscopic Determination of Surface Charge at the Gold/Electrolyte Interface: The Inadequacy of Classical GCS Theory in Describing the Double-Layer Charge Distribution. *The Journal of Physical Chemistry B* **105**, 5217–5222 (2001).
4. Naji, A., Jungblut, S., Moreira, A. G. & Netz, R. R. Electrostatic interactions in strongly coupled soft matter. *Physics Applied to Biological Systems* **352**, 131–170 (2005).
5. Quesada-Pérez, M., González-Tovar, E., Martín-Molina, A., Lozada-Cassou, M. & Hidalgo-Álvarez, R. Overcharging in Colloids: Beyond the Poisson-Boltzmann Approach. *ChemPhysChem* **4**, 234–248 (2003).
6. Netz, R. R. & Orland, H. Beyond Poisson-Boltzmann: Fluctuation effects and correlation functions. *Eur. Phys. J. E* **1**, 203–214 (2000).
7. Cheng, H. & La Cruz, De, M. O. Rod-like polyelectrolyte adsorption onto charged surfaces in monovalent and divalent salt solutions. *Journal of Polymer Science Part B: Polymer Physics* **42**, 3642–3653 (2004).
8. Parsons, D. F., Deniz, V. & Ninham, B. W. Nonelectrostatic interactions between ions with anisotropic ab initio dynamic polarisabilities. *Colloids Surf., A* **343**, 57–63 (2009).
9. Ben-Yaakov, D., Andelman, D., Podgornik, R. & Harries, D. Ion-specific hydration effects: Extending the Poisson-Boltzmann theory. *Curr. Op. Col. Interf. Sci.* **16**, 542–550 (2011).
10. Leal, S. S., Botelho, H. M. & Gomes, C. M. Metal ions as modulators of protein conformation and misfolding in neurodegeneration. *Metal Ions in Neurodegenerative Diseases* **256**, 2253–2270 (2012).
11. Boström, M., Williams, D. R. M., Stewart, P. R. & Ninham, B. W. Hofmeister effects in membrane biology: The role of ionic dispersion potentials. *Phys. Rev. E* **68**, 041902 EP (2003).
12. Szekely, O. *et al.* The Structure of Ions and Zwitterionic Lipids Regulates the Charge of Dipolar Membranes. *Langmuir* **27**, 7419–7438 (2012).
13. Besteman, K., Van Eijk, K. & Lemay, S. G. Charge inversion accompanies DNA condensation by multivalent ions. *Nat Phys* **3**, 641–644 (2007).
14. Contera, S. A., Voitchovsky, K. & Ryan, J. F. Controlled ionic condensation at the surface of a native extremophile membrane. *Nanoscale* **2**, 222 (2010).
15. Heberle, J., Riesle, J., Thiedemann, G., Oesterheld, D. & Dencher, N. A. Proton migration along the membrane surface and retarded surface to bulk transfer. *Nature* **370**, 379–382 (1994).
16. Zakeeruddin, S. M. & Grätzel, M. Solvent-Free Ionic Liquid Electrolytes for Mesoscopic Dye-Sensitized Solar Cells. *Adv. Funct. Mater.* **19**, 2187–2202 (2009).
17. Netz, R. Electrofriction and Dynamic Stern Layers at Planar Charged Surfaces. *Phys. Rev. Lett.* **91**, 138101 (2003).
18. Dunn, S., Sharp, S. & Burgess, S. The photochemical growth of silver nanoparticles on semiconductor surfaces—initial nucleation stage. *Nanotechnology* **20**, 115604 (2009).
19. Agudo, E. R. & Putnis, C. V. Direct observations of mineral fluid reactions using atomic force microscopy: the specific example of calcite. *Mineral. Mag.* **76**, 227–253 (2012).
20. Ricci, M., Spijker, P., Stellacci, F., Molinari, J.-F. & Voitchovsky, K. Direct Visualization of Single Ions in the Stern Layer of Calcite. *Langmuir* **29**, 2207–2216 (2013).
21. Ricci, M., Spijker, P. & Voitchovsky, K. Water-induced correlation between single ions imaged at the solid-liquid interface. *Nat. Commun.* **5** SP, (2014).
22. Pashley, R. M. DLVO and hydration forces between mica surfaces in Li⁺, Na⁺, K⁺, and Cs⁺ electrolyte solutions: A correlation of double-layer and hydration forces with surface cation exchange properties. *Journal of Colloid and Interface Science* **83**, 531–546 (1981).

23. Pardhy, N. P. & Budhlall, B. M. Pickering Emulsion as a Template to Synthesize Janus Colloids with Anisotropy in the Surface Potential. *Langmuir* **26**, 13130–13141 (2010).
24. Parsons, D. F., Boström, M., Maceina, T. J. & Salis, A. Why Direct or Reversed Hofmeister Series? Interplay of Hydration, Non-electrostatic Potentials, and Ion Size. *Langmuir* **26**, 3323–3328 (2009).
25. Park, C., Fenter, P. A., Nagy, K. L. & Sturchio, N. C. Hydration and Distribution of Ions at the Mica-Water Interface. *Phys. Rev. Lett.* **97**, 016101 EP (2006).
26. Fukuma, T., Higgins, M. & Jarvis, S. Direct Imaging of Lipid-Ion Network Formation under Physiological Conditions by Frequency Modulation Atomic Force Microscopy. *Phys. Rev. Lett.* **98**, 106101 (2007).
27. Ferber, U. M., Kaggwa, G. & Jarvis, S. P. Direct imaging of salt effects on lipid bilayer ordering at sub-molecular resolution. *Eur Biophys J* **40**, 329–338 (2010).
28. Loh, S.-H. & Jarvis, S. P. Visualization of Ion Distribution at the Mica–Electrolyte Interface. *Langmuir* **26**, 9176–9178 (2010).
29. Schlegel, M. L. *et al.* Cation sorption on the muscovite (001) surface in chloride solutions using high-resolution X-ray reflectivity. *Geochimica et Cosmochimica Acta* **70**, 3549–3565 (2006).
30. Lee, S. S., Fenter, P., Nagy, K. L. & Sturchio, N. C. Monovalent Ion Adsorption at the Muscovite (001)–Solution Interface: Relationships among Ion Coverage and Speciation, Interfacial Water Structure, and Substrate Relaxation. *Langmuir* **28**, 8637–8650 (2012).
31. Lee, S. S., Fenter, P., Park, C., Sturchio, N. C. & Nagy, K. L. Hydrated Cation Speciation at the Muscovite (001)–Water Interface. *Langmuir* **26**, 16647–16651 (2010).
32. Kimura, K. *et al.* Visualizing water molecule distribution by atomic force microscopy. *J. Chem. Phys.* **132**, 194705 (2010).
33. Siretanu, I. *et al.* Direct observation of ionic structure at solid-liquid interfaces: a deep look into the Stern Layer. *Sci. Rep.* **4**, (2014).
34. Hembacher, S., Giessibl, F. J. & Mannhart, J. Force Microscopy with Light-Atom Probes. *Science* **305**, 380–383 (2004).
35. Kilpatrick, J. I., Loh, S.-H. & Jarvis, S. P. Directly Probing the Effects of Ions on Hydration Forces at Interfaces. *Multiple values selected* **135**, 2628–2634 (2013).
36. Voïtchovsky, K., Kuna, J. J., Contera, S. A., Tosatti, E. & Stellacci, F. Direct mapping of the solid-liquid adhesion energy with subnanometre resolution. *Nature Nanotechnology* **5**, 401–405 (2010).
37. Voïtchovsky, K. Anharmonicity, solvation forces, and resolution in atomic force microscopy at the solid-liquid interface. *Phys. Rev. E* **88**, 022407 EP (2013).
38. Voïtchovsky, K. & Ricci, M. High-resolution imaging of solvation structures with amplitude-modulation atomic force microscopy. in (Parak, W. J., Yamamoto, K. & Osinski, M.) **8232**, 82320O–8 (SPIE, 2012).
39. Lee, S. S., Fenter, P., Nagy, K. L. & Sturchio, N. C. Monovalent Ion Adsorption at the Muscovite (001)–Solution Interface: Relationships among Ion Coverage and Speciation, Interfacial Water Structure, and Substrate Relaxation. *Langmuir* **28**, 8637–8650 (2012).
40. Sakuma, H. & Kawamura, K. Structure and dynamics of water on Li⁺, Na⁺, K⁺, Cs⁺, H₃O⁺-exchanged muscovite surfaces: A molecular dynamics study. *Geochimica et Cosmochimica Acta* **75**, 63–81 (2010).
41. Argyris, D., Cole, D. R. & Striolo, A. Ion-Specific Effects under Confinement: The Role of Interfacial Water. *ACS Nano* **4**, 2035–2042 (2010).
42. Leng, Y. Hydration Force between Mica Surfaces in Aqueous KCl Electrolyte Solution. *Langmuir* **28**, 5339–5349 (2012).
43. Ho, T. A., Argyris, D., Cole, D. R. & Striolo, A. Aqueous NaCl and CsCl Solutions Confined in Crystalline Slit-Shaped Silica Nanopores of Varying Degree of Protonation. *Langmuir* **28**, 1256–1266 (2012).
44. Wander, M. C. F. & Shuford, K. L. Alkali Halide Interfacial Behavior in a Sequence of Charged Slit Pores. *J. Phys. Chem. C* **115**, 23610–23619 (2011).
45. Bourg, I. C. & Sposito, G. Molecular dynamics simulations of the electrical double layer on smectite surfaces contacting concentrated mixed electrolyte (NaCl–CaCl₂) solutions. *Journal of Colloid and Interface Science* **360**, 701–715 (2011).
46. Spagnoli, D., Gilbert, B., Waychunas, G. A. & Banfield, J. F. Prediction of the effects of size and morphology on the structure of water around hematite nanoparticles. *Geochimica et Cosmochimica Acta* **73**, 4023–4033 (2009).
47. Alcantar, N., Israelachvili, J. & Boles, J. Forces and ionic transport between mica surfaces: implications for pressure solution. *Geochimica et Cosmochimica Acta* **67**, 1289–1304 (2003).
48. Xu, L. & Salmeron, M. An XPS and Scanning Polarization Force Microscopy Study of the Exchange and Mobility of Surface Ions on Mica. *Langmuir* **113**, 17604–17607 (1998).

-
49. Luna, M., Rieutord, F., Melman, N. A., Dai, Q. & Salmeron, M. Adsorption of Water on Alkali Halide Surfaces Studied by Scanning Polarization Force Microscopy. *J. Phys. Chem. A* **102**, 6793–6800 (1998).
 50. Kendall, T. A. & Martin, S. T. Mobile ions on carbonate surfaces. *Geochimica et Cosmochimica Acta* **69**, 3257–3263 (2005).
 51. Impey, R. W., Madden, P. A. & McDonald, I. R. Hydration and mobility of ions in solution. *J. Phys. Chem.* **87**, 5071–5083 (1983).
 52. Jeffery, S. *et al.* Direct measurement of molecular stiffness and damping in confined water layers. *Phys. Rev. B* **70**, 054114 (2004).
 53. Lee, S. S., Fenter, P., Park, C., Sturchio, N. C. & Nagy, K. L. Hydrated Cation Speciation at the Muscovite (001)–Water Interface. **26**, 16647–16651 (2010).
 54. Fenter, P., Park, C., Nagy, K. L. & Sturchio, N. C. Resonant anomalous X-ray reflectivity as a probe of ion adsorption at solid–liquid interfaces. *Thin Solid Films* **515**, 5654–5659 (2007).
 55. Sakuma, H. & Kawamura, K. Structure and dynamics of water on muscovite mica surfaces. *Geochimica et Cosmochimica Acta* **73**, 4100–4110 (2009).
 56. Sakuma, H., Kondo, T., Nakao, H., Shiraki, K. & Kawamura, K. Structure of Hydrated Sodium Ions and Water Molecules Adsorbed on the Mica/Water Interface. **115**, 15959–15964 (2011).
 57. Bourg, I. C. & Sposito, G. Connecting the Molecular Scale to the Continuum Scale for Diffusion Processes in Smectite-Rich Porous Media. *Environ. Sci. Technol.* **44**, 2085–2091 (2010).
 58. Argyris, D., Ashby, P. D. & Striolo, A. Structure and Orientation of Interfacial Water Determine Atomic Force Microscopy Results: Insights from Molecular Dynamics Simulations. **5**, 2215–2223 (2011).
 59. de Beer, S., Otter, den, W. K., van den Ende, D., Briels, W. J. & Mugele, F. Can Confinement-Induced Variations in the Viscous Dissipation be Measured? *Tribol. Lett.* **48**, 1–9 (2012).
 60. Behrens, S. H. & Borkovec, M. Electrostatic Interaction of Colloidal Surfaces with Variable Charge. *The Journal of Physical Chemistry B* **103**, 2918–2928 (1999).
 61. Carney, R. P. *et al.* Electrical Method to Quantify Nanoparticle Interaction with Lipid Bilayers. *ACS Nano* **7**, 932–942 (2012).
 62. McLaughlin, A., Grathwohl, C. & McLaughlin, S. The adsorption of divalent cations to phosphatidylcholine bilayer membranes. *Biochimica et Biophysica Acta (BBA) - Biomembranes* **513**, 338–357 (1978).
 63. Israelachvili, J. N. *Intermolecular and Surface Forces*. (ELSEVIER, 2011).
 64. Frumkin, A. N. Electrocapillary curve of higher aliphatic acids and the state equation of the surface layer. *Zeitschrift für Physikalische Chemie* **116**, 466–470 (1925).
 65. Mezzasalma, S. & Baldovino, D. Characterization of Silicon Nitride Surface in Water and Acid Environment: A General Approach to the Colloidal Suspensions. *Journal of Colloid and Interface Science* (1996).
 66. Anczykowski, B., Gotsmann, B., Fuchs, H., Cleveland, J. P. & Elings, V. B. How to measure energy dissipation in dynamic mode atomic force microscopy. *Applied Surface Science* **140**, 376–382 **180**, 413–420 (1999).
 67. Maslova, M. V., Gerasimova, L. G. & Forsling, W. Surface Properties of Cleaved Mica. **66**, 322–328 (2004).
 68. Verma, A. *et al.* Surface-structure-regulated cell-membrane penetration by monolayer-protected nanoparticles. *Nature Materials* **7**, 588–595 (2008).
 69. Dougherty, G. M. *et al.* The zeta potential of surface-functionalized metallic nanorod particles in aqueous solution. *Electrophoresis* **29**, 1131–1139 (2008).

Chapter 4

Hydration correlation effect at the Stern Layer investigated at the single ion level

In this chapter, I will show how high-resolution AFM can not only describe the ionic distribution of water-immersed surfaces, but also detect important phenomena at the Stern Layer, that are otherwise undetectable and not considered in the classical description of the electrical double layer.

First, a summary of the standard Gouy-Chapman-Stern model that describes the electrical double layer will be presented (subsection 4.1.1). The assumptions necessary to obtain an analytical expression of the ionic charge distribution at the interface will be discussed and the limitations of this model will be presented with particular emphasis to phenomena that, although extremely relevant, cannot be described with the standard continuum model (subsection 4.1.2).

In the second section (section 4.2), I will show the first AFM observation of a new form of correlation energy that plays an important role in the Stern Layer lateral organization. The coverage analysis presented in Chapter 3 reveals an anomaly in the adsorption of some ionic species on the mica surface. By introducing an extra correlation energy term in the Langmuir adsorption model we could account for this unsuspected phenomenon. In section 4.2 I will present the MD-simulations showing that this correlation energy is dictated by the hydration landscape of the surface and of the ions. In the case of the highly hydrated negatively charged mica, I will show that some metal monovalent ions can spontaneously form ordered surface-structures. The structures are laterally stabilised only by water molecules with no need for specific interactions between the surface and the ions. We named this new form of correlation energy ‘hydration correlation energy’.

This correlation mechanism is controlled by the hydration landscape of both the surface and the adsorbed ions and is very general. In fact, I will show that it plays an important role even in other relevant surface phenomena such as OH⁻ terminated self-assembled monolayer on gold and lipid bilayers (section 4.3).

4. 1 Gouy-Chapman-Stern model: theory and limitations

4.1.1 Gouy-Chapman-Stern (GCS) model

If a surface with charge-density σ is in contact with a liquid (for example water) in which some ions are dissolved, the electrostatic potential will propagate into the liquid thus varying the mean ionic-density in the proximity. In particular, close to the surface, there will be an excess of oppositely charged ions (counterions) and a depletion of the same charged ones (co-ions). Given moderate surface potential and ionic strength, the GCS model can analytically describe the charge-density profile or the electrostatic potential in the vicinity of the surface.

In this model a dense monolayer of counterions, the so-called Stern or Helmholtz layer (hereafter called Stern layer) is considered as adsorbed onto the surface of the solid (see Fig. 4.1). Since the ions have a finite size and cannot approach the surface any closer than the ionic radius (hydrated or not, depending on the surface and the ions) we can define a plane of closest approach for the centers of the ions at a distance x_2 (see Fig. 4.1) called the *Outer Helmholtz plane* (OHP). As firstly suggested by Gouy and Chapman independently, at a distance $x > x_2$, there is a diffuse layer of ions that obeys the Poisson-Boltzmann (PB) equation. This equation links the electrostatic potential $\phi(x)$ in a liquid of dielectric constant ε to the ionic density of charge $\rho(x)$, presenting, as expected from statistical mechanics, a Boltzmann distribution:

$$\frac{d^2\phi(x)}{(dx)^2} = -\frac{1}{\varepsilon \varepsilon_0} \rho(x) = -\frac{e}{\varepsilon \varepsilon_0} \sum_i n_i^0 z_i e^{-\frac{z_i e \phi(x)}{k_B T}} \quad (4.1)$$

In equation 4.1, ε_0 is the vacuum permittivity, e is the electron charge, z_i is the signed charge of the ionic species i with a bulk concentration (away from the surface) n_i^0 , k_B is the Boltzmann constant and T the absolute temperature.

For a symmetrical electrolyte (i.e. the absolute value of z is equal for cations and anions) we can obtain the following equation imposing to Eq. 4.1 the electrostatic potential $\phi(x)$ and the derivative $\frac{d\phi(x)}{dx}$ to be 0 far from the surface ($x \rightarrow \infty$):

$$\frac{\tanh\left(\frac{z e \phi(x)}{4 k_B T}\right)}{\tanh\left(\frac{z e \phi(x_2)}{4 k_B T}\right)} = e^{-\kappa(x-x_2)} \quad \text{for } x > x_2 \quad (4.2)$$

where $\phi(x_2)$ is the electrostatic potential at the OHP and κ , known as the inverse of the Debye Length, is defined as:

$$\kappa = \sqrt{\frac{2 n^0 z^2 e^2}{\varepsilon \varepsilon_0 k_B T}} \quad (4.3)$$

In the case of $\phi(x_2)$ sufficiently low, Eq. 4.2 can lead to an exponential decaying potential with a typical decaying length of $1/\kappa$.

$$\phi(x) = \phi(x_2) e^{-\kappa(x-x_2)} \quad \text{for } x > x_2 \quad (4.4)$$

Eq. 4.4 is known as Debye-Hückel equation. Eq. 4.4 applies to symmetrical electrolyte solutions. Grahame has derived equations that apply to asymmetrical electrolytes and for low $\phi(x_2)$ they all reduce Eq. 4.4 but now the Debye Length $\tilde{\kappa}$ is more generally defined as:

$$\tilde{\kappa} = \sqrt{\sum_i \frac{n_i^0 z_i^2 e^2}{\varepsilon \varepsilon_0 k_B T}} \quad (4.5)$$

where now z_i and n_i^0 are respectively the valence and the bulk concentration of the ionic species i in solution.

Before the OHP ($0 < x < x_2$) the model assumes a null charge-density. This implies that the potential profile in the compact layer is linear and the total potential drop across the double layer is:

$$\phi(0) = \phi(x_2) - \left. \frac{d\phi(x)}{dx} \right|_{x=x_2} x_2 \quad (4.6)$$

where $\phi(0)$ is the surface potential (we set at the beginning $\phi(\infty)$ to zero). The model is summarized in Fig. 4.1. Once the potential $\phi(x)$ is obtained the density of charge $\rho(x)$ can be extracted using the PB equation.

For a complete and detailed description of the model please refer to the book of Bard & Faulkner¹ or to the book of Israelachvili².

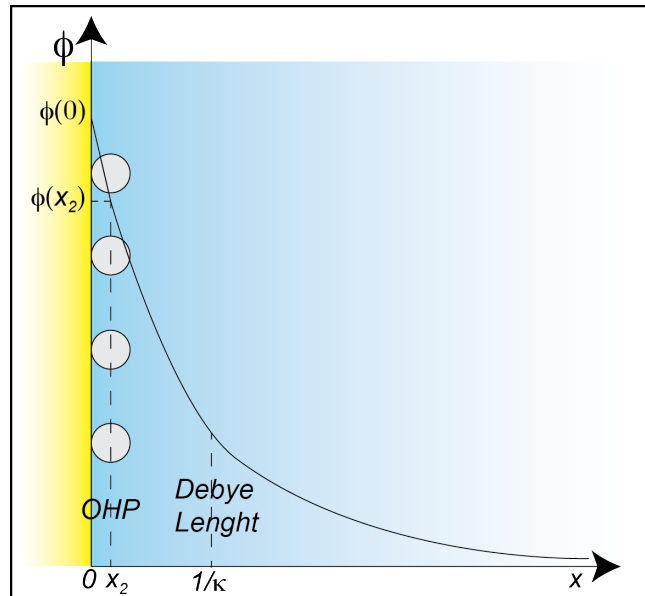


Fig. 4.1: Schematic representation of the GCS model. On the y-axis the electrostatic potential as a function of the distance x (x -axis) from the surface. The OHP is defined as the closed approach for the centers of the ions.

Pressure between two charged surfaces

The standard way to measure the effect of the electrostatic double layer is to measure the pressure between two charged surfaces. This conformation allows numerous situations that mainly depend on the charge of the surfaces and the relative distance D .³ The PB equation is still valid but the specific situation will give different boundary conditions that can lead to different solutions for both ionic distribution and pressure.

In the standard case of symmetric surfaces (same charge, same sign) the first boundary condition follows from the symmetry requirement that the field must vanish at the midplane and the second boundary condition follows from the requirement of overall electroneutrality—that is, that the total charge of the counterions in the gap must be equal (and opposite) to the charge on the surfaces. If the distance D between the two surfaces is infinite the same ionic distribution of the GCS has to be obtained. The interaction pressure between two identically charged surfaces in an electrolyte solution can be derived quite simply as follows. At any point x in the gap between the two surfaces at distance D the pressure $P_x(D)$ is given by:

$$P_x(D) = k_B T \left[\sum_i \rho_i^m(D) - \sum_i \rho_i^m(\infty) \right] \quad (4.7)$$

where $\rho_i^m(D)$ is the ionic concentration of the ionic species i at the midplane ($x = D/2$) when the two surfaces are at distance D and $\rho_i^m(\infty)$ correspond to what was previously called n_i^0 , the bulk concentration of the electrolyte species i . The pressure acting on the electrolyte ions and on the surfaces across the gap is uniform (independent of position x). The above result shows that P is simply the excess osmotic pressure of the ions in the midplane (or equivalently at the surfaces²). The problem then reduces to finding the midplane concentration of ions $\rho_i^m(D)$ when D is finite. Here certain assumptions have to be made to obtain an analytic result. A proper treatment of the specific situations that involve some approximation on the type of ions and the potential $\phi(m)$ intensity at the midplane can be found in Ref. [2]. Most of the analytical expressions are accurate only for surface separations bigger than at least one Debye length. At smaller separations the numerical solutions of the Poisson-Boltzmann equation has to be implemented to obtain the exact interaction potential for which there are no simple solutions that cover all possible situations. Generally two limiting cases are considered: the constant charge and constant potential limit. These two limits correspond in setting as boundary condition a constant charge in x_2 or constant potential $\phi(x_2)$.³ In both cases it is assumed that the surface charge density remains constant and that there is no ion binding. This is not true and often it is observed that the counterions bind at the surface as D decreases. This process is generally called charge regulation. The effect is that experimentally P falls below this limit, and the PB equation must now be solved self-consistently by including the dissociation constants of the adsorbing ions (see section 4.1.2). So long as the Poisson-Boltzmann equation remains valid, the double-layer forces between two symmetrical charge-regulating surfaces always lie between the constant surface charge and constant surface potential limits. When the PB equation breaks down or when other forces, such as ion-correlation forces (see section 4.1.2), are present, then the resulting interaction can be very different. Even in the charge-regulating framework, it is assumed that while the two surfaces approach one another there is a continual exchange of ions with the bulk reservoir. In reality if the process is fast, thermodynamic equilibrium may not be reached at each distance D . This out-of-equilibrium situation is not only determined by the diffusion of ions into and out of the interaction zone but also by the ion-exchange processes at the interfaces that can be slow (minutes) and becomes the rate-limiting part of the overall interaction. Labuda *et al.* proposed these hysteretic ion dynamics as another plausible damping mechanism at the solid-liquid interfaces.^{4,5}

4.1.2 Gouy-Chapman-Stern (GCS) Model: limitations and examples of phenomena not accounted

The implicit assumptions used in the GCS model are the following:

1. The ions are considered as point charges that can be described as a continuum density of charge $\rho(x)$. The only “size effect” of the ions is introduced with the concept of OHP.
2. The liquid is a continuous media represented in the entire model by the constant (in space) dielectric constant ϵ .
3. The surface is a homogeneous charge distribution and in fact all the equations lead to the dependence of the potential or the charge density from the distance x from the surface.

Due to the assumptions listed above this model, still widely used, cannot account for a series of phenomena that arise mainly from the finite size of the constituents of the system (surface, solvent molecules and ions). These phenomena, even though happening at the nanoscale, can have significant effects like the charge inversion of the surface, as reported, for example, in the case of DNA molecules in the presence of multivalent ions⁶. Hereafter, I first describe some of the effects that deviate significantly from the standard GCS description and some proposed modification of the theory that can account for these deviations.

The dielectric constant of the media is not constant

The first improvement to the GCS considers the variation of the dielectric constant at the solid-liquid interface. We have already seen in Chapter 1 that a surface alters both the hydrogen-bonding network and the mean orientation of the water molecules thus changing how the interfacial water reacts to an electric field in comparison to the bulk. The easiest way to take into account these solvent effects is generally to introduce a modified value of the dielectric constant depending on the distance from the surface (but decaying rapidly to the bulk values as the 1-2 hydration shells are overcome). The closer the distance from the surface, the lower the value of the dielectric constant of the interfacial water is. In reality, as pointed out by Gruen *et al.*⁷ the concept the dielectric constant is not applicable at the microscopic level: there is no general fixed local relation between applied external electric field and molecular which spatial variation is simply determined by overall minimization of the free energy. Once this is achieved, the spatial distribution of the dielectric constant can be inferred⁷. We will see, for example in the next sections, that not only the presence of the surface can locally modify the dielectric properties of the water molecules but even the density of the ions affects the dielectric constant of the medium. Moreover, this effect is specific to the ionic species and the interaction they have with the solvent molecules. If we want to maintain a continuum approximation, the PB equation should be modified by introducing, not only a spatially dependent dielectric constant but also an ionic density dependent dielectric constant.

Specific ion adsorption (IHP)

From the current state of theoretical and experimental studies, it is clear that ion-specific effects are due to the interplay between the ion-ion, ion-solvent, and ion-surface interactions, taking into consideration both electrostatic and non-electrostatic interactions. However, which physical and chemical properties of the solutes and solvent determine these specific interactions remain unclear.⁸

A common example is the specific ion adsorption on surfaces that cause a variation of the apparent surface charge generally measured experimentally with electrophoretic and force measurements. This adsorption process, often referred to as ‘chemical’ interaction, occurs when some ionic species in solution interacts ‘specifically’ with the surface. The mechanism of interaction is unexplained, but simpler models are employed to contemplate the unexpected variation of the surface charge. In this case an extra inner layer of ‘special’ counterions are bound to the surface of the solid and act as potential or charge determining ions. This layer determines the inner Helmholtz plane (IHP) and was first proposed by Grahame in 1947⁹. After this first layer, the counterions follow the GCS model. The density of ions in the IHP can be described generally by some adsorption equations (we used for example the Langmuir isotherm in our work) that determine the effective charge of the surface and generally derive a binding constant of the ions at the surface. In this situation the Stern Layer should be composed of both specifically and non-specifically interacting ions defining the OHP (sometimes called hydrated ions) although this distinction is often not clear¹⁰.

This widely used model has, in my opinion, brought lot of confusion in the community and specifically on the location of the OHP with respect to the surface and the match between the concept of OHP and electro-kinetic measurements. Moreover, common improper use of the terminology often generates confusion.¹¹ The problems usually derive from the need of matching discrete microscopic concepts (ion-size, solvent molecules, etc.) and a continuum description.

To identify which ions are specifically interacting with the surface, Lykema¹¹ proposes to look at the point of zero charge (*p.z.c.*), the pH at which the surface is uncharged. This quantity plays a role only for amphoteric surfaces, such as oxides. For non-specifically interacting electrolytes the *p.z.c.* is independent of electrolyte concentration, but for electrolytes containing ‘chemically’ adsorbing cations/anions, it shifts to higher/lower pH values. This ‘specificity’ has not yet been chemically or physically described along with the nature of the surface-bound species. According to Lykelma¹¹: “By ‘specific’ is understood: adsorption by non-coulombic forces, i.e. not accountable by PB theory. Such forces include the formation of a chemical bond, a hydrogen bridge, complex formation at the interface, hydrophobic bonding and other water structure-

mediated interactions.” Chemical aspects regarding the formation of a covalent or ionic bond between the ionic species and the surface groups cannot be discussed in a general picture. The water-mediated interactions, though, have been extensively explored and will be presented in the next section.

Specific ion-water and water-surface interaction: the Hofmeister series.

In the classical GCS model the interaction-specificity between ion-ion, ion-water, ion-surface and water-surface are not considered. Deriving a general analytical model that takes these interactions into account is particularly challenging.

The first interest in ion-specific effects dates back to the end of the 19th century, when Franz Hofmeister and co-workers measured the thermodynamic properties of protein precipitation in various salt solutions. They tested numerous salt species and found that protein solubility can be changed according to ionic content. This classification of cations and anions is known today as the *Hofmeister series*.⁸ Theoretical treatments offer a variety of perspectives regarding the origin of the ion-specific effects.

The first commonly used explanation to this ionic-specific effect was first proposed by Gurney¹² and then extensively used by Collins¹³ in a more biophysical contexts. Electrolytes dissolved in water dissociate into ions that are hydrated. The large electric field around the (smaller) ions causes the dipolar water molecules to rearrange themselves in the hydration shells around them with structures differing from that in bulk water. The ionic field causes the water in the hydration shell to have a larger mean density than pure water and a different average orientation. The idea of Gurney was that different ions could affect the structure of the water network in different ways. In particular they can induce an ordered (kosmotropic ions) or disordered (chaotropic ions) water layer around them. The actual ‘order’ in terms of physical parameter is still under debate and in particular a clear quantitative definition of the structure of water is not well accepted yet.¹⁴ The average number of hydrogen bonds, water molecule rate of exchange, dipole orientation correlation parameter and molar entropy of the water molecules in the hydration shell with respect to bulk water (far from the ions) were considered and are important to define the local ‘structure’ of a liquid.¹⁴ Also, the distance-range in which ions exert any influence in aqueous solutions has not yet been settled. First, hydration shells exist around most ions, even large monovalent ions, and well-defined second hydration shells are commonly found around ions with higher charge. Beside a general disagreement on the definition, the physical phenomenon itself, i.e. the specific modification of the local properties of the water structures around ions, has been demonstrated beyond any doubt.

Since the publication of Gurney’s book¹², the concepts of ‘structure making’ and ‘structure breaking’ ions and the effects they have on the water molecules, have been generally accepted and applied to the explanation of a variety of phenomena exhibited by electrolyte solutions. Collins¹³ presented a simple and convincing explanation for the famous Hofmeister effect based on the concept of chaotropes/kosmotropes ions, known as the ‘concept of matching water affinities’. To explain the different types of interaction, Collins makes the assumption that two strongly hydrated small ions of opposite charge experience a very strong reciprocal attraction. Consequently, they can come together forming direct ion pairs and expelling the hydration spheres between them. In the case of weakly hydrated ions, the situation is different, but the result is the same: the hydration spheres are so loosely bound that the chaotropic ions can also form direct ion pairs expelling the hydration water between them. The interaction between a kosmotrope and an oppositely charged chaotrope ion is then straightforward: the attraction by the soft ion is not strong enough to free the hard ion from the hydration shell. As a consequence, a chaotrope/kosmotrope ion pair should always be separated by water and cannot form strong ion pairs. This concept is a particular application of the more general rule ‘like seeks like’ that often can be applied in chemistry and can be in principle extended to solid hydrated surfaces.¹⁵ This model, although quite simplistic, provides a first indication of the different interactions experienced by ions with the same net charge in water. Qualitatively it often provides an accurate explanation for the observed experimental data, but it has to be applied with caution.

Recently, dispersion interactions depending on the polarizability of the ions have been proposed to provide the missing link between ionic profiles and ion-specific interactions. The static dielectric function of an electrolyte solution is generally found to be smaller than that of the pure solvent.⁸ This decrement of the dielectric constant has been attributed to various sources, which underlie the changes in the dielectric response of the solution. The most important ones are the ionic polarizability and the hydration shell. Each ion in an aqueous solution creates a cavity and displaces one or several water molecules in the process. Because the ions usually have smaller static and dynamic polarizabilities than water, they lower the dielectric response of the solution. The dielectric decrement in aqueous electrolytes is also connected to the structural modification of the water molecules' network in the ionic vicinity, due to large electrostatic fields emanating from the dissolved ions.⁸ Phenomenological modifications of the standard PB theory have been proposed to take into account the effect of the counter-ion concentration on the local dielectric constant.⁸ For example, one approach is to introduce in Eq. 4.1 a dielectric constant that depends linearly on the ionic density through a salt specific phenomenological coefficient. In this way not only the variation of the dielectric constant is considered but even a degree of specificity is introduced.⁸

Beyond the effect on the dielectric constant, ions are themselves polarizable, and therefore interact with water and interfaces through van der Waals (dispersion) forces, which are ion specific. In addition, ions are not point-like particles and also interact via steric interactions, which depend on the effective ionic radii.¹⁶ Parsons *et al.*¹⁷ believes that the key for ion-specific effects rely on the starting point for classical theories: namely the *ansatz* separating electrostatics from dispersion forces acting on ions is too drastic an approximation. They propose to modify the Boltzmann factor of Eq. 4.1 by introducing the total potential $U(z)$ that contains both the dispersion and the electrostatic contributions.¹⁷ The model, even if more accurate, relies on values of non-electrostatic dispersion potential extracted from simulations (generally *ab initio* quantum chemistry), which is complex to implement. Interestingly Parson *et al.*¹⁷ attributes the secondary hydration force (see Chapter 1) between two surfaces to the ionic dispersion forces. They state that once these contributions are included, a longer range, 'secondary hydration force' appears.

The singular effect of ion correlation and condensation

Charge reversal is the classical manifestation of what is normally attributed to correlation effects of ions. However, even specific ion adsorption can explain this phenomenon.¹⁸ The terms "overcharging", "charge reversal", and "charge inversion" are often synonymous and refer to situations in which an electric double layer, if studied electrokinetically, or if inferred from interaction studies, appears to contain more countercharge than needed to compensate the surface charge.¹¹

There are several physical possibilities for this process to manifest itself. One possible explanation is specific ionic effects, as mentioned in the previous sections, where ions bound to the surface can induce a variation of the effective surface charge.¹¹ The second possible explanation is ion correlation/ion condensation at the surface of the solid.¹⁹ In principle the two can coexist but they have to be considered carefully, particularly in case of charge regulation.¹¹

Naji *et al.*²⁰ offers an explanation of the possible correlation-condensation effects which depends on the coupling strength of the system: low coupling strengths in a high-temperature regime and high coupling strengths in the low-temperature regime. In general, to determine the regime of the system it is important to consider the typical interaction lengths of the columbic forces between the different components of the systems when compared to the thermal energy.

The Coulombic interaction energy $V(r)$ between counterions defines the well-known Bjerrum length l_B that measures the distance at which two elementary charges interact with thermal energy $k_B T$:

$$\frac{V(l_B)}{k_B T} = 1 = \frac{q^2 e^2}{l_B 4 \pi \epsilon \epsilon_0 k_B T} \rightarrow l_B = \frac{q^2 e^2}{4 \pi \epsilon \epsilon_0 k_B T} \quad (4.8)$$

where q is the valency of the counterions, e the elementary charge, r the distance between the counterions, ε_0 the vacuum permittivity and ε the dielectric constant of the medium. The Coulombic interaction energy between the charged surface and the counterions in solution defines the famous Gouy–Chapman length μ , which measures the distance at which the thermal energy equals the counterion–wall interaction energy $U(z)$:

$$\frac{U(\mu)}{k_B T} = 1 = \frac{\mu q e^2 \sigma_S}{2 \varepsilon \varepsilon_0 k_B T} \rightarrow \mu = \frac{2 \varepsilon \varepsilon_0 k_B T}{q e^2 \sigma_S} = \frac{q}{2 \pi l_B \sigma_S} \quad (4.9)$$

The dimensionless ratio Ξ between these two quantities l_B and μ is relevant and describes the physical regimes of the system:

$$\Xi = \frac{l_B}{\mu} = 2 \pi q \sigma_S l_B \propto q^3 \quad (4.10)$$

Ξ is known as the electrostatic coupling parameter. For a small coupling parameter $\Xi \ll 1$ (weak coupling or WC regime), the counterion–wall system has a relatively large Gouy–Chapman length (or small Bjerrum length), which indicates a loosely bound counterion cloud at the charged wall. For a large coupling parameter $\Xi \gg 1$ (strong coupling or SC regime), the Gouy–Chapman length is relatively small (or the Bjerrum length is large) indicating that counterions are strongly attracted toward the charged wall.^{20,21}

Further insight into the structure of the counterionic layer may be obtained by considering the typical distance between counterions at the surface. The mean lateral area per counterion is determined by the surface charge density σ_S and defines a length scale a_\perp associated to the local electroneutrality condition:

$$\pi a_\perp^2 = \frac{q}{\sigma_S} \quad (4.11)$$

This distance can be expressed in terms of Ξ :

$$\frac{a_\perp}{\mu} = \sqrt{2 \Xi} \quad (4.12)$$

For small coupling strength, it is possible to employ the mean-field approximation to describe the counterionic layer since each counterion interacts with a diffuse cloud of similar ions. The mean-field PB theory is obtained in the exact limit of $\Xi \rightarrow 0$. This regime is adequate for low valency counterions and/or weakly charged surfaces and represents the physical situation in which the width of the counterion layer close to the oppositely charged surface is much larger than the separation between two neighboring counterions in the layer (see Eq. 4.10). Thus the counterion layer behaves essentially as a three-dimensional gas and a collective mean-field approach of the PB type is justified.^{20,21}

On the other hand, the SC regime is appropriate for high valency counterions and/or highly charged surfaces (see Eq. 4.10). In this situation the PB equation is no longer valid, the lateral distance between ions is larger than the separation they have from the wall (see Eq. 4.12) and thus the layer is essentially flat and two-dimensional. The counterions are highly localized laterally and form a strongly correlated quasi-two-dimensional layer right next to an oppositely charged surface. The structure of such layer is dominated by mutual repulsions between counterions, which freeze-out lateral degrees of freedom. Hence counterions become laterally correlated and surrounded by a large correlation hole of size a_\perp from which neighboring counterions are statistically depleted. Strong coupling parameters decrease the effect of the wall over the mutual ion-ion interaction.

As pointed out by Kjellander *et al.*²² for moderately low ion concentrations and fairly small ionic radii, but still a non null value of Ξ , the ion-ion correlation can be described as a local reduction in the average ion density around each ion due to the electrostatic repulsion between them.

Consequently, compared to the PB theory prediction, more ions are allowed closer to the walls, because the region between each ion and the closest wall is, on average, depleted of other ions. Ionic gathering close to the walls leads to a concentration decrease in the diffuse layer. If the pressure between two approaching surfaces is measured, the ion depletion at the midplane causes a less repulsive contribution to the interaction force (supposing two identical surfaces).²² This effect can be described in terms of ‘ion condensation’ in the electrical double layer and can be treated by a model in which the surface charge is considered as an ‘effective surface charge’, smaller than the actual charge on the electrode because of the condensed ionic counter charge. Often the confusion between the correlation effect and specific ion adsorption resides on the variation of effective surface charge, which without proper investigation can be interpreted as both correlation effect and specific ion adsorption.

In conclusion, this section showed that different theoretical approaches have been developed to explain the interactions between surfaces, ions and water molecules. However, this field lacks direct experimental data to understand the processes and ion dynamics at the Stern Layer where all the continuous assumptions are no longer valid.

4.2 The example of Mica: the new concept of hydration correlation

As seen in the previous chapter we used the surface of mica to explore the effect of ions in the AFM imaging process. We found a good match between what appeared as protrusions on the mica surface in the AFM images and the actual ionic coverage obtained with X-ray reflectivity²³. This indicated a direct correlation between a protruding feature and a single ion on the surface of mica. Hereafter the single protrusions in the AFM images will be referred to as ions. By varying the bulk ionic concentration of RbCl we were able to obtain a trend in terms of coverage vs. bulk concentration that could be fitted with the Frumkin model (see section 3.6). Interestingly, we had to add an attractive correlation between the ions on the mica surface to describe our experimental data. In this section I analyze first the effect of this correlation energy in terms of distribution of the ions at the mica surface. Then I present the MD-simulations performed by Peter Spijker that provided us an explanation of the mechanism of ion-ion correlation. I will conclude with the effect of other monovalent cations on the mica surface.

4.2.1 Statistical analysis of the ionic distribution at the mica surface

In order to directly and objectively assess the presence of ion-ion attractive correlations in the AFM images, as found in the previous chapter with the Frumkin model, we conducted a systematic, automatized analysis of the images that establishes the number of nearest neighbours (n_{nn}) for each adsorbed ion. In the presence of attractive correlations (as modelled in the Frumkin isotherm) between adsorbed ions, we expect to observe an increased value of n_{nn} when compared with an identical situation without correlations (random ions adsorption at a same ionic coverage). We therefore compare the nearest neighbours’ distribution functions n_{nn}^{AFM} derived from AFM images with that derived from computer-generated images of random ion distributions n_{nn}^{random} on an identical lattice and with the same density coverage. An example of the analysis procedure is presented in Fig. 4.2.

Based on a Fast Fourier Transform (FFT) of the raw AFM phase image (Fig. 4.2A), the underlying mica lattice is identified (Fig. 4.2B). This is achieved by filtering the 2D FFT of the image to retain only the maxima corresponding to the two lowest frequencies. The filtered spectrum is then back transformed (inverse FFT) into real space yielding the reference lattice. This approach, although reliable, does not take into account local distortions of the image (e.g. due to irregular drift) and the resulting lattice is perfect by construction. To mitigate any discrepancy between the lattice in the raw image and that of the reference lattice, the latter is automatically aligned (in real space) with the raw image to best match adsorbed ions with reference lattice points. Ions are then identified in the raw image using a thresholding approach, and subsequently associated to the nearest reference lattice point, if they are within a distance of

$0.6d$ where d is the smallest lattice parameter. Protrusions located further than $0.6d$ from any reference lattice point are discarded. The thresholding relies on the clear signature of the adsorbed ions in the phase images where they can be associated with a local minimum. The threshold value is typically set between 3 to 4 standard deviations of the average phase value, depending on the ionic density on the surface. This threshold is rather conservative and at times excludes ions, but it ensures no false positive for artificial features or noise. The results of this automated procedure applied to Fig. 4.2A are visible in Fig. 4.2C showing all coordinates of the ions in the reference lattice. A direct comparison between the raw data and the identified ions can be seen in Fig. 4.2D, showing the high reliability of the program except for some minor deviations near the edges of the figures due to local drift in the raw image. Significantly, these distortions should not affect the results of the analysis.

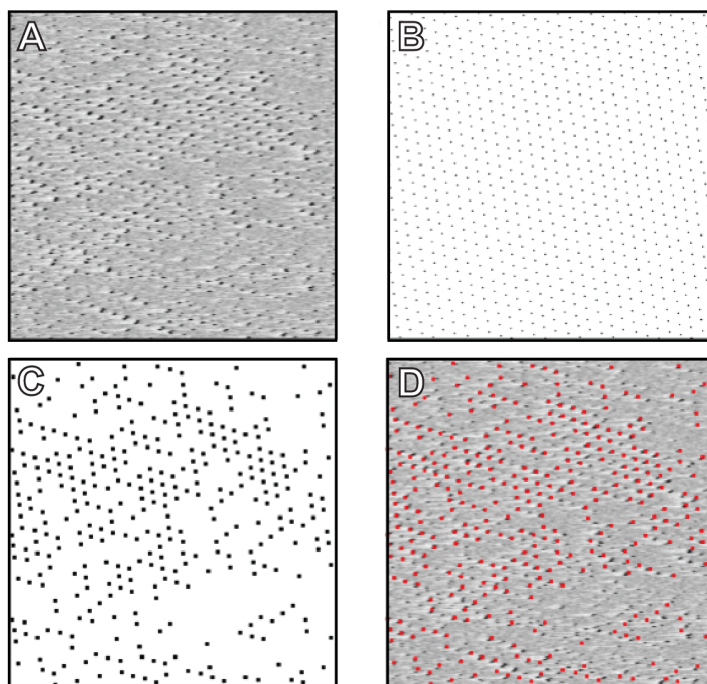


Fig. 4.2: Example of statistical analysis of an AFM image. In the raw phase image (A), the ions appear as dark spots aligned on a lattice. A reference lattice (B) can be constructed from the FFT of the raw image and used to identify the ions by thresholding (C). A superimposition (D) of the raw image with the identified ions (in red) confirms the attribution. The image size is 15 nm in both directions. The ions have been enlarged in (C) and (D) for better visibility.

Once the position of each ion on the reference lattice is known, a simple routine counts the number of nearest neighbours (excluding cells at the edges) and creates a n_{nn}^{AFM} statistical distribution function (Fig. 4.3A). The same analysis can be applied to a randomly generated ion distribution based on the same reference lattice and at identical surface coverage (Fig. 4.3B). Averaging n_{nn}^{random} over 50 of such ‘random ionic distribution’ images creates a robust reference to be compared with n_{nn}^{AFM} (Fig. 4.3A).

The results show that adsorbed ions in the AFM image tend to have more nearest neighbours than ions adsorbed randomly on an identical lattice. This induces a shift of the n_{nn}^{AFM} distribution towards a larger number of neighbours (see in Fig. 4.3A).

The same trend was observed to a different extent in more than 20 analysed AFM images, and over all the ionic concentrations (2mM, 3mM and 4mM) where the Stern layer is only partially full. More examples are presented in Fig. 4.4.

In order to establish the statistical significance of the trend presented above, an analysis of variance (ANOVA) was conducted on the difference between n_{nn}^{random} and n_{nn}^{AFM} for each of the selected AFM images. For a given image, n_{nn}^{AFM} was subtracted from n_{nn}^{random} for each of the randomly generated structures. Under the null hypothesis (n_{nn}^{random} and n_{nn}^{AFM} are equivalent), the resulting residual series for each number of nearest neighbours (0 to 6) should be statistically identical. A one-way ANOVA analysis was hence conducted on the residuals series and

consistently found a statistically significant difference between the series ($F/F_{\text{crit}} > 10$) for a 99% confidence level ($p < 0.01$).

With this analysis we concluded that the Rb^+ ions at the surface of mica experimentally have an attractive correlation energy that systematically translated to a higher number of nearest neighboring ions.

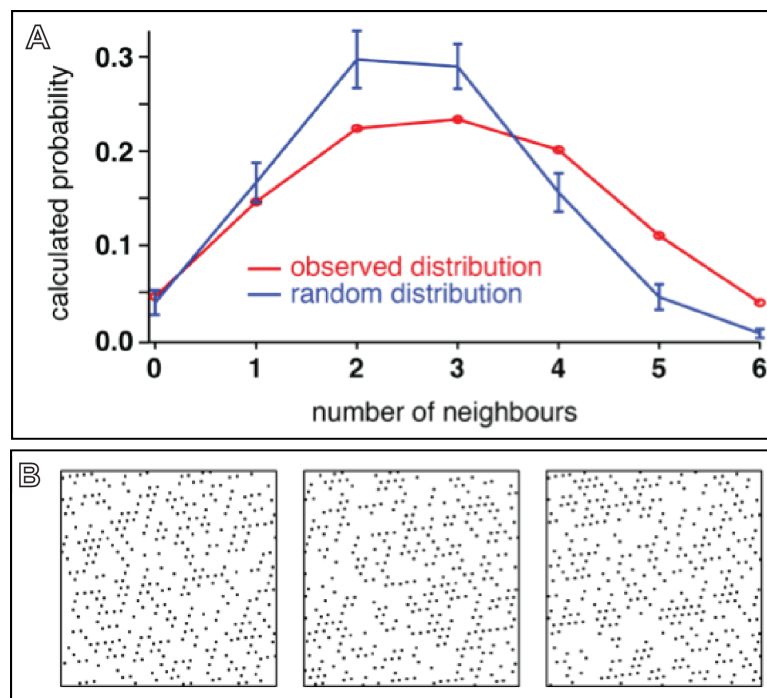


Fig. 4.3: (A) Nearest neighbour statistical distribution probability calculated for the AFM image presented in Fig. 4.2A. The random distribution probability was calculated from 50 images such as presented in (B), based on the same lattice as the AFM image, and assuming the observed 41.7% sites occupancy. The error bars in the n_{nn}^{random} distribution in (A) represents two standard deviations.

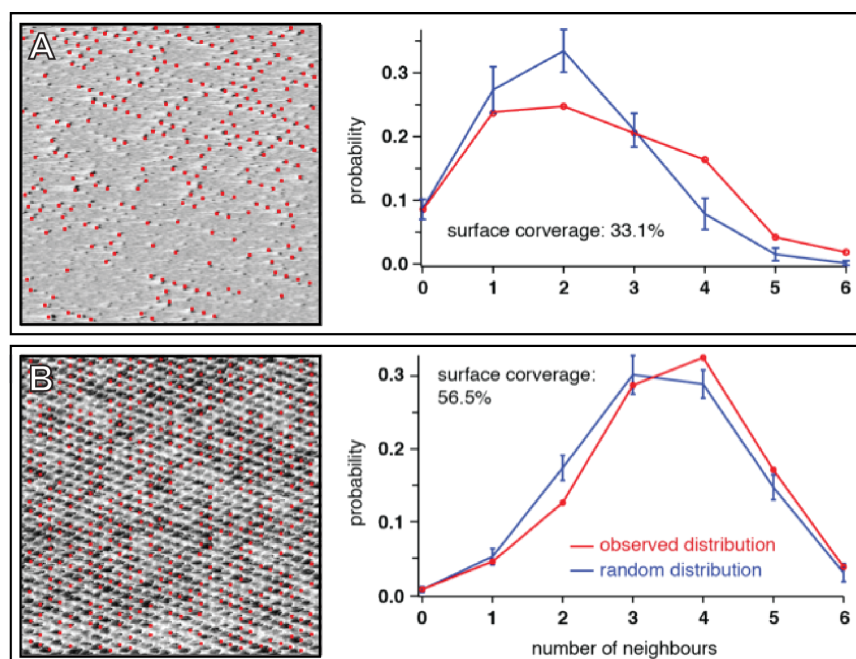


Fig. 4.4: Statistical analysis of the ion distribution in AFM images. (A) Analysis of the image obtained in 2mM RbCl bulk ionic concentration. (B). Example of analysis at 4mM. The image, acquired with a different tip than (A), shows a slightly different contrast but remains consistent with the results. Both images are phase images with XY size of 15 nm.

4.2.2 MD-simulations and the concept of hydration correlation energy

This correlation can have two possible origins, either direct electrostatic interactions between adsorbed ions or hydration effects. Electrostatic correlations are known to play an important role in systems with high charge density^{24,25} such as multivalent ions on DNA⁶, but here they are unlikely to play a significant role due to the low charge density of the ions involved. We propose instead that the correlation is induced by a better coordination of the water molecules in the global hydration structure of neighbouring ions, compared to the hydration shell of single adsorbed ions. Under this hypothesis, although electrostatic interactions occur between solvent molecules, ions and the surface, the correlation is effectively controlled by the structural organisation of water molecules at the interface.

To test this hypothesis, we conducted molecular dynamics (MD) simulations to obtain a full molecular-level picture of the Rb⁺ ions dynamics at the surface of mica in water. A ‘free’ interface (that is without the presence of an AFM probe) was used in the simulations in order to assess whether the AFM observations reflect the ‘unperturbed’ interface. Due to limited computational power, current simulations cannot directly replicate AFM experiments in terms of duration or system size. We therefore decided to compare the intrinsic stability of different geometrical configurations for adsorbed ions at the surface of mica in water. Three starting configurations were studied, progressively increasing the average number of direct neighbours between ions: (i) with the cations randomly distributed at the surface of mica (Fig. 4.7A), (ii) with the cations forming a single row on mica (Fig. 4.7B), and (iii) with the cations grouped in a single hexagonal domain on the surface (Fig. 4.7C). Additionally, since hydration forces are expected to play an important role in the correlation effects, we also conducted the simulations with K⁺ ions and Na⁺ ions. The K⁺ ions are generally seen as chaotropic¹⁴ similarly to Rb⁺ ions, but are naturally present in mica. In contrast, Na⁺ ions are kosmotropic and exhibit a smaller primary solvation shell with higher hydration energy than K⁺ and Rb⁺.

The density profiles of Na⁺, K⁺, and Rb⁺ obtained from MD-simulations in the direction perpendicular to the muscovite surface (z-direction) are given in Fig. 4.5. The positions of the ions along the same perpendicular axis are much harder to resolve in experiments, particularly for the smaller Na⁺-ion. The few comparisons with X-ray data^{23,26-31} that are possible show good agreement for K⁺ and Rb⁺, but less for Na⁺. The latter could be explained by the difficulty in X-ray experiments to distinguish between water and Na⁺-ions, as they both have the same number of electrons. Nonetheless, qualitative agreement with the available experimental data and simulations on the ion densities^{23,26-31} strengthens the confidence in our simulations model.

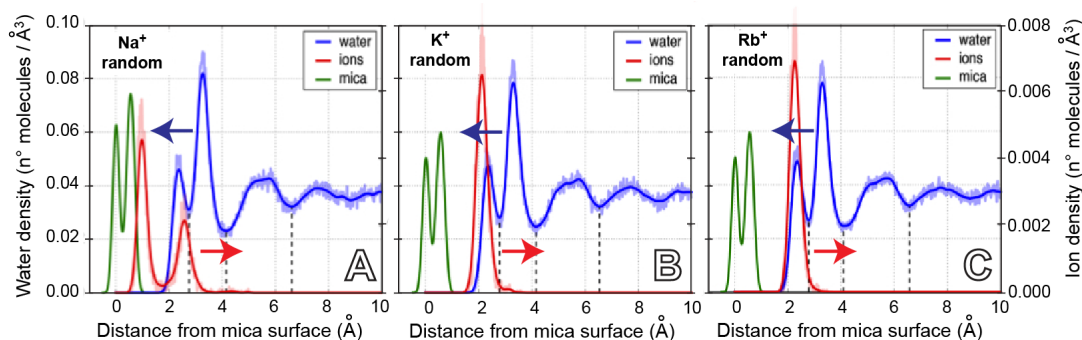


Fig. 4.5: Density profiles perpendicular to the surface. The density of the outer muscovite structure is depicted in green, the water density (oxygen) in blue and the respective ions in red. Distances from the surface are measured from the outermost muscovite layer containing the Si-atoms.

In Fig. 4.5, the black vertical dotted lines separate the first three hydration layers. On average these three hydration layers have the following thickness: 2.78 ± 0.02 Å (first), 1.39 ± 0.03 Å (second), and 2.39 ± 0.06 Å (third). The most structured part of the water extends 6.56 ± 0.07 Å into the solvent.

The density profiles of the hydration layers show the effect of ions being adsorbed on the surface (in any arrangement) extending into the first and second layer, but only very marginally into the third hydration layer. This effect can be clearly seen when plotting the density of the water molecules (to be precise: the oxygen atoms of water) in each hydration layer as a 2D map above the mica surface (Fig. 4.6). The water molecules counted in each layer are delimited by the dotted lines in Fig. 4.5. Additionally, a row of K^+ has been placed on the surface of mica to illustrate the effect of adsorbed K^+ ions on the different hydration layers. The ions can be easily seen in the first hydration layer (bright dots around $y = 27\text{\AA}$). The effect they have on the second layer is a local decrease of oxygen atoms density directly above the occupied position at the surface (empty row around $y = 27\text{\AA}$). Almost no effect can be seen in the third layer. Similar observations are made for the hexagonal arrangement of K^+ . For the random deposition of atoms the effect is much less pronounced, indicating that grouping of ions has a stronger effect on the hydration structure of water near the mica interface.

For all simulations involving Na^+ ions the density maps show a less clear pattern. This is probably due to the weaker binding between Na^+ and the mica surface in the presence of water. The Na^+ ions tend to diffuse easily into the “bulk” water if compared to the K^+ and Rb^+ counterparts. The Na^+ ions are also found closer to the mica surface (i.e., deeper in the hexagonal pockets of the muscovite surface) due to the smaller hydration shell (see Fig. 4.9).

At the level of the second hydration layer the difference between Na^+ and the other two ions, K^+ and Rb^+ , is even more striking. The last two ions are rarely present in this hydration layer while the actual peak corresponding to the second hydration state of the Na^+ ions (see peak at around 3\AA in Fig. 4.5) has a consistent part of the right tail into the second hydration layer region.

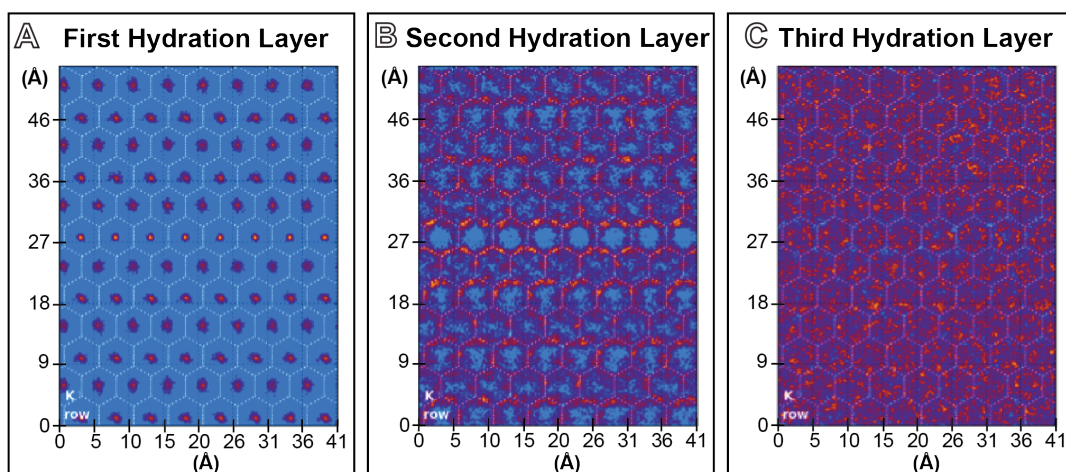


Fig. 4.6: Density profiles for each of the three hydration layers for the system with K^+ ions arranged in a row. Yellow colours indicate a high density, whereas cyan means low. These profiles are constructed by counting the ions and oxygen atoms of the water molecules in bins sized $0.25 \times 0.25\text{\AA}$ over the entire length of the simulations trajectory and in the current hydration layer. The black dotted lines indicate the size of the mica unit cell (to allow for visual inspection of periodicity) and the white dotted hexagons are the structure formed by the Si- and Al-atoms in the outer layer of the muscovite mica.

Calculation of the different energy contributions

The simulations comprise of ion-ion and ion-mica electrostatic interactions as well as hydration interactions between water molecules, ions and the mica. An ion located within 4\AA of the mica’s hydroxyl oxygen is considered adsorbed. The time-averaged interaction energies of the simulations runs are presented in Fig. 4.7D for each ion type in the three different starting configurations, always with a similar number of ions.

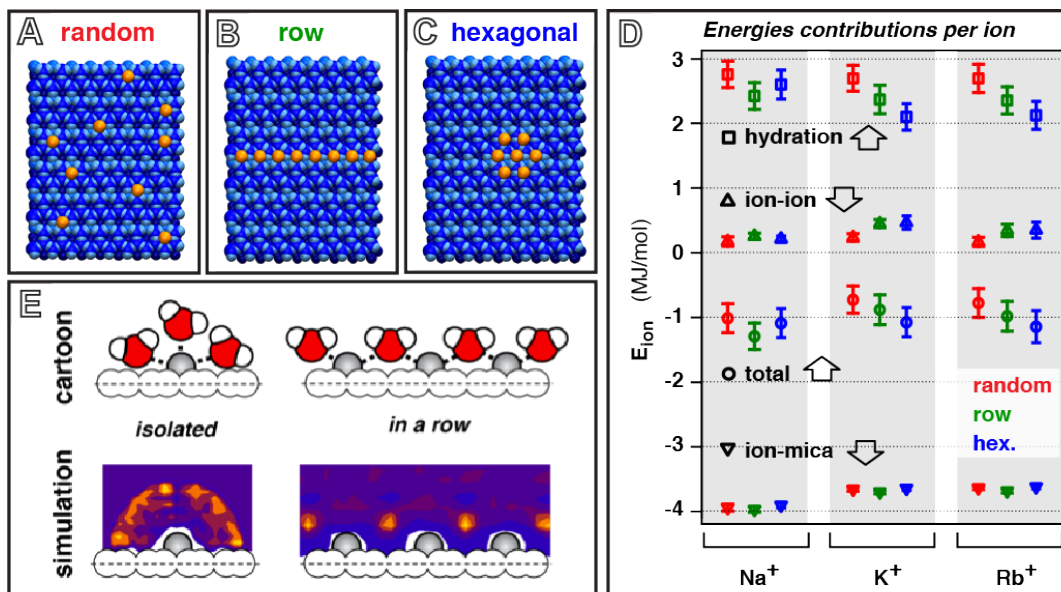


Fig. 4.7: Data from the molecular dynamics simulations of mica in aqueous solution. Three different starting configurations have been tested: with the cations randomly adsorbed (A), forming a row on mica (B) or a hexagon (C). The average hydration (open square), electrostatic (open triangles) and total (open circles) free energy of the adsorbed ions is given for each type of ion and each starting configuration (D). This is a “potential” energy per ion. These energies can be arbitrary shifted and what actually matters is the true free energy difference between the states in solution and at the surface (not computed here). The numbers on the y-axis are actually mostly meaningless, while their relative positions and trends are the actual real data. The data in (D) is extracted from the evolution of the hydration energy per adsorbed ion throughout the simulations. The error bars in (D) are two standard deviations. In (E) a schematic depiction of the water surrounding adsorbed K^+ . A clear difference is visible between isolated ions or ions forming geometrical patterns where the location of shared water molecules is well defined. From MD-simulations, the density of oxygen atoms of the water molecules is also shown. In the case of single ion the value of the oxygen density is the radial average around the K^+ ion. In the case of row of K^+ the average oxygen density is obtained by considering a rectangle of 0.5 nm width aligned with the row of the ions and centred on them.

The grouping of ions in particular geometrical structures (in this case rows or hexagons) improves the overall stability. To obtain a more quantitative argument for this observation we computed the potential energies between several selected groups of atoms, based on the trajectory obtained from the MD-simulations. We selected the interactions between surface ions (less than 4 Å from the hydroxyl oxygen in the mica surface), between ions and the mica, and between ions and the water atoms. Only the non-bonded interactions are taken into account as there are no bonded interactions between the selected groups, and they comprise the Lennard-Jones and Coulomb interactions. The potential energies between each of the aforementioned groups are computed based on the non-bonded interactions as dictated by Lennard-Jones and Coulomb potentials. The total potential energy acting between two atoms i and j is given as:

$$\begin{aligned}
 V_{ij}(r_{ij}) &= V_{ij}^{LJ}(r_{ij}) + V_{ij}^{Coul}(r_{ij}) \\
 &= 4\epsilon_{ij} \left[\left(\frac{\sigma_{ij}}{r_{ij}} \right)^{12} - \left(\frac{\sigma_{ij}}{r_{ij}} \right)^6 \right] + \frac{q_i q_j}{4\pi\epsilon_0\epsilon_r r_{ij}}
 \end{aligned} \tag{4.13}$$

where r_{ij} is the distance between the two atoms. The Lennard-Jones parameters ϵ_{ij} and σ_{ij} are the interaction energy and collision diameter respectively, and the Coulomb charges q_i and q_j are dependent on the specific atom types. Both ϵ_0 and ϵ_r are (dielectric) constants. For each surface ion the potential energy is computed with all the surrounding atoms (either in the mica, the water or the neighboring ions) by simply summing all the individual contributions. Long-range electrostatic effects are also taken into account (via particle mesh Ewald summation). We verified that this method gives exactly the same potential energy as the simulations output when not only selected atoms are taken into account, but all atoms in the system.

The computation of the potential energy as described above is repeated for every saved snapshot of the simulations trajectory (typically around 2000 for a 1 ns simulations run), which results in an evolution of the potential energy for each group with respect to time. A better approach would have been to compute the free energy difference between ions present on the surface or not, but we believe most of the effects can already be observed from the potential energy differences, computed as explained above. To verify this claim we conducted a separate set of simulations where we compute the free energy difference between a single ion on the surface or none (results not shown). When comparing this to the potential energy change, similar behavior was found, thus agreeing with our initial ideas.

A direct comparison between the simulations runs show that the overall free energy per ion is always higher when adsorbed in random configuration (Fig. 4.7D). The energy dependence of the ion configuration is largely dominated by the hydration energy. The latter is about an order of magnitude larger than the ion-ion electrostatic potential, and always largest for the random configuration regardless of the type of ions considered. In the case of K^+ and Rb^+ , the hydration energy (and the total free energy) per ions decreases with the number of immediate neighbours. This trend is however not as clear for the Na^+ ions, mainly due to the particularly high mobility of Na^+ and the presence of multiple solvation states²⁶ leading to a rapid dissolution of the initial geometrical arrangements. This is not the case for K^+ and Rb^+ ions, which exist mainly in a single hydration state and tend to remain at the usual ion binding sites when adsorbed^{23,26,27,29}. They also exhibit little mobility throughout the simulations, hence allowing for a more direct interpretation of the influence of the adsorption configuration on the respective free energy.

The evolution of this hydration energy is shown for all nine possible configurations (different ions and arrangements) in Fig. 4.8A. The total number of surface ions at any given time in the simulations is shown in Fig. 4.8B, indicating that Na^+ ions (dashed lines) tend to be substantially more mobile than K^+ (dotted line) or Rb^+ ions (full line).

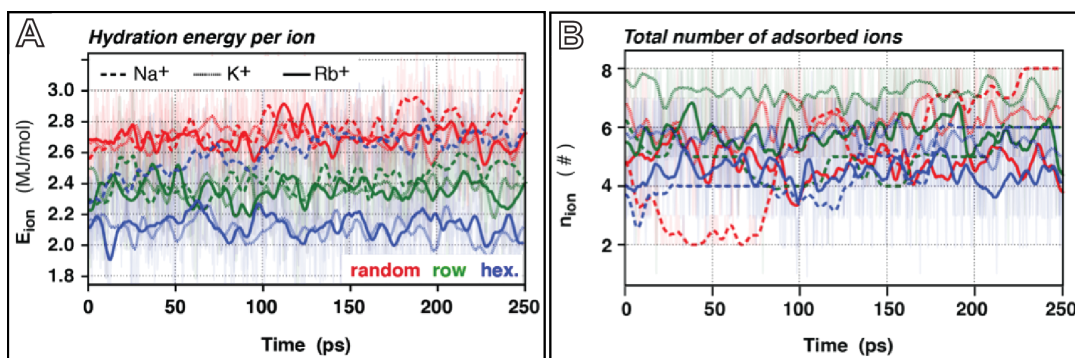


Fig. 4.8: In (A) the hydration energy per adsorbed ion throughout the final 250 ps of the simulations are shown. In (B) the evolution of the total number of adsorbed ions throughout the different simulations is shown. In each case, the simulations started with all ions adsorbed (8 ions for the “row” and “random” configurations and 7 ions for the “hexagonal” configuration). The number of Rb^+ and K^+ ions tend to remain constant throughout the simulations, indicating a relatively low diffusivity on the timescale investigated. Due to small spatial fluctuations of the ions around the binding sites, the total count of ions at the interface (i.e. within 4 Å from the hydroxyl oxygen in the mica surface) is always slightly lower than the number of ions in the initial configuration. The curves in both panels are a smoothed representation of the actual data (semi-transparent in the background).

The fact that the interaction energy between surface ions is hardly affected by the arrangement they have on the surfaces indicates again that the driving force has to come from the water, specifically from the hydration energy.

The simulations confirm that K^+ and Rb^+ ions on the surface are more stable when they sit in geometrical arrangements like rows or hexagons. Although not all possible arrangements have been tested, the two extreme cases have been computed (with less and most neighbours) and we believe that our results, combined with simulations of random deposition of ions on the surface show that any ordered arrangement might be favoured over a random one.

One-way ANOVA analysis of the results demonstrated that the differences in total free energy between geometrical configurations are statistically meaningful for K^+ and Rb^+ ($p < 0.01$).

Simulations also show that correlating ions have 10-15% less neighbouring water molecules over the entire length of the simulations compared to randomly adsorbed ions. This shows indirectly that the system favours an ordered ionic arrangement, further supporting hydration as the mechanism driving the local structuring of ions. In Fig. 4.7E a simulation snapshot illustrating a possible mechanism is presented. Ions neighbouring each other can share coordinated water molecules and improve the hydration structure compared to a randomly adsorbed ion.

It is however important to keep in mind that the MD-simulations discussed here only cover a small amount of real time in terms of AFM experiments (approximately 1 ns) and both K^+ and Rb^+ ions showed virtually no diffusion throughout the simulations. Furthermore, the AFM tip was not taken into account in the simulations and consequently the tip-effect cannot be directly assessed. Nonetheless, the good agreement between experimental and simulations trends gives us confidence in our interpretation of the results.

4.2.3 Different monovalent ions

In order to verify experimentally the MD-predictions for K^+ and Na^+ ions, we obtained AFM images of the surface of mica in KCl and NaCl solutions (Fig. 4.9A-C). As for $RbCl$, we imaged the mica surface in ultrapure water and progressively increased the concentration of the desired type of ion. In order to ensure consistency of the results, we performed all the experiments for a given type of ion on the same day and using the same tip. At least two concentrations were studied for each type of salt.

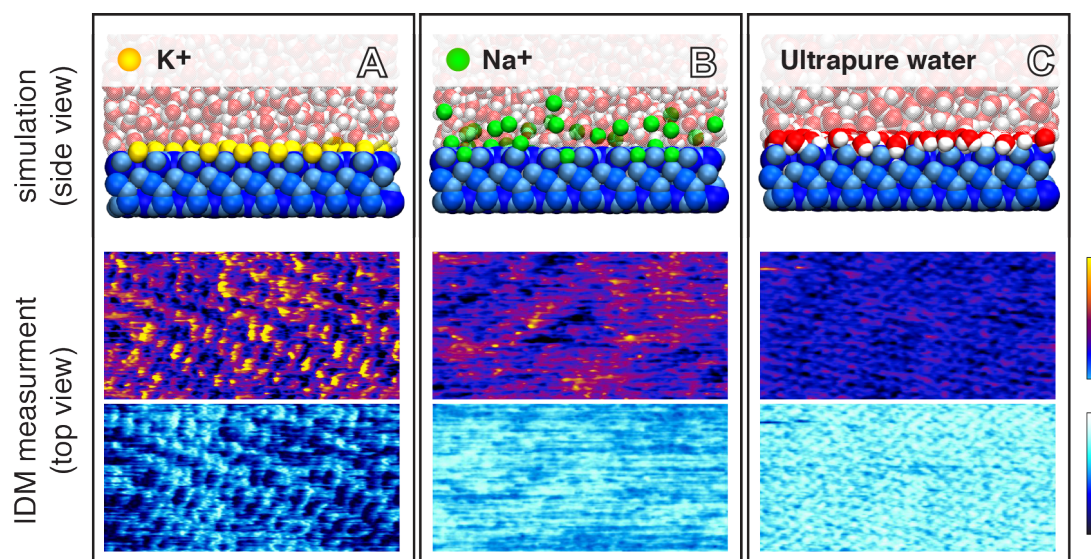


Fig. 4.9: Adsorption of K^+ and Na^+ ions at the surface of mica seen by simulations and AFM (A, B). An image captured in ultrapure water (C) is also given for comparison. In each case, a simulation snapshot with semi-transparent water molecules is shown (top) together with the corresponding AFM image (bottom). All the AFM data were acquired with a similar cantilever/tip and in identical operating conditions. The KCl and NaCl bulk concentration are 1mM and 0.5mM so as to ensure only partial coverage of the mica in each case. The adsorbed ions consistently induce a darker contrast in the phase (as for Rb^+). This contrast is however less pronounced for Na^+ ions due to the positions more “embedded” in the mica. The Na^+ ions sitting further from the surface are only occasionally imaged by the tip. This is also reflected in the smoother topographic image achieved in NaCl. The colour scale bars are 1 nm (A) and 0.5 nm (B, C) for topography and 30° (A-C) for phase.

The AFM images presented in Fig. 4.10 show the mica surface at 0mM, 1mM and 5mM KCl concentration. At 1mM the surface appears already half covered while full coverage is reached at 5mM. As for Rb^+ , most of the imaged K^+ ions are likely to be in the inner sphere hydration coordination, which is naturally prevalent for both ions at the interface with mica, hence allowing the high-resolution imaging. The images are however marginally noisier for K^+ than for Rb^+ , probably reflecting K^+ ions’ higher (albeit small) fraction of ions in the outer sphere configuration which starts to affect imaging (see section 4.2.2). Given the millisecond timescale of AFM

measurement, the tip encounters a time average of the two solvation coordinations which may destabilize imaging. This effect is much more pronounced for Na^+ ions where the fractions of ions in each of the two main coordinations are comparable (see section 4.2.2). In such case, a clear interpretation of the AFM images become difficult since the water structure at the surface becomes irregular. The imaging also tends to become noisier (Fig. 4.9B).

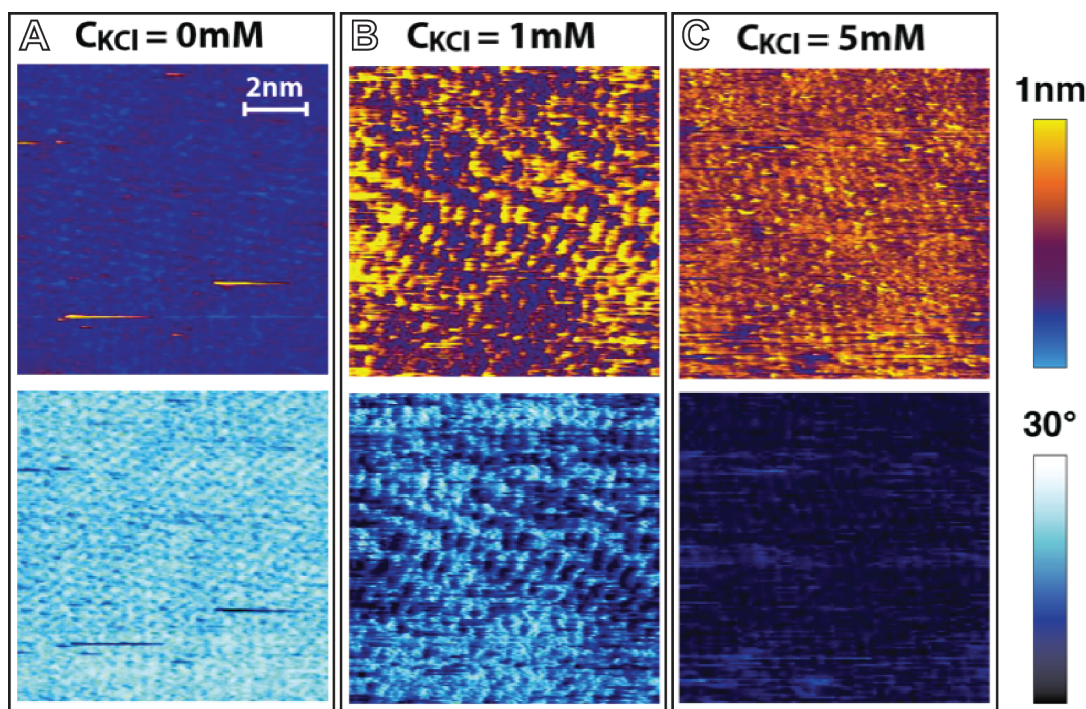


Fig. 4.10: AFM images of the surface of the mica in three different ionic concentration of KCl (0mM (A), 1mM (B) and 5mM (C) from left to right). The top images show topography and bottom images phase. The colour scales used are identical in each condition. The estimated ionic surface coverage at 1mM KCl is around 40%, while in the case of 5mM it is almost 100%.

The results are fully consistent with the simulations: the K^+ ions appear similar to Rb^+ ions, forming domains and rows on the surface and allowing imaging conditions almost as stable as in RbCl . In contrast, Na^+ ions appear poorly defined and show no clear structural organisation on the surface. Furthermore the high cations mobility on the surface and the presence of multiple hydration states prevented stable AFM imaging.

Interestingly, the phase shift observed for images of K^+ and Na^+ is different despite using the same cantilever/tip and identical imaging conditions. This difference reflects that of the two ions' hydration shells, suggesting that AFM can differentiate between adsorbed ions through the specific modification of the interfacial hydration structure (see Chapter 3). Differences between ions are likely to be enhanced in AFM measurements due to the momentary confinement of the interface by the AFM tip pushing water around the ions' solvation shell. Previous studies have shown that the hydration structure of a particular ion often dominates on the interfacial behaviour under confinement³². In AFM measurements, although confinement effects are limited by the small surface of the tip effectively imaging and the slow confining speed ($<50 \mu\text{m/s}$), they may nonetheless enhance the observations of ion-ion correlations that would otherwise be difficult to capture. Indeed, previous RAXR measurements were unable to detect correlations between Rb^+ ions within experimental uncertainty²³. Present MD-simulations of the 'free' (that is unconfined) interface show that correlation effects constitute an intrinsic property of the system, which we believe is, at best, enhanced by the AFM measurements (see sections 3.5 and 3.6).

4.2.4 General discussions on the system

Muscovite mica with the formula unit $\text{KAl}_2(\text{Si}_3\text{Al})\text{O}_{10}(\text{OH})_2$ can be easily cleaved to expose the [001] face. By the cleaving process a surface with hexagonal symmetry and lattice parameters of 5.2 Å and 9.0 Å is exposed (see Fig. 4.11)^{33,34}. Some residual K^+ ions are normally present on freshly cleaved surface and because of the hydrophilic properties, if the cleavage is performed in air, a layer of water is immediately formed on the surface.

When immersed in water the hydroxyl groups of the basal plane are normally considered not reactive, and the surface is free from any pH-dependent charge (at list in the range of pH normally explored)³⁵. The only reaction that can take place is the substitution of the residual K^+ ions with H_3O^+ or the added ions (in our case Na^+ and Rb^+)³⁶. This is the reason why normally the surface, without taking into account the adsorbed ions (we consider hydronium as an adsorbed ion), is permanently negatively charged with a charge density of $\sim 1e^-$ per unit cell area. The adsorbed monovalent ions are normally found in the ditrigonal cavity of the distal layer as preferential inner-sphere complexes, in agreement with our AFM data and the MD-simulations^{23,26-31}. Meleshyn, using Monte Carlo Simulations, in three different papers^{34,37,38} found that, in the case of strongly hydrated cations (Ca^{2+} , Mg^{2+} , Sr^{2+} , Ba^{2+}), the preferred adsorption site as an inner-sphere complex is on the oxygen triad. Loh *et al.*³⁹ conducted a FM-AFM study. They suggested that the oxygen triad is the preferential adsorption sites even for Li^+ and Na^+ ions. From our AFM measurements we cannot address the issue of the actual binding site of Na^+ ions due to the lack of single ion resolution (see Fig. 4.9) but our MD-simulations indicate clearly that the preferential adsorption of Na^+ is in the ditrigonal cavity as for Rb^+ and K^+ .

Beside the inner-sphere complexes, monovalent ions can adopt an outer-sphere adsorption, depending on the ionic hydration energy. Lee *et al.*^{26,27} found a relationship between the hydration enthalpy and the ratio between inner and outer sphere complexes on mica. This model seems to match with our MD-simulations where the Na^+ ions, with higher hydration energy^{14,40,41} are found to be more mobile and with two hydration states. Recently, Lee *et al.*⁴² with X-ray reflectivity measurement found out that both K^+ and Rb^+ ions can adsorb as outer-sphere complex even if in a minor extent compared to Na^+ . That we do not observe this in our MD-simulations, probably due to the limited computational time, different ranges of concentration and model sensitivity.

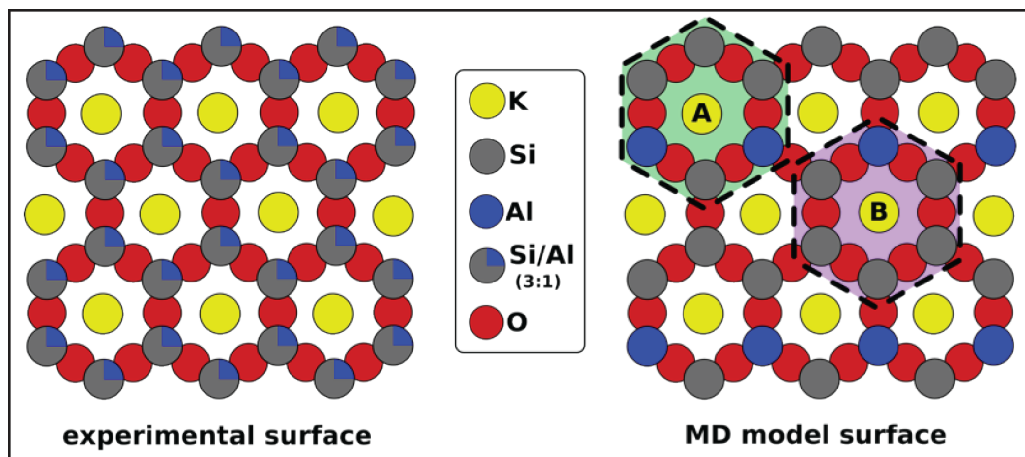


Fig. 4.11: The tetrahedral sheets in the exposed mica surface contain a ration of 3:1 of Si and Al atoms. A priori it is not known where the Al and Si atoms are located. On the left hand side blue/gray circles graphically represent this 3:1 ratio. In the MD-simulations the Al and Si atoms are placed as shown on the right hand side. This leads to two possible hexagonal ring structures with two (A) or one (B) Al atoms.

The permanent negative charge of the mica surface is normally attributed to the substitution of one or two silicon atoms in the tetrahedral sheet with aluminum atoms. This substitution enables the creation of two kinds of hexagonal rings Si_4Al_2 and Si_5Al on the mica surface³⁴ as shown on the right hand side in Fig. 4.11 (where Si_4Al_2 is labeled (A) and Si_5Al (B)). To be sure that all the possible inner-sphere complexes are equivalent as implicitly assumed in the Frumkin isotherm

model used in the previous chapter, we performed some MD-Simulations where we calculate the energy of single or a couple of ions (both K^+ and Rb^+) placed in the possible different inner-sphere complexation sites (labelled (A) or (B) in Fig. 4.11). An additional adsorption site was tested: no charge difference between Si and Al atoms in the hexagonal ring is present. We achieve this by averaging the charges of all Al's and Si's in the hexagonal rings to create a more homogeneous surface charge distribution while keeping the overall surface charge constant (the original Al charge is from 1.575e to 1.96875e and similarly for Si the charge is changed from 2.10e to 1.96875e). For each of these additional systems we collected the hydration energies as before and compared them to the original data. A one-way ANOVA test of these new energy distributions with the previous ones showed with great significance ($p < 0.01$) that these distributions are very likely similar, or, in other words, we have not found any evidence that the location of the Si or Al atoms in the hexagonal rings have influence on our MD-simulations. These additional results strengthen our observations that it is the hydration forces that drive the formation of ion correlations on the surface, as in this case local charge differences play no significant role.

The overall picture emerging from AFM measurements and MD-simulations highlights the importance of the interplay between the hydration properties of adsorbed ions and of that of the surface for ordering the ions. In the case of mica, chaotropic ions such as K^+ or Rb^+ appear mostly located within the first hydration layer with limited effect over the distal layers. This minimal disruption of the mica's interfacial water structure allows the formation of stable ionic structures guided by the particular hydration landscape of mica. The self-assembly takes place within mica's first hydration layer and is guided by a minimisation of the overall hydration energy of both the mica and the adsorbed ions. The resulting correlation effect does not require any specific interaction between the ions and the surface and can, in principle, occur at any interface which exhibiting an appropriate hydration landscape. The possible manifestation of this effect in other systems will be analysed in section 4.3.

4.3 Hydration correlation in other systems

In the previous section, we have shown that single metal ions can form ordered structures at solid-liquid interfaces through water-induced correlation effects. The effect, observed experimentally at the single-ion level by AFM, is driven by the interfacial water, and depends on the hydration properties of the ions considered. The simplicity of the system and the generality of the effect suggest that it may spontaneously occur in a large variety of systems, provided a well-defined hydration structure at the surface of the solid that can guide the adsorption of the ions.

In the light of the previous results we decided to explore different, more general systems such as self-assembled monolayer (SAM) on gold and supported lipid bilayers.

4.3.1 Self-Assembled-Monolayer on gold

To test the generality of our findings we assessed a series of experiments on a self-assembled monolayer (SAM) on Au(111) surface exposing polar but neutral alcohol headgroups (mercaptohexanol, inset Fig. 4.13C).

SAM on gold are widely studied and characterized both on flat surfaces and on spherical particles.⁴³ SAMs are organic assemblies formed by the adsorption of molecular constituents from solution or gas phase onto the surface of solids. These molecules are called ligands. The adsorbates organize spontaneously (and sometimes epitaxially) into crystalline (or semicrystalline) structures. The ligands that form SAMs have a chemical functionality, or "headgroup", with a specific affinity to a substrate being able to displace adsorbed adventitious organic materials. In the case of gold, the chemical group normally employed in the functionalization process is the thiol. The gold-thiol bond has a binding energy of 40-45 kcal mol⁻¹ and is more commonly known as a surface bound thiolate. If a linear molecule is used as a ligand, at the opposite side of the thiol there is the chemical functionality (e.g. amines, acids,

alcohols, sulfonates, phosphates, esters, methyl groups, etc.), which can interact with the solvent once the SAM is formed.

In ambient atmosphere, thiolated molecules on the gold surface form a highly dynamic monolayer that can rearrange and form different phases. The structural arrangement of the adsorbates plays an important role in determining the evolving macroscopic properties of the interfaces.⁴⁴ There are several phases of the alkanethiols ($\text{CH}_3(\text{CH}_2)_{n-1}\text{SH}$) molecules on the Au(111) surface: a low density two-dimensional gas of highly mobile, surface-bound molecules; a more dense phase which can coexist with the previous and undergo structural transitions as a function of coverage; and the densely packed $(\sqrt{3}\times\sqrt{3})R30^\circ$ phase.⁴³ The last one is normally associated to the structure of a completely formed monolayer. The molecular packing significantly influences the chemical and physical properties of the surfaces, such as the passivation efficiency, lubricity, and frictional coefficient.⁴⁴

Generally STM is the technique used to characterize the structure at the molecular lever of SAMs both in air⁴⁵ and liquid (under electrochemical conditions)⁴⁶⁻⁴⁸. Recently AFM has been used to image SAMs in UHV⁴⁹ or moderate vacuum environment⁵⁰ and liquid⁵¹⁻⁵⁴.

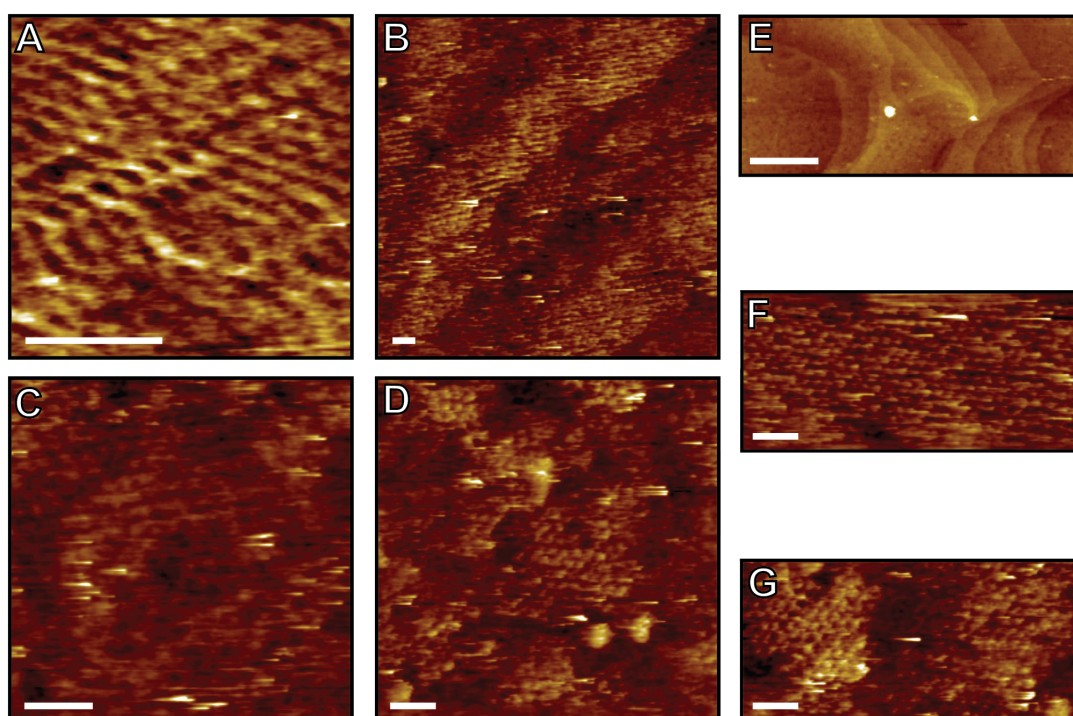


Fig. 4.12: OH-terminated SAM on gold imaged in liquid (water or RbCl solution). The scale bar is for all the images 2 nm, beside (E) where it is 100 nm. The colour scales are respectively: 0.4 nm (A), 1.5 nm (B), 0.6 nm (C), 1.2 nm (D), 7.2 nm (E), 1.7 nm (F) and 1.2 nm (G).

Structure of the SAM

When the monolayer forms, holes usually appear on the on the gold surface (see Fig. 4.12E). They are known as etch pits and are caused by the thiol adsorption on the gold surface. They are generally associated with the formation of a more condensed adlayer.⁴⁶ In Fig. 4.12 a monolayer of mercaptohexanol on gold imaged in water with AM-AFM is presented. The surface generally appeared inhomogeneous with holes and steps. The periodicity of the OH terminal groups is clearly distinguishable even at lower magnification (see Fig. 4.12B). At higher magnification ordered protruding features appeared on the surface (see Fig. 4.12F). We identified these features as the -OH terminal groups of the SAM. The distance between two neighboring protrusions, regardless of the apparent height, is about 0.5-0.6 nm, corresponding to roughly $\sqrt{3}$ times of the Au lattice constant.⁴⁶ This lattice parameter suggests that the molecules in this case were in the condense phase presenting a $(\sqrt{3}\times\sqrt{3})R30^\circ$ pseudo-hexagonal lattice. Sometimes a modulation in the height of the protrusions is reported in literature reflecting the non-identical conformation

of the adsorbed molecules. This generates a $c(4 \times 2)$ superlattice on the $(\sqrt{3} \times \sqrt{3})R30^\circ$ phase.^{46,53} In our experiment the surface was particularly non-homogeneous rendering hard the determination of the presence of the superlattice structure. Sometimes, increasing the magnification of the images caused the appearance of a different contrast (see Fig. 4.12A) more “rod-like” than “point-like”, as mentioned even in the work of Hiasa *et al.*⁵³. They associated this type of contrast to a pair of two mercaptohexanol molecules laid on the surface, suggesting that the actual monolayer density was lower than the $(\sqrt{3} \times \sqrt{3})R30^\circ$ phase. In our case the dominance of the pseudo-hexagonal packing suggests that the molecules were densely packed on the surface, as expected for a complete monolayer.

Ion-correlation at the water-mercaptohexanol SAM interface

The molecular packing of the SAM creates at the nanoscale a hydration landscape similar to that of the mica surface.^{53,55} Therefore ion-ion correlation effect is expected to occur even in this system.

The SAM-functionalised gold surface develops a surface potential in aqueous solution. Previous reports indicate zeta-potentials ranging between -40 and -50 mV for gold nanoparticles coated with alcohol-terminated alkanes in an aqueous solution at a similar pH^{18,56,57}. The SAM surface potential is therefore weaker than that of mica. Significantly, the SAM surface in direct contact with the liquid is not charged and the polar alcohol groups interact with the liquid mainly through the formation of hydrogen bonds. The surface potential of the SAM can hence be seen as a diffused background creating an incentive for cations to form an EDL close to the SAM's surface.

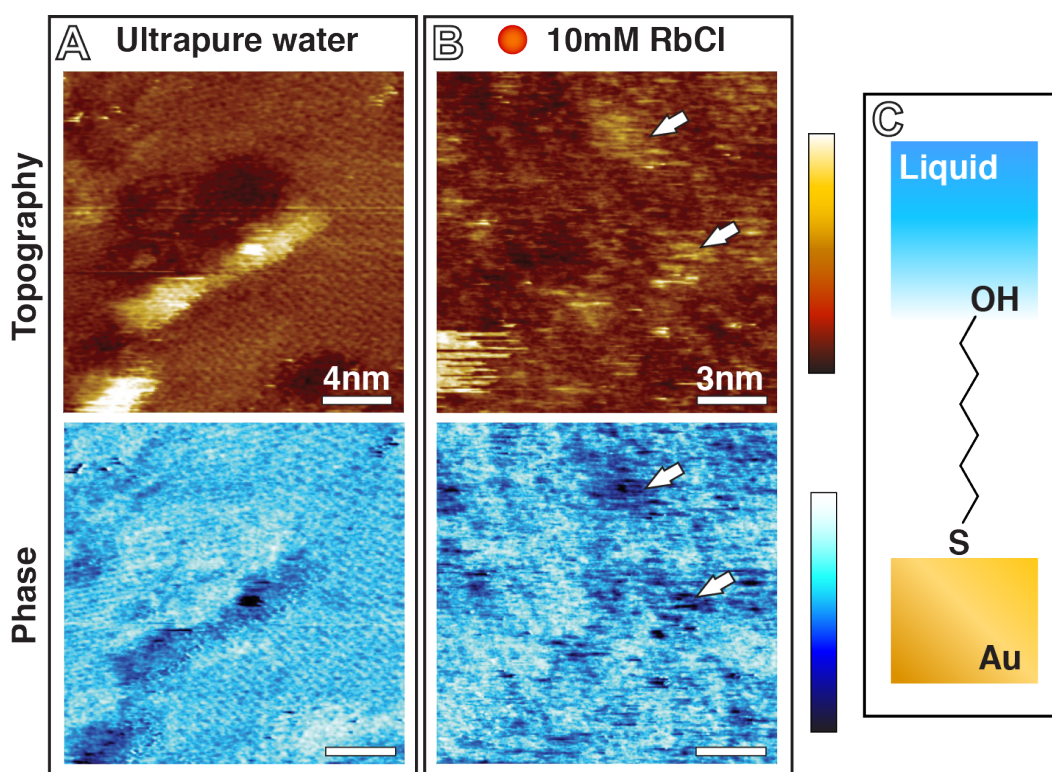


Fig. 4.13: Comparison between mercaptohexanol SAMs imaged in water (A) and in a 10mM RbCl solution (B). In both cases, the SAM lattice can be identified. In the presence of the salt, Rb⁺ ions can be seen clustering at the SAM surface (arrows), creating a consistent darker contrast in the phase image. The ion clusters are however easily removed by the scanning tip, making them appear less clearly than on mica due to a weaker surface potential. (C) the chemical structure of a mercaptohexanol molecule. The colour scale bars are 0.7 nm for topography and 20° for phase.

Fig. 4.13 compares high-resolution AFM images acquired in ultrapure water and in 10mM RbCl. In presence of the salt Rb⁺ clusters can be identified at the surface of the SAM, yielding a phase contrast consistent with the results on mica. The clusters are however less clearly defined than on mica and can easily be removed by the tip. This can be explained by the relatively weak surface

potential of the SAM that limits the incentive for adsorbed ions to remain at the surface. We found that Rb^+ clusters could be observed by AFM, confirming the presence of Rb^+ - Rb^+ attractive correlations. Nonetheless, the result confirms that the surface chemistry of the solid is not critical, nor is the surface potential. The key ingredient is the surface hydration landscape, which imposes a particular disposition of the adsorbed ions, inducing ion-ion correlations for suitably hydrated ions.

4.3.2 Lipid bilayers

Given the ubiquity of K^+ ion in biology, the type of water-induced correlation that has shown to play a fundamental role in the mica-water interface can be a commonplace even at the surface of biomembranes. Gel-phase phospholipid domains tend to adopt an arrangement with a similar periodicity as the mica lattice or the SAM. Moreover we have already seen in Chapter 2 that they have a peculiar hydration properties finely tuned in both lateral and vertical directions.^{58,59} Biological interfaces are however more complex: most of the interfacial properties depend strongly and locally on the surrounding pH and the conformational flexibility of the constituting molecules renders the surfaces highly dynamic and variable. Correlated ionic networks are however likely to play key roles in charge transfer^{60,61} and membrane shaping⁶². In this subsection I present the preliminary results obtained on two types of lipid bilayers supported on mica. The lipid molecules used in this study are the zwitterionic DPPC (1,2-dipalmitoyl-*sn*-glycero-3-phosphocholine) and the negatively charged DPPA (1,2-dipalmitoyl-*sn*-glycero-3-phosphate). By keeping the ionic concentration fixed at 10mM and changing the ionic species in solution we studied the specific interaction of NaCl, KCl and RbCl on the bilayers. We decided not to introduce any buffering agent in the water solution to prevent the possible interaction of unknown molecules with the lipid bilayers.⁵⁹ This decision didn't allow us to control the pH rendering the interpretation of the results challenging.

DPPC lipid bilayer

A DPPC lipid molecule has a zwitterionic phosphatidylcholine (PC) headgroup consisting of a negatively charged phosphate and a positively charged choline group. This PC group is characteristic of the major lipid component of cell membrane and of the pulmonary surfactants. DPPC molecules spontaneously form a bilayer in aqueous solution with the hydrophilic headgroups in contact with water and hydrophobic alkyl chains inside the bilayer. At room temperature, DPPC bilayer is in the gel phase. The alkyl chains are closely packed in a crystalline fashion and exhibit relatively small thermal fluctuation. The hydration properties of DPPC lipid bilayers at room temperature have been investigated with FM-AFM^{58,59,63}, showing a fine tuning of the water density in both vertical and lateral directions. The hydration landscape of DPPC bilayers should be, in principle, ideal for hydration-driven correlation effects to occur. However, the headgroups exhibit large thermal fluctuation, even in the gel phase, due to the gap between them. This allows the ions present in solution to directly and specifically interact with the lipid headgroups by penetrating in the fluctuating surface.

The presence of the ions has shown to selectively affect the structure of the bilayer even at low concentration.⁶⁴⁻⁶⁶ Using MD-simulations, Pandit *et al.*⁶⁷ observed that the addition of salt to a DPPC bilayer slightly decreased the area per headgroup. The Na^+ ions were found to be tightly bound to the lipids, creating ion-lipid complexes comprising on average two lipids per ion.⁶⁷ The complexes were coordinated through phosphate and carbonyl portions of the lipid headgroups. Somewhat unexpectedly, Cl^- ions were only very slightly bound to the surface of the lipids. A similar result was obtained by Lee *et al.*⁶⁶. They observed extensive coordination of Na^+ ions by DPPC carbonyl oxygens throughout the simulations, resulting in high densities of Na^+ ions at the lipid carbonyl region of the membrane-water interface. Conversely, K^+ showed significantly less coordination by lipid carbonyl oxygens and, as a result, was distributed more uniformly away from the carbonyl region of the lipid-water interface. Moreover Cl^- ions were largely excluded

from the interfacial region, particularly in the case of K^+ adsorption, while in the case of Na^+ they were distributed at the surface.⁶⁶

Different monovalent ions have proved to visibly modify the structural arrangement of the lipid head groups even in the work of Ferber *et al.*⁶⁴. They investigated a DPPC bilayer in the gel phase in the presence of three cations Ca^{2+} , Na^+ and K^+ always using Cl^- as anion. Their findings indicate that the area per unit cell does not significantly change in these three salt solutions. However the lipid molecules do reorder non-isotropically under the influence of the three different cations. They attribute this reordering to a change in the highly directional intermolecular interactions caused by a variation in the dipole-dipole bonding arising from a tilt of the headgroup out of the membrane plane.

Garcia-Celma *et al.*⁶⁸, using electrochemical measurements, also found that different cations and anions have different interactions with the DPPC membrane. They measured the charge displacements on the lipid bilayer supported on a gold electrode. Different species of ions are characterized relative to a reference (Na^+ for cations and Cl^- for anions) by monitoring the sign of the electrical current that develops as the ionic solution is exchanged. A positive charge displacement after a cation exchange or a negative charge displacement after an anion exchange (at constant concentration) imply that the average equilibrium position of the substituting ions is closer to the underlying electrode than that of Na^+ (for cations) or of Cl^- (for anions). Alternatively more ions are allowed to reside close to the bilayer surface. In the experimental study Garcia-Celma *et al.* found that chaotropic anions and kosmotropic cations were attracted to the surface independently of the membrane composition. In particular, the same behavior was found for lipid headgroups bearing no charge, like monoolein. In the case of DPPC and uncharged molecules, the translocated charge showed an approximately linear dependence on the hydration energy of the ions (the anion is always Cl^- for the cation series) yielding the following series (for PC): $La^{3+} > Ca^{2+} > Mg^{2+} > Ba^{2+} > Sr^{2+} > Li^+ > Na^+ > K^+, Rb^+, Cs^+$. The anions showed the reverse behavior with respect to the free energy of hydration.

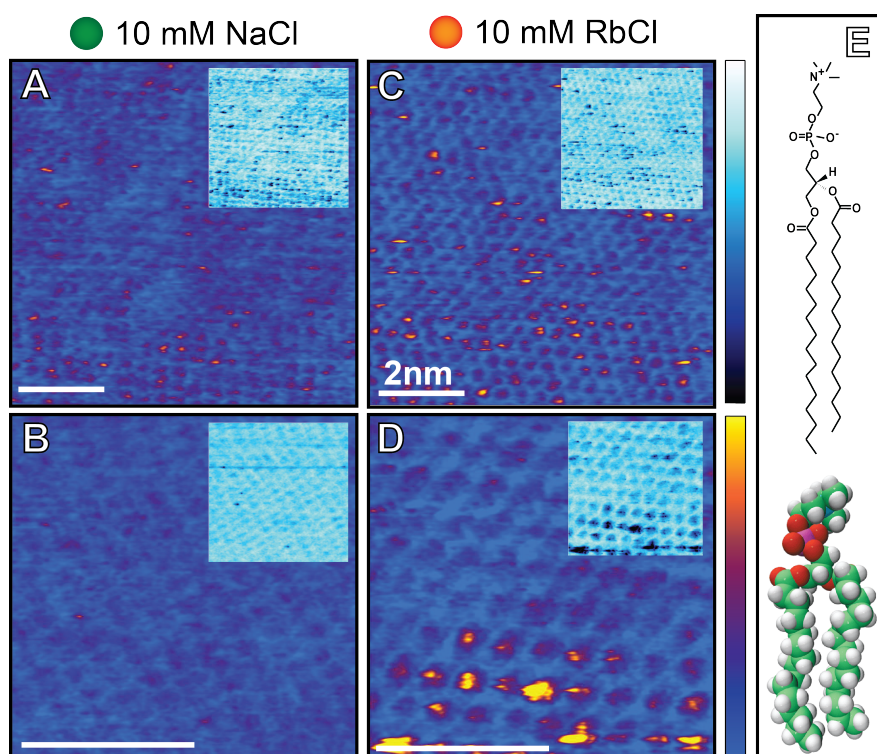


Fig. 4.14: DPPC (E molecular structure) lipid bilayer on mica imaged in 10mM NaCl (A and B) and 10mM RbCl (C and D). The phase images corresponding to the topographic ones are presented as an inset with the blue color scale. The images have not been drift corrected, hence the lattice appearing square at time in the higher resolution frames. Height color scale corresponds to 0.8 nm. Phase color scale corresponds to 30°.

Using high-resolution AFM, we investigated the surface of DPPC bilayers in aqueous solutions containing NaCl, KCl and RbCl. Results in KCl were inconclusive, probably affected by some contaminations on the AFM tip, and will hence not be considered. The AFM images revealed some clear protrusions coinciding with the position of lipid headgroups and that can be ascribed to adsorbed ions (Fig. 4.14). From the above discussion, we expect Na^+ to penetrate the bilayer in the headgroup region, while K^+ (and consequently Rb^+) is expected to remain mostly on the surface.⁶⁸ Cl^- ion can, in principle, also be located in the vicinity of the surface and hence render the interpretation of the results challenging. The protrusion visible in the images of Fig. 4.14 cannot be univocally identified as a specific ionic species and more careful experiments should be performed by changing, for example, the anion in solution. It is reasonable to assume that the protrusions are caused by the ions adsorbed on the surface and not by ions that penetrate inside the bilayer, unless the latter are able to locally modify the hydration properties around the surface groups. Under this assumption, the protrusions appearing in RbCl can be linked to the Rb^+ ions that ‘sit’ on the bilayer surface. However, being AM-AFM measurements performed in a non-buffered solution, a local pH variation cannot be excluded. Any local fluctuation of pH could in principle propagate at the surface of the membrane and modify the charge of the headgroups adding an extra complication to the interpretation of the experimental results. Summing up all these considerations, it becomes difficult and risky to attribute the eventual ordered structures on the bilayer surface to a hydration-correlation effect.

It is interesting to compare the images obtained in FM-AFM on DPPC bilayer by Fukuma *et al.*⁶⁹ and Ferber *et al.*⁶⁴ with those obtained here in AM-AFM in the same conditions. Following the interpretation provided in this thesis on the imaging contrast formation, FM-AFM should be able to see more clearly the ionic distribution in the compact headgroup region and hence be more sensitive to ions like Na^+ . On the contrary AM-AFM images should reflect the distribution of ions such as K^+ , Rb^+ and Cl^- that are able to affect the hydration layer at the membrane’s surface. The complementary information gained from the two operation modes will thus provide a more complete comprehension of the ionic distribution at the membrane-water interface.

DPPA lipid bilayer

Phosphatidic acid (PA)-terminated lipid is a phospholipid with a small, highly negatively charged headgroup located close to the glycerol backbone (see Fig. 4.15G). PA is the precursor for the biosynthesis of many other lipids and is known to influence membrane curvature, playing an important role in both vesicles fusion and fission.^{70,71} Even in the case of DPPA, the structure of the water molecules in close proximity of the lipid membrane is substantially modified by the presence of the surface, as shown by Faraudo *et al.*⁷² using MD-simulations. They showed that the mean number of hydrogen bonds per water molecule strongly decreased near the phospholipids. The perturbation was appreciable even at distances of 1.5 nm from the membrane’s surface. The density of water, however, remained similar to the bulk value almost up to the interface. This implies the presence of a region near the interface where water shows bulk density values but with a different hydrogen bond structure.⁷²

The charge of the DPPA molecule depends on environmental conditions such as pH and the concentration of cations in solution.⁷² Isolated PA molecules can have three protonation states: PA, PA^- and PA^{2-} . The first pK_a^1 is 2.1 and the second pK_a^2 is 7.1.⁷² This implies that, at the experimental pH of 6.8 (un-buffered ionic solutions used here), the lipid molecules could have either a single or a double negative charge. The situation is, however different in a membrane in contact with aqueous solution containing counterions. Counterions compete with the hydronium for the oxygen binding sites, modifying the overall charge of the phospholipids membrane. This effect is already observed for monovalent ions^{73,74}, but becomes more drastic for divalent⁷² or trivalent ions.

Our experimental results (Fig. 4.15) clearly showed differences between 10mM NaCl, KCl and RbCl. In RbCl, bigger and more frequent protrusions appeared on the surface of the DPPA bilayer. Given the negative charge of the surface it is possible to associate the differences of the surface topography to the monovalent cations. However, the flexibility of the headgroups and possible local variations of pH render the information possible to extract more qualitative than

quantitative. A more careful characterization in a controlled pH is required, possibly in alkaline solution with $\text{pH} > \text{pK}_a^2$. Results would help modeling the system in a more quantitative manner and draw a parallel with the mica surface.

So far, we can say that a correlation between adsorbed Rb^+ ions seems to take place, as visible in the Fig. 4.15E and F. The origin of this correlation has to be further investigated but the similarities in terms of hydration properties with the surface of mica suggest that the hydration landscape is again playing an important role in the ordering of the ions at the Stern Layer.

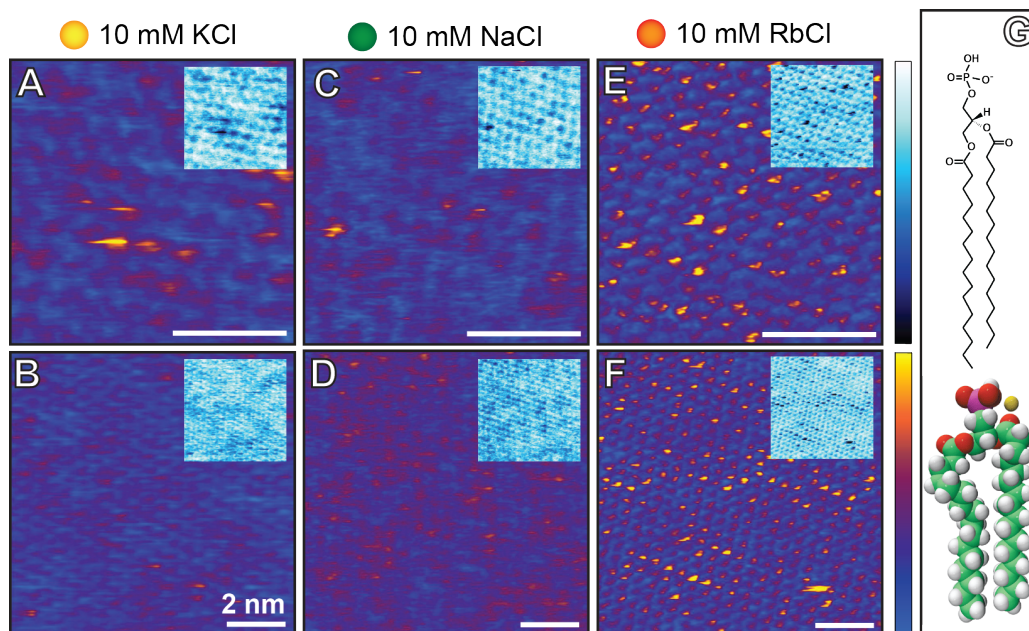


Fig. 4.15: AFM imaging of DPPA ((G) molecular structure) in different ionic solutions: (A, B) 10mM KCl; (C, D) 10mM NaCl; (E,F) 10mM RbCl. For a given ionic solution, higher and lower resolution images are presented in the upper a lower frame respectively. The corresponding phase images are presented as insets in the blue color scale. The presence of adsorbed ions induces consistently a darker phase contrast. The images have not been drift corrected, hence the lattice appearing square at time in the higher resolution frames. Height color scale corresponds to 0.6 nm while phase color scale to 20° .

4.4 Materials and Methods

4.4.1 Atomic Force Microscopy experiments on mica

All the AFM data were acquired on a Multimode Nanoscope IIIa (Digital Instruments). The sample and the scanning tip were fully immersed into the imaging solution. Before each experiment, the AFM liquid cell was thoroughly washed by consecutive sonication in isopropanol and ultrapure water and then dried under nitrogen flow. A cantilever was then mounted on the cell and engaged over clean mica in ultrapure water. After the AFM had reached thermal equilibrium, the ultrapure water was removed and the desired solution was injected into the cell. We used standard silicon nitride cantilevers (Olympus RC800 PSA, Olympus, Tokyo) with two different lever length but identical tip design. The nominal spring constant of the levers were $k_s=0.1$ N/m (softer lever) or $k_h=0.76$ N/m (stiffer lever). Cantilevers from a same wafer were used to allow for better comparison of the results. The cantilever were calibrated using the thermal spectra⁷⁵ after each experiment and found to have typical stiffness and Q-factors of $k_h \sim 0.5$ N/m and $Q_h \sim 4.4$ (stiffer lever), and $k_s \sim 0.1$ N/m and $Q_s \sim 2.5$ (softer lever). The cantilever was driven acoustically in a liquid cell, close to the resonance frequency. Typical working amplitudes A were kept between 0.8 nm and 1.5 nm with the setpoint ratio A/A_0 as large as possible where A_0 is the free vibration amplitude of the lever in the liquid far from the mica surface. When operated in these conditions, atomic-level resolution topographic and phase images could be routinely achieved. We found that

too small amplitudes (<0.5 nm) resulted in no apparent surface coverage by the ions due to the tip 'sweeping' the ions sideways.

Generally, since the AFM tip can mechanically remove ions from the surface, we always carefully balanced the imaging setpoint so as to keep it as large as possible. Nonetheless, minute setpoint variations were sufficient to introduce variations in the apparent surface coverage; this is the main source of error in our statistical analysis.

High quality muscovite mica (grade V) was purchased from SPI supply (West Chester, PA, USA) and used in all the experiments. The mica was freshly cleaved with adhesive tape and rinsed copiously with ultrapure water (18.2 M Ω , Merck Millipore, Billerica, MA, USA) before use. All the solutions were prepared in ultrapure water with 99.9% pure salts purchased from Sigma-Aldrich and used as received.

4.4.2 MD-simulations on mica

Based on the previously reported crystal structure of muscovite⁷⁶ we constructed for the molecular dynamics (MD) simulations a crystal measuring approximately $41 \times 55 \times 40$ Å with the (001) plane set parallel to the xy-plane of the simulations referential. The locations of the Si and Al atoms in the tetrahedral sheets of the mica crystal are depicted in Fig. 4.11. This positioning results in the creation of two different hexagons A and B, with either 2 or 1 Al atoms (see Fig. 4.11). The exposed plane naturally contains potassium ions and depending on the required starting configuration all, none or a selected number of these ions were removed or replaced with a different ion species, resulting in either a random, row or hexagon configuration for the surface ions. When building the entire simulations system one of our main goals is to keep the overall charge of the system neutral (charge neutrality is a prerequisite for accurate long-range electrostatic computations using Ewald methods). Initially both mica surfaces (on either side of the crystal) are covered with K⁺ ions. This system, however, has a total net charge equal to exactly the number of ions on one side of the surface when fully covered. Since we want to study patterns of ions on the surface we focus on one side only and can ignore the other exposed surface on the other side of the crystal. On this particular side, we remove all ions that are not needed to achieve the desired pattern. On the other side of the mica crystal (the surface we are not interested in) we remove exactly the number of ions necessary to create the desired pattern. In this way, the correct number of ions has been removed from both sides (i.e., exactly the number necessary for one fully covered surface) to make the system charge neutral. This setting-up method allow us to ignore counter ions (like Cl⁻) at this stage, even though they appear in the experiments, as without them the system is already neutral. This fully atomistic model of muscovite is centred in a periodic simulation box and solvated in the direction perpendicular to the exposed plane, ensuring a water thickness on top of the mica of at least 5 nm.

To describe the interactions between all atoms, two force fields are used. For the muscovite mica interactions and all ion interactions we used the CLAYFF force field⁷⁷, which is a general force field suitable for the simulation of hydrated and multicomponent mineral systems and the interfaces with aqueous solutions. The interactions between water molecules were described by the TIP3P model of the CHARMM force field⁷⁸. Recently it has been shown that the CLAYFF and CHARMM force fields are compatible and can be used together⁷⁹⁻⁸¹. All simulations have been performed using the MD-code NAMD⁸². For visual inspection VMD⁸³ was used and most of the analysis was performed using the Python library MDAnalysis⁸⁴.

Three different surface arrangements were examined for each type of ion: (i) a row of ions along the (100) direction, (ii). a hexagon and (iii) ions randomly placed. In the case of the row and the random distributions, 8 ions were placed at the surface, while 7 ions (a full hexagon) were used in the hexagonal configuration.

For each of the nine different MD-simulations a similar protocol is followed. This includes an initial minimisation of the energy associated to the water only (allowing bad contacts to be removed), followed by a short dynamics run of 5 ps to equilibrate the entire system at ambient conditions, and finally the production run of 1 ns. Only the latter is used for analysis. The current simulations set-up and protocol is similar to the setup used previously to study the interaction

between calcite, water and ions⁸⁵, but in the current work all simulations are performed in duple to improve statistical accuracy and to account for individual aberrations.

In order to verify our muscovite model we computed basic properties such as water residence time near the muscovite surface and around the ions in solution, as well as the hydration numbers for these ions. We found all of the measured properties to be in good agreement with previously reported data^{27,29,86}. For instance, the hydration numbers computed from our simulations are 5.8, 7.1 and 7.9 for Na⁺, K⁺ and Rb⁺, respectively in bulk water. As rubidium is a less common ion to encounter in mineral force fields like CLAYFF or organic force fields like CHARMM, the properties for this ion were checked more carefully and found comparable to experimental values reported^{23,26,31}.

4.4.3 Synthesis of the self-assembled monolayers

The SAM of mercaptohexanol were created on gold substrates. The substrates, commercially available (PHASIS, Geneva, Switzerland) consisted of gold evaporated on mica packaged in a sealed nitrogen atmosphere. Upon opening the substrates were immediately placed in vials containing 10 ml of ethanolic solution of 6-mercaptohexan-1-ol (mercaptohexanol, MH) (TCI America, Portland, Oregon, USA). The thiol concentration was 0.01 mM. The substrates were left in the solution in dark at room temperature for a period of 7 days, at which point they were rinsed with ethanol seven times and dried under a gentle argon-flow.

All the solutions were prepared in ultrapure water with 99.9% pure salts purchased from Sigma-Aldrich and used as received.

4.4.4 Lipid bilayer preparation

1,2-dipalmitoyl-*sn*-glycero-3-phosphocholine (DPPC) and 1,2-dipalmitoyl-*sn*-glycero-3-phosphate (DPPA) were purchased from Avanti Polar Lipid (Avanti Polar Lipids, Alabama, USA). All the solvents were purchased from Sigma Aldrich unless specified. For all the experiments we used ultra pure Milli-Q water (18.2 MΩ, Merck Millipore, Billerica, MA, USA). The lipids were stored in chloroform at a temperature of -20°C. Two days before the experiment an ampule containing 50 mg of the desired lipid (DPPC or DPPA) in chloroform was opened and we transferred the entire content directly into a glass vial previously clean (see for the cleaning procedure section for the glassware). We added extra chloroform to the ampule and wash out to the glass vial so as to remove all the lipids. The chloroform was then evaporated completely under a gentle stream of nitrogen until visibly dry (approximately 20–30 min) and then left under vacuum overnight to dry completely. Then we added 10mL of Milli-Q water to the 50mg of lipids to obtain a final concentration of 10mg/mL in water. The solution was first vortexed for 10 min and then sonicated at 50°C for 30min. The final result of this procedure was a milky solution that we transferred into several 2mL Eppendorf and stored in the -20°C freezer if not used immediately.

The method used for the formation of the supported lipid bilayer was the vesicles fusion. We added 100μL of the lipid solution in Milli-Q previously prepared to 900μL of 20mM NaCl in Milli-Q. The final lipid concentration was 1mg/mL. 1mL of this solution was extruded more than 21 times (but always an odd number of times) at 70°C for DPPA and 55°C for DPPC through a membrane with 100 nm pores (PC Membranes 0.1 μm, Avanti Polar Lipids, Alabama, USA). The lipid vesicles obtained were left to cool down at room temperature and then diluted with the 20mM NaCl solution to a final lipid concentration of 0.1mg/mL (10mL in total).

High quality muscovite mica disks (grade V) were purchased from SPI supply (West Chester, PA, USA) and used in all the experiments. The mica was freshly cleaved with adhesive tape and positioned on the bottom of a low-form cylindrical weighing bottle with a ground glass cup previously cleaned with the procedure described in the cleaning procedure section. The lipid solution was then added on top of the substrates and everything sealed with the glass cup to avoid evaporation.

The jar was put in the oven preheated at 80°C for DPPA and 50°C for DPPC. The transition temperature from liquid to gel state of DPPA is reported to be 67°C and for DPPC 41°C. The initial temperature of the oven has to be set at a temperature higher than the transition temperature and the phase transition has to happen very slowly to give time to the system to reach the thermodynamic equilibrium. We decreased the temperature of the oven from the initial value to 5°C below the transition temperature by lowering 1°C every half an hour. Then, we simply left the oven to cool down at room temperature overnight.

The samples were rinsed copiously with the imaging solution (10mM NaCl, 10mM KCl and 10mM RbCl respectively) before the transfer to the AFM stage. The samples were dried on one side with a precision wipe (KIMTECH) and glued on a metallic disk with carbon tape. The samples were mounted on the AFM stage and a drop of the imaging solution was injected on top of the sample.

4.4.5 Cleaning procedures

The cleaning procedure for the glassware was the following: the glass containers and vials were sonicated for 10 minutes in Milli-Q water, 10 minutes in isopropanol, 10 minutes in Milli-Q water again and then dried in the oven at 60°C. Afterwards, they were put in the UV-ozone cleaner for 30 minutes and immediately rinsed with isopropanol and sonicated again in it for 10min. Finally, the glass containers were rinsed with Milli-Q water, immersed in it for 15 minutes while sonicating, and dried in the oven again.

Bibliography Chapter 4

1. Bard, A. J. & Faulkner, L. R. *Electrochemical Methods*. (Wiley, 2000).
2. Israelachvili, J. N. *Intermolecular and Surface Forces*. 1–706 (ELSEVIER, 2011).
3. Parsegian, V. A. & Gingell, D. On the Electrostatic Interaction across a Salt Solution between Two Bodies Bearing Unequal Charges. *Biophysical Journal* **12**, 1192–1204 (1972).
4. Leng, Y. Hydration Force between Mica Surfaces in Aqueous KCl Electrolyte Solution. *Langmuir* **28**, 5339–5349 (2012).
5. Labuda, A., Kobayashi, K., Suzuki, K., Yamada, H. & Grütter, P. Monotonic Damping in Nanoscopic Hydration Experiments. *Phys. Rev. Lett.* **110**, 066102 (2013).
6. Besteman, K., Van Eijk, K. & Lemay, S. G. Charge inversion accompanies DNA condensation by multivalent ions. *Nat Phys* **3**, 641–644 (2007).
7. Gruen, D. W. R. & Mar elja, S. Spatially varying polarization in water. A model for the electric double layer and the hydration force. *J. Chem. Soc., Faraday Trans. 2* **79**, 225 (1983).
8. Ben-Yaakov, D., Andelman, D. & Podgornik, R. Dielectric decrement as a source of ion-specific effects. *J. Chem. Phys.* **134**, 074705 (2011).
9. Grahame, D. C. The electrical double layer and the theory of electrocapillarity. *Chem. Rev.* **41**, 441–501 (1947).
10. Hiemstra, T. & Van Riemsdijk, W. H. A Surface Structural Approach to Ion Adsorption: The Charge Distribution (CD) Model. *Journal of Colloid and Interface Science* **179**, 488–508 (1996).
11. Lyklema, J. Overcharging, charge reversal: Chemistry or physics? *Colloids Surf., A* **291**, 3–12 (2006).
12. Gurney, R. W. *Ionic processes in solution*. (McGraw-Hill Book Company, Inc, 1953).
13. Collins, K. D. Ions from the Hofmeister series and osmolytes: effects on proteins in solution and in the crystallization process. *Methods* **34**, 300–311 (2004).
14. Marcus, Y. Effect of Ions on the Structure of Water: Structure Making and Breaking. *Chem. Rev.* **109**, 1346–1370 (2009).
15. Kunz, W. Specific ion effects in colloidal and biological systems. *Current Opinion in Colloid & Interface Science* **15**, 34–39 (2010).
16. Parsons, D. F., Deniz, V. & Ninham, B. W. Nonelectrostatic interactions between ions with anisotropic ab initio dynamic polarisabilities. *Colloids Surf., A* **343**, 57–63 (2009).
17. Parsons, D. F., Bostrom, M., Nostro, Lo, P. & Ninham, B. W. Hofmeister effects: interplay of hydration, nonelectrostatic potentials, and ion size. *Physical Chemistry Chemical Physics* **13**, 12352–12367 (2011).

18. Wang, J. & Bard, A. J. Direct Atomic Force Microscopic Determination of Surface Charge at the Gold/Electrolyte Interface: The Inadequacy of Classical GCS Theory in Describing the Double-Layer Charge Distribution. *The Journal of Physical Chemistry B* **105**, 5217–5222 (2001).
19. Attard, P., Mitchell, D. J. & Ninham, B. W. Beyond Poisson–Boltzmann: Images and correlations in the electric double layer. I. Counterions only. *J. Chem. Phys.* **88**, 4987–4996 (1988).
20. Naji, A., Jungblut, S., Moreira, A. G. & Netz, R. R. Electrostatic interactions in strongly coupled soft matter. *Physics Applied to Biological Systems* **352**, 131–170 (2005).
21. Moreira, A. G. & Netz, R. R. Simulations of counterions at charged plates. *Eur. Phys. J. E* **8**, 33–58 (2002).
22. Kjellander, R. & Marčelja, S. Double-layer interaction in the primitive model and the corresponding Poisson–Boltzmann description. *J. Phys. Chem.* **90**, 1230–1232 (1986).
23. Park, C., Fenter, P. A., Sturchio, N. C. & Nagy, K. L. Thermodynamics, Interfacial Structure, and pH Hysteresis of Rb⁺ and Sr²⁺ Adsorption at the Muscovite (001)–Solution Interface. *Langmuir* **24**, 13993–14004 (2008).
24. Kanduč, M., Naji, A., Forsman, J. & Podgornik, R. Dressed counterions: Strong electrostatic coupling in the presence of salt. *J. Chem. Phys.* **132**, 124701–15 (2010).
25. Kanduč, M., Naji, A., Forsman, J. & Podgornik, R. Dressed counterions: Polyvalent and monovalent ions at charged dielectric interfaces. *Phys. Rev. E* **84**, 011502 (2011).
26. Lee, S. S., Fenter, P., Park, C., Sturchio, N. C. & Nagy, K. L. Hydrated Cation Speciation at the Muscovite (001)–Water Interface. *Langmuir* **26**, 16647–16651 (2010).
27. Lee, S. S., Fenter, P., Nagy, K. L. & Sturchio, N. C. Monovalent Ion Adsorption at the Muscovite (001)–Solution Interface: Relationships among Ion Coverage and Speciation, Interfacial Water Structure, and Substrate Relaxation. *Langmuir* **28**, 8637–8650 (2012).
28. Sakuma, H., Kondo, T., Nakao, H., Shiraki, K. & Kawamura, K. Structure of Hydrated Sodium Ions and Water Molecules Adsorbed on the Mica/Water Interface. *J. Phys. Chem. C* **115**, 15959–15964 (2011).
29. Sakuma, H. & Kawamura, K. Structure and dynamics of water on Li⁺, Na⁺, K⁺, Cs⁺, H₃O⁺-exchanged muscovite surfaces: A molecular dynamics study. *Geochimica et Cosmochimica Acta* **75**, 63–81 (2010).
30. Park, S.-H. & Sposito, G. Structure of Water Adsorbed on a Mica Surface. *Phys. Rev. Lett.* **89**, 085501 (2002).
31. Park, C., Fenter, P. A., Nagy, K. L. & Sturchio, N. C. Hydration and Distribution of Ions at the Mica–Water Interface. *Phys. Rev. Lett.* **97**, 016101 (2006).
32. Pashley, R. M. & Israelachvili, J. N. A comparison of surface forces and interfacial properties of mica in purified surfactant solutions. *Colloids and Surfaces* **2**, 169–187 (1981).
33. Kuwahara, Y. Comparison of the surface structure of the tetrahedral sheets of muscovite and phlogopite by AFM. *Phys Chem Min* **28**, 1–8 (2001).
34. Meleshyn, A. Adsorption of Sr²⁺ and Ba²⁺ at the cleaved mica–water interface: Free energy profiles and interfacial structure. *Geochimica et Cosmochimica Acta* **74**, 1485–1497 (2009).
35. Maslova, M. V., Gerasimova, L. G. & Forsling, W. Surface Properties of Cleaved Mica. *Colloid Journal* **66**, 322–328 (2004).
36. Pashley, R. M. DLVO and hydration forces between mica surfaces in Li⁺, Na⁺, K⁺, and Cs⁺ electrolyte solutions: A correlation of double-layer and hydration forces with surface cation exchange properties. *Journal of Colloid and Interface Science* **83**, 531–546 (1981).
37. Meleshyn, A. Potential of Mean Force for Ca²⁺ at the Cleaved Mica–Water Interface. *J. Phys. Chem. C* **113**, 17604–17607 (2009).
38. Meleshyn, A. Potential of Mean Force for Mg²⁺ at the Cleaved Mica–Water Interface. *J. Phys. Chem. C* **113**, 12946–12949 (2009).
39. Loh, S.-H. & Jarvis, S. P. Visualization of Ion Distribution at the Mica–Electrolyte Interface. *Langmuir* **26**, 9176–9178 (2010).
40. Marcus, Y. A simple empirical model describing the thermodynamics of hydration of ions of widely varying charges, sizes, and shapes. *Biophysical Chemistry* **51**, 111–127 (1994).
41. Hribar, B., Southall, N. T., Vlachy, V. & Dill, K. A. How Ions Affect the Structure of Water. *J. Am. Chem. Soc.* **124**, 12302–12311 (2002).
42. Lee, S. S., Fenter, P., Nagy, K. L. & Sturchio, N. C. Monovalent Ion Adsorption at the Muscovite (001)–Solution Interface: Relationships among Ion Coverage and Speciation, Interfacial Water Structure, and Substrate Relaxation. *Langmuir* **28**, 8637–8650 (2012).
43. Love, J. C., Estroff, L. A., Kriebel, J. K., Nuzzo, R. G. & Whitesides, G. M. Self-Assembled Monolayers of Thiolates on Metals as a Form of Nanotechnology. *Chem. Rev.* **105**, 1103–1170

-
- (2005).
44. Munuera, C. & Ocal, C. Real time scanning force microscopy observation of a structural phase transition in self-assembled alkanethiols. *J. Chem. Phys.* **124**, 206102–5 (2006).
 45. Jackson, A. M., Myerson, J. W. & Stellacci, F. Spontaneous assembly of subnanometre-ordered domains in the ligand shell of monolayer-protected nanoparticles. *Nature Materials* **3**, 330–336 (2004).
 46. Liu, Y.-F., Yang, Y.-C. & Lee, Y.-L. Assembly behavior and monolayer characteristics of OH-terminated alkanethiol on Au(111): *in situ* scanning tunneling microscopy and electrochemical studies. *Nanotechnology* **19**, 065609 (2008).
 47. Arce, F. T., Vela, M. E., Salvarezza, R. C. & Arvia, A. J. Dynamic characteristics of adsorbed monolayers of 1-dodecanethiol on gold (111) terraces from in-situ scanning tunneling microscopy imaging. *Electrochimica Acta* **44**, 1053–1067 (1998).
 48. Esplandiú, M., Carot, M., Cometto, F., Macagno, V. & Patrito, E. M. Electrochemical STM investigation of 1,8-octanedithiol monolayers on Au(111). Experimental and theoretical study. *Surface Science* **600**, 155–172 (2006).
 49. Fukuma, T., Kobayashi, K., Horiuchi, T., Yamada, H. & Matsushige, K. Alkanethiol self-assembled monolayers on Au(111) surfaces investigated by non-contact AFM. *Appl Phys A* **72**, S109–S112 (2014).
 50. Fukuma, T., Ichii, T., Kobayashi, K., Yamada, H. & Matsushige, K. True-molecular resolution imaging by frequency modulation atomic force microscopy in various environments. *Appl. Phys. Lett.* **86**, 034103 (2005).
 51. Hiasa, T., Kimura, K. & Onishi, H. Minitips in Frequency-Modulation Atomic Force Microscopy at Liquid–Solid Interfaces. *Jpn. J. Appl. Phys.* **51**, 025703 (2012).
 52. Hiasa, T., Kimura, K. & Onishi, H. Hydration of hydrophilic thiolate monolayers visualized by atomic force microscopy. *Phys. Chem. Chem. Phys.* **14**, 8419 (2012).
 53. Hiasa, T. & Onishi, H. Mercaptohexanol assembled on gold: FM-AFM imaging in water. *Colloids Surf., A* **441**, 149–154 (2014).
 54. Kuna, J. J. *et al.* The effect of nanometre-scale structure on interfacial energy. *Nature Materials* **8**, 837–842 (2009).
 55. Fukuma, T., Ueda, Y., Yoshioka, S. & Asakawa, H. Atomic-Scale Distribution of Water Molecules at the Mica-Water Interface Visualized by Three-Dimensional Scanning Force Microscopy. *Phys. Rev. Lett.* **104**, 016101 (2010).
 56. Verma, A. *et al.* Surface-structure-regulated cell-membrane penetration by monolayer-protected nanoparticles. *Nature Materials* **7**, 588–595 (2008).
 57. Dougherty, G. M. *et al.* The zeta potential of surface-functionalized metallic nanorod particles in aqueous solution. *ELECTROPHORESIS* **29**, 1131–1139 (2008).
 58. Fukuma, T., Higgins, M. J. & Jarvis, S. P. Direct Imaging of Individual Intrinsic Hydration Layers on Lipid Bilayers at Ångstrom Resolution. *Biophysical Journal* **92**, 3603–3609 (2007).
 59. Asakawa, H., Yoshioka, S., Nishimura, K.-I. & Fukuma, T. Spatial distribution of lipid headgroups and water molecules at membrane/water interfaces visualized by three-dimensional scanning force microscopy. *ACS Nano* **6**, 9013–9020 (2012).
 60. Mulkidjanian, A. Y., Heberle, J. & Cherepanov, D. A. Protons @ interfaces: Implications for biological energy conversion. *Biochimica et Biophysica Acta (BBA)* **1757**, 913–930 (2006).
 61. Contera, S. A., Voitchovsky, K. & Ryan, J. F. Controlled ionic condensation at the surface of a native extremophile membrane. *Nanoscale* **2**, 222 (2010).
 62. Lacoste, D., Menon, G., Bazant, M. & Joanny, J. Electrostatic and electrokinetic contributions to the elastic moduli of a driven membrane. **28**, 243–264 (2009).
 63. Higgins, M. J. *et al.* Structured Water Layers Adjacent to Biological Membranes. *Biophysical Journal* **91**, 2532–2542 (2006).
 64. Ferber, U. M., Kaggwa, G. & Jarvis, S. P. Direct imaging of salt effects on lipid bilayer ordering at sub-molecular resolution. *Eur Biophys J* **40**, 329–338 (2010).
 65. Akutsu, H. & Seelig, J. Interaction of metal ions with phosphatidylcholine bilayer membranes. *Biochemistry* **20**, 7366–7373 (1981).
 66. Lee, S.-J., Song, Y. & Baker, N. A. Molecular Dynamics Simulations of Asymmetric NaCl and KCl Solutions Separated by Phosphatidylcholine Bilayers: Potential Drops and Structural Changes Induced by Strong Na⁺-Lipid Interactions and Finite Size Effects. *Biophysical Journal* **94**, 3565–3576 (2008).
 67. Pandit, S. A., Bostick, D. & Berkowitz, M. L. Molecular Dynamics Simulation of a Dipalmitoylphosphatidylcholine Bilayer with NaCl. *Biophys J* **84**, 3743–3750 (2003).
 68. Garcia-Celma, J. J., Hatahet, L., Kunz, W. & Fendler, K. Specific Anion and Cation Binding to

-
- Lipid Membranes Investigated on a Solid Supported Membrane. *Langmuir* **23**, 10074–10080 (2007).
69. Fukuma, T., Higgins, M. & Jarvis, S. Direct Imaging of Lipid-Ion Network Formation under Physiological Conditions by Frequency Modulation Atomic Force Microscopy. *Phys. Rev. Lett.* **98**, (2007).
 70. Blackwood, R. A. *et al.* Phospholipase D activity facilitates Ca²⁺-induced aggregation and fusion of complex liposomes. *American Journal of Physiology-Cell Physiology* **41**, C1279 (1997).
 71. Weigert, R. *et al.* CtBP/BARS induces fission of Golgi membranes by acylating lysophosphatidic acid. *Nature* **402**, 429–433 (1999).
 72. Farauo, J. & Travesset, A. Phosphatidic Acid Domains in Membranes: Effect of Divalent Counterions. *Biophysical Journal* **92**, 2806–2818 (2007).
 73. Bu, W., Vaknin, D. & Travesset, A. Monovalent counterion distributions at highly charged water interfaces: Proton-transfer and Poisson-Boltzmann theory. *Phys. Rev. E* (2005).
 74. Bu, W., Vaknin, D. & Travesset, A. How Accurate Is Poisson-Boltzmann Theory for Monovalent Ions near Highly Charged Interfaces? *Langmuir* (2006).
 75. Butt, H.-J., Cappella, B. & Kappl, M. Force measurements with the atomic force microscope: Technique, interpretation and applications. *Surface Science Reports* **59**, 1–152 (2005).
 76. Richardson, S. M. & Richardson, J. W. Crystal structure of a pink muscovite from Archer's Post, Kenya: Implications from reverse pleochroism in dioctahedral mica. *American Mineralogist* **67**, 69–75 (1982).
 77. Cygan, R. T., Liang, J. J. & Kalinichev, A. G. Molecular Models of Hydroxide, Oxyhydroxide, and Clay Phases and the Development of a General Force Field. *The Journal of Physical Chemistry B* **108**, 1255–1266 (2004).
 78. Brooks, B. R. *et al.* CHARMM: The biomolecular simulation program. *J. Comput. Chem.* **30**, 1545–1614 (2009).
 79. Heine, D. R., Rammohan, A. R. & Balakrishnan, J. Atomistic simulations of the interaction between lipid bilayers and substrates. *Molecular Simulation* **33**, 391–397 (2007).
 80. Christina M Payne, Xiongce Zhao, Lukas Vlcek, A. Peter T Cummings. Molecular Dynamics Simulation of ss-DNA Translocation between Copper Nanoelectrodes Incorporating Electrode Charge Dynamics. *The Journal of Physical Chemistry B* **112**, 1712–1717 (2008).
 81. Skelton, A. A., Fenter, P., Kubicki, J. D., Wesolowski, D. J. & Cummings, P. T. Simulations of the Quartz(1011)/Water Interface: A Comparison of Classical Force Fields, Ab Initio Molecular Dynamics, and X-ray Reflectivity Experiments. *J. Phys. Chem. C* **115**, 2076–2088 (2011).
 82. Phillips, J. C. *et al.* Scalable molecular dynamics with NAMD. *J. Comput. Chem.* **26**, 1781–1802 (2005).
 83. Humphrey, W., Dalke, A. & Schulten, K. VMD: visual molecular dynamics. *J Mol Graph* **14**, 33–8, 27–8 (1996).
 84. Michaud-Agrawal, N., Denning, E. J., Woolf, T. B. & Beckstein, O. MDAAnalysis: A toolkit for the analysis of molecular dynamics simulations. *J. Comput. Chem.* **32**, 2319–2327 (2011).
 85. Ricci, M., Spijker, P., Stellacci, F., Molinari, J.-F. & Voitchovsky, K. Direct Visualization of Single Ions in the Stern Layer of Calcite. *Langmuir* **29**, 2207–2216 (2013).
 86. Wang, J., Kalinichev, A. G., Kirkpatrick, R. J. & Cygan, R. T. Structure, Energetics, and Dynamics of Water Adsorbed on the Muscovite (001) Surface: A Molecular Dynamics Simulation. *The Journal of Physical Chemistry B* **109**, 15893–15905 (2005).

Chapter 5

The dynamic interface between calcite and ionic solutions

In this chapter, I will examine the molecular surface topography and properties of the calcite ($10\bar{1}4$) surface (section 5.1.1) in presence of aqueous ionic solutions. First, a discussion on the hydration landscape of the surface and the development of a surface charge will be presented (section 5.1.2). A study of the interaction of specific ions such as Na^+ , Rb^+ , Cl^- and Ca^{2+} with calcite's surface by means of high-resolution AFM and MD-simulations (section 5.1.3) will follow. I will show that the hydration properties of the flat areas prevent the ions, which constitute the crystal and are dissolved in solution, to directly contact the surface's groups. However, dissolution and growth are well-known and documented phenomena that require the exchange of ions between the surface and the solution. These processes take place at the step edges (section 5.2.1) where the hydration properties are different from those of flat areas and are specific to the type of step considered. I will finally present a series of experiments in which the growth and dissolution of the crystal is monitored in real time as a function of the ionic composition and concentration of the solution (section 5.2.2). The results demonstrate how specific ionic effects can modify the shape of the newly grown steps depending on the type of ions.

5.1 Interaction of ions with the $(10\bar{1}4)$ surface of calcite

Calcite (calcium carbonate, chemical formula CaCO_3) is among the main components of the earth's crust where it can primarily be found in sedimentary rocks such as limestone.¹ It is also the main constituent of the shells of marine organisms, and the relative abundance is largely linked to bio-mineralization processes.^{2,4} Calcite can grow or dissolve rapidly depending on the environment⁵ and plays a fundamental role in preserving the biosphere through the ability to regulate the acidity of oceans.⁶ The dynamical physico-chemical transformation occurring at the surface is also key to countless industrial processes, for example in the polymer industry,⁷ cement manufacturing,⁸ nuclear waste storage,^{9,10} waste water treatment¹¹ and the petroleum industry¹²⁻¹⁵. The large majority of these processes strongly depend on reactions occurring at the interface between the surface of calcite and a surrounding aqueous environment. Water molecules,^{16,17} ions,¹⁸⁻²¹ biomolecules²² or organic components¹² (see also Chapter 6) can all interact with calcite's surface and influence the morphology, crystal growth and dissolution as well as the structural properties.²³⁻²⁶

Most experimental investigations rely on surface- or interface-sensitive techniques, such as low-energy electron diffraction,²⁷ X-ray reflectivity,^{17,28} photoelectron spectroscopy,^{16,27} and AFM²⁹⁻³⁴. Most AFM studies are primarily focused on the reactions and surface dynamics occurring out of equilibrium at calcite's atomic step-edges (see section 5.2). Furthermore, investigations providing an atomic-level description of both the calcite surface and the interacting molecule or ion considered are scarce, particularly in conditions near equilibrium. Although experimentally more challenging, this type of investigation can provide valuable insight into slowly evolving systems such as oceanic floors and oil reservoirs, where water, ions and organic molecules are in contact mainly with calcite's surface.³⁵

Here, I present different means of interaction between single metal ions and the $(10\bar{1}4)$ surface of calcite (subsection 5.1.1). Away from steps, the crystallographic alternation of the calcium atoms and carbonate groups at the $(10\bar{1}4)$ surface (Fig. 5.1A) induces strong local variations in rock's surface charge. This charge distribution is particularly suitable for adsorbed water molecules that can orient the oxygen atom towards the calcium and the hydrogen atoms toward the carbonates (see section 5.1.2).^{16,19} As a result, the surface is hydrophilic, and if the calcite is exposed to standard atmospheric humidity, several nanometers of water condense on it.³⁶ Most small charged molecules or ions have to pay a substantial energetic penalty to reach calcite's surface. This penalty represents the cost of stripping the molecule from the hydration shell as it traverses the surface-bound water layers.³⁷ Given the peculiar hydration properties and the surface structure of the $(10\bar{1}4)$ calcite surface, the adsorption of a particular ion depends on the hydration energy and charge (see section 5.1.3).

5.1.1 Surface structure of the $(10\bar{1}4)$ cleavage plane of calcite

Numerous theoretical and experimental studies have focused on the $(10\bar{1}4)$ cleavage plane of calcite, the most stable and abundant facet.³⁴ The crystalline structure of bulk calcite and of the $(10\bar{1}4)$ cleavage plane is presented in Fig. 5.1A. Calcite possesses a trigonal-rhombohedral bulk unit cell (R $\bar{3}2/m$ space group).³⁸ The bulk-truncated, unreconstructed $(10\bar{1}4)$ surface of calcite has a rectangular unit cell with dimensions of $4.99 \times 8.10 \text{ \AA}^2$ comprising two calcium ions and two carbonate (CO_3) groups. The unit cell vectors are oriented along the $[010]$ and $[\bar{4}\bar{2}1]$ crystallographic directions. The carbonate groups, in the bulk, are tilted by an angle of 44.63° with respect to the $(10\bar{1}4)$ plane,^{16,19} with one oxygen atom protruding above the plane and the others lying below (Fig. 5.1A). Additionally, these two carbonate groups are rotated with respect to each other, causing the topmost oxygen atom to point either to the left or to the right in a zigzag fashion along the $[\bar{4}\bar{2}1]$ direction (Fig. 5.1A-B) as often reported in AFM studies.²⁹⁻³³

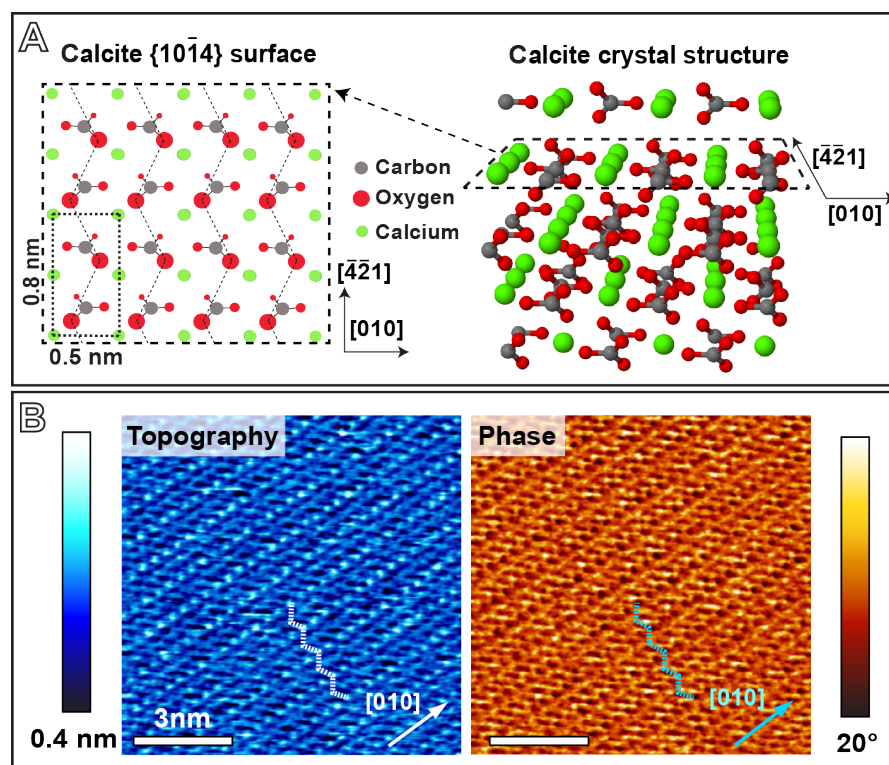


Fig. 5.1: (A) Crystal structure of calcite. The atomic arrangement of the calcium and carbonate ions is shown for the bulk crystal (right) and the $(10\bar{1}4)$ surface (left), together with the main crystallographic directions and the unreconstructed unit cell. The zigzag patterns of the protruding oxygen atoms of the $(10\bar{1}4)$ surface are marked with thin dotted lines. (B) Typical AM-AFM image of the $(10\bar{1}4)$ surface equilibrated in ultrapure water. Both the topography and phase image are shown. The zigzag structure is indicated by a dotted line in both images. The contrast obtained is the V_1 according to the classification of Rahe *et al.*³⁰ (see text).

The $(10\bar{1}4)$ surface belongs to the plane symmetry group pg , which contains glide reflections as the only symmetry element. A glide reflection is a combination of a reflection with respect to a given line and a translation along it. For CaCO_3 only one glide reflection axis oriented along the $[4\bar{2}1]$ direction with a shift of half unit cell along that direction is found.³⁹ Early AFM and low-energy electron diffraction (LEED) experiments have indicated the existence of two surface reconstructions. One reconstruction is known as the “row-pairing” reconstruction, and the other has been identified as a (2×1) reconstruction. While the (2×1) reconstruction has now been observed with techniques different from AFM such as LEED¹⁶ and is, thus, considered a real surface property, the “row-pairing reconstruction” has so far only been identified by AFM.

The results of these reconstructions on the image contrast obtained in high resolution images was thoroughly analyzed by Rahe *et al.*³⁰ in UHV. They propose a classification of the type of contrast obtained in FM-AFM, depending on modulation of the “vertical” (V_i , modulation of the protruding height of the surface features) or the “lateral” (L_i , lateral disposition of the surface features) contrast of the base contrast B (see Fig. 5.2). Even if the conditions of image acquisition in our experiments differ from those by Rahe *et al.*³⁰ (we use AM-AFM in liquid, they carried out FM-AFM in UHV), the proposed classification is nonetheless useful to qualitatively discuss our results and I will use it to categorize our AFM images whenever possible. Interestingly, the presence of the ions in the imaging solution induces deviation from the ‘standard’ imaging contrast that can be characterized by this classification.

The (2×1) reconstruction

The (2×1) reconstruction consists in a modulation of the contrast along the $[010]$ direction, resulting in the appearance of one spot every two as higher. First experimental indication for a (2×1) reconstruction has been observed by Stipp *et al.* using LEED.^{16,27} Later, this reconstruction

has directly been revealed by different research groups using both contact mode AFM in liquid³¹ and FM-AFM in liquid³³ and vacuum^{29,30}. However, similar AFM studies by other groups did not reveal this reconstruction, prompting a debate in literature whether the (2×1) reconstruction is a true surface property. A possible explanation of this contradiction was given by Stipp *et al.*¹⁶ proposing an adsorbate-induced effect due to the presence of water molecules. Subsequently, computer simulations showed that this reconstruction is a structural phenomena and not simply a result of surface hydration.^{40,41} Akiyama *et al.*⁴² used density-functional theory simulations to show that the energy difference between the reconstructed and unreconstructed surface is small and that the formation of cleavage steps, which occasionally appear on the surface, could change the relative stability between the two. These experimental and theoretical works suggest that the (2×1) reconstruction is a real feature of the calcite surface, even if not always present or observable with AFM.

The “row-pairing” reconstruction

The “row-pairing” is a reconstruction within the surface unit cell. It has been observed only with AFM, both in liquid^{31,33} and vacuum^{29,30,39}. The contrast observed in the high-resolution AFM images consists in the variation of the height of the two protruding feature within the unit cell. The result is an alternation along the $[\bar{4}21]$ direction of rows of ‘prominent’ and ‘sunken’ protrusions. For the sake of clarity these terms (‘prominent’ and ‘sunken’) will be used throughout this thesis for designating the respective rows of protruding features when the ‘row pairing’ is visible. If the AFM contrast is given by the protruding oxygen atoms, which is still under debate³⁰, they should be equivalent and no contrast variation is expected in the bulk truncated surface. Physically, the difference could arise from a rotation of the CO_3 groups as proposed by Jin *et al.*⁴³ or any other structural or electronic reconfiguration. The other possibility is the existence of a tip-induced effect that creates a difference in interaction between the probe and the two carbonate groups. In our experimental images this type of reconstruction is often present. The “row-pairing” is well visible in the topographic image of Fig. 5.2 with every other row of oxygen atoms along the $[\bar{4}21]$ direction appearing more prominent. Since no other techniques than AFM have been able to detect this controversial reconstruction, the same existence is still under debate and the hypothesis of an intrinsic measurement artifact is currently preferred.

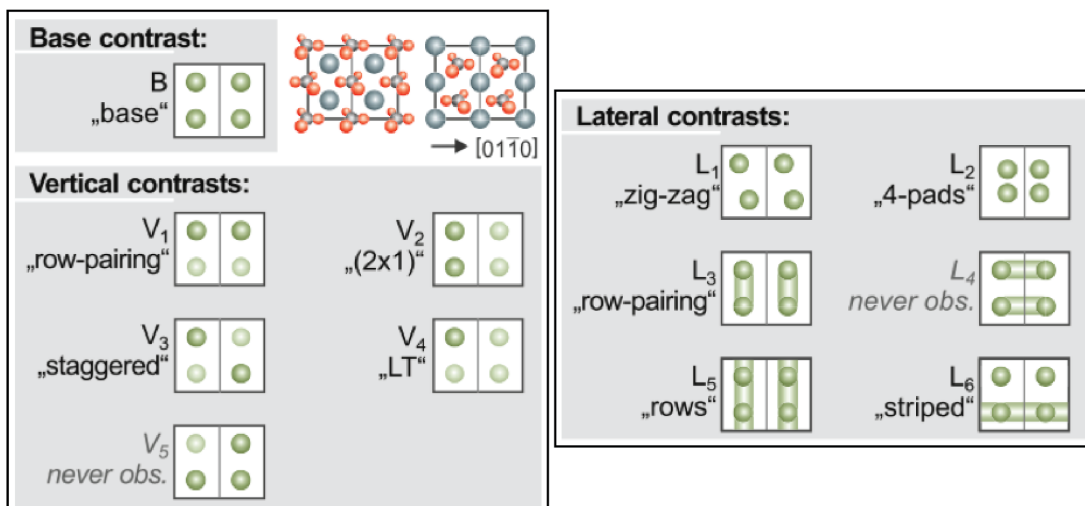
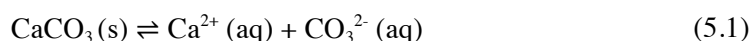


Fig. 5.2: Classification scheme proposed by Rahe *et al.*³⁰ describing the FM-AFM contrasts on the calcite $(10\bar{1}4)$ surface. Up to four interaction maxima are present within the (2×1) surface reconstructed cell. The difference in these maxima lateral positions and intensities gives rise to three classes of contrast: (i) ‘base’ contrast mode B , (ii) vertical contrast modes V_i and (iii) lateral contrast modes L_i . Figure adapted from Ref. [30].

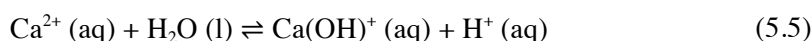
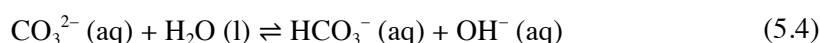
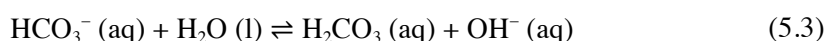
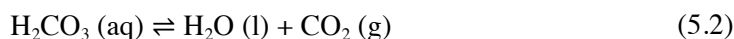
5.1.2 Hydration properties and surface charge of the calcite

The surface charge of oxide minerals results from a charge excess that develops as the surface equilibrates with the contacting solution. In a conceptual model, the termination of an oxide bulk structure results in dangling bonds on the outer-most oxygen and metal atoms. These atoms, once in contact with the water solution, react with the H^+ and OH^- ions that can adsorb on the oxygen atoms or on the metal ions respectively. Each mineral has a characteristic surface charge that is a function of the activity of the potential-determining ions, typically H^+ and OH^- . The pH at which particles of the considered oxide have no surface charge is defined as the point of zero charge (pH_{pzc}). This should, in principle, be independent from other ionic species in solution. The case of calcite is much more complex. Stipp¹⁶ suggested that the differences between calcite and the other oxides result from the particular character of oxygen atoms in the crystal. In oxides, oxygen coordinate directly with metal cations, whereas in carbonates, it is covalently bonded in CO_3^{2-} groups. As a result, the resultant charge on the dangling O site as well as the character of electron-sharing are different for the two types of solids.

The first main difference between the calcite surface and the standard oxide minerals is the fact that as soon as it is in contact with the water solution desorption or adsorption of Ca^{2+} and CO_3^{2-} start to take place. This process mainly happens at the step edges because of the specific hydration properties of the flat (10 $\bar{1}$ 4) surface (see subsection 5.2.1). The thermodynamic processes of calcite dissolution and growth in aqueous solutions is described by Eriksson *et al.*⁴⁴. Calcite dissolves in water according to the following reaction:



At equilibrium, the pH and distribution of different ionic species are dependent on the partial pressure of CO_2 in solution. In other words, the species distribution can be controlled by modifying the pH and the concentration of CO_2 in the solution. The governing reactions are:



Once in solution desorbed ions can react with H^+ , OH^- and CO_2 according to the Reactions 5.1-5.6. An equilibrium between the dissolved species and the external CO_2 pressure occurs at a certain pH called ‘equilibrium pH’, which generally differs from the initial pH value of the non-equilibrated ionic solution. The term ‘equilibrium pH’ is rather ambiguous for calcite dispersions, since it is a very dynamic system as pointed out by Eriksson *et al.*⁴⁴. Somasundaran *et al.*⁴⁵ studied pH changes in calcite dispersions as a function of time and concluded: “upon addition of the calcite particles the change in pH is ‘immediate’ and after the initial change in pH, it may slowly drift (in one direction, maximum around one pH unit) for a period of several weeks”.

Even for calcite we can define, similarly to other metal oxides, the pH_{pzc} at which the surface charge is zero. However for calcite, pH_{pzc} varies considerably depending on the sample’s source, history, and dissolved Ca^{2+} and carbonate species.¹⁶ This suggests that potential-determining ions are bonded differently than on the other oxide mineral. Foxall *et al.*⁴⁶ showed that the potential-determining ions for calcite are Ca^{2+} and CO_3^{2-} , not H^+ and OH^- . They stated that the role of pH is only to control whether the carbonate ion species that dominate in solution are CO_3^{2-} , HCO_3^- or H_2CO_3 . They showed that when pCa is constant, the zeta-potential, is also constant, independent of pH. The results suggest that the concept of pH_{pzc} for this system is not a meaningful parameter but rather of pCa_{pzc} and pCO_{3pzc} should be used in the case of calcite, an argument also supported

by Stipp *et al.*¹⁶.

The main controversy, in the case of the surface charge of calcite, arises from the indisputable, molecular-scale evidence for the presence of strongly bound water molecules on the surfaces that do not enable the direct contact between the potential-determining ions and the surface. In fact, Ca^{2+} and the other negatively charged ionic species are generally shown to not form inner-sphere complexes on the calcite surface as expected from the ions that regulate the surface charge in the classical picture of the Stern Layer. To solve this discrepancy, both Stipp¹⁶ and Heberling *et al.*¹⁹ proposed to place the slip plane further apart from the actual calcite surface to include the layers of structured water, the ions at the OHP and even some ions that reside in the diffuse layer. For Stipp, the dangling bonds at the surface satisfy themselves with chemisorbed H and OH. Because of their chemical nature, this surface- H and OH bonds are much stronger than the surface-potential determining ions interaction energy. Thus, the terminated calcite surface is hydrolyzed with a layer of H and OH to satisfy the local charge imbalance.¹⁶ Heberling *et al.*¹⁹ combined surface diffraction techniques and zeta potential measurements of calcite suspensions in equilibrium (and not) in a varying ionic solution. They again found that carbonate and calcium ions are the charge-determining ions and changes in pH have only a weak effect in non-equilibrium solutions. However, the data cannot be explained with a full hydrolysis layer: they found that the reaction of the water molecules with the surface produces a negative charge at the surface level in a range of pH varying between 5 and 11 (from the non-equilibrium data). Ions such as Ca^{2+} and CaCO_3^{2-} (or the other possible ionic species) adsorb in the OHP that is spaced from the surface by two water molecule layers. In this case, the zeta potential is mainly determined by outer-sphere adsorbed ions similarly to Stipp¹⁶. In reality the situation is even more complex since the calcite surface reactivity is controlled even by the topography.^{47,48}

What is generally accepted and reported by most of the surface diffraction technique are two well-ordered layers of water molecules at the calcite surface. MD-simulations of the calcite-water system, performed by our collaborator Peter Spijker, showed a strong ordering of water near the calcite surface (see Fig. 5.3A), as expected from the experiments and literature.^{16,19,49} The computed density profiles (see Fig. 5.3B) perpendicular to the surface was in good agreement with comparable X-ray scattering measurements¹⁷ and other numerical simulations.^{50,51} Two main peaks of oxygen density at the calcite surface are individuated (see Fig. 5.3B). The ordering of the layers can be seen not only in the direction perpendicular to the surface. In fact, water molecules of the first layer are preferentially located above the surface calcium ions with the oxygen atoms pointing toward the surface. Even the water molecules of the second layer are preferentially located above the surface carbonate ions with one hydrogen atom pointing towards the oxygen of the carbonate group (see Fig. 5.3A).

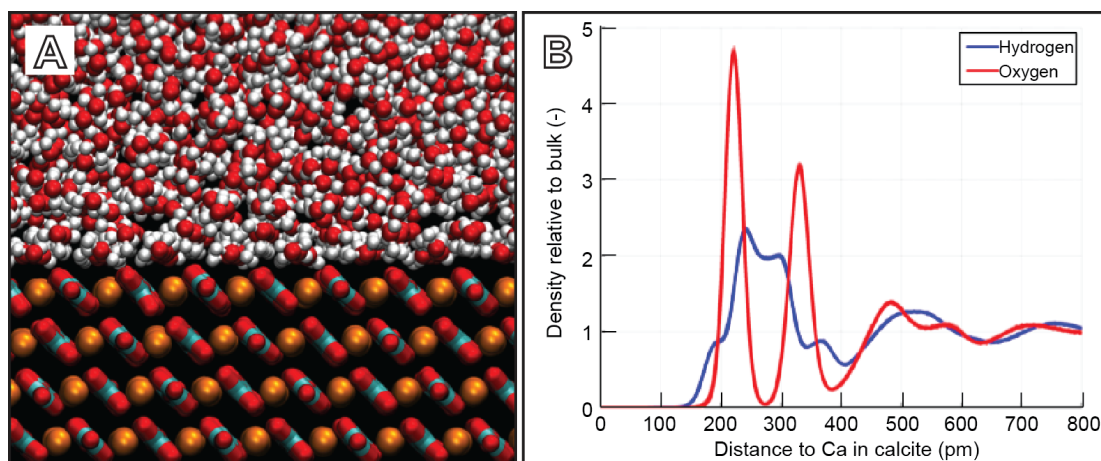


Fig. 5.3: (A) Snapshot of the simulated calcite-water interface. The calcium (orange) and carbonates (red/blue) of the calcite crystal are visible. The oxygen and the hydrogen atoms of the water molecules are depicted in red and white, respectively. Ions in solution have been omitted for clarity. (B) Water density perpendicular to the calcite surface, representing the density oxygen atoms (red) and hydrogen atoms (blue). The density is normalized with respect to the density in the bulk water phase and the surface calcium atoms are used as a reference for the distance measurement.

The peaks in oxygen density reflect a 2D ordered structure of water molecules parallel to the surface. The lateral density variation of the oxygen atoms in the first and second layer (Fig. 5.4A) showed the typical structure observed in AFM experiments (e.g. Fig. 5.1B), including the zigzag structure described previously. Although a density profile cannot be directly compared with the topography and phase images obtained from AFM measurements, the striking resemblance provides at least qualitative insight. A more careful examination of the lateral arrangement of the water density presented in Fig. 5.4A, revealed two vertical rows (around 1 nm and 7 nm) where the zigzag structure is broken. Analysis of the trajectory of the simulations revealed that, during the minimization and relaxation of the crystal structure, one carbonate molecule in each of these two rows is spontaneously rotated, subsequently forcing the entire carbonate row to rotate as well. Although not of direct significance in the present results, the actual rotating process is interesting and deserves some more detailed analysis in the future, considering the current debate about the reconstruction of calcite's surface (see subsection 5.1.1).

5.1.3 Ion adsorption on the calcite surface

Calcite ($10\bar{1}4$) exhibits peculiar hydration properties. Here we examine the consequences for the arrangement of adsorbing ions at the surface. I first present the MD-simulations and then the corresponding AFM experiment of the calcite surface at equilibrium with different ionic solution.

MD-simulations of ion adsorption: Na^+ , Cl^- and Ca^{2+}

Our collaborator Peter Spijker performed a series of MD-simulations of a flat calcite surface in contact with two ionic solutions in which either NaCl or CaCl_2 were dissolved. The concentration of ions used in the MD-simulations is high (~ 250 mM) when compared to the experiments. This strategy was applied in order to get sufficient statistics in the short time scale of the simulations. Combining the results of ten independent runs for each ion-pair allowed for the computation of a clean density distribution perpendicular to the surface (see Fig. 5.4B). These density distributions are in good agreement with previous numerical simulations of similar systems^{52,53} and showed that none of the ions manage to penetrate the final water layer to reach the calcite surface.

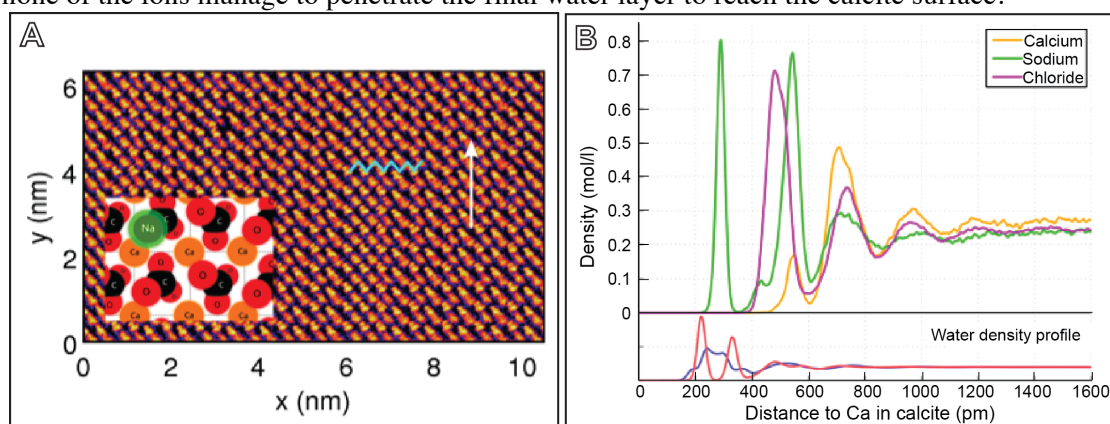


Fig. 5.4: (A) Density distribution for oxygen atoms (H_2O) in the first and second structured layer parallel to the calcite surface. The zigzag structure ascribable to the calcite surface is indicated with the blue line as well as the [010] direction (white arrow). The inset shows schematically sodium ions closest to the surface being typically located above the nearby oxygen of the carbonate group. (B) Density profiles (mol/l) for three different ions (Na^+ , Ca^{2+} and Cl^-) perpendicular to the calcite surface. The density of the water atoms is given at the bottom for comparison (see also Fig. 5.3B).

Sodium gets closest but remains on top of the first water layer. Calcium ions mostly remain outside calcite's structured water as well as Cl^- . This is in good agreement with the model proposed by both Stipp¹⁶ and Heberling *et al.*⁴⁹. To clarify these results a 2D-density distribution of water perpendicular to the surface is shown (Fig. 5.5), where the locations of several arbitrary but representative ions are indicated. In the inset of Fig. 5.4A the location of the sodium ions when closest to the surface is presented: above the oxygen atoms of the carbonate groups

protruding above the surface plane. These ions take the place of one of the water molecules of the second hydration layer.

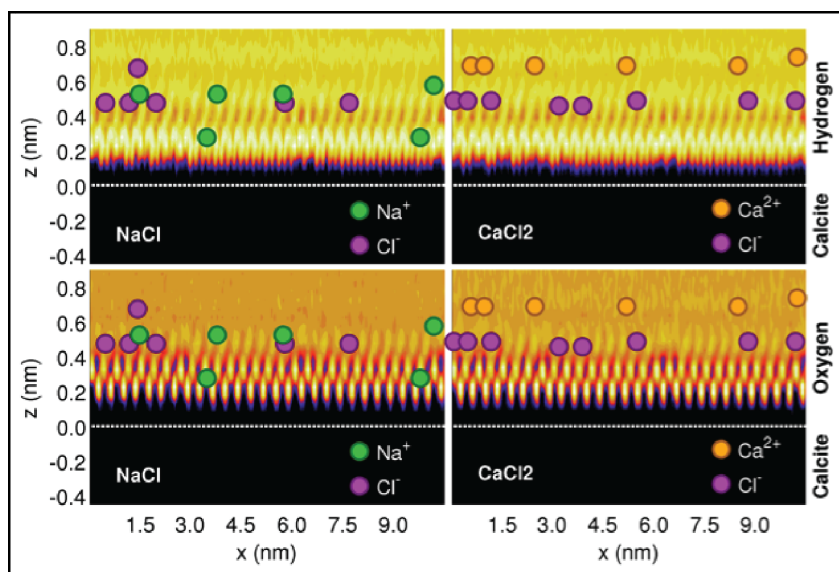


Fig. 5.5: Two-dimensional density distribution of the hydrogen (top) and oxygen (bottom) atoms of water molecules perpendicular to the calcite surface reconstructed from MD-simulations. The brighter colors (yellow) represent higher densities for a given location. A clear multilayered structure is visible (up to three hydration layers are easily identifiable). Sites corresponding to high concentrations of ions (Na^+ , Ca^{2+} , Cl^-) are indicated by the colored circles (orange Ca^{2+} , green Na^+ , and purple Cl^-). Sodium ions get closer to the surface than any of the other ions. The dotted white line indicates the plane containing the calcium atoms of calcite's surface. This plane is used as the origin of distance measurements on the z-axis.

AFM imaging of calcite in Sodium Chloride

The (10 $\bar{1}$ 4) surface of calcite imaged in the presence of added NaCl is shown in Fig. 5.6. At 1mM NaCl (pH 8.0 \pm 0.1, see Fig. 5.6E), as well as at 5mM NaCl (pH 7.9 \pm 0.1), the calcite surface appeared very similar to the images obtained in equilibrated pure water (pH 8.4 \pm 0.1, Fig. 5.1B). The “row-pairing” reconstruction can be recognized.

At 10mM NaCl (pH 7.8 \pm 0.1), the prominent oxygen rows sometimes appeared locally broader (Fig. 5.6A, red arrows) because of the additional protrusions located on the surface. These protrusions were, however, unstable and could easily be removed by increasing the force exerted by the AFM tip on the surface. By decreasing the imaging setpoint it was possible to recover the alternated oxygen rows (Fig. 5.6B), similarly to those obtained at lower salt concentration or in water.

Using gentle scanning conditions, we were able to obtain higher resolution images of the salt-induced protrusions (Fig. 5.6C, red arrow). These showed the occasional adsorption of ~ 3 Å wide objects adjacent to the prominent oxygen atoms and opposite to the underlying surface calcium ions. We attributed these objects to hydrated Na^+ ions (Fig. 5.6D). This is particularly clear when the surface unit cells are highlighted as in Fig. 5.7A (red arrows point to Na^+ ions). This observation is compatible with MD-simulations results apart for a small deviation: the AFM results showed the hydrated Na^+ adjacent to the prominent carbonate oxygen while the MD-simulations showed the Na^+ exactly on top of the oxygen (see Fig.5.4A). This small discrepancy may be explained in two different manners. First, the AFM is perturbing the system during the imaging process. The imaged ion is confined between the calcite surface and the AFM tip. Thus, the resulting potential minimum may not necessarily be located exactly on top of the considered oxygen atom. This effect is expected to strongly depend on the imaging conditions such as the tip shape and average pressure on the sample. Second, the oxygen “row pairing”, visible in the AFM, may shift the equilibrium position of the monovalent cations with respect to the MD-simulations where this surface reconstruction is not visible. Moreover, by repeating the experiment several times, we occasionally observed a height modulation of the most prominent oxygen atoms instead of the usual adjacent Na^+ -induced protrusion. This is visible in Fig. 5.7B where a profile taken

over the prominent oxygen row (red) is compared to a profile obtained over the adjacent sunk oxygen row (yellow). In the red profile, some of the protrusions appeared unusually high compared to the neighboring oxygen atoms, suggesting that they were effectively induced by a Na^+ ion, forming a complex hydration structure on the surface. These unusually high protrusions appeared randomly distributed along the $[010]$ direction and did not follow any particular surface reconstruction pattern. Although only occasionally observed, this picture is fully consistent with the MD-simulations predictions and further support the hypothesis that adsorbed Na^+ ions explore several minima of the energy landscape when imaged by the AFM tip.

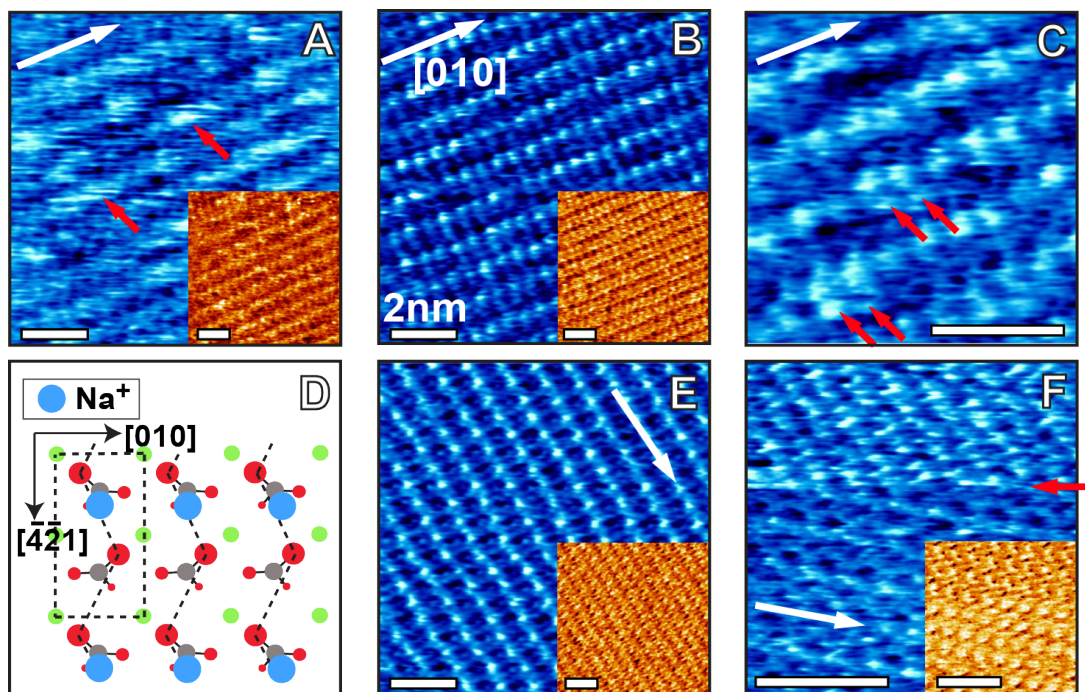


Fig. 5.6: Calcite's $(10\bar{1}4)$ surface imaged in NaCl. The topography appears in blue and the phase is shown as inset in yellow color scale. The phase images provide an indication of the local interfacial energy with darker regions corresponding to local energy minima. At 1mM (E), no significant difference with the equilibrated water case can be seen. The contrast in (E) is L_6+V_1 , according to Rahe *et al.*³⁰. At 10mM (A, C) new protrusions appear on the surface, locally broadening the prominent oxygen rows along $[010]$ direction (red arrows). Decreasing the scanning setpoint (larger tip-sample pressure) removes the protrusions (B) and the surface appears again similar to when imaged in water. The contrast in (B) is V_1 , according to Rahe *et al.*³⁰ (C) Higher resolution imaging over the protrusions suggests that Na^+ ions are located next to the protruding oxygen atoms of the carbonate group. The contrast in (C) is a modulated V_1 , according to Rahe *et al.*³⁰ (D) Cartoon representation of the presumed location of adsorbed Na^+ ions at 10mM NaCl. Increasing the NaCl concentrations to 100mM (F) shows a surface almost covered with ions (upper part), which can be removed using harsher imaging conditions (red arrow, lower part). In all images, the white arrow indicates the $[010]$ direction.

At 100mM (pH 8.2 ± 0.1) considerably more protrusions were visible (Fig. 5.6F) and the “row pairing” was less clear, probably due to the adsorbed ions. Lowering the setpoint did still induce a transition (Fig. 5.6F, red arrow) but a direct interpretation of the images becomes more difficult. Firstly the surface is expected to have much higher ion coverage; therefore Cl^- ions may have to be considered to ensure charge neutrality. Secondly the surface charge of the tip could have artificially increased the apparent ionic coverage (see section 3.6 for the tip effects during AFM imaging). This second effect becomes evident in CaCl_2 .

In order to further confirm the presence of adsorbed ions at 10mM NaCl, we acquired simultaneous amplitude and phase versus distance curves (spectroscopy) in conditions identical to those used for imaging. A selection of ten representative curves is presented in Fig. 5.8 and compared with the same results obtained in water. In each case, one curve has been highlighted in red. In water, both the amplitude and phase were well reproducible and the curves show little variation. In 10mM NaCl, the curves showed a much larger variation with two distinct populations. The first was very similar to the curves obtained in water. The second population

(red curve in Fig. 5.8) showed a distinctive but poorly reproducible step (white arrow in Fig. 5.8) visible in both amplitude and phase. Note that due to our detection limit, no long-range forces (distance > 2 nm), were observed in water or 10mM NaCl.

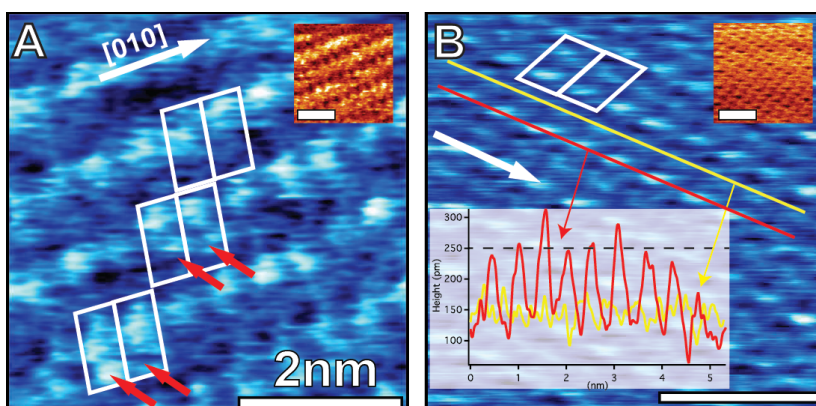


Fig. 5.7: Calcite ($10\bar{1}4$) surface imaged by AFM in 10mM NaCl. The topography appears in blue and the phase is shown as inset in yellow color scale. In all images, the white arrows indicate the $[010]$ direction, the scale bar is 2 nm and the white parallelepipeds indicate the unreconstructed unit cell. In the image (A) the red arrows indicate the location of the sodium ions. In the image (B), the white box of the inset presents two line profiles corresponding to the prominent (red) and sunken (yellow) rows of the oxygen atoms. In the prominent row not all the atoms have the same maximum height and this modulation cannot be associated with the 2×1 reconstruction. The contrast in both images is a modulated V_1 , according to Rahe *et al.*³⁰. Note that the unit cells, determined using the SPIP analysis software, appear distorted due to imaging drift.

We attributed these steps to the presence of adsorbed Na^+ ions that are removed by the tip as it approaches the surface. The poor reproducibility between different curves in 10mM NaCl is expected to be due to the weak adsorption of the ions on the surface, leading to different trajectories of the tip as it expels them from the tip-sample gap. The ease with which the Na^+ ions could be removed suggests that they are not directly adsorbed onto the calcite surface, but separated by at least one layer of water molecules, consistent with the idea of a strongly hydrated calcite surface^{16,19}. Hydrated Na^+ ions would have to pay a significant energy corresponding to the partial loss and restructuring of the hydrations shell in order to penetrate calcite's solvation structure.^{16,51}

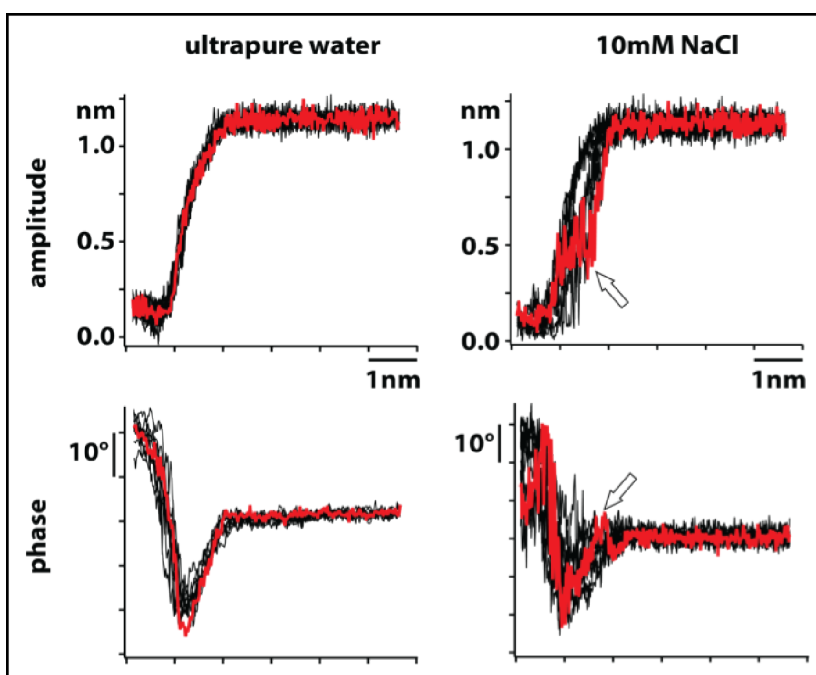


Fig. 5.8: Amplitude and phase vs. distance curves (10 curves in each case) obtained in ultrapure water and 10mM NaCl. The curves were acquired immediately after imaging. One representative curve is highlighted in red in each case.

AFM of calcite in Rubidium Chloride

In order to further substantiate our findings, we repeated the previous experiments using RbCl as salt. The choice of RbCl is motivated by the large cation size and the loose hydration shell. The dehydration argument developed for the Na^+ ions, if true, should allow Rb^+ ions to sit even closer to the calcite's surface. Moreover, AFM results obtained with Rb^+ ions may provide a point of comparison for future X-Ray reflectivity experiments where Rb^+ ions are usually preferred.¹⁷ The main results are presented in Fig. 5.9.

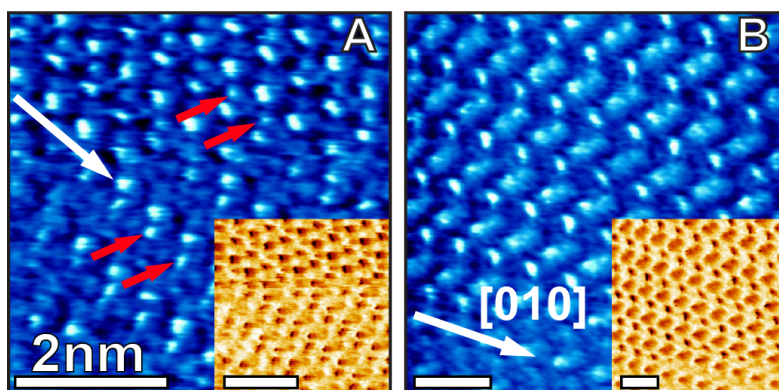


Fig. 5.9: Calcite's $(10\bar{1}4)$ surface imaged in RbCl. The color scales and image presentations are as for Fig.5.6. At 10mM (A), additional protrusions in the unit cell of the calcite crystal are visible along the $[010]$ direction (red arrows). When increasing the RbCl concentration, the protrusions progressively merge together and the interpretation of the height contrast becomes difficult. At 100mM (B), a reconstruction of the surface is visible with a lattice periodicity doubled in both the $[010]$ and $[\bar{4}21]$ directions. White arrows indicate the $[010]$ direction.

The evolution of the imaging contrast of the calcite $(10\bar{1}4)$ surface as a function of the RbCl concentration is presented in the Fig. 5.10. In each case, several unit cells are superimposed to the image. The unit cells appear sometimes distorted (parallelogram) due to uncorrected imaging drift. At low RbCl concentration (<5 mM) the surface of calcite was similar to the situation in equilibrated pure water (Fig. 5.10A). In the absence of added salt (see e.g. Fig. 5.1B), the unit cell of calcite $(10\bar{1}4)$ usually contains two protrusions when imaged by AFM. When adding RbCl a consistent deviation from the “classical height contrast” could be observed with the appearance of an extra protrusion within the unit cell (pointed with red arrows in both Fig. 5.9 and 5.10).

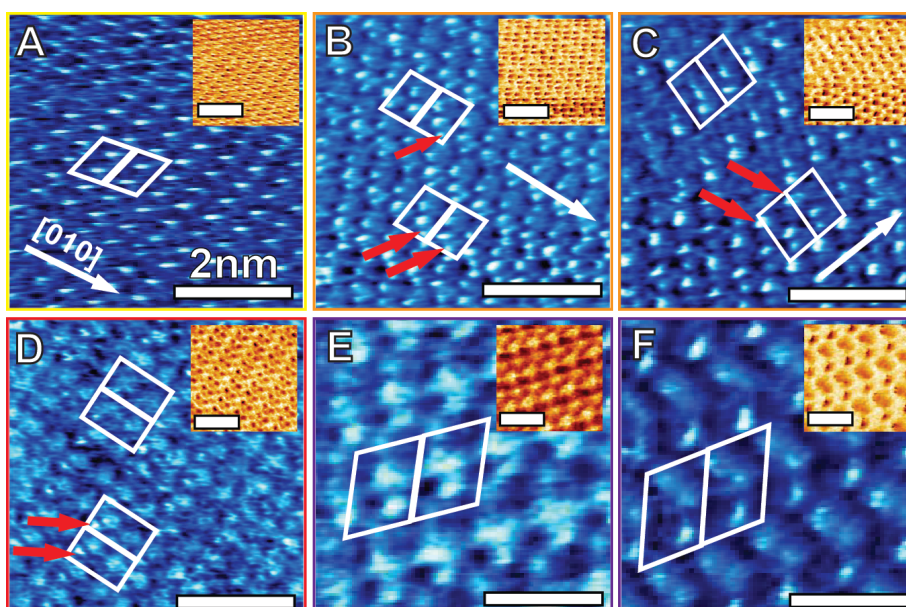


Fig. 5.10: AFM imaging of calcite $(10\bar{1}4)$ surface in RbCl. The topography appears in blue and the phase in yellow color scale. The white arrows indicate the $[010]$ direction, and the white parallelograms indicate the unit cells. The images were taken in 1mM (A), 10mM (B and C), 50mM (D) and 100mM (E and F) RbCl solutions. Occasional extra protrusions in the surface unit cells are indicated with red arrows. The scale bar is 2 nm in every image.

At 10 mM RbCl (Fig. 5.10B and C), this effect was already visible on the surface. The new protrusions, attributed to Rb⁺ ions, were not always observed and it was generally possible to find unaffected unit cells within the same image (Fig. 5.10B and C). These Rb⁺ ions were visible at low concentration when the ‘row pairing’ contrast was still detected. The location of Rb⁺ coincided with that of Na⁺ ions in the previous experiments (Fig. 5.9A, red arrows) following the reconstructed surface and adsorbing every other oxygen row along the [010] direction. However, in this case, the cations induced a clearer and better-defined contrast. Adsorbed Rb⁺ ions were also more resistant to the scanning AFM tip, consistent with the dehydration argument in which ions possessing a looser hydration shell reside closer to the calcite surface.

At 50 mM (Fig. 5.10D) the image contrast became difficult to interpret and harsh imaging conditions were necessary to reveal the underlying calcite structure. The extra Rb⁺ protrusions were still visible within the unit cell (red arrows in Fig. 5.10D). Interestingly, the protrusion often appeared to merge with one of the neighboring oxygen atom, effectively becoming a unique larger hydration structure.

Finally, at 100mM RbCl (Fig. 5.10E and F) the unit cell appeared completely different and substantially larger (almost doubled in size). This observation indicates that a reconstruction is occurring at higher salt concentration, making it difficult to identify the structure of the calcite surface underneath, regardless of the imaging conditions (Fig. 5.10F). Generally, for all the images obtained in RbCl (beside at very low concentrations) it is very difficult to apply the categorization proposed Rahe *et al.*³⁰ to describe the AFM contrast. This suggests that the ions in this case have a strong effect on the imaging process.

These results confirm the trend observed with NaCl and support the idea that hydration effects dominate the energy required for ions and charged molecules to approach the surface of calcite.

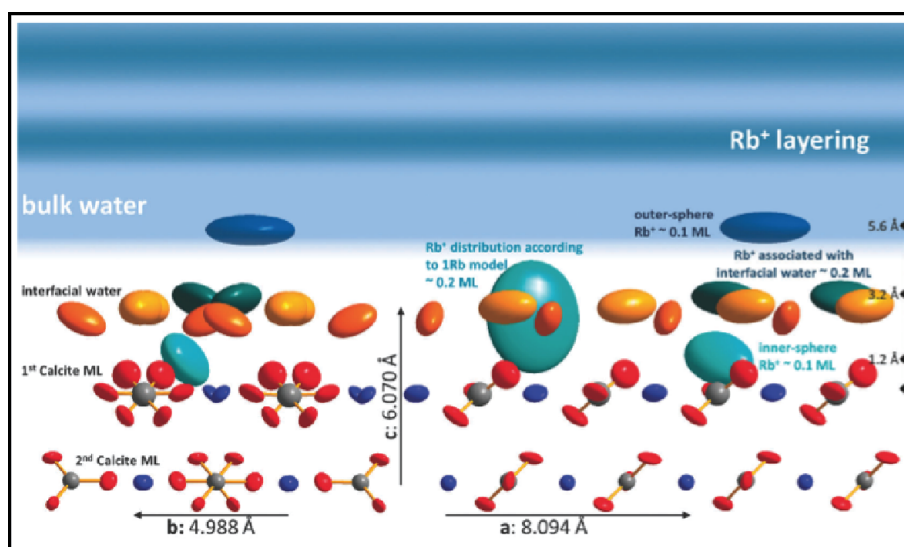


Fig. 5.11: Schematic representation of the calcite (10 $\bar{1}$ 4)–water interface structure in the presence of Rb⁺. Image taken from Ref. [49]. Vibrational ellipsoids show 50% probability regions (Ca – blue, O – red, C – grey, oxygen of the 1st water layer – orange, oxygen of the 2nd water layer – yellow, Rb – different shades of turquoise). The calcite (10 $\bar{1}$ 4)–water interface is shown from two perspectives. The left side shows a projection along the [010] direction and the right side shows a projection along the [4 $\bar{2}$ 1] direction. Both perspectives contain the Rb⁺ adsorption species according to models presented in Ref. [49]. The right image additionally contains the Rb⁺ species corresponding to single complexation model that was later refined with the three complexation-model as described in the text.

Recently, after the publication of our results in RbCl, Heberling *et al.*⁴⁹ performed a resonant anomalous X-ray reflectivity (RAXR) measurement of the (10 $\bar{1}$ 4) calcite surface in 10mM and 5mM RbCl solutions. Interestingly, these results confirm our AFM data. They found that Rb⁺ ions could form inner-sphere complexes on the calcite surface. There are though three distinct Rb⁺ adsorption species: one is located 1.2 Å above the surface, the second associated with surface adsorbed water molecules at 3.2 Å above the surface, and the third adsorbed in an outer-sphere fashion at 5.6 Å distance (see Fig. 5.11). Accordingly to the data, the different contrast observed

in the AFM images of Fig. 5.10 could be explained as the predominance of one of the three complexation sites on the other on the specific location imaged by the AFM tip. In particular a different effect can be expected in the contrast formation between the two closest complexation sites at the calcite surface reflecting the two possible contrasts observed in the Fig. 5.10.

AFM of calcite in Calcium Chloride.

High concentration of calcium can be found in seawater as well as in certain rivers, prompting us to investigate the surface of calcite in presence of CaCl_2 . Furthermore, when at equilibrium in water, calcium ions dissolve from the calcite, typically reaching concentrations of 0.4mM under normal atmospheric conditions. Since Ca^{2+} is a divalent ion, the solvation shell is bigger and more strongly bound than that of monovalent cations. Ca^{2+} can therefore be expected to pay a larger energy penalty of dehydration than Na^+ and Rb^+ to reach the surface of calcite. AFM images of the calcite surface in CaCl_2 are presented in Fig. 5.12.

At 1 mM CaCl_2 (pH 8.1 ± 0.1), the ionic strength of the solution is higher than the corresponding one in monovalent salts but still comparable to that naturally present in ultrapure water after equilibration. At this concentration the surface do not show significant deviations from the contrast observed in equilibrate water (Fig. 5.12A).

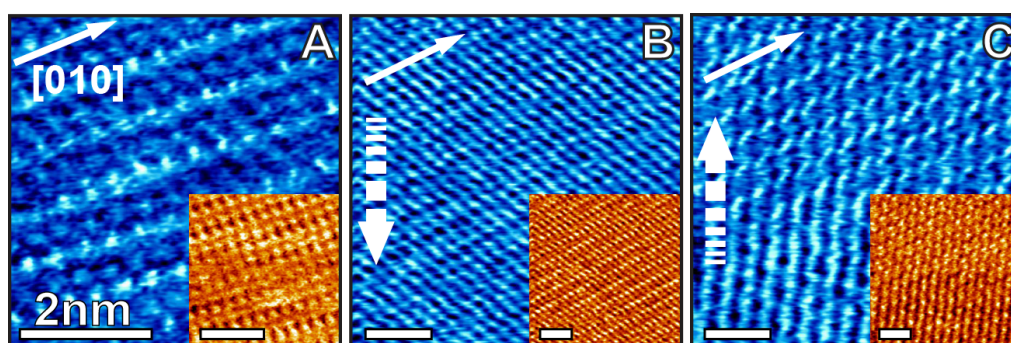


Fig. 5.12: Calcite's ($10\bar{1}4$) surface imaged in CaCl_2 . At 1mM (A), the surface of calcite appears similar than in water. The contrast in (A) is a modulated L_6+V_1 , according to Rahe *et al.*³⁰. At 10mM tip-induced effects become important and two consecutive AFM images acquired from top to bottom (B) and bottom to top (C) can look different, although the underlying symmetry is preserved. The full white arrows indicate the [010] direction and the large dotted arrows in (B) and (C) indicate the direction of the slow scan axis.

At 10 mM CaCl_2 (pH 7.7 ± 0.1), the calcite surface appeared different, with lines following the crystal lattice instead of distinct surface atoms (Fig. 5.12C). Although the imaged structure is correlated with calcite's lattice, it is clearly influenced by the scanning tip in fact two images acquired consecutively show different structures (Fig. 5.12C). In Fig. 5.12C, the familiar 'row pairing' is recovered toward the end of the image acquisition (upper part). This result indicates that the divalent Ca^{2+} ions interact more weakly with the surface of calcite than the monovalent Na^+ and Rb^+ ions, which is consistent with a dehydration-dominated interaction. As a result, the AFM tip can easily push the loosely adsorbed but strongly hydrated Ca^{2+} ions as it scans across the surface. It is important to note that in the same locations also Cl^- ions are supposed to adsorb which complicates the interpretation of the results. The charge distribution at calcite's surface then becomes a guiding potential landscape for the ions, which tend to follow preferential directions (the lines) when confined between the tip and the crystal. The negative surface charge of the SiN tip will also affect divalent Ca^{2+} ions more than monovalent ions. This suggests that the resulting images can be seen as maps of calcite surface potential probed by tip-bound hydrated Ca^{2+} ions.

5.1.4 General Discussion of the system

The calcite-ionic solution interface is more complex than the systems examined so far in this thesis. The surface is dynamic and the ions can reside on different complexation sites. Proper coverage quantification like that performed in Chapter 3 would be much more challenging here

and our analysis is therefore rather qualitative than quantitative. Despite these complications we were able to extract valuable information on the system. Moreover the results were recently confirmed by independent experimental measurements.⁴⁹

The MD-simulations were in good agreement with the experimental results, particularly when taking into account the difference in the hydration shell of Na^+ and Ca^{2+} ions. The coordination numbers of water molecules (around 6 for Na^+ and 8 for Ca^{2+}) showed a larger hydration shell for Ca^{2+} . This is consistent with the fact that a higher energy barrier has to be overcome in order to get closer to the calcite-water interface. The simulation results also indicated two highly ordered water layers at a distance of 222 pm and 330 pm from calcite's surface. These water layers prevent the ions in solutions to approach the surface over flat areas: the main mechanism originates from the energy penalty that the ions have to pay for the removal of the hydration shell as they traverse the 'ice-like' water layers.⁵¹ A second mechanism may also play a role: the ordering of the water layers creates an alternation of positive and negative charges in the direction perpendicular to the surface, due to the oxygen and hydrogen atoms of the oriented water molecules.⁵¹ This alternation creates a modulation of the free energy barrier experienced by ions that are approaching the surface. The barrier, observed in simulation studies,⁵¹ depended mainly on the ion charge density. Monovalent cations experienced a lower free energy barrier compared to divalent ions, but the nature of the considered ions has to be taken into account when considering the dehydration energy penalty. Our AFM results suggested that sodium and rubidium ions are favorable in the interaction with the calcite surface compared to calcium and could approach closer to the surface. Our images also provided preferential locations for these ions to adsorb on calcite. These findings were confirmed by MD-simulations in the case of sodium and calcium.

Based on the MD-simulations, we were able to compute the residence time of the different ions within a certain distance from the calcite surface (vertical mobility). The distance was selected to match maxima in the density peak of the considered type of ion (see Fig. 5.4B). Although the derived numbers must be considered cautiously, they provide a good point of comparison for differences in mobility between the considered ionic species close to calcite's surface. Calcium ions resided approximately 750 ps at their density peak (~550 pm from the calcium atoms of the calcite surface). For chloride ions the residence was around 475 ps at the first peak (~480 pm from the calcium atoms of the calcite surface) while sodium ions remained for more than 5 ns at their first density peak (~290 pm from the calcium atoms of the calcite surface), which exceeds the duration of the entire simulation run. Estimation of the ions lateral mobility when 'trapped' in the first water layers of the calcite surface were difficult to derive. We estimated that the diffusion coefficient for sodium ions was decreased by at least a factor 200 with respect to the bulk value. In the case of calcium ions the lateral diffusivity was only of one order of magnitude lower than that of the bulk value and 1 order of magnitude larger than the lateral diffusivity of sodium ions in the first density peak. These observations are consistent with the differences observed in the AFM images where the possibility to distinguish single ions seems to be a prerogative of the monovalent Na^+ and Rb^+ .

Our results also bring new insight into the important problem of the electrical double layer at the surface of calcite. This model defines the Stern layer as the plane where the outer-sphere complexation of 'adsorbed' ions is located (see Chapter 4). The determination of the thickness of the Stern layer, and particularly the position of the OHP is essential for the modeling of the EDL.^{4,16,19} Our results showed that the position at which the complexation with the calcite surface takes place depends substantially on the type of ion. The Na^+ ions are able to come closer to the surface while Ca^{2+} and Cl^- ions stay further away. It is important to note that continuum classical theory often falls short in the explanation of interfacial phenomena at the nano-scale, thus highlighting the necessity to consider the aforementioned specifics of hydration.⁵⁴

In this section we explored the interface between calcite ($10\bar{1}4$) and different ionic solutions combining AFM experiments and MD-simulations. The surface of calcite is strongly hydrated and the approaching ions have to pay a substantial energy penalty incurred by the loss or restructuring of the hydration shell when traversing calcite's ice-like hydration layers. In the next section I will concentrate on edge effects where calcite's solvation structure is known to break down and where

different ions can interact directly with the surface.^{55,56}

5.2 Growth and dissolution process of calcite

AFM's ability to probe samples locally with atomic-level resolution and in liquid has established the technique as a tool of choice to study calcite growth and dissolution in different saline and pH environments.^{23,24,31,33,36,57-60} *In-situ* real-time AFM experiments have explored the nucleation and kinetics of surface kinks and steps⁴⁰ as a function the Ca^{2+} to CO_3^- concentration ratio, a factor often used to characterize oceanic and continental waters that are super-saturated with calcite.⁶¹ The presence of different background electrolytes⁶² as well as particular ions such as Li^+ , Sr^{2+} , Mg^{2+} and Ba^{2+} have been shown to influence the progression of acute or obtuse steps, sometimes even specifically.^{18,24,56,58,63-65} Organic molecules can have similar effects on the surface of calcite,^{4,66} with obvious consequences for bio-mineralization and oil extraction (see Chapter 6).

In this section I will examine the hydration properties of two types of steps present on the $(10\bar{1}4)$ calcite surface (subsection 5.2.1). I will then present the real-time growth and dissolution processes of the surface observed by AFM in ionic solutions at different concentrations (subsection 5.2.2). I use the term 'brine' to refer to ionic solutions with compositions and concentrations that mimic seawater. The use of this term, as opposed to simple ionic solutions, stresses the geochemical relevance of the processes examined. I will explore the effect of brines on the growth and dissolution of the calcite's surface, with particular attention to the role of specific ions in this process (subsection 5.2.3).

5.2.1 Hydration properties at the calcite's steps

The hydration properties of the calcite $(10\bar{1}4)$ surface along flat areas prevent the direct interaction of Ca^{2+} and carbonate ions with the surface. The growth and the dissolution processes are nonetheless observed experimentally and well documented. This indicates that the ionic constituent of the crystal must somehow leave the crystal or be reabsorbed on the surface. This happens at step edges, where the water adsorbed has significantly different properties from the ones of flat terraces. This difference is directly visible in the AFM image presented in Fig.5.13 obtained in equilibrated water. A step on the $(10\bar{1}4)$ calcite surface is visible and the atomic structure is recognizable. An area of several nanometers with a higher crystal-water affinity is clearly evident in the phase image (Fig.5.13B), related to the effective work of adhesion between solid and liquid molecules.

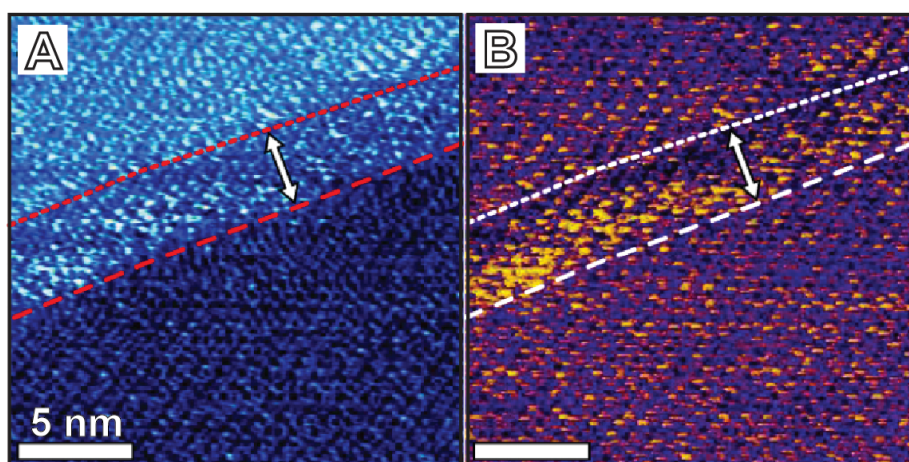


Fig. 5.13: AM-AFM of a calcite step in aqueous with atomic-level details. (a) topographic image, (b) water-calcite affinity (effectively work of adhesion) extracted from the AFM data (see Section 1.4). The scale bar corresponds to 5 nm. Images and data analysis done by Kislun Voitchovsky and published in Ref. [67].

The surface chemistry and crystal structure have a direct influence on the restructuring behavior of calcite, including the mechanisms by which trace elements are incorporated and released. To reach equilibrium, the crystal restructures itself through growth and/or dissolution processes. A mineral dissolves if the contacting solution is undersaturated and crystallizes if the solution is supersaturated with respect to the solid phase. The surface changes can be predicted by calculating the brines saturation indices (using for example the PHREEQC software,⁶⁸). The saturation index (SI) is defined as the logarithm of the ratio between the ion activity products and the equilibrium constant of a certain mineral. Negative SI corresponds to an unsaturated solution respect to the specific mineral; positive values correspond to a supersaturated solution. Situations where $SI=0$ correspond to the equilibrium. The commonly used conceptual model for dissolution and growth of calcite starts with the nucleation of kink/antikink pairs on the step, followed by lateral retreat and formation of the individual kinks along it until they annihilate or reach a corner terminating the step.^{60,69} The typically observation by AFM that dissolving steps remain straight, suggests that the single kinks propagate along the step much faster than new kink/antikink pairs form; otherwise a wavy step would be produced.⁴⁰ Different is the situation when impurities are present in solution, as we will see in subsection 5.2.3.

During growth and dissolution, the $(10\bar{1}4)$ calcite surface contains four types of step edges that reflect the rhombohedral symmetry of the crystal. These steps are parallel to the $[\bar{4}41]_+$, $[48\bar{1}]_+$, $[\bar{4}41]_-$ and $[48\bar{1}]_-$ directions (Fig. 5.14A). The subscripts + and - follow the convention used by Agudo *et al.*¹⁸. These steps differ in local atomic arrangement and are named obtuse (+) and acute (-) depending on the angle they form with the underling surface layer. The structurally equivalent $[\bar{4}41]_-$ and $[48\bar{1}]_-$ steps intersect the bottom of the lower crystallographic plane at an angle of 78° , whereas the $[\bar{4}41]_+$ and $[48\bar{1}]_+$ steps at an angle of 102° (Fig. 5.14B).¹⁸ Non-equivalent steps show a remarkable kinetic anisotropy during the restructuring processes^{18,57} that reflects differences in structural and hydration properties.

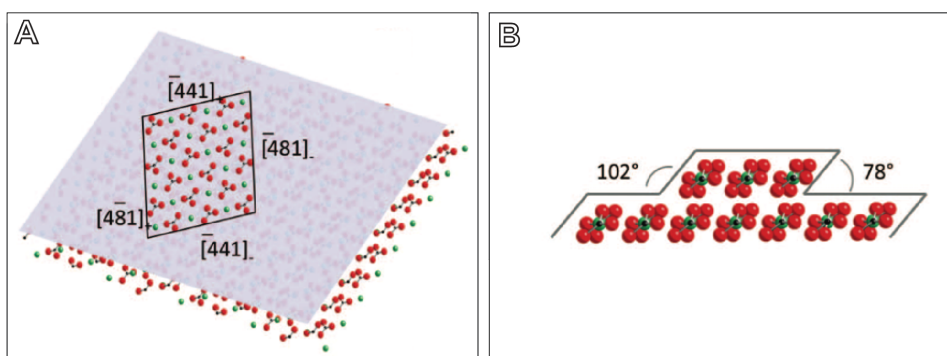


Fig. 5.14: Sketch showing non-equivalent steps on the calcite $(10\bar{1}4)$ surface along the $[\bar{4}41]_+$, $[48\bar{1}]_+$, $[\bar{4}41]_-$ and $[48\bar{1}]_-$ directions. Obtuse (+) and acute (-) steps form respectively an angle of 102° and 78° with the lower surface plane.

After cleavage, relaxation changes the atomic structure of the surface: ions constituting the crystal are drawn into the bulk, further opening each step. For the obtuse step, the two distinct CO_3 anions rotate such that the orientations with respect to the surface plane become very similar, contrarily to acute step, where the orientations remain different. The calculated step energies show that the obtuse step is energetically favored and imply that they are more abundant on freshly cleaved surfaces.⁴⁰

The difference in the energy between the two types of steps translates into a different interaction with the water molecules once the surface is put in contact with an ionic solution. Lardge *et al.*⁷⁰ found that water molecules bind more strongly to acute than to obtuse steps, confirming that the latter are more stable. Moreover, water molecules were found to exhibit very strong binding to surface vacancies.⁷⁰ Wolthers *et al.*⁴⁷ found subtle differences in hydrogen bonding around acute versus obtuse edges and corners. These subtle differences translate into markedly different charging behavior versus pH. Therefore the results show that the reactivity of calcite's surface is directly related to surface topography. Similar results were found by Andersson *et al.*⁴⁸. These

differences in hydration properties between acute and obtuse steps play a fundamental role when the calcite surface and the contacting ionic solution are out of equilibrium.

Dissolution process

The dissolution process consists in the progressive erosion of material from the preexisting steps or from the newly formed etch-pits nucleated at dislocations. The result is a layer-by-layer removal of material from the mineral surface. Mineral dissolution rates can be controlled by the kinetics of the surface reactions and/or by the mass transport of the dissolved species from the crystal surface. The slowest of these processes controls the kinetic.¹⁸ Mass transport is commonly important at acidic pH, whereas surface reaction kinetics generally control calcite dissolution in far-from-equilibrium conditions (highly undersaturated, $SI \ll 0$) at neutral or slightly alkaline pH values. During dissolution, the local pH of the solution may vary even non-homogenously from the surface to the fluid. The maintenance of this gradient would also depend on the flow rate of the solution. The steps' retreat velocities are extremely sensitive to experimental conditions: pH, the degree of supersaturation, the solution composition, Ca^{2+} to CO_3^{2-} concentration ratio, ionic strength and the presence of organic matter adsorbed on the surface (see Chapter 6). Generally obtuse steps have higher retreat velocity than acute steps, but even this phenomenon is highly system and condition-specific.¹⁸

Growth process

In-situ observations by AFM have confirmed that calcite growth takes place by the spreading of pre-existing steps, or by two-dimensional surface nucleation. Teng *et al.*⁷¹ showed that the crystal growth mechanism depends on how far from equilibrium the calcite crystal and the ionic solution are. Close to equilibrium, growth takes place by the advancement of steps emerging from surface defects, including screw dislocations. However, once a threshold supersaturation is exceeded, two-dimensional nucleation becomes an increasingly important mechanism of the growth process. Perdikouri *et al.*⁷² found moreover that, for a given supersaturation, the maximum calcite growth rate occurs in a non-stoichiometric solution with a calcium/carbonate activity ratio close to two. These observations suggest that calcium ions have lower integration frequencies than carbonate ions during growth. The cation attachment is the rate-limiting process since they dehydrate at slower rates than carbonate ions. Recent studies by Larsen *et al.*⁷³ have shown that the velocities of acute and obtuse step spreading have different sensitivities to solute activity ratios. This anisotropy in obtuse and acute step kinetics is most probably due to differences in step hydration and the processes controlling the kink formation and spreading.¹⁸ Obtuse step advancement may be controlled mainly by the availability of calcium in solution, whereas acute step advancement may be governed by kink-site nucleation and ultimately by the hydration of carbonate groups at the surface. This effect is important when ionic species other than Ca^{2+} and CO_3^{2-} are present in solution, thus competing with them during the restructuring process (see section 5.2.2).

5.2.2 Growth and Dissolution process

If the ionic solution and the calcite crystal are out of equilibrium the surface restructures by growing or dissolving. We experimentally monitored these effects by creating 3 types of brines with different concentrations and compositions.

	Brine1 (g/l)	Brine2 (g/l)	Brine3 (g/l)
NaCl	126.41	164.64	164.64
KCl	-	0.95	0.95
$CaCl_2 \times 2 H_2O$	53.19	60.81	60.81
$MgCl_2 \times 6 H_2O$	27.17	18.63	18.63
$SrCl_2 \times 6 H_2O$	-	-	3.96
$Na_2SO_4 \times 10 H_2O$	0.35	0.67	0.67
$NaHCO_3$	0.22	0.12	0.12

Table 5.1: Salt composition of the different brines.

Throughout the text, I will consistently refer to these brines as Brine1, Brine2, etc. The composition of the brines was suggested by Shell petroleum in the framework of a collaboration. All these brines have a positive SI for the calcite, hence promote the growth once in contact with the crystal. To explore the effect of the dissolution process, the brines have been diluted several times during the course of an experiment, until reaching negative SI. Throughout the text I will refer to diluted brines as e.g. Brine1_ \times 20 for a 20 times dilution of Brine1.

In this subsection I will present the experiments in which the evolution of the calcite crystal is monitored in real time in Brine1 as a function of the concentration. The brine was injected into the fluid cell of the AFM and the sample was subsequently imaged in liquid. Using a syringe system it was possible to exchange the liquid on the sample and progressively dilute the concentration while following the topological evolution of the same area of the sample (Fig.5.15).

Growth and dissolution in Brine1

In Table 5.2 we present the values of pH and ionic strength of Brine1 as measured and calculated with the program PHREEQC. In the first row we present the measured values of pH for the different brine dilutions. In the second row are listed the pH values calculated with PHREEQC for the different dilution of the Brine1 before the equilibration with the calcite crystal while in the third row the same values obtained after the equilibration process.

	Equilibration with Calcite	Brine1	$\times 2$	$\times 5$	$\times 10$	$\times 20$	$\times 50$	$\times 10^2$	$\times 10^3$	$\times 10^4$
pH measured	no	6.8	7.3	7.7	7.5	8.1	7.3	7.4	6.3	6.7
pH calculated	no	7.8	7.8	7.6	7.4	7.2	6.9	6.6	5.8	5.6
pH + calcite calculated	yes	7.0	7.2	7.4	7.6	7.7	7.8	7.9	8.2	8.2
Ionic strength	no	3.6	1.8	0.73	0.36	0.18	$7.3 \cdot 10^{-2}$	$3.6 \cdot 10^{-2}$	$3.6 \cdot 10^{-3}$	$3.7 \cdot 10^{-4}$
Ionic strength + calcite	yes	3.6	1.8	0.73	0.36	0.18	$7.4 \cdot 10^{-2}$	$3.7 \cdot 10^{-2}$	$5.0 \cdot 10^{-3}$	$1.8 \cdot 10^{-3}$

Table 5.2: pH values (measured and calculated with PHREEQC) and ionic strength (expressed in molality, calculated with PHREEQC) of different dilutions of Brine1 equilibrated or not (see second column) with a calcite crystal.

Calculations with PHREEQC indicate that, at equilibration with ultrapure water, the concentration of the ions in solution at atmospheric pressure is $1.5 \cdot 10^{-3}$ molal of ionic strength and pH 8. This means that the highest dilution had a lower starting concentration of ions than at equilibrium with calcite. The composition of the 1,000 and 10,000 times diluted brine after the equilibration is dominated by ions dissolved from the calcite.

Phase/SI	Brine1	$\times 2$	$\times 5$	$\times 10$	$\times 20$	$\times 50$	$\times 10^2$	$\times 10^3$	$\times 10^4$
Aragonite CaCO ₃	1.61	1.08	0.27	-0.39	-1.08	-2.03	-2.79	-5.12	-6.44
Calcite CaCO ₃	1.76	1.22	0.41	-0.24	-0.93	-1.89	-2.64	-4.98	-6.30
Dolomite CaMg(CO ₃) ₂	3.41	2.25	0.59	-0.75	-2.14	-4.07	-5.58	-10.25	-12.90

Table 5.3: Saturation Indices of different dilutions of Brine1 calculated with PHREEQC program.

As visible in Table 5.3, Brine1 is promoting the growth of the calcite crystal up to a $\times 5$ dilution. As soon as in contact with Brine1 $\times 10$ the calcite crystal is expected to dissolve. The trend is confirmed experimentally in Fig. 5.15: the surface of the crystal is growing until in contact with Brine1 $\times 5$ where the surface is almost microscopically stable in time. As soon as Brine1 $\times 10$ is injected the surface starts to dissolve: the steps recede and the classical etch-pits appear the surface. The fact that the calculated SI and the experimental observation coincide so well is probably to be attributed to the extremely stable and well-sealed liquid cell of the Cypher-ES used for this experiment (see section 5.3). Experiments conducted with other AFM systems such as the Veeco Multimode did not allow such a good agreement between the experiments and the theoretical SI.

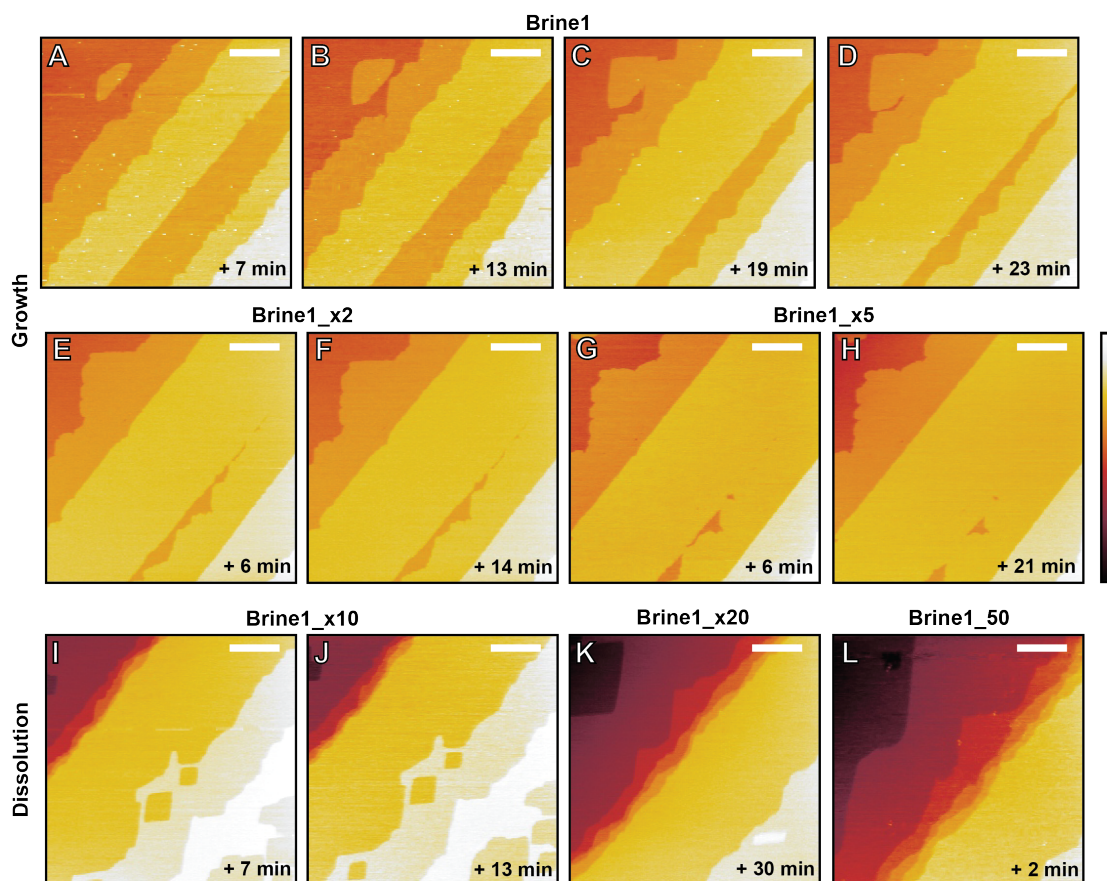


Fig. 5.15: Real time dissolution and growth of the calcite surface exposed to different dilutions of the Brine1. Images from (A) to (D) correspond to different moments after the injection of Brine1. Images (E) and (F) were acquired after the injection of Brine1 $\times 2$, images (G) and (H) after the injection of Brine1 $\times 5$; (I) and (J) after injecting Brine1 $\times 10$; (K) after the injection of Brine1 $\times 20$ and (L) after the injection of Brine1 $\times 50$. The acquisition time relative to the respective brine injection is indicated on the right-bottom of the image. From image (A) to (H) the growth process is monitored while for Brine1 $\times 10$ (I) dissolution of the surface starts to take place instantaneously after injection. The scale bar in the images correspond to 1 μm while the color scale is 3.5 nm. The images are not drift corrected.

5.2.3 Influence of different ions on the growth-dissolution process

In Fig. 5.16 the same area of the sample is presented at two consecutive times when exposed to Brine2 (Fig. 5.16A and B) and Brine3, respectively (Fig. 5.16D and F). In the case of Brine2 the growing monoatomic steps appear more regular compared to the one of Brine3 in which simply SrCl_2 was added in solution.

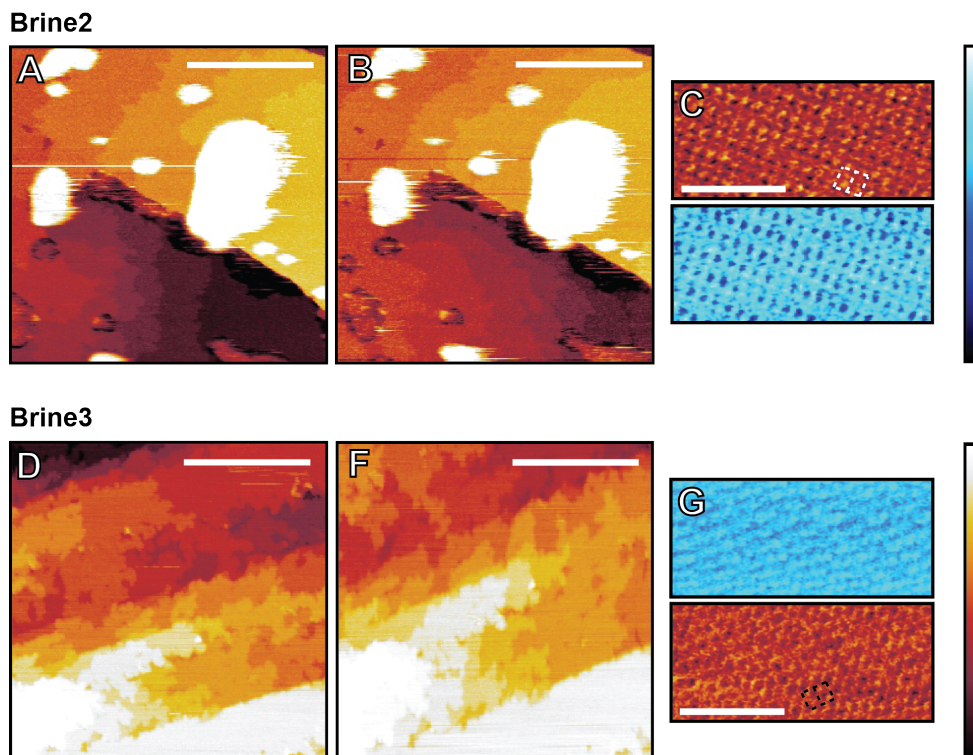


Fig. 5.16: Growth of Calcite steps respectively in Brine2 (A and B) and Brine3 (C and D). Image B shows the advancing steps of calcite immersed in Brine2 after ~ 2 min after image A was acquired. Image F shows the advancing steps of calcite immersed in Brine3 after ~ 2 min after image D was acquired. C and G are high-resolution images of the $(10\bar{1}4)$ calcite surface obtained respectively in Brine2 and Brine3. The blue color scale is used for the phase images. The scale bars are 200 nm (A, B, D, F) and 4 nm (C, G). The color scale bars are 11° (phase, blue color scale), 5.5 nm (topography, A, B), 3.5 nm (topography D, F) and 0.4 nm (topography C, G). The images are not drift corrected.

At high concentrations ($c > 2\times$), not only calcite but also Aragonite (CaCO_3), a mineral polymorphic to calcite, Dolomite ($\text{CaMg}(\text{CO}_3)_2$) and in the case of Brine3 also Strontianite (SrCO_3) can grow due to positive SI. We believe that the presence of a calcite crystal in contact with the solution favors growth of calcite on the surface, but we cannot exclude the presence of some Mg^{2+} and Sr^{2+} ions in the newly formed crystal.⁵⁸

The presence of impurities can have two possible effects on the growth process, depending on the model considered: the ‘*impurity-incorporation*’ model assumes that the impurities are incorporated into the crystal during the growth process, while the ‘*step-pinning*’ model predicts a decrease of the advancing velocity of steps due to impurities adsorbing at step-edges.¹⁸

The ‘*impurity-incorporation*’ model predict that the impurities incorporated into the calcite structure decrease the solubility of the solid phase (compared to the pure calcite crystal) since the ‘foreign’ ions destabilize the lattice⁵⁸. As a result, the supersaturation of the aqueous solution with respect to an impurity mixed-surface layer will be lower thus implying that the growth step velocity will always be below that in the pure system. Mg^{2+} has shown to obey to this model.⁵⁸

This is the reason why we noticed in our experiment that the freshly grown material (calcite mixed with impurities) dissolves first and fast when the saturation index decreases. At sufficient dissolution, the surface will appear as it was before the growth process had taken place.

The step-pinning model assumes that impurity adsorption at kink sites on step edges causes the pinning of the steps hindering further advancement. If the impurity concentration is high enough, steps fail to advance and no growth occurs, thus producing a dead zone. Impurity adsorption is a reversible process in this model. When a threshold supersaturation is reached, adsorbed impurities are removed from the mineral surface, allowing growing steps to rapidly reach the velocity characteristic of the pure solid at this concentration. Unlike Mg^{2+} ions, Sr^{2+} ions follow the *step-pinning* model, resulting in a highly irregular growth process⁶⁰ as seen in Fig. 5.16D and F. We attribute the appearance of these flowery-shaped steps in Brine3 to the introduction of this Sr^{2+}

ion. Incorporation of Mg^{2+} , and to a certain extent Sr^{2+} in the newly formed crystal⁶⁴ cannot be excluded, but Sr^{2+} ions show a drastic effect on the morphology of the calcite steps.

In our experiments we noticed that the two directions of faster dissolution (for all the brines) correspond to the acute steps, while the obtuse steps dynamic is much slower. This kind of behavior is anomalous and contradicts the usual reported trend for calcite dissolution^{18,74}, although the similar observations have previously been reported⁶⁵ in the presence of Mg^{2+} , even at very low concentrations.⁷⁵ Other ions such as K^+ have been reported to increase the spreading rate of both acute and obtuse steps⁶². While SO_4^{2-} is known to induce elongation of the each pits⁷⁶, Mg^{2+} dominates ionic effects on the morphology of the crystal (rounding of the obtuse/obtuse corner of etch pits^{65,75}) and determines of the preferred dissolution directions. Studies have also shown that magnesium has a strong preference for acute steps if surface reactivity is the growth-limiting factor, as shown by morphological changes of the grown features in the presence of this ion. In contrast, when calcite growth is controlled by mass transport, magnesium tends to preferentially incorporate at obtuse steps.⁷⁷

5.3 Materials and Methods

5.3.1 MD-simulations of ions on calcite

From previous experiments and simulations, the coordinates of the atoms were obtained within a single unit cell in the calcite crystal with the $(10\bar{1}4)$ plane exposed.^{50,78} A calcite crystal of $14 \times 14 \times 14$ unit cells was constructed with a final dimension of $105 \times 64 \times 40 \text{ \AA}^3$. As the molecules that make up the calcite-water system (carbonate, calcium, water and ions) are of biological nature, the empirical force field CHARMM was used in all computations,⁷⁹⁻⁸¹ which were carried out using the molecular dynamics code NAMD.⁸²

After the creation of the initial calcite crystal, several short minimization and relaxation simulations were performed to stabilize the system. Once a stable calcite crystal was obtained, the system was solvated on the side of the $(10\bar{1}4)$ plane, keeping the periodic boundaries in mind. Approximately 68,000 water molecules were introduced to the system, enlarging the z-dimension to 108 \AA . Besides water molecules, also 100 ion-pairs (either NaCl or CaCl_2) were added to the water phase of the system, giving a molarity of $\sim 250 \text{ mM}$. For each ion-pair 10 different set-ups were constructed to improve statistical accuracy, each with the 100 pairs placed at different random locations and different initial velocities. Besides short minimization and equilibration runs, the production run covered 5 ns in real time at ambient conditions (310 K and 1 bar). The simulations were run in parallel on a typical Linux commodity cluster.

Analysis of the simulations were performed either visually using VMD⁸³ or numerically using the Python library MDAnalysis⁸⁴ and Matlab.

5.3.2 Sample preparation for AFM in the experiments of ion adsorption at flat surfaces

Optically clear Island Spar calcite samples were used for this study. The samples were cleaved with a razor blade and incubated in $\sim 15 \text{ ml}$ of the relevant aqueous solution for more than 24 h before being used so as to allow the system to equilibrate. All the solutions were prepared with ultrapure water (18.2 \Omega M , $< 4 \text{ ppm}$ organics, Merck-Milipore, Billerica, MA, USA) and a solution-specific type of salt, NaCl , CaCl_2 or RbCl . In order to ensure that equilibrium was effectively reached, we measured the pH of the solution after equilibration and found to be in agreement with corresponding theoretical calculations (by the software PREEQC). The samples were then mounted onto a stainless steel support and loaded into the AFM. Attention was paid to always keep the surface of calcite in contact with liquid from the equilibrated solution. More solution ($\sim 150 \text{ \mu l}$) was added prior to imaging.

When calcite is equilibrated with ultrapure water, the ionic strength of the resulting solution is typically 1.5×10^{-3} in normal atmospheric conditions, mainly due to the presence of dissolved calcium and carbonate ions in the solution. Although the AFM images obtained under these conditions (Fig. 5.1B) appear comparable to results achieved in ultra high vacuum,³⁰ the dissolved ions may still play a role in the imaging and interact with the negatively charged AFM tip.³³ In order to avoid any ambiguity in the interpretation of the AFM results, we systematically varied the ionic concentration of the salt so as to identify consistent trends. This strategy also allows a more robust comparison of the results in the different salts.

All the AFM measurements were carried out in liquid with a commercial Multimode Nanoscope IIIA (Digital Instruments, now Bruker, Santa Barbara, CA, USA) equipped with an external lock-in amplifier. We used standard silicon nitride cantilevers (RC800-PSA, Olympus, Japan) with a nominal stiffness $k_c = 0.76$ N/m. The cantilevers were mounted in a fluid cell and fully immersed into the liquid for the experiment. The system was allowed to thermalize at room temperature ($24 \pm 2^\circ\text{C}$) for 30 to 60 minutes before acquiring any data so as to minimize drift. The liquid cell was equipped with an O-ring to limit evaporation of the liquid and imaging conditions were routinely kept stable for several hours without need for adding liquid into the cell. The AFM was operated in amplitude-modulation mode ('tapping' in the AFM commercial software) with free amplitudes A_0 typically smaller than 1.5 nm and imaging amplitudes A so as to keep the setpoint ratio A/A_0 as high as possible (typically $A/A_0 \geq 0.8$). Operated in these conditions, the AFM tip mostly probes the interfacial liquid interacting with the surface of the solid, without directly and significantly interacting with the solid itself.⁸⁵⁻⁸⁷ The images therefore represent the solvation structure formed by the water and the adsorbed ions at the surface of calcite. The phase images provide an indication about the local solvation free energy with darker contrasts revealing local maxima.⁸⁵

Image analysis was performed using SPIP (Image Metrology, Denmark). The images were flattened and lightly low-pass filtered. Amplitude and phase versus distance curves were acquired in each experiment and subsequently analyzed using routines programmed in Igor Pro (Wavemetrics, Lake Oswego, OR, USA).

5.3.3 Sample preparation for AFM in the experiments of growth and dissolution

Optically clear natural calcite samples were used for this study. The samples were cleaved with a razor blade to expose the $(10\bar{1}4)$ surface. Immediately after cleaving the samples were imaged in the desired brine concentration. The calcite samples were attached on a metallic disk (SPIP supply) to be mounted on the AFM stage. Two strategies were normally used: in the first case the bare samples were cleaved and in a second moment attached to the magnetic disks with some carbon tape. In the second case we attached the samples on the metallic disk using 5 min epoxy glue (Araldite, Denver, USA). After complete curing of the glue, the samples were cleaved to expose a fresh surface. This strategy avoided contamination of the surface and provided a good stability during the imaging process. We generally suggest the use of the second method if possible because it provides a better stability during the imaging process.

The supersaturated solutions reflect some typical brines' compositions used for reservoir flooding and were suggested by Shell. The desired amount of different salts (Sigma Aldrich, St Louis, MO 63103, USA) was dissolved in ultrapure water (Milli-Q, 18.2 ΩM , <4 ppm TOC, Merck-Milipore, Billerica, MA, USA) and are listed in Table 5.1.

All the experiments were performed at room temperature. The experiments performed with Brine2 and Brine3 were carried out with a commercial Multimode Nanoscope IIIA (Digital Instruments, now Bruker, Santa Barbara, CA, USA) equipped with an external lock-in amplifier. For these experiments we used standard gold coated silicon nitride cantilevers (RC800-PSA, Olympus, Japan) with a nominal stiffness $k_c = 0.76$ N/m. The cantilevers were mounted in a fluid cell. The desired brine was injected into the fluid cell and the sample imaged in liquid in tapping mode. Using a homemade syringe system it was possible to exchange the liquid on the sample

and progressively dilute the concentration of the brine. The evolution of the same area of the sample was followed in real time. During the liquid exchange process, the tip was lifted a few microns above the surface (z-piezo retraction) but not disengaged. Using the same machine was possible to obtain routinely high resolution on the calcite surface using the same procedure and imaging conditions as described in our previous works.^{21,85,87,88} We have seen that the surface changes can be predicted by calculating the brine's saturation indices. We performed this calculation for Brine2 and Brine3 as a function of the brines dilutions. The saturation indices of the two brines are positive for the calcite until 2× dilutions and then become negative. Our experimental results show that the dissolution process starts to take place only when the 20× brine is injected despite having a negative saturation index already at 5×. We can explain this discrepancy by the lack of stability of our system; evaporation is taking place during the experiment and changes the true concentration of the brine. Unfortunately this effect cannot be controlled with the setup employed, inducing a systematic error on the concentration of the brine during imaging. This limitation may be overcome with suitable equipment, such as a sealed environmental chamber, but was not used for these two brines.

The experiments with Brine1 were performed on a Cypher ES (Asylum Research, Oxford Instrument, Santa Barbara, USA). For these experiments we used the same type of cantilevers used on the Multimode Nanoscope IIIA (RC800-PSA with a nominal stiffness $k_c = 0.76$ N/m). The perfect sealing of the environmental scanner eliminates any evaporation issue, apart from a short initial transient time when the vapor in the chamber equilibrates with the liquid. This ensures consistent brine concentrations throughout the experiment.

To obtain high-resolution images in the brines, like the one presented in Fig.5.16C and 5.16D the operating conditions were similar to the one described in subsection 5.3.2.

In the other AFM images obtained in AM-AFM in liquid, different working conditions have been used to enable a better tracking of the very rough surface: a bigger free amplitude (>2 nm) was employed and the ratio A/A_0 was lower (normally <0.8). Generally, the phase contrast in AM-AFM has been related to the energy dissipated due to non conservative tip-sample interaction forces.^{85,89-93} Depending on the imaging conditions (environment, free amplitude, set-point, specific tip-sample interaction, etc.), the channels affecting the dissipation of energy can vary even with the same tip and sample so that a correct interpretation of the phase images becomes a challenging task. In these conditions it is complicated to determine the actual mechanism of energy dissipation and so interpret correctly the phase contrast. Supposing that in this case the energy dissipation is mainly dominated by the contact mechanic between the tip and the sample, the phase contrast reflects a variation of stiffness and viscosity of the material.^{91,93-95}

Image analysis was performed using Gwiddion (<http://gwiddion.net>) and SPIP (Image Metrology, Denmark).

Bibliography Chapter 5

1. Oates, T. *Lime and Limestone*. (Kirk-Othmer Encyclopedia of Chemical Technology, 2000). doi:10.1002/0471238961.1209130507212019.a01.pub3
2. Qiu, S. R. & Orme, C. A. Dynamics of biomineral formation at the near-molecular level. *Chem. Rev.* **108**, 4784–4822 (2008).
3. Hoch, A. R., Reddy, M. M. & Aiken, G. R. Calcite crystal growth inhibition by humic substances with emphasis on hydrophobic acids from the Florida Everglades. *Geochimica et Cosmochimica Acta* **64**, 61–72 (2000).
4. Chen, C.-L., Qi, J., Zuckermann, R. N. & DeYoreo, J. J. Engineered Biomimetic Polymers as Tunable Agents for Controlling CaCO₃ Mineralization. *J. Am. Chem. Soc.* **133**, 5214–5217 (2011).
5. Andersson, A. J., Mackenzie, F. T. & Bates, N. R. Life on the margin: implications of ocean acidification on Mg-calcite, high latitude and cold-water marine calcifiers. *Mar Ecol Prog Ser* **373**, 265–273 (2008).
6. Kuffner, I. B., Andersson, A. J., Jokiel, P. L., Rodgers, K. U. S. & Mackenzie, F. T. Decreased abundance of crustose coralline algae due to ocean acidification. *Nature Geoscience* **1**, 114–117 (2007).
7. Levita, G., Marchetti, A. & Lazzeri, A. Fracture of ultrafine calcium carbonate/polypropylene

-
- composites. *Polym Compos* **10**, 39–43 (1989).
8. Taylor, H. F. W. *Cement Chemistry*. (Thomas Telford Ltd, 1997).
 9. Hartmann, E., Geckeis, H., Rabung, T., Lützenkirchen, J. & Fanghänel, T. Sorption of radionuclides onto natural clay rocks. *Radiochimica Acta* **96**, (2008).
 10. Glasser, F. P., Marchand, J. & Samson, E. Durability of concrete — Degradation phenomena involving detrimental chemical reactions. *Cement and Concrete Research* **38**, 226–246 (2008).
 11. Choi, W. H., Shin, J. W., Kim, J. J. & Park, J. Y. Calcite-packed columns for the removal of fluoride in industrial wastewater. *Desalination and Water Treatment* **30**, 247–253 (2011).
 12. Thomas, M. M., Clouse, J. A. & Longo, J. M. Adsorption of organic compounds on carbonate minerals: 1. Model compounds and their influence on mineral wettability. *Chemical Geology* **109**, 201–213 (1993).
 13. Hassenkam, T., Pedersen, C. S., Dalby, K., TT, A. & Stipp, S. L. S. Pore scale observation of low salinity effects on outcrop and oil reservoir sandstone. *Colloids Surf., A* **390**, 179–188 (2011).
 14. Yousef, A. A., Salah, A. S., Abdulaziz, A. K. & Mohammed, A. J. Laboratory Investigation of the Impact of Injection-Water Salinity and Ionic Content on Oil Recovery From Carbonate Reservoirs. *SPE Reservoir Evaluation & Engineering*, 1–16 (2011).
 15. Karoussi, O. & Hamouda, A. A. Imbibition of Sulfate and Magnesium Ions into Carbonate Rocks at Elevated Temperatures and Their Influence on Wettability Alteration and Oil Recovery. *Energy Fuels* **21**, 2138–2146 (2007).
 16. Stipp, S. L. S. Toward a conceptual model of the calcite surface: hydration, hydrolysis, and surface potential. *Geochimica et Cosmochimica Acta* **63**, 3121–3131 (1999).
 17. Geissbühler, P. *et al.* Three-dimensional structure of the calcite–water interface by surface X-ray scattering. *Surface Science* **573**, 191–203 (2004).
 18. Agudo, E. R. & Putnis, C. V. Direct observations of mineral fluid reactions using atomic force microscopy: the specific example of calcite. *Mineral. Mag.* **76**, 227–253 (2012).
 19. Heberling, F. *et al.* Structure and reactivity of the calcite–water interface. *Journal of Colloid and Interface Science* **354**, 843–857 (2011).
 20. Kerisit, S. & Parker, S. C. Free Energy of Adsorption of Water and Metal Ions on the {10 $\bar{1}$ 4} Calcite Surface. *J. Am. Chem. Soc.* **126**, 10152–10161 (2012).
 21. Ricci, M., Spijker, P., Stellacci, F., Molinari, J.-F. & Voitchovsky, K. Direct Visualization of Single Ions in the Stern Layer of Calcite. *Langmuir* **29**, 2207–2216 (2013).
 22. Yang, M., Mark Rodger, P., Harding, J. H. & Stipp, S. L. S. Molecular dynamics simulations of peptides on calcite surface. *Molecular Simulation* **35**, 547–553 (2009).
 23. Stipp, S. L. S., Konnerup-Madsen, J., Franzreb, K., Kulik, A. & Mathieu, H. J. Spontaneous movement of ions through calcite at standard temperature and pressure. *Nature* **396**, 356–359 (1998).
 24. Harstad, A. O. & Stipp, S. L. S. Calcite dissolution: Effects of trace cations naturally present in Iceland spar calcites. *Geochimica et Cosmochimica Acta* **71**, 56–70 (2007).
 25. Vavouraki, A. I., Putnis, C. V., Putnis, A. & Koutsoukos, P. G. Crystal Growth and Dissolution of Calcite in the Presence of Fluoride Ions: An Atomic Force Microscopy Study. *Crystal Growth & Design* **10**, 60–69 (2010).
 26. Karoussi, O., Skovbjerg, L. L., Hassenkam, T., Stipp, S. L. S. & Hamouda, A. A. AFM study of calcite surface exposed to stearic and heptanoic acids. *Colloids Surf., A* **325**, 107–114 (2008).
 27. Stipp, S. & Hochella, M. Structure and bonding environments at the calcite surface as observed with X-ray photoelectron spectroscopy (XPS) and low energy electron diffraction (LEED). *Geochim. Cosmochim. Acta* **55**, 1723–1736 (1991).
 28. Fenter, P., Geissbühler, P., DiMasi, E. & Srajer, G. Surface speciation of calcite observed in situ by high-resolution X-ray reflectivity. *Geochimica et Cosmochimica Acta* **64**, 1221–1228 (2000).
 29. Schütte, J. *et al.* Clear Signature of the (2 × 1) Reconstruction of Calcite (10 $\bar{1}$ 4). *Langmuir* **26**, 8295–8300 (2010).
 30. Rahe, P., Schütte, J. & Kühnle, A. NC-AFM contrast formation on the calcite (1014) surface. *J. Phys.: Condens. Matter* **24**, 084006 (2012).
 31. Stipp, S. L. S., Eggleston, C. M. & Nielsen, B. S. Calcite surface structure observed at microtopographic and molecular scales with atomic force microscopy (AFM). *Geochimica et Cosmochimica Acta* **58**, 3023–3033 (1994).
 32. Ohnesorge, F. Towards atomic resolution non-contact dynamic force microscopy in a liquid. *Surf. Interface Anal.* **27**, 379–385 (1999).
 33. Rode, S., Oyabu, N., Kobayashi, K., Yamada, H. & Kühnle, A. True Atomic-Resolution Imaging of (10 $\bar{1}$ 4) Calcite in Aqueous Solution by Frequency Modulation Atomic Force Microscopy. *Langmuir*

-
- 25**, 2850–2853 (2009).
34. Kuhn, S. *et al.* Identifying the absolute orientation of a low-symmetry surface in real space. *Phys. Rev. B* **90**, 195405 (2014).
 35. Zullig, J. J. & Morse, J. W. Interaction of organic acids with carbonate mineral surfaces in seawater and related solutions: I. Fatty acid adsorption. *Geochimica et Cosmochimica Acta* **52**, 1667–1678 (1988).
 36. Bohr, J., Wogelius, R. A., Morris, P. M. & Stipp, S. L. S. Thickness and structure of the water film deposited from vapour on calcite surfaces. *Geochimica et Cosmochimica Acta* **74**, 5985–5999 (2010).
 37. Freeman, C. L. *et al.* New Forcefields for Modeling Biomineralization Processes. *J. Phys. Chem. C* **111**, 11943–11951 (2007).
 38. Maslen, E. N., Streltsov, V. A. & Streltsova, N. R. X-ray study of the electron density in calcite, CaCO₃. *Acta Crystallogr B Struct Sci* **49**, 636–641 (1993).
 39. Rahe, P., Kuhn, S. & Kühnle, A. Is Calcite (1014) a Chiral Surface? *JUNQ* **3**, 21–25 (2013).
 40. Kristensen, R., Stipp, S. L. S. & Refson, K. Modeling steps and kinks on the surface of calcite. *J. Chem. Phys.* **121**, 8511–8523 (2004).
 41. Rohl, A. L., Wright, K. & Gale, J. D. Evidence from surface phonons for the (2 x 1) reconstruction of the (1014) surface of calcite from computer simulation. *Am. Mineralogist* **88**, 921–925 (2003).
 42. Akiyama, T., Nakamura, K. & Ito, T. Atomic and electronic structures of CaCO₃ surfaces. *Phys. Rev. B* **84**, 085428 (2011).
 43. Jin, M., Shimada, E. & Ikuma, Y. Observation of Calcite (1014) Surface by AFM in Air and Surface Structure Analysis. *J. Ceram. Soc. Jap.* **107**, 1166–1170 (1999).
 44. Eriksson, R., Merta, J. & Rosenholm, J. B. The calcite/water interface: I. Surface charge in indifferent electrolyte media and the influence of low-molecular-weight polyelectrolyte. *Journal of Colloid and Interface Science* **313**, 184–193 (2007).
 45. Somasundaran, P. & Agar, G. E. The zero point of charge of calcite. *Journal of Colloid and Interface Science* **24**, 433–440 (1967).
 46. Foxall, T., Peterson, G. C., Rendall, H. M. & Smith, A. L. Charge determination at calcium salt/aqueous solution interface. *J. Chem. Soc., Faraday Trans. 1* **75**, 1034–1039 (1979).
 47. Wolthers, M., Di Tommaso, D., Du, Z. & de Leeuw, N. H. Calcite surface structure and reactivity: molecular dynamics simulations and macroscopic surface modelling of the calcite-water interface. *Phys. Chem. Chem. Phys.* **14**, 15145–15157 (2012).
 48. Andersson, M. P. & Stipp, S. L. S. How acidic is water on calcite? *J. Phys. Chem. C* **116**, 18779–18787 (2012).
 49. Heberling, F., Eng, P., Denecke, M. A., Lützenkirchen, J. & Geckeis, H. Electrolyte layering at the calcite(104)–water interface indicated by Rb⁺- and Se(vi) K-edge resonant interface diffraction. *Physical Chemistry Chemical Physics* **16**, 12782–12792 (2014).
 50. Stöckelmann, E. & Hentschke, R. Adsorption Isotherms of Water Vapor on Calcite: A Molecular Dynamics–Monte Carlo Hybrid Simulation Using a Polarizable Water Model. *Langmuir* **15**, 5141–5149 (1999).
 51. Kerisit, S. & Parker, S. C. Free energy of adsorption of water and calcium on the {10 $\bar{1}$ 4} calcite surface. *Chem. Comm.* 52–53 (2004).
 52. Spagnoli, D., Cooke, D. J., Kerisit, S. & Parker, S. C. Molecular dynamics simulations of the interaction between the surfaces of polar solids and aqueous solutions. *J Mater Chem* **16**, 1997–2006 (2006).
 53. Perry, T. D., IV, Cygan, R. T. & Mitchell, R. Molecular models of a hydrated calcite mineral surface. *Geochimica et Cosmochimica Acta* (2007).
 54. Ben-Yaakov, D., Andelman, D., Podgornik, R. & Harries, D. Ion-specific hydration effects: Extending the Poisson-Boltzmann theory. *Curr. Op. Col. Interf. Sci.* **16**, 542–550 (2011).
 55. Spagnoli, D., Kerisit, S. & Parker, S. C. Atomistic simulation of the free energies of dissolution of ions from flat and stepped calcite surfaces. *Journal of Crystal Growth* **294**, 103–110 (2006).
 56. de Leeuw, N. H. Molecular Dynamics Simulations of the Growth Inhibiting Effect of Fe²⁺, Mg²⁺, Cd²⁺, and Sr²⁺ on Calcite Crystal Growth. *The Journal of Physical Chemistry B* **106**, 5241–5249 (2002).
 57. Gratz, A. J. & Hillner, P. E. Poisoning of calcite growth viewed in the atomic force microscope (AFM). *Journal of Crystal Growth* **129**, 789–793 (1993).
 58. Davis, K. J., Dove, P. M. & De Yoreo, J. J. The role of Mg²⁺ as an impurity in calcite growth. *Science* **290**, 1134–1137 (2000).
 59. Bisschop, J., Dysthe, D. K., Putnis, C. V. & Jamtveit, B. In situ AFM study of the dissolution and

-
- recrystallization behaviour of polished and stressed calcite surfaces. *Geochimica et Cosmochimica Acta* **70**, 1728–1738 (2006).
60. De Yoreo, J. J. *et al.* Rethinking Classical Crystal Growth Models through Molecular Scale Insights: Consequences of Kink-Limited Kinetics. *Crystal Growth & Design* **9**, 5135–5144 (2009).
 61. Ruiz-Agudo, E., Putnis, C. V., Rodriguez-Navarro, C. & Putnis, A. Effect of pH on calcite growth at constant ratio and supersaturation. *Geochimica et Cosmochimica Acta* **75**, 284–296 (2010).
 62. Ruiz-Agudo, E., Putnis, C. V., Wang, L. & Putnis, A. Specific effects of background electrolytes on the kinetics of step propagation during calcite growth. *Geochimica et Cosmochimica Acta* **75**, 3803–3814 (2011).
 63. Wang, L., Ruiz-Agudo, E., Putnis, C. V. & Putnis, A. Direct observations of the modification of calcite growth morphology by Li⁺ through selectively stabilizing an energetically unfavourable face. *Cryst Eng Comm* **13**, 3962 (2011).
 64. Wasylenki, L. E., Dove, P. M., Wilson, D. S. & De Yoreo, J. J. Nanoscale effects of strontium on calcite growth: An in situ AFM study in the absence of vital effects. *Geochimica et Cosmochimica Acta* **69**, 3017–3027 (2005).
 65. Arvidson, R. S. *et al.* Magnesium inhibition of calcite dissolution kinetics. *Geochimica et Cosmochimica Acta* **70**, 583–594 (2005).
 66. Elhadj, S., De Yoreo, J. J., Hoyer, J. R. & Dove, P. M. Role of molecular charge and hydrophilicity in regulating the kinetics of crystal growth. *Proceedings of the National Academy of Sciences* **103**, 19237–19242 (2006).
 67. García, R. *Amplitude Modulation Atomic Force Microscopy*. (John Wiley & Sons, 2011).
 68. Parkhurst, D. L. & Appelo, C. A. J. *User's guide to PHREEQC (Version 2): A computer program for speciation, batch-reaction, one-dimensional transport, and inverse geochemical calculations*. U.S. Geological Survey : Earth Science Information Center (1999).
 69. Nielsen, L. C., De Yoreo, J. J. & DePaolo, D. J. General model for calcite growth kinetics in the presence of impurity ions. *Geochimica et Cosmochimica Acta* **115**, 100–114
 70. Lardge, J. S., Duffy, D. M., Gillan, M. J. & Watkins, M. Ab Initio Simulations of the Interaction between Water and Defects on the Calcite (10 $\bar{1}$ 4) Surface. *J. Phys. Chem. C* **114**, 2664–2668 (2010).
 71. Teng, H. H., Dove, P. M. & De Yoreo, J. J. Kinetics of calcite growth: surface processes and relationships to macroscopic rate laws. *Geochimica et Cosmochimica Acta* (2000).
 72. Perdikouri, C., Putnis, C. V., Kasiotas, A. & Putnis, A. An Atomic Force Microscopy Study of the Growth of a Calcite Surface as a Function of Calcium/Total Carbonate Concentration Ratio in Solution at Constant Supersaturation. *Crystal Growth & Design* **9**, 4344–4350 (2009).
 73. Larsen, K., Bechgaard, K. & Stipp, S. L. S. The effect of the Ca²⁺ to activity ratio on spiral growth at the calcite surface. *Geochimica et Cosmochimica Acta* **74**, 2099–2109 (2010).
 74. Hillner, P. E., Gratz, A. J., Manne, S. & Hansma, P. K. Atomic-scale imaging of calcite growth and dissolution in real time. *Geology* **20**, 359–362 (1992).
 75. Ruiz-Agudo, E., Putnis, C. V., Jiménez-López, C. & Rodriguez-Navarro, C. An atomic force microscopy study of calcite dissolution in saline solutions: The role of magnesium ions. *Geochimica et Cosmochimica Acta* **73**, 3201–3217 (2009).
 76. Vavouraki, A. I., Putnis, C. V., Putnis, A. & Koutsoukos, P. G. An Atomic Force Microscopy study of the growth of calcite in the presence of sodium sulfate. *Chemical Geology* **253**, 243–251 (2008).
 77. Wasylenki, L. E., Dove, P. M. & De Yoreo, J. J. Effects of temperature and transport conditions on calcite growth in the presence of Mg²⁺: Implications for paleothermometry. *Geochimica et Cosmochimica Acta* **69**, 4227–4236 (2005).
 78. Dove, M. T., Winkler, B., Leslie, M., Harris, M. J. & Salje, E. K. H. A new interatomic potential model for calcite: applications to lattice dynamics studies, phase transition, and isotope fractionation. *American Mineralogist* **77**, 244–250 (1992).
 79. MacKerell A D *et al.* All-Atom Empirical Potential for Molecular Modeling and Dynamics Studies of Proteins. *The Journal of Physical Chemistry B* **102**, 3586–3616 (1998).
 80. Mackerell, A. D. Empirical force fields for biological macromolecules: Overview and issues. *J. Comput. Chem.* **25**, 1584–1604 (2004).
 81. Brooks, B. R. *et al.* CHARMM: The biomolecular simulation program. *J. Comput. Chem.* **30**, 1545–1614 (2009).
 82. Phillips, J. C. *et al.* Scalable molecular dynamics with NAMD. *J. Comput. Chem.* **26**, 1781–1802 (2005).
 83. Humphrey, W., Dalke, A. & Schulten, K. VMD: visual molecular dynamics. *J Mol Graph* **14**, 33–8, 27–8 (1996).

-
84. Michaud-Agrawal, N., Denning, E. J., Woolf, T. B. & Beckstein, O. MDAnalysis: A toolkit for the analysis of molecular dynamics simulations. *J. Comput. Chem.* **32**, 2319–2327 (2011).
 85. Voitchovsky, K., Kuna, J. J., Contera, S. A., Tosatti, E. & Stellacci, F. Direct mapping of the solid-liquid adhesion energy with subnanometre resolution. *Nature Nanotechnology* **5**, 401–405 (2010).
 86. Kuna, J. J. *et al.* The effect of nanometre-scale structure on interfacial energy. *Nature Materials* **8**, 837–842 (2009).
 87. Voitchovsky, K. & Ricci, M. High-resolution imaging of solvation structures with amplitude-modulation atomic force microscopy. in (Parak, W. J., Yamamoto, K. & Osinski, M.) **8232**, 82320O–8 (SPIE, 2012).
 88. Ricci, M., Spijker, P. & Voitchovsky, K. Water-induced correlation between single ions imaged at the solid-liquid interface. *Nat Commun* **5 SP**, (2014).
 89. Cleveland, J. P., Anczykowski, B., Schmid, A. E. & Elings, V. B. Energy dissipation in tapping-mode atomic force microscopy. *Appl. Phys. Lett.* **72**, 2613–2615 (1998).
 90. Anczykowski, B., Gotsmann, B., Fuchs, H., Cleveland, J. P. & Elings, V. B. How to measure energy dissipation in dynamic mode atomic force microscopy. *Applied Surface Science* **140**, 376–382 (1999).
 91. Melcher, J. *et al.* Origins of phase contrast in the atomic force microscope in liquids. *PNAS* 1–6 (2009). <<http://www.pnas.org/cgi/doi/10.1073/pnas.0902240106>>
 92. Voitchovsky, K. Anharmonicity, solvation forces, and resolution in atomic force microscopy at the solid-liquid interface. *Phys. Rev. E* **88**, 022407 (2013).
 93. Garcia, R. *et al.* Identification of Nanoscale Dissipation Processes by Dynamic Atomic Force Microscopy. *Phys. Rev. Lett.* **97**, 016103 (2006).
 94. Magonov, S. N., Elings, V. & Whangbo, M. H. Phase imaging and stiffness in tapping-mode atomic force microscopy. *Surface Science* **375**, L385-L391 (1997).
 95. Kiracofe, D. & Raman, A. Nonlinear dynamics of the atomic force microscope at the liquid-solid interface. *Phys. Rev. B* **86**, 205405 (2012).

Chapter 6

Interaction of organic molecules with the surface of calcite in ionic solutions

In the previous chapter, the properties of the calcite (10 $\bar{1}$ 4) surface in presence of ionic solutions have been explored. In this chapter, I will add one more ingredient to the system: fatty acid organic molecules (subsection 6.1.1). These molecules are known to strongly interact with the calcite surface creating an organic monolayer that renders the initially hydrophilic surface more hydrophobic. This process is relevant for several industry-related processes, particularly for petroleum industry. AFM will be used to explore the heterogeneous system composed by water, ions, calcite surface and organic molecules. All these components are interacting together in an out-of equilibrium environment.

In the first section (section 6.1) I will examine the dynamical changes occurring at the surface of calcite in the presence of adsorbed stearic acids (SA), one the main polar component of crude oil. I will first characterize the mechanical properties of the organic patches in air and in liquid (subsection 6.1.2). Then I will explore how these patches modify the restructuring dynamic of the crystal surface when exposed to several brines with different concentrations (subsection 6.1.3). The growth and dissolution processes at a higher degree of organic coverage will also be studied (subsection 6.1.4).

In the last section (section 6.2) I will study how the carboxylic functional group, responsible for the anchoring of the SA to the surface, changes the affinity with the calcite surface as a function of the ionic environment and pH. To explore this effect, a series of adhesion force measurements between a carboxylic-terminated functionalized AFM tip and the surface of calcite will be presented. I will explore different functionalization strategies (subsection 6.2.1), to finish with the critical analysis of the data (subsections 6.2.2- 6.2.4).

6.1 Interaction of carboxylic acids with the (10 $\bar{1}$ 4) surface of calcite

In Chapter 5, we showed that high-resolution atomic force microscopy (AFM) in liquid^{1,2} was able to provide a molecular description of the specific interaction that ions, such as Na⁺, Cl⁻, Ca²⁺ and Rb⁺, have with the (10 $\bar{1}$ 4) surface of calcite. The results, recently confirmed by X-ray reflectivity³, showed that, the ordered layer of water molecules that naturally hydrates the calcite surface, is controlling the ionic adsorption. Depending on the hydration properties and density of charge of the ion, different complexation sites are possible but, generally, the ions that constitute the crystal cannot physically approach the flat regions.⁴ In this description, the Ca²⁺ ions, can only reach the surface at singularities such as step edges where the surface hydration properties are altered.^{5,6} These observations reconcile the experimental evidence of growth and dissolution of the calcite crystal.

We will now examine a more complex situation in which fatty acids are attached on the surface of the crystal. This more complex system is relevant for the petroleum industry.

In petroleum-related applications, calcite occupies a central role given the natural abundance; calcareous rocks enclose more than 40% of known oil reserves. Important research efforts have hence been dedicated to the study of the calcite in contact with oil,^{7,8} in particular under conditions that mimic natural reservoirs.^{9,10} Understanding the molecular interactions between heavy organics and the surface of calcite is not only essential for efficient oil recovery, but also for predicting the geological fate of emptied reservoirs and optimizing remediation in the case of spills. In all these processes, calcite is generally out of equilibrium with the surrounding causing a rapid evolution of the surface morphology. So-called water-flooding is one of the most common secondary oil recovery methods for oil extraction. Water-flooding consists of the injection of saline water in a pre-existing oil reservoir in order to extract further oil after the primary production which uses the reservoir's natural energy. Since 1967¹¹ the use of saline solutions with low ionic strength during the water-flooding has shown to increase the efficiency in the recovery process if compared to high salinity brine injection.¹²⁻¹⁴ To date, convincing evidence demonstrates that recovery from sandstone reservoirs can be improved in this manner (see e.g. Morrow *et al.*¹⁵). It is generally believed that the mechanism driving this low ionic strength phenomenon in sandstones is related to wettability alterations of the minerals that compose the reservoir, from an oil-wet towards a more water-wet state.^{16,17} Recently, studies have attempted to extend the findings to carbonate reservoirs, with experimental evidence suggesting that the wettability of carbonate rock can also be altered by a reduction of the ionic strength of the brine.^{9,12-14} However, much less is known about effects in low ionic strength involving carbonated rocks and a consistent molecular-level explanation of the wettability alteration mechanism has not yet emerged. This is largely due to the fact that calcite is a highly dynamic surface when wetted by an aqueous solution. The interfacial phenomena occurring at the calcite's surface depend on a complex interplay between the mineral itself, the composition of the contacting ionic solution and the organic components that are naturally present. At the molecular level, structural changes occur within seconds, rendering any relevant study particularly challenging.

Substantial research efforts have addressed the question of how different ionic species that are naturally present in the water phase can influence the growth and dissolution of calcite during biomineralization processes.¹⁸⁻²⁸ A large amount of literature has also focused on the interaction of organic molecules with the rock surface, and the resulting alteration of the kinetic process of calcite restructuring.²⁹⁻³² However, the inherent complexity of the system and the large number of variables that influence the surface dynamics of calcite often result in conflicting findings.^{21,33} This is partly due to the fact that most of the results lack of molecular-level description of the interaction process of organics with calcite.

Here, we apply a similar AFM approach as described in Chapter 5 to study the dynamical changes occurring at the surface of calcite in brine solutions with different ionic composition and concentrations, and in the presence of adsorbed fatty acids.³⁴ Oil-soluble fatty acids with long carbon chains such as stearic acids (SA) play an important role in altering the wettability of the

calcite. They adsorb to the surface and expose the hydrophobic components to the aqueous/oily mixture.^{35,36} As a result the surface of the rocks becomes more hydrophobic.

6.1.1 Fatty acids-calcite surface interaction mechanism

Fatty acids are organic molecules composed by a carboxylic (COOH) acid with an aliphatic chain. The shortest fatty acid is formic acid (HCOOH) and the longest chain can be longer than 22 carbon atoms. The solubility in water is inversely related to the length of the aliphatic chain, the shorter the fatty acid the higher the water solubility. The solubility depends also on the protonation state of the molecule; a protonated and electrically neutral molecule has a lower solubility than in the dissociated state. However, once the fatty acids reach a solid surface and start to form a monolayer, longer carbon chain molecules achieve a higher gain in energy when creating a densely packed layer, which is associated to a more stable configuration. Osman *et al.*³⁷ found that the longer the alkyl chain of the fatty acids the higher the degree of ordering on the calcite surface. This was also associated with a larger population of trans molecules, i.e. carbon chains that align vertically on the surface with a lower degree of freedom, as expected in the case of a densely packed monolayer. In particular the stearic acid (18-carbon chain) monolayer was found to form an ordered solid-like phase that, at the highest density, corresponds to 0.20 nm² per molecule. This corresponds exactly to the area occupied by one calcium atom on the (10 $\bar{1}$ 4) calcite surface. In general, reported experimental results varied in terms of packing and density and were largely affected by both the preparation method (dry or wet preparation in organic or water solvents) and conditions in which the measurements were performed.^{38,39} Another aspect to be considered is the strong interaction between the organic molecules themselves. This interaction is stronger between molecules with longer alkyl chains, as in the case of SA. When increasing the amount of organic molecules on the surface, bilayers or multilayers may form. It has been reported that a bilayer formation can even begin before completion of the monolayer.⁴⁰ The second layer was found to be weakly attached onto the surface and hence considered physisorbed. The formation of bilayer also depend on the surrounding environment and has been shown to occur particularly in water-based media.^{38,39}

We have seen in Chapter 5 that some hydroxyl groups are bound to the calcite–water interface at the >Ca sites, even in ambient humidity.^{41,42} >Ca denotes a surface calcium site. Fenter *et al.*⁴³ observed, using X-ray reflectivity, that the stearate molecular coverage matched, within measurement error, with the density of >Ca sites. They also noticed the removal from the surface of the -OH groups upon monolayer formation. Accordingly to these observations they concluded that the stearate molecules are bound to the surface through a site-specific Ca–O bond, and thus, likely to be chemisorbed. On the basis of these observations, the adsorption reaction may be described as:



where R indicates the hydrocarbon chain of the fatty acid molecule.⁴³ A similar conclusion was obtained by Osman *et al.*³⁷ by a combination of various techniques, including TGA, NMR and FTIR.

The situation where fatty acid molecules are in water solutions of variable pH and different types of ions is even more complicated. In this case a competitive absorption between protons as well as monovalent and divalent ions, possibly with specific affinity, affects the functional group of the organics even before they reach the surface of the mineral. This specific effect will be discussed in section 6.2.

Here, we start from a monolayer or bilayer already formed on the surface of a calcite crystal in air (see section 6.3.1 for the preparation method). We first characterize properties of the SA coated surface in air and then expose the surface to a supersaturated ionic solution which is able to trigger the growth process of the calcite surface. We will use the same brine solutions and notation as listed in section 5.2.2.

6.1.2 Structure of the SA patches at the surface of calcite in air and in liquid

Before studying the structural changes occurring at the calcite surface in the different brines, it is necessary to establish a reference experiment to correctly interpret the AFM images. The interpretation of the results can be challenging due to the embedding of SA patches into the calcite crystal after growth. It is therefore necessary to use a technique that is able to differentiate organic SA patches from the inorganic calcite surface, regardless of topography or imaging conditions. This was achieved with PeakForce Quantitative Nanomechanical Property Mapping (QNM). QNM can simultaneously map the adhesion force experienced by the scanning tip when touching the sample. The results are presented in Fig.6.1 on the sample of calcite first in air (Fig.6.1A and B) and then in Brine3 (Fig.6.1C and D).

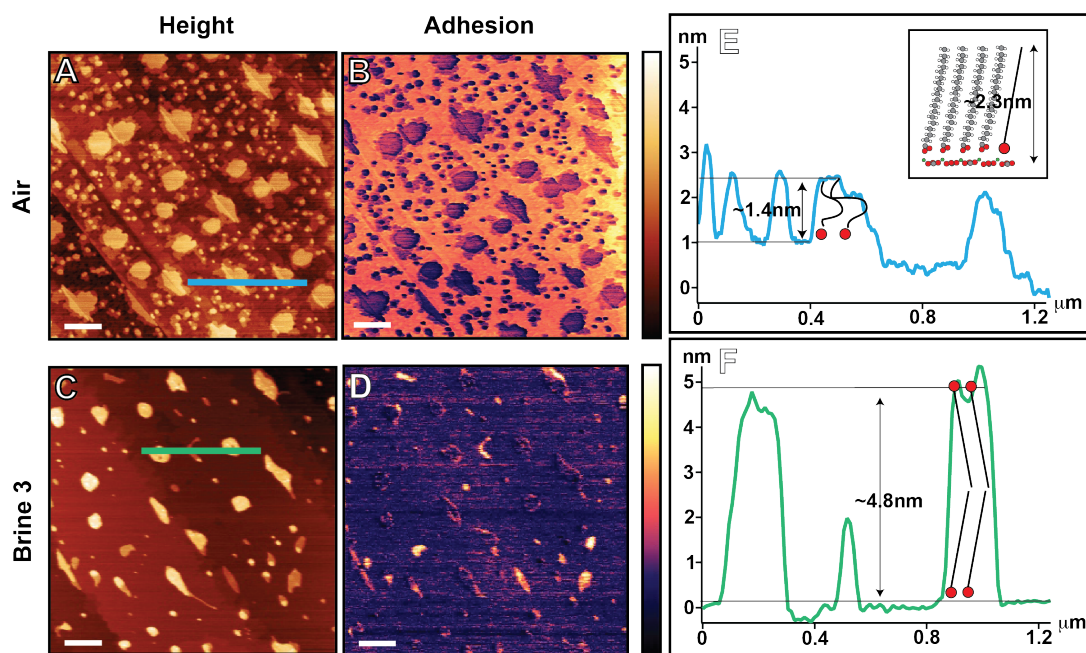


Fig. 6.1: QNM measurements on a calcite surface partially covered with SA molecules. We present the height (A and C) and adhesion (B and D) channels recorded on the same sample first in air (A, B) and then in Brine3 $\times 2$ (C, D) with the same AFM tip on the same area of the sample. The scale bar is 400 nm (A-D). The color scale bars are 4 nm (A), 1.1nN (B), 9 nm (C) and 21.8nN (D). Image (E) and (F) are the line profile highlighted respectively in (A) and (C). In the inset of (E) a schematic representation of the SA molecules completely extended on the calcite surface. The figure is obtained from the X-ray reflectivity data of Fenter *et al.*⁴³ and the vertical scale match the scale of the line profiles.

Irregular patches that appear brighter in topography are visible at calcite steps in air (see Fig. 6.1A). They preserve shape and are stable in time upon scanning. These SA patches present a lower mean adhesion (~ 18 nN) compared to of the rest of the calcite surface (~ 22 nN). We attribute the main contribution of the adhesion force to the capillary force occurring between the tip and the sample in air. Consistently, the hydrophilic calcite surface presents a higher adhesion force than the hydrophobic organic patches. The change in adhesion force can be related to the tip radius, the surface tension of the liquid and the wetting properties of the tip and the sample.⁴⁴

The apparent height of the organic patches varied between 1.1 nm and 1.4 nm over different samples and different imaging conditions. This value is significantly lower than previously reported for for a densely packed SA monolayer in standing up phase (2.3-2.4 nm).^{45,43} Several causes may lead to a reduction of the expected SA monolayer height. Some of them are related to a real physical property of the organic layer, like a loose packing of the SA molecules. Others are related to an artifact of the AFM measurement, like the mechanical indentation of the soft SA patches by the AFM tip. In order to discard the latter, we quantified the maximum tip indentation with QNM (see Fig. 6.2) and were able to rule out tip-induced effects, confirming a maximum SA thickness of the order of 1.1-1.4 nm. We therefore explain the reduced SA higher by a loose packing of the organic molecules on the surface, as previously reported by Sauthier *et al.*⁴⁵ and

Kumar *et al.*⁴⁶ on different substrates. Mihajlović *et al.*⁴⁷ even reported some inhomogeneity in terms of coverage on the SA-modified calcite surface, using the ‘dry modification method’. They suggested that the alkyl chains can be partially arranged horizontally or tilted on the surface. This does not imply that the patches are composed by a lying down phase of SA, which would result in an even lower apparent height. We rather believe that that the SA patches are formed by a disordered phase of organics (schematically depicted in Fig. 6.1E).

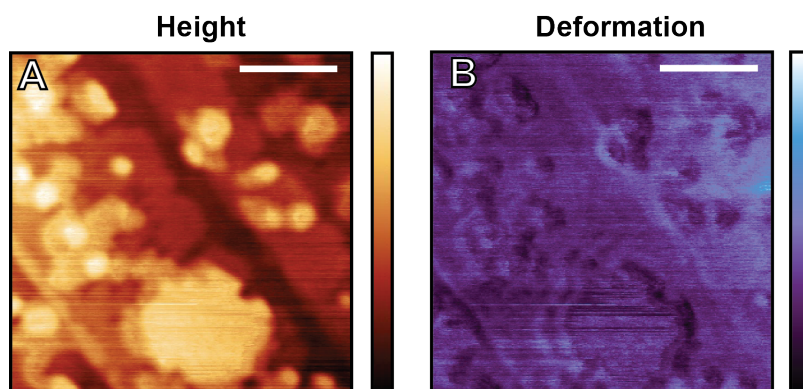


Fig. 6.2: QNM measurement on a magnified area of the sample presented in Fig. 6.1 performed in air. The height channel (A) and the deformation channels (B) are presented. The scale bars in the images correspond to 200 nm. The height color scale is 3.5 nm while the deformation color scale is 0.55 nm.

Immersing the sample into Brine3_×2 (twice diluted to limit calcite growth) revealed taller patches whose height is consistent with densely packed SA multilayers (generally between 2 to 4 layers, see Fig. 6.3). This result supports the idea of a water-induced reorganization of the SA molecules that minimizes hydrophobic exposure. The observed adhesion forces between the tip and the sample do not showed much contrast between SA and calcite, confirming that most SA regions exposed the hydrophilic heads to the liquid. A few exceptions could be identified (Fig. 6.1D) in which thinner patches appeared to still expose the hydrophobic alkyl chains to the ionic solution. The general trend found confirm that, in the presence of a highly polar solvent like water, the structure of the steric acid layer tended to rearrange to minimize the hydrophobic exposure. This means that SA in water arranges into taller bi- and multilayer patches, even before the first chemisorbed layer of stearic acid is completely formed (see also Fig. 6.3 and 6.9).

In the Fig. 6.3 we report a different experiment with a slightly higher amount of organics on the surface being exposed to Brine2. On the surface there were several patches of different dimensions and height. In the related histogram (Fig. 6.3) it is possible to distinguish 4 different peaks, where the peak centered at 0 nm in height corresponds to the substrate. There are 3 additional peaks: the first one at 4.7 nm corresponds to the bilayer configuration of the SA; the last one at 10 nm can be attributed to 4 layers of SA while the second one at 6.5 nm can be attributed to 3 layers of SA. It is surprising that in this case the height of the third layer is roughly 1.8 nm and not 2.3-2.4 nm as expected in a conventional standing up phase of densely packed SA. The patches in liquid were generally taller than the single layer observed in air and two layers were normally observed consistently with a bilayer structure, each one of roughly 2.3-2.4 nm. The presence of the bilayer conformation is known to happen at a higher organic coverage when the first monolayer is completely formed, but it has been shown that the final structure of depends considerably on the preparation method. Shi X. *et al.* characterized the property of the stearic acid layer obtained with different preparation methods and in different solvents in two consecutive papers^{38,39}. They showed that the bilayer conformation can be found even if the first monolayer of chemisorbed stearic acid is not completely formed. They attributed the presence of the bilayer to the applied water-coating method, which involved mixing calcium carbonate particles with a stearin soap emulsion. In this case they couldn't reach the expected maximum chemisorbed coverage even when increasing the amount of organic in solution.³⁸ Although our preparation method is different, we found that in the presence of a highly polar solvent like water, the structure of the SA layer tends to rearrange to minimize the hydrophobic exposure to water. This

means that SA forms taller bilayer patches when immersed in water even if the chemisorbed layer of stearic acid is not completely formed (see also Fig. 6.9).

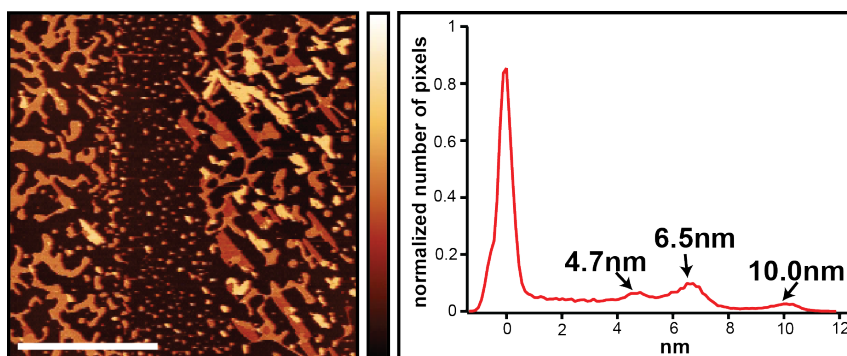


Fig. 6.3: Multilayer formation upon immersion of the calcite covered with SA into Brine2. Left: AM-AFM image of the surface of calcite covered with stearic acid immediately after the immersion of the sample in the Brine2_{×2}. On the surface there are several patches of different dimensions and height. Right: Histogram, where the height distribution of the image is presented. The scale bar in the image corresponds to 2 μm and the color scale to 16 nm.

6.1.3 Dissolution and growth of calcite in the presence of low SA coverage

When a sample partially covered with SA was immersed into a supersaturated brine, the calcite crystal grows. The organic patches initially appeared as protruding features on the surface (light colored in Fig. 6.4), but with proceeding crystal growth the surface level of the calcite exceeded the patch high. Protruding patches thus became holes in the surface (dark colored, Fig. 6.4). The process can be reversed upon dilution of the brine (see Fig. 6.5), exposing to the solution the same organic patches that had been embedded inside the rock (see Fig. 6.4). Similarly to the dilution and growth experiments presented in Chapter 5 for organic-free calcite, it was possible to follow in real time the morphology of the surface (see section 5.4.3). The results are presented in the series of time-lapse images of the region of interest as a function of the time and Brine2 concentration. It was evident that the presence of the organic molecule on the surface slows down the dynamical changes of the calcite surface.

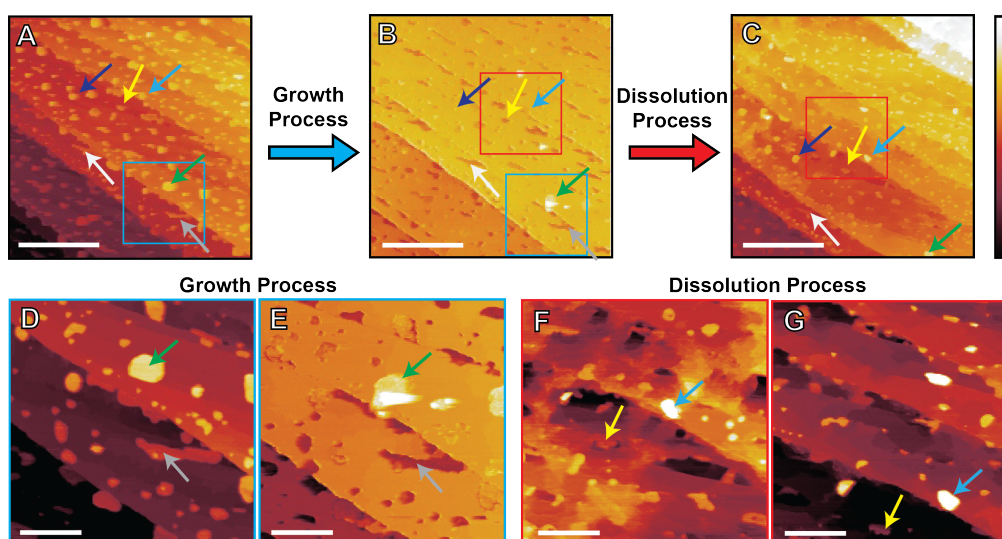


Fig. 6.4: Following the growth and dissolution process of calcite covered with patches of SA in Brine2. In images (A), (B) and (C) the same area of the sample is followed in time at different concentrations of Brine2. Image (A) is taken immediately after the injection of Brine2_{×2} and image (B) at the end of the growth process, immediately after the injection of Brine2_{×10}. Image (C) is captured after several hours from the injection of Brine2_{×50}. Images (D) and (E) are magnification of the respective images (A) and (B). Images (F) and (G) follow the dissolution process in Brine2_{×50} (F) and immediately after the injection of Brine2_{×100} (G). Arrows with different colors indicate the same patch of SA at different times of the growth and dissolution process. The scale bars are 1 μm (A-C) and 250 nm (D-G). The color scale bars are 20 nm (A-E) and 10 nm (F, G).

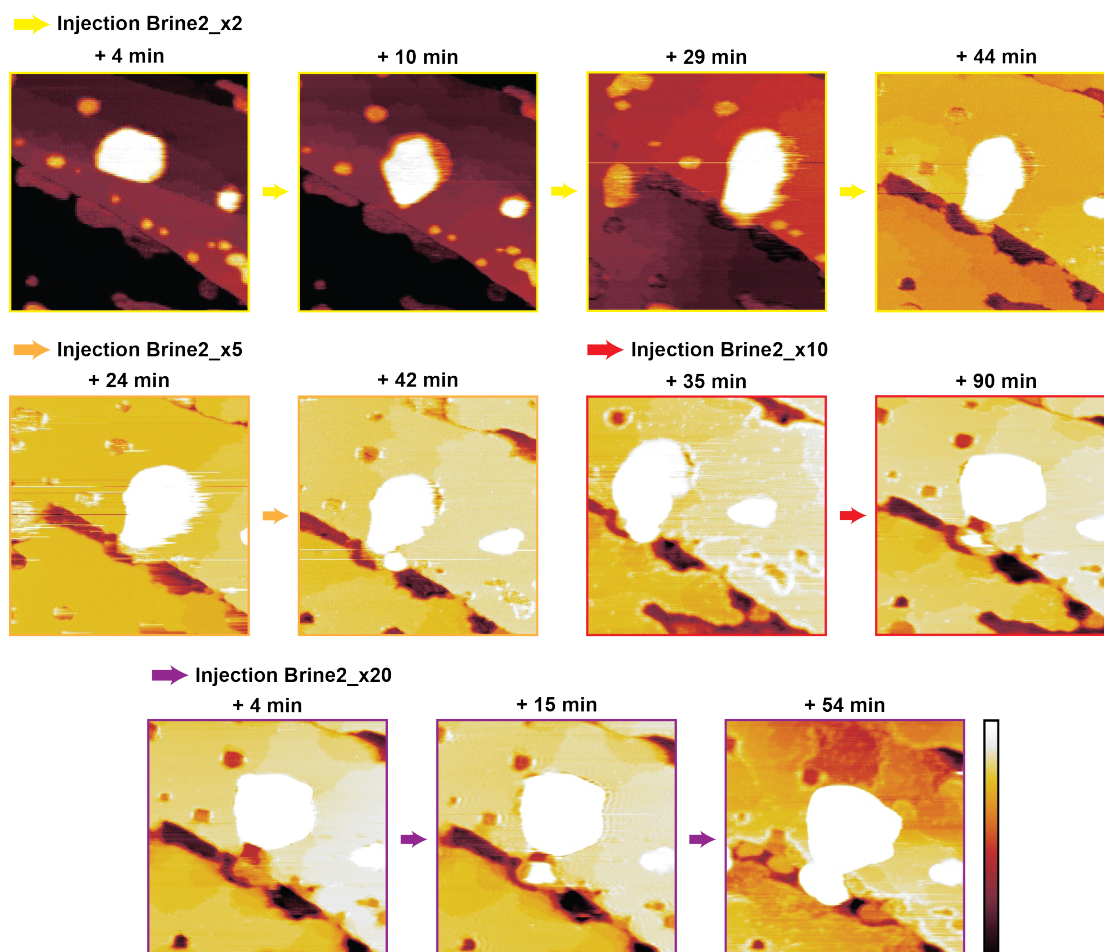


Fig. 6.5: Series of images of the same area of the sample at different time and in different concentrations of Brine2. All images have a scan-size of 500 nm and are not drift corrected. The color scale refers to a total height variation of 11 nm. The time is indicated on top of the images and refers to moment of injection of the brine concentration indicated on top of the related images.

Fig. 6.4 shows the growth and dissolution of the calcite surface in Brine2 at different concentrations in the presence of SA patches. The organic patches were stable throughout the process (Fig. 6.4A, B and C). The growth phase tended to level the surface of calcite, which became flatter and more regular. As a result, protruding patches that were initially located on highest steps could not be reached by the growing crystal and embedded into solid (compare green arrows in Fig. 6.4A and B and in Fig. 6.4D and E), while other patches got easily incorporated. The subsequent brine dilution recovered a more irregular surface (compare Fig. 6.4B and C) and the organic patches embedded in the newly formed crystal turned again into protrusions on the calcite surface (compare Fig. 6.4B and C, Fig. 6.4F and G). In Fig. 6.5, the same experiment is presented focusing on the variation of the surface morphology. When Brine2_{x2} was injected the calcite surface started to grow around the organic patches and reached a final equilibrium with the solution after almost 1 hour. Note that no surface rearrangement is visible on the time scale of the measurement (several minutes). The injection of Brine2_{x5} and Brine2_{x10} did not exhibit comparable growth kinetics and the restructuring process was much slower. Finally, when Brine2_{x20} was injected the inverse process occurred and patches previously trapped in the holes built up by the calcite crystal reemerged on the surface.

In Brine3 a very similar trend was observed in terms of calcite growth and dilution around the stearic acid patches (we show only the dilution part of the process in Fig. 6.6).

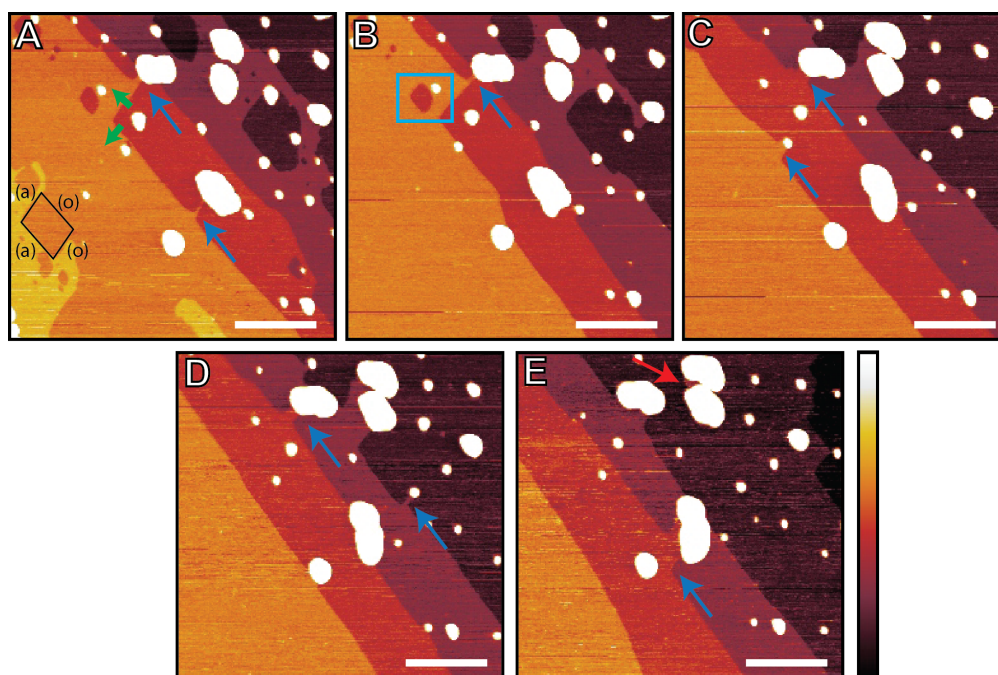


Fig. 6.6: Dissolution process of calcite with patches of SA in Brine3_x20. The acquisition time was as follows: Image (A) – 0min; (B) – 4min; (C) – 8min; (D) – 13min; (E) – 21min. The green arrows in (A) indicate the preferential directions for calcite dissolution, while the typical etch pit structure (example in the blue box of image (B)) is presented as a sketch on the left of the same image. The obtuse and acute steps are indicated respectively as (o) and (a). The blue arrows indicate pinning points. The scale bar and is 250 nm. The color scale bar corresponds to a height variation of 2 nm.

Similarly to Sr^{2+} ions, adsorbed SA slowed the growth and dissolution of calcite with patches acting as pinning points. This is visible in Fig. 6.6, where consecutive images of the same area of the surface in Brine3_x20 show that the organic patches are pinning the step (see blue arrows in Fig. 6.6). This result is consistent with previous findings that organics act as growth inhibitor for calcium carbonate.^{31,48} De Leeuw *et al.*, found, using MD-simulations, that the carboxylic acid is a growth inhibitor by replacing water molecules at calcite steps, thus blocking the access to new growing material.⁴⁹ The pinning effect of the adsorbed organic patches further complicates the dissolution process: when the step edge reaches the SA patch, it needs to first dissolve laterally to avoid the protective organic layer. By doing so, it exposes crystallographic directions that dissolve more slowly, hence creating a residual step behind the organic patch (white arrow in Fig. 6.6D). The anchoring point of the organic patch on the calcite surface remains intact, allowing the formation of stable calcite terraces despite the dissolution (see red arrow in Fig. 6.6E). The same process is found to happen in Brine2 as shown in Fig. 6.7 for a comparison.

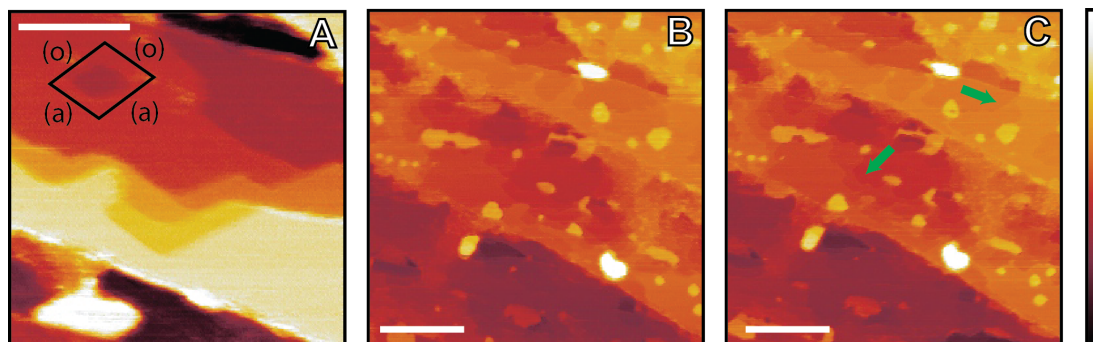


Fig. 6.7: Dissolution of the calcite surface covered by patches of SA in the Brine2_x100 (A) or Brine2_x50 (B and C). Image (A) represents an example of an etch pit formation on the surface that enable us to identify the orientation of obtuse and acute steps on the calcite surface. Images (B) and (C) exhibit the identical region of interest at two consecutive times. The directions of fast dissolution are indicated with the green arrows. Even in this case they correspond to the acute steps (see Fig. 6.6). Image (A): scale bar 100 nm, color scale 4 nm. Images (B) and (C): scale bars 250 nm, color scale 17 nm.

6.1.4 Higher SA coverage on calcite

Experiments presented in the previous sections indicate that organic molecules can act as a protecting layer on the surface of calcite and substantially slow down the restructuring dynamic. To confirm our finding, we repeated the experiments described in the previous section on samples presenting a higher SA coverage.

Fig. 6.8 shows the surface of calcite imaged in air one day after the deposition of the organic (see even Fig. 6.10A). Usually, when imaged in air immediately after cleaving, the calcite surface presents monoatomic steps with the characteristic triangular shape. The ambient humidity induces surface restructuring⁵⁰⁻⁵² and at intermediate surface coverage in air (Fig. 6.1A), higher calcite domains could be seen around the organic patches at step edges. These domains presented the height of a calcite step (~0.3 nm) and could be seen several hours after the sample being exposed to ambient atmosphere. In the case of the sample presented in Fig. 6.8 (and then in Fig. 6.10) this restructuring process was not observed even after 1 day of exposure to atmospheric humidity. We believe that the presence of a high content of SA organic molecules was able to substantially slow down the reconstruction process, leaving the triangular-shaped steps still visible after a full day exposure to ambient atmosphere. Additionally, the surface appeared homogenous, suggesting a uniform SA coverage. This further supports the idea that when densely packed, the adsorbed organics act as a protective layer precluding reconstruction of the calcite surface.

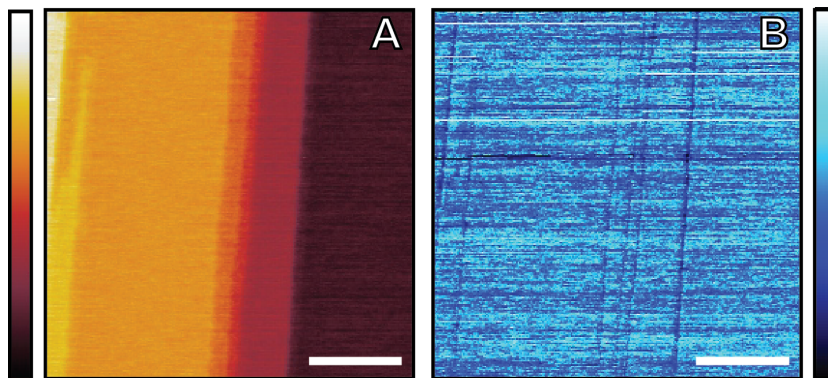


Fig. 6.8: Calcite surface covered by a higher amount of organic molecules imaged in air. From the phase image (B) it is possible to see that the surface is homogeneous and the steps straight and linear like if the standard reconstruction of calcite in air due to the exposure to humid environment is inhibited. The scale bars correspond to 100 nm. The height color scale corresponds to 7 nm while the phase color scale (blue) to a total phase shift of 20°.

Immersion of the sample in Brine3 triggered an immediate restructuring of the organic layer (see Fig. 6.10B and C). Two main regions could be identified, both in the phase and in the topography. This is particularly clear in the phase image (Fig. 6.10C), where the organic layers show a brighter contrast. These big patches are stacked multilayers of SA molecules, as evident from the line profiles presented in Fig. 6.9. Kumar *et al.*⁴⁶ noticed a restructuring process for a SA monolayer deposited on a silicon oxide surface when in contact with an aqueous solution. They reported the formation of multilayers in the presence of Ca²⁺ in the aqueous phase. Our findings concur with the work of Kumar *et al.*⁴⁶ even if the substrate and related binding mechanisms of the SA are different.

After more than an hour in Brine3, the height contrast was completely reversed and the areas protruding from the surface in Fig. 6.10B had become holes in Fig. 6.10D. This can be explained as follows. Initially darker regions in the phase (Fig. 6.10C) corresponded to the free calcite surface, which started to grow as soon as in contact with the supersaturated brine. In the other regions, the presence of the organic molecules slowed down the calcite growth. As a result the areas covered with organic appeared as holes on the surface in Fig. 6.10D, acquired one hour after the injection (see also Fig. 6.11).

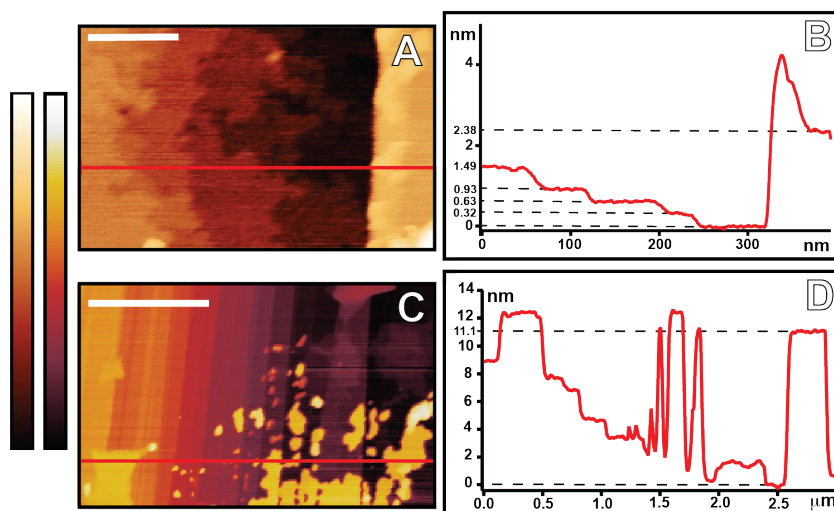


Fig. 6.9: Line profiles and corresponding images showing the height of the Stearic Acid patches before (A and B) the growth process of calcite in Brine3 and after (C and D) the dissolution of the surface in Brine3_{x20}. The scale bars represent 100 nm (A) and 1 nm (C), respectively. The color scale of image (A) corresponds to a height variation of 26.5 nm while the one of image (C) of 42.1 nm.

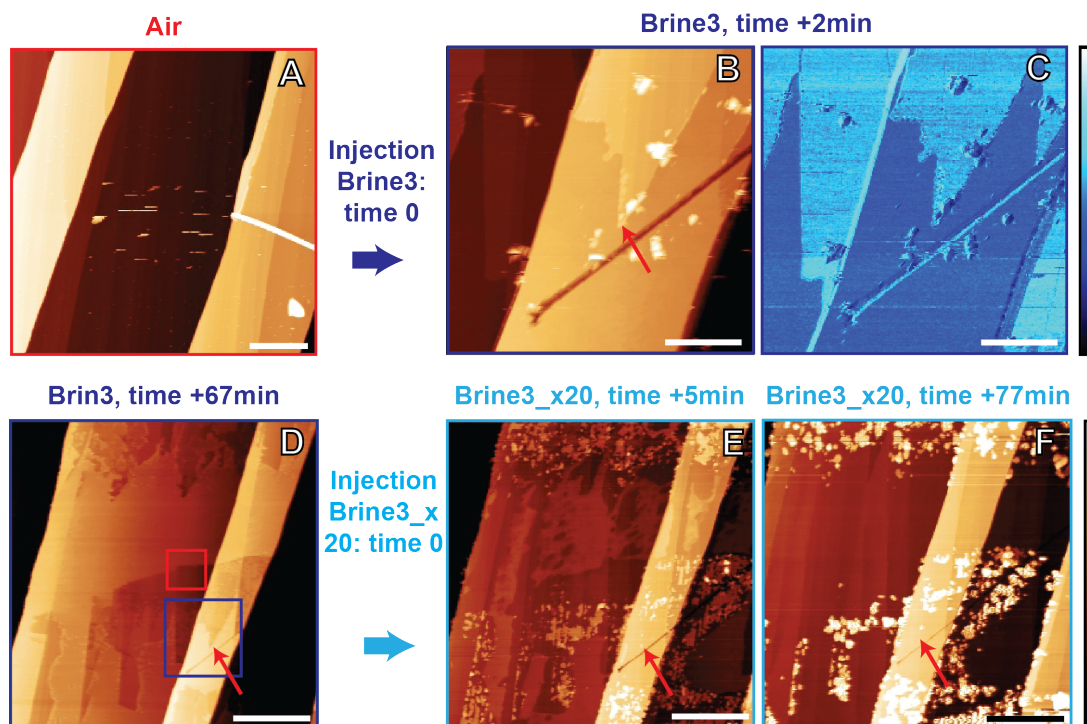


Fig. 6.10: Growth and dissolution of calcite in Brine3 at a higher coverage of SA. The surface is first imaged in air (A) and then after 2min of immersion in Brine3 (B) height and (C) phase images). The phase contrast in (C) reveals the presence of two distinct areas: one covered by an organic layer and the other composed by the standard calcite surface. The same area of the sample is then followed in time and as a function of the dilution of Brine3. The image (D) is acquired after 67 min from the first injection of Brine3. In (D) the blue box represents the area presented in (B) and the red box the area presented in Fig. 6.11. Images (E) and (F) are acquired after 5 min and 77 min respectively from the injection of Brine3_{x20}. The length scale bars represent 1 μm (A), 500 nm (B, C) and 2 μm (D-F), respectively. The color scale bars are 50 nm (A, B, D-F) and 45° (C).

We followed the evolution of an area close to edge between an organic patch and the free calcite surface during the growth process (see Fig. 6.11). While it was possible to see the calcite steps advancing fast in the sample region exposed to the ionic solution, only a few calcite steps were proceeding in the lower area covered with the organic. These steps ‘pushed’ the SA molecules in the central area, far from the edge of the patch, concentrating them in a more confined space and thus enhancing the formation of multilayers of SA (see Fig. 6.9 and 6.11). This phenomenon is

particularly evident by observing the same surface when the unsaturated solution (Brine3_×20) was injected and the dissolution process started to take place. In Fig. 6.10E and F, the newly formed crystal dissolved and exposed the organic patches to the solution (see Fig. 6.10F and G and Fig. 6.9C). In Fig. 6.10F the taller patches correspond to concentrated multilayers of SA on the calcite surface. In this case the growth and dissolution processes have affected the organization of the organic layer by concentrating the SA into confined regions.

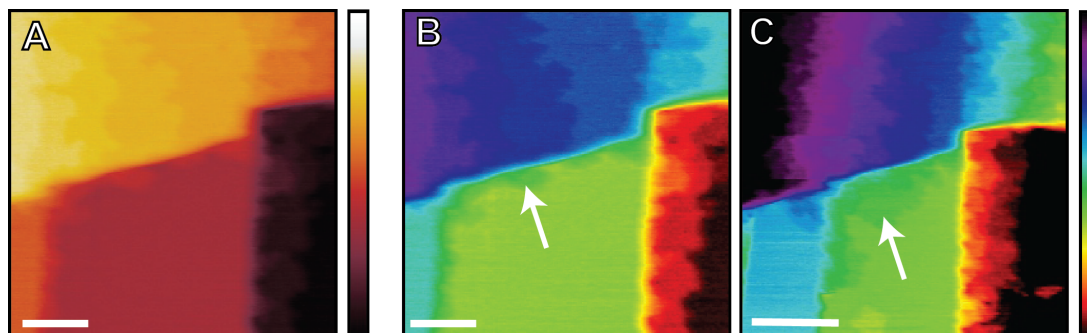


Fig. 6.11: Zoom in the Fig. 6.10E on the border area between the free calcite surface (upper one) and the stearic acid covered region (lower one). (A) and (B) are the actually same AFM image with two different color scale to enhance the contrast between the calcite steps. (C) is taken 5min after (B). It is possible to notice the calcite steps advancing in the upper part of the image and starting to grow from the border of the organic patch (white arrows). Scale bars in (A) and (B) correspond to 200 nm, while in C to 400 nm. All the color scales refer to a height variation of 9 nm.

6.1.5 Conclusions on the dynamic restructuring of the calcite in the presence of SA molecules on the surface

Our results show a rearrangement of the stearic acid layer aimed at minimizing the hydrophobic contact with the solution. The formation of bilayers or multilayers was observed even at low organic coverage. We saw calcite restructuring around the organic patches that were slowly trapped into a well, which was formed by the crystal during the growth process. At higher organic coverage, the growth process concentrated the SA in a confined area where big multilayer patches appeared on the surface. Calcite tended to restructure around the organic patches, incorporating the impurities present in solutions during the growth process. Subsequent dilution in brine with low ionic content removed the freshly grown calcite and exposed the previously incorporated organic layer. The presence of the organic on the calcite surface slowed down both the growth and dilution processes, with organic patches acting as pinning point for receding calcite steps. Organic patches acted as pinning points on the calcite surface, precluding crystal growth and dilution along preferential crystallographic directions, similarly to other organics.^{31,49}

Our time-lapse images provide real-time, molecular-level insight of the calcite restructuring dynamics in a relevant environment. Significantly, we showed that the restructuring of the calcite surface in the presence of low and high salt brine, and not the desorption of the organic molecules from the surface, is one of the main mechanisms affecting the wettability alteration of the SA-modified calcite's surface.¹² These results provide insight on important, yet often overlooked changes that occur during the brine dilution: the surface of the carbonate rocks is not a static object but constantly restructures depending on the environment. These observations could contribute in explaining the high variability observed in imbibition experiments but even provide a molecular-level insight into different bio-mineralization processes where the growth of calcite is happening in the presence of organic material. Our results suggest that, in the case of oil recovery, the history of the reservoir is as important as the ionic strength of the injected brine. Moreover the dissolution of calcite may expose some organic material previously trapped inside the rock.

6.2 Chemical affinity of the carboxyl functional group with the calcite surface in different ionic solutions

In this section we will try to understand how the affinity of the carboxylic functional group with the surface is changing as a function of the ionic environment in which the organic molecules are immersed. I will focus on the effect that the dilution of the Brine1 (see section 5.2) has on the interaction between the carboxylic group and the calcite ($10\bar{1}4$) surface. The carboxylic group is responsible for the anchoring of the fatty acids to calcite (see section 6.1.1). To explore this effect we performed adhesion force measurements between the calcite surface and an AFM tip functionalized with molecules that expose a terminal carboxylic acid. We follow similar work by T. Hassenkam *et al.*^{8,17} who used the same strategy to measure the adhesion between $-\text{COOH}$ and $-\text{CH}_3$ terminated tips on different surfaces of silicates (illite, mica and SiO_2). Hassenkam *et al.*^{8,17} claim to be able to detect a clear signature of low salinity effect with a decrease of adhesion between a carboxylate tip and the SiO_2 surface in the case of low ionic content. Here we attempt to perform the same study on the calcite surface.

The measurement relies on AFM force spectroscopy: the direct measurement of the tip-sample interaction forces as a function of the distance between them (Fig. 6.12 and section 6.3.3 for a description of the experimental procedure). In this specific case we are interested in the adhesion force between our sample (freshly cleaved calcite crystal) and the functionalized AFM tip (see Fig. 6.12A and sections 6.2.1 and 6.3.4). The adhesion force is defined as the minimum force obtained during the retraction curve of the force curve (see Fig. 6.12C). A series of force curves were performed (force mapping) on the calcite surface immersed in the desired brine while scanning the surface (Fig. 6.12B). The adhesion force value can be extracted from each retraction curve (see Fig. 6.12C), and an adhesion map like the one presented in Fig. 6.12D is automatically created. The AFM tip was then withdrawn from the sample and the solution exchanged. The results are summarized in histograms, exemplarily shown in Fig. 6.12E, to facilitate the quantification of the adhesion force and the comparison between different experiments.

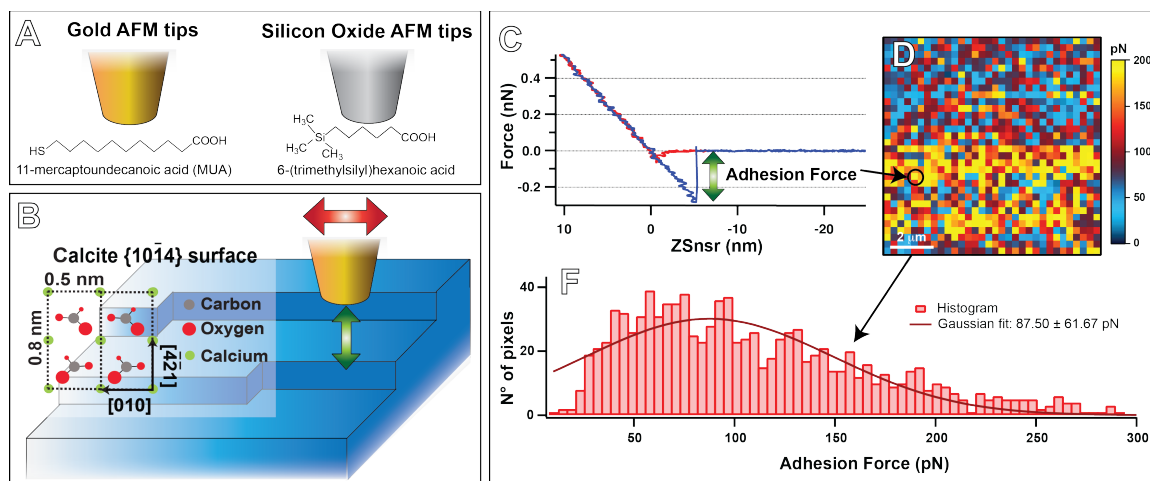


Fig. 6.12: Schematic representation of the functionalization strategies (A), the calcite surface (B) and the force map experiments (C-F). Image (C) is an example of a single force curve, with the red trace representing the extension curve and the blue one the retraction curve. The adhesion force (green arrow in (C)) is extracted from each force curve and an adhesion map is obtained (image (D)) by scanning the sample. Finally, the adhesion map is summarized with a histogram (E) and fitted with a Gaussian distribution to obtain the mean adhesion force and the standard deviation (red continuous line in (E)).

The complexity of this type of experiment, though, does not enable to draw clear conclusions with respect to the possible variation of adhesion between the carboxyl terminated AFM tip and the calcite surface as a function of the ionic strength of the injected brine (section 6.2.3). We will see how the functionalization method can change both density and stability of attached ligand molecules. At the same time the ions of the brine that are in contact with the tip and the calcite

surface can specifically affect both of them. A restructuring of the calcite is taking place, causing a variation of the roughness of the surface and a variation of the ionic composition of the brine as soon as the equilibrium is established. All these contributions create a very dynamical system and increase the variability of the results. To carefully rule out different aspects of the problems, we conducted a series of control experiments (section 6.2.1 and 6.2.2) that will be presented in this section together with a first set of mostly inconclusive preliminary results (section 6.2.3). We explored two different functionalization procedures (section 6.2.1 and 6.3.4) to understand the stability of the grafted molecules on the surface of the AFM tip (“ageing effect”). We suppose in fact that the repetitive contact of the tip with the sample can cause the detachment or degradation of the carboxylated molecules. At the same time the freshly cleaved surface of calcite has a roughness that depends on the cleaving procedure and is highly irreproducible. We also used probes with different radii to see if by changing the contact area more reproducible results could be obtained but it appears that the roughness is dominating effect in the adhesion process. Moreover the inequivalence from a chemical and hydrational point of view between the flat areas and the different steps of the surface is expected to play a role in the interaction between the functional groups and the local properties of the surface. All these effects will be discussed in section 6.2.2. The specific effect of the degree of protonation of the carboxylic acid will be explored in section 6.2.4 as we vary the pH of the ionic solutions.

6.2.1 Tips/surfaces functionalization strategies

Choosing a proper functionalization strategy for the AFM tips is extremely important. Different types of chemistry can be used to link the relevant molecules to AFM tips of various material compositions. The most widely used tips are made of silicon nitride and are known to present a natural thick layer of silicon oxide on them. This is due to the standard oxidation process taking place at the surface when exposed to atmospheric conditions. In this case the silane chemistry is generally preferred to form a SAM of ligand molecules on the surfaces. The driving force for this self-assembly is the in situ formation of polysiloxane, which is connected to surface silanol groups (-SiOH) via Si-O-Si bonds. The other possibility is to use gold-coated tips. In this case, SAMs are formed by using thiol-terminated molecules as described in Chapter 4.

The two functionalization strategies briefly mentioned before were employed, using either (i) thiol-terminated carboxylates for gold tips (*protocol 1*) or (ii) silane-terminated carboxylate (*protocol 2*) for the silicon oxide tips (see schematic illustration of Fig. 6.12A and subsection 6.3.4 of Materials and Methods). This last procedure has first been characterized on flat silicon oxide surfaces with high-resolution AFM to ensure a positive outcome of the functionalization process. The results of the two functionalization protocols in terms of stability and reproducibility are examined in subsection 6.2.2.

Functionalization of silicon oxide surfaces with silane molecules

The functionalization *protocol 2* (6-(trimethylsilyl)hexanoic acid on silicon oxide surfaces) was examined with AFM to see whether the ligand molecules were attaching on the surface in different solvent environments (methanol or toluene). We performed a series of high-resolution AFM images in Milli-Q water on the silicon wafer surface before and after the functionalization to identify the presence of the ligands.

The bare surface of the silicon wafer appears contaminant-free and homogeneous as shown in Fig. 6.13A-C, where we present different magnifications of the same area of the sample. There are some features with a periodicity of 3-4 nm, which may be associated to the amorphous silicon oxide surface. Figs. 6.13D-F present the surface of the silicon wafer after the functionalization with the 6-(trimethylsilyl)hexanoic acid dissolved in toluene, while Fig. 6.13G-I present the functionalization with the same molecules in methanol. The effect of the molecule deposition on the surface is evident. In the case of methanol organic patches appear on the surface, thus providing a brighter contrast in the phase images. In the case of the functionalization in methanol,

there are probably even loosely attached or physisorbed ligands on the surface that interact with the AFM tip and render the imaging process more complicated.

These results indicate the presence of the molecules on the surface of silicon oxide. For a better and more reliable result, we decided to rinse the surface more carefully and use the procedure of MeOH functionalization.

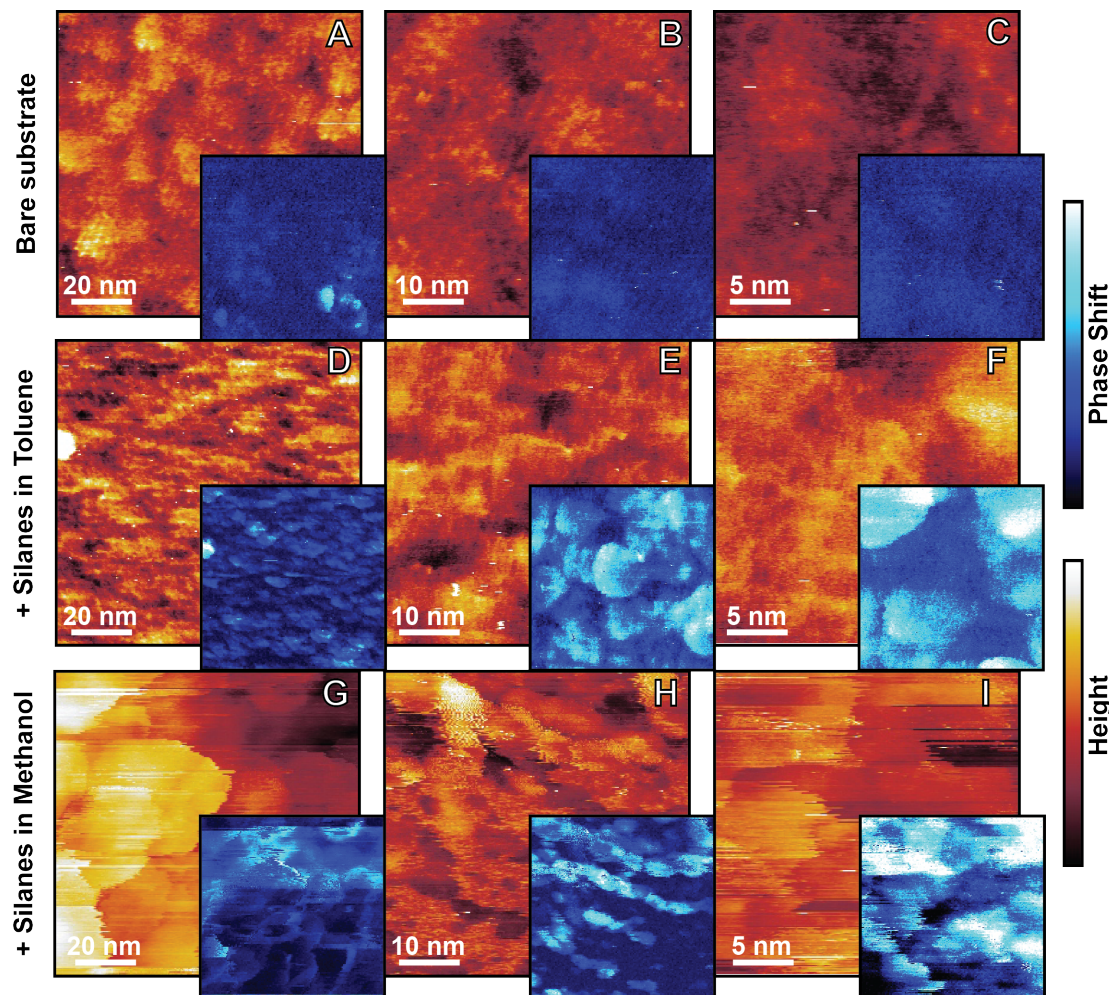


Fig. 6.13: High resolution images in Milli-Q water of a silicon wafer substrate before and after the functionalization process with $-\text{COOH}$ terminated silanes. Images (A), (B) and (C) are different magnifications of the bare substrate before the functionalization. Images (D), (E) and (F) are different magnification of the silicon wafer after the functionalization in toluene. (G), (H), (I) and (J) are different magnification of the silicon wafer after the functionalization in methanol. The height color scale correspond to 1.5 nm for images (A-G), to 20 nm for image (H) and to 5 nm for images (I) and (J). The phase color scale correspond to a phase difference of 20° for images (A- G) and to 40° for images (H-J). The images are not drift corrected.

6.2.2 Control experiments

“Ageing” effect of the functionalized tips

If we suppose that the material of the tip (gold or silicon oxide) is not contributing (or is a constant contribution) to the adhesion force between the tip and the sample, it is reasonable to assume that the functionalization strategy (gold or silane chemistry) can affect the final results through both different densities and stabilities of the $-\text{COOH}$ terminated molecules on the surface of the AFM tip.

Different surface densities of reacting molecules result in different values of adhesion forces on the same sample and in the same brine concentration. This can be considered as a systematic error in the measurement. We aim to eliminate this source of error by always referring to the variation of the adhesion force as a consequence of the ionic content of the brine, thus reporting the

adhesion relative to the initial value. A similar systematic error may arise from variation in the contact area in case of tip apex of different sizes. Even in this case a relative measurement can, in principle, solve the problem.

The stability of the ligand molecules on the surface of the tip is one of the major concerns in the experiment, after possible contamination. If the ligands are loosely attached on the surface of the tip, we may progressively lose part of the interacting molecules by repeating contact between the tip and the surface and, thus, register a lower value of adhesion in time. This phenomenon is what we identify as one of the “aging” effects of the measurement. Another aging effect is related to the tip blunting due to the pressure exerted during the contact part of the force curve. This effect is causing an increase of the contact area with time and, assuming no other physical parameters are changing in the system, should cause a systematic increase of the adhesion force.

Control experiment with Au-Coated tips

In order to test the reproducibility of the thiolated carboxylate-Au tips functionalization, we compared measurements conducted by a same tip directly after functionalization and after multiple measurements on the same region of the sample. In Fig. 6.14 two force maps are compared (Fig. 6.14E standard AFM image obtained in AM-AFM). The tip was functionalized accordingly to *protocol 1* and immersed in Brine1. We obtained the two histograms presented in Fig. 6.14E from the two adhesion maps (Fig. Fig. 6.14A and C). The histograms were then fitted with a Gaussian distribution and the results in terms of mean value and standard deviation are presented in the inset of Fig. 6.14E.

It is possible to notice how with this functionalization strategy the mean adhesion value obtained in the second map is barely 50% of that of the first map. This experiment is a clear example of what we define as aging effect: upon the interaction of the tip with the sample, part of the organic molecules can desorb from the tip surface, leading to a decrease of the mean adhesion force on the exact same area of the sample (compare Fig. 6.14B, D and F) in the exact same conditions. Possible detachment of the gold coating from the tip apex under the excessive stress further complicates the ageing.

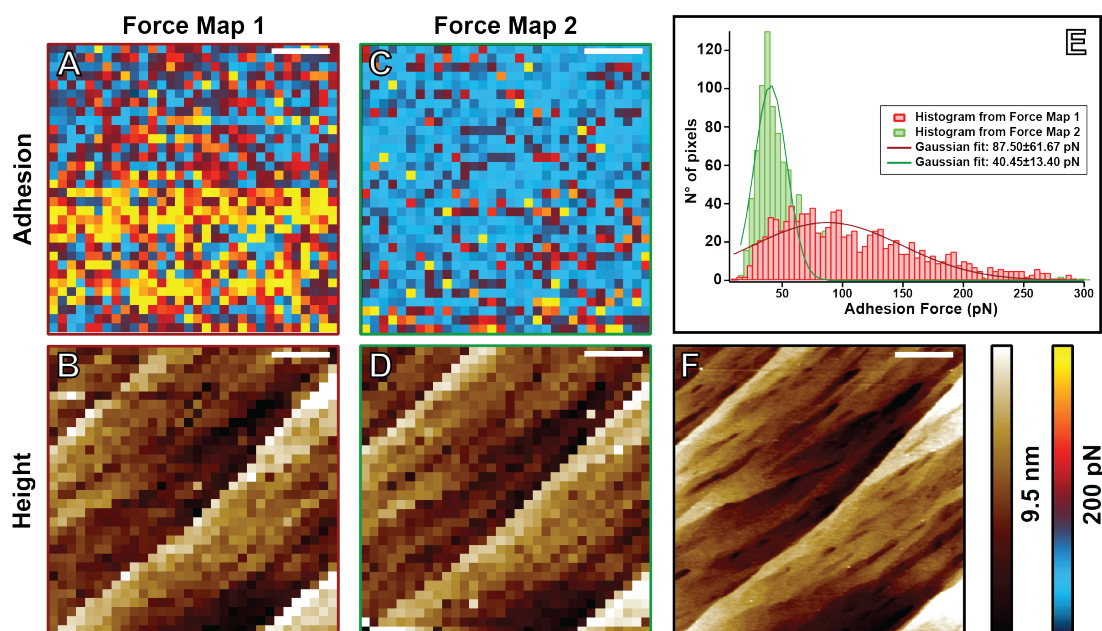


Fig. 6.14: Example of “ageing effect” in the case of functionalization *protocol 1*. The first adhesion map (A) was obtained immediately after the immersion of the TR400PB functionalized tip in Brine1. After the force map 1 a standard AM-AFM image was obtained (F). Finally, the Adhesion Map 2 (C) was acquired. (B) and (D) are the height images reconstructed respectively from the force maps (A) and (C). In (E) the histograms of the two adhesion maps are presented with the relative Gaussian distribution fit. The results of the fits are indicated in the inset of (E) in terms of mean value \pm standard deviation. The AFM images are flattened but not drift corrected. The scale bars correspond to 1 μm .

As an alternative second functionalization strategy we considered the silane chemistry (*protocol 2*). This approach helps estimating the contribution of the tip itself on the total adhesion force. We further performed a series of control experiments using similar but non-functionalized tips.

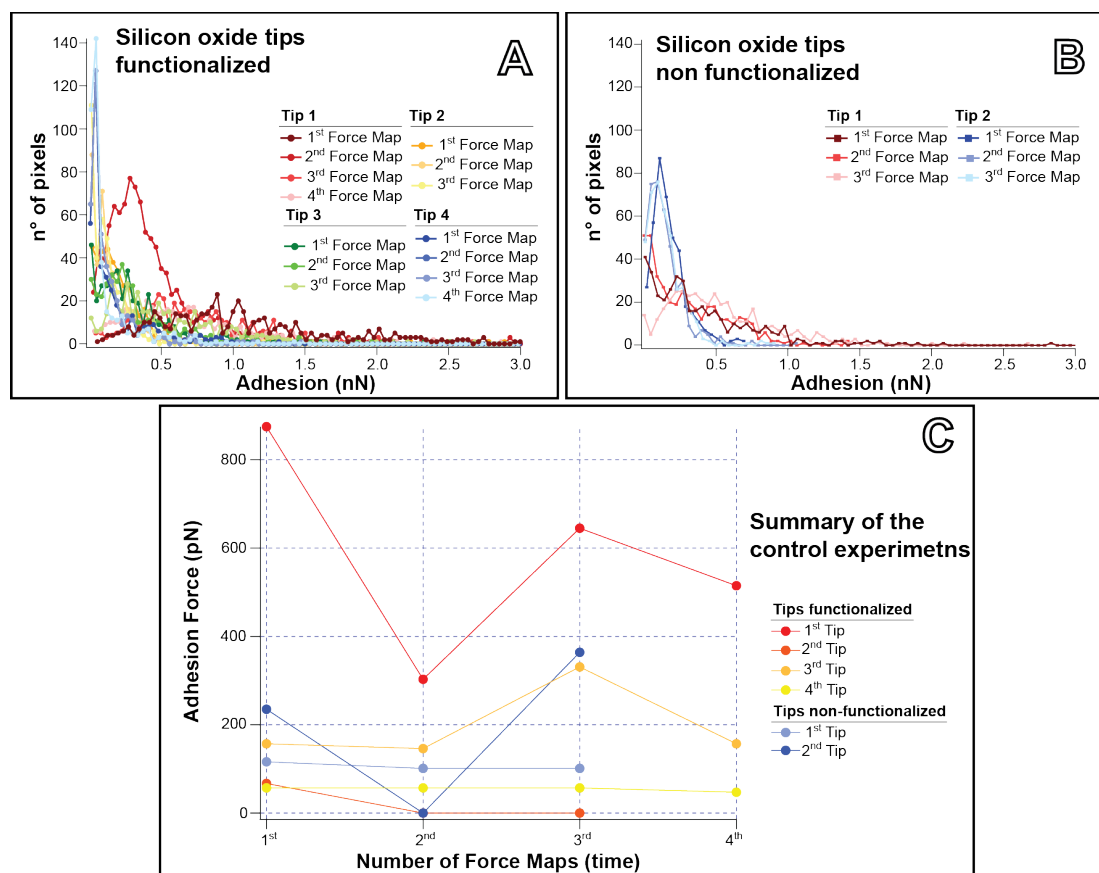


Fig. 6.15: Example of “ageing effect” in the case of functionalization *protocol 2* on calcite in milli-Q water. A series of RC800PSA AFM tips were functionalized (A) or not (B) using the *protocol 2*. With the same tip we performed consecutive adhesion maps on the same sample and in the same area. Then we changed the tip and repeated the same procedure. After the exchange of the tip we were sometimes not able to relocate the same area of the sample. From the force maps (not presented here) we extract the histograms presented in (A) and (B) respectively for functionalized and non-functionalized tips. The data are summarized in (C) where the mean adhesion value for each force maps and each tips is presented as a function of the number of consecutive force maps performed.

Control experiments with Silicon nitride tips

A similar experiment as that just described for the gold-coated tips was conducted to estimate the ligand stability in the second functionalization protocol and test the reproducibility of the adhesion maps. We performed on a freshly cleaved calcite surface in milli-Q water consecutive force maps on the identical sample area. We used different functionalized and unmodified silicon nitride tips with *protocol 2*. From each of the force maps we obtained a histogram similar to those presented in Fig. 6.15A and B from which we could extract the mean adhesion force values summarized in Fig. 6.15C. First of all, a significant variability between different tips is evident. This effect may be related to several causes:

1. differences in the ligand density on the AFM tip
2. differences in the radius of curvature of the tip
3. attachment of contaminants on the AFM tip
4. sample roughness variation between different areas of the sample (see discussion next section)
5. presence of nanoasperities on the AFM tip

The trend in terms of aging with a progressive reduction of the mean adhesion force by increasing the number of force maps can only be clearly extracted for tip 2, shown in in Fig. 6.15C. Assuming a successful functionalization process, this suggests that the molecules on tip are

relatively stable and do not detach in time. Another noticeable effect is the big variations of the adhesion force values between different force maps with sudden increase of the adhesion. This can be explained by either the absorption of contaminants on the surface of the AFM tip or by a sudden removal of a nanoasperity from the AFM tip with the consequent uncontrolled variation of contact area between tip and sample. Unfortunately, these effects cannot be easily controlled.

Generally, there is not a significant difference between the adhesion of the functionalized and non-functionalized tips. If the ligand molecules interact specifically with the calcite surface, a significantly higher adhesion value is expected compared with the bare non-functionalized surface. As it is not the case, either the functionalization process has not succeeded or the molecules are not contributing significantly to the adhesion between tip and sample. Generally, we obtained a similar trend with the other functionalization protocol.

Surface roughness

An important effect that we noticed throughout this experimental series was a general non-homogeneity of the adhesion force on the surface of the sample. In particular, in proximity of defects like step edges or possible etch pits, a variation of the adhesion force was detected. In Fig. 6.16 the same calcite sample is first immersed in Brine1 (Fig. 6.16A and B) and then in acidic Brine1 (Fig. 6.16C and D). Two adhesion maps (Fig. 6.16A and C) were obtained and we consistently noticed an increase of the adhesion force at step edges on the surface (Fig. 6.16B and D).

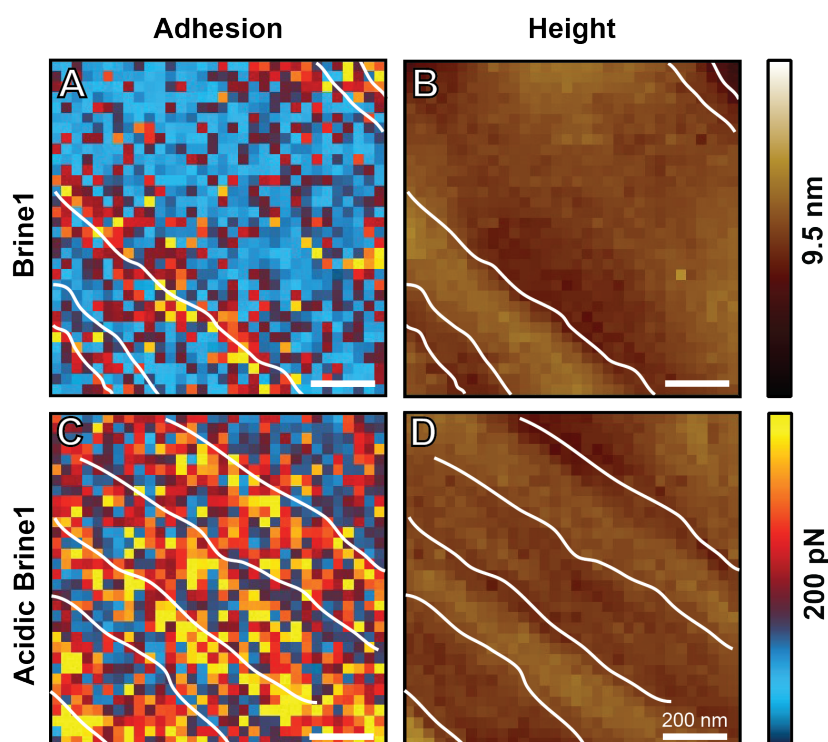


Fig. 6.16: Example of morphological effect of the adhesion force on the calcite surface in proximity of step edges. Two force maps were acquired in the same area of the sample with a TR400PSA tip functionalized with the *protocol 2*. The adhesion (A) and height (B) images were obtained first in the standard brine and then in the acid brine (adhesion in (C) and height in (D)). White lines serve as guide to the eyes and to recognize different areas that appear clear in topographic images (C) and (D) on the related adhesion maps (A) and (C).

We identified two main causes as possible explanation of this effect.

The first is related to the actual physical/chemical interaction of the carboxylic group with the calcite surface. The nature of this interaction has been debated for a long time. Generally it is accepted that the $-\text{COOH}$ group react with the OH groups absorbed in proximity of the calcium atoms on the calcite surface, forming in this way a new complex $>\text{CaOOC-R}$.⁴⁷ Inhomogeneity of the sample can influence the adhesion of the $-\text{COOH}$ terminated tip with the surface: Usher *et al.*⁵³

showed a preferential interaction of formic acid at step edges and de Leeuw *et al.*⁴⁹ reported a preferential attachment of the carboxylic group to step edges. We can thus expect to have variation in adhesion between different areas of the samples and in particular an enhancement of the adhesion at step edges.

The second cause, less exciting, is related to the presence of asperities on the tip and/or on the surface (considered as roughness effect). The presence of these asperities modifies the contact area between tip and sample even locally. The fact that the roughness is playing a major role in these kinds of experiments on calcite can be easily inferred by the results obtained with the colloidal probes (see Fig. 6.17A for gold colloidal probe and Fig. 6.18C for silica colloidal probe): from the different theories of contact region, a linear dependence between adhesion force and radius of contact is expected.⁵⁴ The nominal radius of the gold colloidal probe is 1.5 μm and for silica 2 μm . Considering that the tip radius of standard AFM tips is of the order of 20-40 nm, an adhesion force 2 orders of magnitude higher is expected with the colloidal probes. However, we observed an adhesion force of the same order of magnitude with gold colloidal probes respect to the standard gold tip (Fig. 6.17A) while in the case of the silica tips we measure an enhancement of 1 order of magnitude (Fig. 6.18C). We attribute this discrepancy to the roughness effects.

Brine dilution experiments also suffer from the influence of roughness on the measured adhesion force: by diluting the brine, the surface of the calcite is modified locally and the surface roughness increases. We cannot completely rule out that observed variations of the adhesion as a function of the brine dilution are actually induced by a roughness effects.

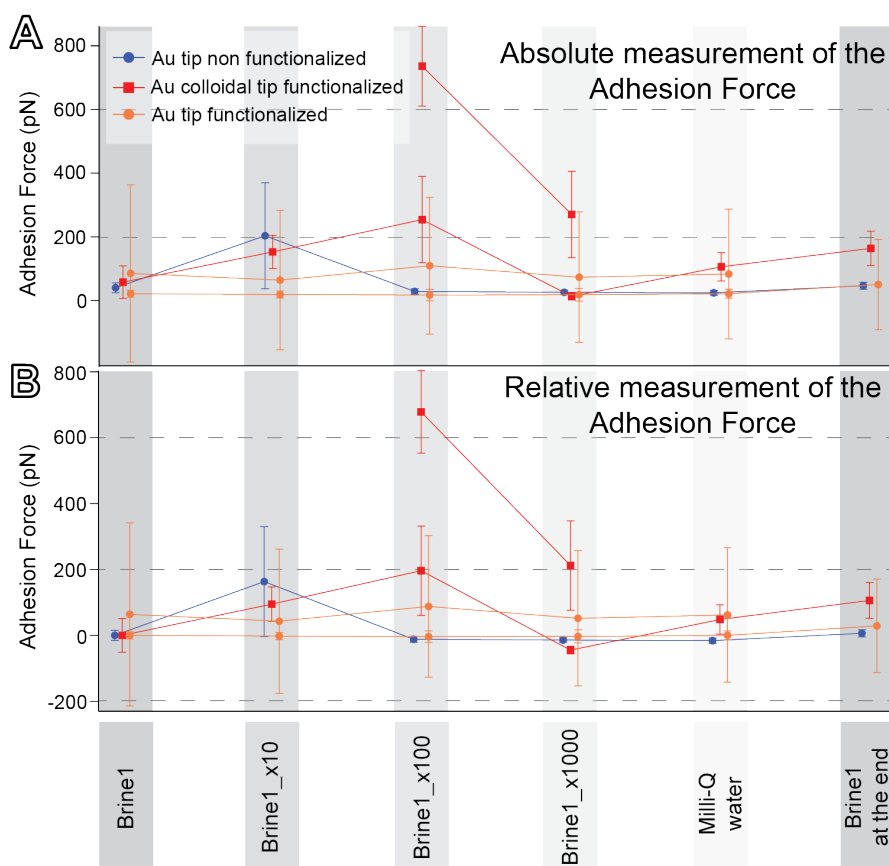


Fig. 6.17: Summary of the “progressive” dilutions experiments performed with gold tips that were either functionalized and not with -COOH terminated ligands. In (A) we present the absolute values of the mean adhesion force obtained from the Gaussian fitting of the histograms. Different colors represent different tips as possible to see in the legend presented as an inset in (A). In the y-axis the absolute value of the adhesion force is presented, while in the x-axis the data are divided accordingly to the dilution of Brine1 in which the experiments were performed. In (B) the same data are presented as values relative to the adhesion measured in the first force map, corresponding to undiluted Brine1. If two points per tip and brine dilution are present, it implies that the histogram was fitted with the superposition of two Gaussian distributions.

6.2.3 Dilution experiments in Brine1

In this section, we present the results obtained with functionalized and unmodified gold and silicon oxide tips and colloidal probes as a function of the Brine1 dilutions.

In Fig. 6.17 the summary of an experimental series of progressive dilution in Brine1 is presented. In these experiments the brine was progressively diluted down to equilibrated water. We present the adhesion values of three different gold tips on the same sample: a standard TR400PB functionalized (orange), a TR400PB unmodified (blue) and a colloidal probe functionalized (red). In Fig. 6.17A the absolute values of the mean adhesion force are plotted as a function of the brine concentration. The error bars do not represent the error of the measurement but the variation in adhesion values measured on the sample. In Fig. 6.17B we plot the adhesion values relative to the first force map performed in Brine1 to better follow the eventual trend of adhesion force as a function of the brine dilutions. Occasionally, we could clearly recognize two distinct peaks in the histograms. In this case we fitted the distribution with a convolution of two Gaussian peaks, resulting in two points in the dataset (see for example the orange data set in Fig. 6.17).

From the data presented in Fig. 6.17, it is not possible to identify a clear trend. The only remarkable difference between the control and the functionalized tips is the occasional appearance of the second peak at higher adhesion values, which seems to be exclusively associated with the functionalized tips.

Generally was very tricky to restore the same adhesion values in undiluted Brine1 at the end of the experimental series, which would typically considered as an indication for a reliable set of measurement. After the previous discussion we may not be surprised by this fact.

To limit what we previously individuated as aging effect, we performed a new series of experiments in which we alternated the Brine1 with Brine1_{×10} without adding more dilutions in between. The results, plotted with the same strategy adopted in the previous graph are presented in Fig. 6.18. While we could occasionally restore the initial adhesion values on the same sample, we were again not able to identify a simple trend related to the brine concentration.

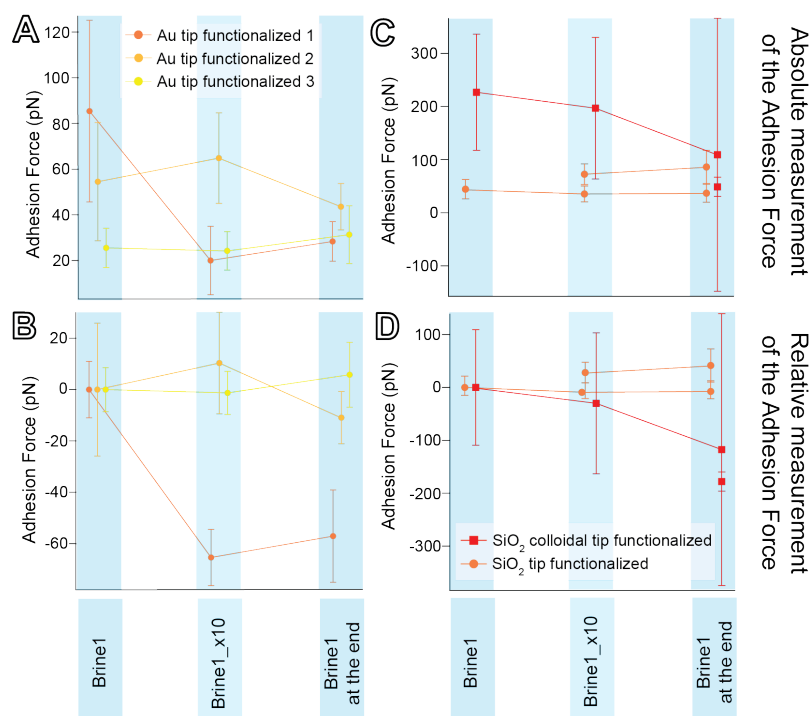


Fig. 6.18: Summary of the “short” dilutions experiments performed with gold (A, B) and silicon oxide (C, D) tips functionalized with $-\text{COOH}$ terminated ligands. In (A) and (C) we present the absolute values of the mean adhesion force. Different colors represent different tips (legend in the inset in A and D). In (A) and (C) the y-axis correspond to the absolute value of the adhesion force, while in the x-axis the data are divided accordingly to the dilution of the Brine1. In (B) and (D) the same data as (A) and (C) are presented as values relative to the adhesion measured in the first map (Brine1).

6.2.4 Dilution experiments in Brine1 and acidic Brine1

The last set of experiments were aimed at individuating the effect of the pH of the solution on the adhesion between the ligand molecules and the calcite surface. By lowering the pH of the brine we can expect an higher amount of protonated carboxylate and so explore the effect of the actual carboxylic acid on the surface.

In the range of pH explored with Brine1 and the dilutions (see Table 5.2), the carboxylic acid terminal group, exposed on the AFM tip, is partially dissociated. The pK_a of the carboxylic acid is 5.6 for a Langmuir Blodgett monolayer at the air-water interface, 4.8 in the bulk⁵⁵ and, of particular relevance, 4.9 for a siloxane-anchored carboxylate monolayer on silicon oxide⁵⁶. As soon as the tip is immersed in the brine, part of the ions in solution will condensate on the surface and some of them will associate with the $-COO^-$ groups, competing with the naturally associated protons. Calvez *et al.*⁵⁷ showed that the balance between the acid and salt species in Langmuir Blodgett monolayer at the air-water interface is obtained for a pH subphase that is different from the carboxylic acid pK_a and that strongly varies with the counterions type. They obtained a half-neutralization at subphase pH values of 6.2, 6.8, and 9 for the Ca^{2+} (3.1mM), Mg^{2+} (3mM), and Na^+ (10mM) counterions, respectively. In our case we have a higher concentration of these ions (the concentration of Ca^{2+} is in the mM range simply by equilibrating the calcite crystal in Milli-Q water), thus we can expect to have more than half of the acidic groups ionized or forming a ionic complexes in the experimental pH.⁵⁸ To explore the actual interaction of the carboxylic acid group with the calcite surface, we decided to decrease the pH of Brine1 to 3-4 by adding HCl, a value below the pK_a of the acid (what we refer as “acidic Brine1”). In this case we can assume that, transiently, a higher percentage of the carboxylic acid on the AFM tip is protonated. The final pH after the equilibrium with the calcite is expected to be between 7 and 8 for the acidic Brine1 and acidic Brine1_x10 (we focused on these two concentrations). However it is still possible to assume that at the beginning of the measurement the effect of the lower pH is active. Such a pH variation suggests even a strong restructuring of the surface.

The results of the typical experiment are presented in Fig. 6.19, where the histograms obtained from the force maps are plotted. We proceeded in the following order: we first performed a force map in Brine1 (functionalization *protocol 2*), then we replaced the solution with the acidic Brine1. As third step we injected the Brine1_x10 to conclude with the two control restoring force maps in acidic brine Brine1 and Brine1.

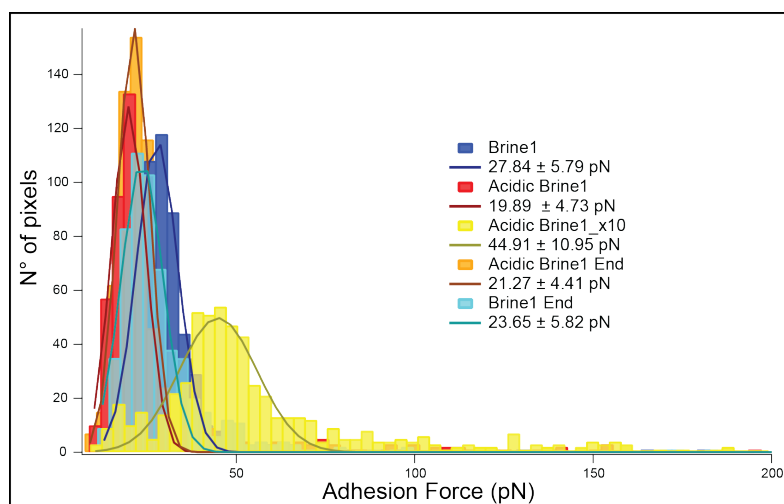


Fig. 6.19: Example of histograms obtained from adhesion maps between silicon oxide tips functionalized and the calcite surface. The adhesion maps were performed in the following order in Brine1, acidic Brine1, acidic Brine1_x10, acidic Brine1 and Brine1. On the histograms the Gaussian fitting are superimposed.

The results seem to consistently indicate a higher adhesion force in the case of the acidic brine diluted 10 times. This trend was noticed even for another functionalized tip (see Fig. 6.10) and seems to be absent in the case of the unfunctionalized tips (blue curves in Fig. 6.10). *Unluckily, I*

had to stop to do experiments and start to write this thesis otherwise I would have never been able to eventually graduate. Under ideal circumstances we should have been able to reproduce the results with a gold-functionalized tip to rule out the possible tip surface effects and further do a real-time dilution to determine the morphological variation of the calcite surface in acidic environment. Nevertheless we believe that this result is due to an actual interaction between the ligands and the surface that can be both related to a higher affinity between the functional group and the calcite surface at this concentration or simply by an increase of reacting point (e.g. steps) on the surface due to the lower ionic concentration and the low acidity.

In general with this spectroscopic technique and in the sampling space (temperature, ionic composition, ionic concentration and pH) explored in our experiments we could not detect any low-salinity effect and actually the opposite effect seems to appear in acidic environment.

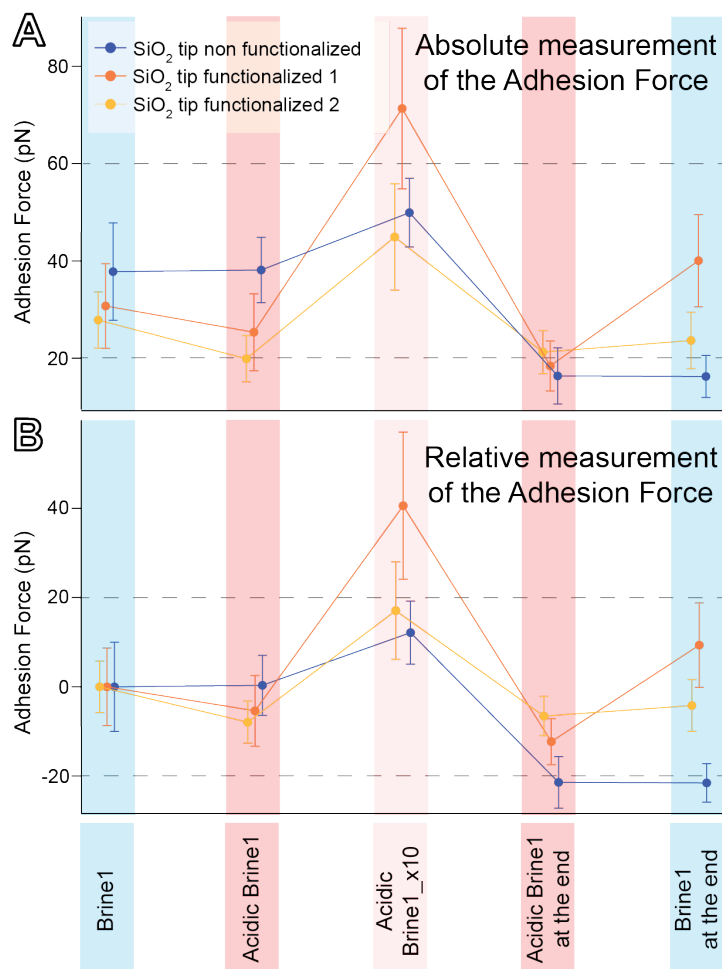


Fig. 6.20: Summary of the dilutions experiments performed with silicon oxide tips in Brine1 and acidic Brine1 depending on the tip functionalization with $-\text{COOH}$ terminated ligands. In (A) we present the absolute values of the mean adhesion force obtained from the Gaussian fitting of the histograms deriving. Different colors represent different tips as possible to see in the legend presented as an inset in (A). In the y-axis, the absolute value of the adhesion force is presented, while in the x-axis the data is divided accordingly to the dilution in which the experiments were performed. In (B) the same data are presented as values relative to the adhesion measured in the first force map corresponding to the Brine1.

6.2.5 Conclusions on the carboxyl group-calcite surface affinity

In this section, the methodology to obtain information on the affinity between a specific chemical group and a surface by functionalizing the AFM tip is described. The interpretation of the results may be challenging and special care has to be taken by doing several control experiments. In the case of calcite and carboxylic acid functionalized the functionalization process is extremely

important and in general the comparison between different functionalization strategies are recommended. Upon repetitive contact between tip and sample, the grafted molecules can desorb and the tip can change shape or even material in the case of gold-coated tips. If comparative measurements are performed by changing parameters, as in our case the ionic strength and pH, this effect has to be taken into account because it may induce a systematic error into the measurement. The effect of the roughness has to be considered especially if it is an evolving parameter, as in this case.

Our results do not show a significant variation of the adhesion force between the carboxylated tips and the calcite surface by reducing the ionic strength of Brine1. The variability of the measurements does not allow to draw significant conclusions. On the other hand, an effect at lower pH and low ionic strength is detected. In particular, it appears that the adhesion force is increasing when the carboxylated molecules are immersed into an acid brine at lower ionic concentration. Though more experiments are necessary to confirm this result, it is indicating that the protonation state of the carboxylic acid is extremely important in the interaction mechanism with the surface.

6.3 Materials and Methods

6.3.1 Samples preparation for the experiments of organic patches on calcite surface.

Optically clear, transparent iceland spar crystals were used for this study. The samples were cleaved with a razor blade to expose the $(10\bar{1}4)$ surface. Immediately after cleaving, the samples were exposed to the vapor of Stearic Acid (Sigma Aldrich, St Louis, MO 63103, USA). The SA was deposited with various degree of surface coverage by hot vapor treatment prior to immersion into the brine. 2 mg of SA in a glass vial of 2 ml were heated to 120°C for at least 15 minutes. The vial was capped with a Teflon tape that was previously punctured and subsequently brought to the desired temperature. The calcite crystal was positioned above the hole to expose the freshly cleaved surface to the SA hot vapor. We were able to obtain different coverage of SA on calcite by tuning the exposure time of the crystal to the vapor. The coverage could be controlled through temperature, the dimension of the hole in the Teflon tape, the depth of the glass vials and the exposure time. Calibration of the coverage could be achieved by setting temperature and hole size, and imaging a samples series in air for various exposure times.

The calcite samples were attached on a metallic disk (SPI Supplies, West Chester, PA 19380, USA) and mounted on the AFM stage. We found that the best strategy to attach the calcite to the metal disks was with 5min epoxy glue (Araldite, Denver, USA). After complete curing of the glue, the samples were cleaved to expose a fresh surface. This strategy avoided contamination of the surface and provided a good stability during the imaging process.

6.3.2 AFM and QNM measurements on the calcite restructuring

All the experiments were performed at room temperature. The QNM measurements were performed on a Veeco Multimode 5 system equipped with a $10\times 10\times 2.5$ μm scanner. The cantilever (Scanasyst-fluid, Bruker, Santa Barbara, CA, USA) deflection sensitivity was calibrated before the experiment and the spring constant was obtained by using the cantilever thermal spectrum in air.⁵⁹ Samples were first imaged in air and subsequently in Brine3.

The experiments presented in Figs. 6.3-6.5 and Fig. 6.7 were carried out with a commercial Multimode Nanoscope IIIA (Digital Instruments, now Bruker, Santa Barbara, CA, USA) equipped with an external lock-in amplifier. For these experiments we used standard gold coated silicon nitride cantilevers (RC800-PSA, Olympus, Japan) with a nominal stiffness $k_c = 0.76$ N/m. The cantilevers were mounted in a fluid cell. Initially a series of images were taken in amplitude-modulation mode ('tapping' in the AFM commercial software) in air to estimate the coverage of

organic molecules. The desired brine was subsequently injected into the fluid cell and the sample was imaged in liquid with the same tip. Using a homemade syringe system it was possible to exchange the liquid on the sample and progressively dilute the concentration of the brine. The evolution of the sample was followed in real time and over the same area of the sample. During the liquid exchange process, the tip was lifted a few microns above the surface (z-piezo retraction) but not disengaged. Using the same machine was possible to obtain routinely high resolution on the calcite surface using the same procedure and imaging conditions as described in our previous work.^{1,2,4,60}

The experiments presented in Fig. 6.6 and Figs. 6.8-6.11 were performed on a Cypher ES (Asylum Research, Oxford Instrument, Santa Barbara, USA), equipped with photothermal excitation (BlueDrive). For these experiments, we used the same type of cantilevers as on the Multimode Nanoscope IIIA (RC800-PSA with a nominal stiffness $k_c = 0.76$ N/m). Similarly to previous experiments, the samples were first imaged in AM-AFM in air and then in different brine concentrations. The perfect sealing of the environmental scanner eliminates any evaporation issue, apart from a short initial transient time when the vapor in the chamber equilibrate with the liquid. This ensures consistent brine concentrations throughout the experiment.

For AM-AFM in liquid, different working conditions than for high-resolution AFM have been employed to enable a better tracking of the very rough surface: a bigger free amplitude (>2 nm) was used and the ratio A/A_0 was lower (normally <0.8). In these conditions it is complicated to determine the actual mechanism of energy dissipation and thus interpret correctly the phase contrast. Assuming, that in this case the energy dissipation is mainly dominated by the contact mechanic between the tip and the sample, the phase contrast reflects a variation of stiffness and viscosity of the material.⁶¹⁻⁶⁴ Image analysis was carried out using Gwiddion (<http://gwyddion.net>) and SPIP (Image Metrology, Denmark).

6.3.3 General procedure for force spectroscopy measurements.

In a force spectroscopy measurement, the AFM tip is extended towards the sample and subsequently retracted from the surface, while monitoring the static deflection of the cantilever as a function of the z piezoelectric displacement. By knowing the spring constant of the cantilever and supposing that it is responding with a linear deformation to the force applied (Hook's law), it is possible to directly obtain the value of the force acting between tip and sample. Forces on the order of a few piconewtons can be routinely measured with a vertical distance resolution smaller than 0.1 nm. It can also provide information about mechanical proprieties of the sample. The adhesion force is defined as the minimum force obtained during the retraction curve (see Fig. 6.12C). The source of the adhesion force can be any attractive force between the tip and sample. In air, van der Waals, electrostatics, specific chemical bonds formation and forces due to the formation of a capillary meniscus may all contribute to the total adhesion. The relative strengths of the contributions depend on parameters such as the Hamaker constant, surface charges, and hydrophilicity. If either sample or the probe surface is hydrophilic, a capillary meniscus will typically form, leading to a higher adhesion that extends nanometers beyond the surface. In liquid the capillary meniscus is not present, so it is possible to probe directly adhesive properties of the two surfaces in contact that are more chemically specific. The theory describing the adhesion force as a function of the surface-tip properties is described by the contact mechanic theories (see Chapter 2 and Ref.⁵⁴)

The experiments were conducted using the following general procedure:

1. The AFM tips were functionalized with the relevant molecules (see Fig. 6.12A and section 6.3.4).
2. After the functionalization, the tips were mounted on the tip holder of a commercial AFM (MFP-3D or Cypher-ES, Asylum Research, Santa Barbara, CA, USA).
3. A freshly cleaved calcite crystal was attached on a standard glass slide using carbon tape and immediately a drop of the brine was placed on the crystal. To limit the spreading of the liquid drop on the glass slide a PDMS ring was used. The glass slide was fixed on the MFP-3D scanner using two magnets. Alternatively the freshly cleaved calcite crystal was

attached with carbon tape on a magnetic disk and mounted on the environmental scanner of the Cypher-ES.

4. The tip was immersed in the solution and left to stabilized for 20-30 minutes. The cantilever was then calibrated obtaining first the “Inverse Optical Lever Sensitivity” (InvOLS) from the contact curve region and then the force constant with the thermal spectra methods.
5. The actual measurement was conducted by performing a series of force curves (force map) in defined region of the sample. This procedure is normally called “Force Map” and consists in performing a series of force curves to map the mechanical properties of the desired area of the sample. The z-piezo is extended in a specific point till the tip first touch the surface and successively reaches a maximum a maximum repulsive force that can be set by the operator (typically in our experiment between 600pN and 1nN). Then the piezo is retracted and the retraction curve measured. The final value of the deflection is normally similar to the initial one, suggesting that after the extension-retraction cycle the tip is again not touching the surface. The user can set the mean velocity of the tip in this cycle by choosing the rate (1Hz) of force curves acquisition and the extension range (normally 100 nm). After the first force curve, the x-y piezos move the sample in a different location and another force curve is performed. This procedure is automatized and the user can choose the total scanned area (typically 5- 20 microns in our experiments) as well as the number of force curves per line (32) and the number of rows (32).
6. The AFM tip was withdrawn from the sample and the solution exchanged. Point 5 was repeated for the new concentration of the brine. We tried to perform the force maps in different brine concentrations on the same area of the sample to limit adhesion variations related to morphological effects.
7. During the collection of the force maps in different brine concentrations, the adhesion forces value was extracted from each retraction curve (see Fig. 6.12C), using an analysis routine of the AFM software (IgorPro, WaveMetrics) and an adhesion map like the one presented in Fig. 6.12D was automatically created. The resulting values relative to a brine concentration could be displayed in a histogram like that presented in Fig. 6.12E to facilitate the quantification of the adhesion force and the comparison between different experiments.

6.3.4 Protocols for tip functionalization

Before proceeding to the tips/substrates functionalization, the following cleaning steps were conducted (in order): 5 minutes in Milli-Q water, 5 minutes in ethanol, 5 minutes in Milli-Q water, drying under a nitrogen flow, exposure to UV-ozone for 10 minutes, 30 minutes in ethanol, rinsing with Milli-Q water and subsequent immersion for 5 minutes, drying under a nitrogen flow, exposure to UV-ozone for 30 minutes immediately before the functionalization.

After the cleaning procedure we used two different functionalization protocols depending on the material of the tips/substrates:

Protocol 1. The gold AFM tips were immersed in a solution of 1mM 11-mercaptoundecanoic acid ($\text{SH}(\text{CH}_2)_{10}\text{COOH}$, MUA) in ethanol for at least 24h. Immediately before the AFM force maps experiments, the tips were extracted from the solution and rinsed with ethanol and dry under nitrogen flow. We followed the same strategy used by Hassenkam *et al.* for this functionalization method.¹⁷ We used three types of tips: TR400PB (Olympus, Japan) with nominal spring constant of 0.09 and 0.02 N/m respectively for the small and the big cantilevers on the same chip; RC800PB (Olympus, Japan) with nominal spring constant of 0.82 and 0.11 N/m; colloidal tips CP-CONT-Au-A (NanoAndMore GmbH, Germany) with nominal spring constant of 0.2 N/m and sphere diameter of 1.5 μm .

Protocol 2. The silicon oxide or silicon nitride (with a natural layer of silicon oxide on the surface) AFM tips and substrates were immersed in a solution of 5mM 6-(trimethylsilyl)hexanoic

acid ((CH₃)₃Si(CH₂)₄COOH, Tractus Company Limited, Hong Kong) in isopropanol or toluene for at least 24 h. The silicon oxide substrates were cut with a diamond tip from a silicon wafer (Okmetic, Vantaa, Finland). Even in this case we used three types of AFM tips: TR400PSA (Olympus, Japan) with nominal spring constant of 0.08 and 0.02 N/m; RC800PSA (Olympus, Japan) with nominal spring constant of 0.76 and 0.10 N/m; colloidal silicon oxide AFM tips CP-PNPL-SiO-A (NanoAndMore GmbH, Germany) with nominal spring constant of 0.32 and 0.08 N/m and sphere diameter of 2 μm.

Bibliography Chapter 6

1. Voitchovsky, K., Kuna, J. J., Contera, S. A., Tosatti, E. & Stellacci, F. Direct mapping of the solid-liquid adhesion energy with subnanometre resolution. *Nature Nanotechnology* **5**, 401–405 (2010).
2. Ricci, M., Spijker, P. & Voitchovsky, K. Water-induced correlation between single ions imaged at the solid-liquid interface. *Nat Commun* **5 SP**, (2014).
3. Heberling, F., Eng, P., Denecke, M. A., Lützenkirchen, J. & Geckeis, H. Electrolyte layering at the calcite(104)-water interface indicated by Rb⁺- and Se(vi) K-edge resonant interface diffraction. *Physical Chemistry Chemical Physics* **16**, 12782–12792 (2014).
4. Ricci, M., Spijker, P., Stellacci, F., Molinari, J.-F. & Voitchovsky, K. Direct Visualization of Single Ions in the Stern Layer of Calcite. *Langmuir* **29**, 2207–2216 (2013).
5. de Leeuw, N. H., Parker, S. C. & Harding, J. H. Molecular dynamics simulation of crystal dissolution from calcite steps. *Phys. Rev. B* **60**, 13792–13799 (1999).
6. de Leeuw, N. H. Molecular Dynamics Simulations of the Growth Inhibiting Effect of Fe²⁺, Mg²⁺, Cd²⁺, and Sr²⁺ on Calcite Crystal Growth. *The Journal of Physical Chemistry B* **106**, 5241–5249 (2002).
7. Thomas, M. M., Clouse, J. A. & Longo, J. M. Adsorption of organic compounds on carbonate minerals: 1. Model compounds and their influence on mineral wettability. *Chemical Geology* **109**, 201–213 (1993).
8. Hassenkam, T., Pedersen, C. S., Dalby, K., TT, A. & Stipp, S. L. S. Pore scale observation of low salinity effects on outcrop and oil reservoir sandstone. *Colloids Surf., A* **390**, 179–188 (2011).
9. Yousef, A. A., Salah, A. S., Abdulaziz, A. K. & Mohammed, A. J. Laboratory Investigation of the Impact of Injection-Water Salinity and Ionic Content on Oil Recovery From Carbonate Reservoirs. *SPE Reservoir Evaluation & Engineering* 1–16 (2011).
10. Karoussi, O. & Hamouda, A. A. Imbibition of Sulfate and Magnesium Ions into Carbonate Rocks at Elevated Temperatures and Their Influence on Wettability Alteration and Oil Recovery. *Energy Fuels* **21**, 2138–2146 (2007).
11. Bernard, G. G. Effect of Floodwater Salinity on Recovery Of Oil from Cores Containing Clays. in *SPE California Regional Meeting* (Society of Petroleum Engineers, 1967). doi:10.2118/1725-MS
12. Zhang, Y. & Sarma, H. Improving Waterflood Recovery Efficiency in Carbonate Reservoirs through Salinity Variations and Ionic Exchanges: A Promising Low-Cost ‘Smart-Waterflood’ Approach. in *SPE International* 1–21 (2012).
13. Romanuka, J. *et al.* Low Salinity EOR in Carbonates. in *SPE International* 1–16 (2012).
14. Yousef, A. A. *et al.* SmartWater Flooding: Industry's First Field Test in Carbonate Reservoirs. in *SPE International* 1–26 (2012).
15. Morrow, N. & Buckley, J. Improved Oil Recovery by Low-Salinity Waterflooding. *Journal of Petroleum Technology* **63**, 106–112 (2011).
16. Austad, T., RezaeiDoust, A. & Puntervold, T. Chemical Mechanism of Low Salinity Water Flooding in Sandstone Reservoirs. in *SPE International* 1–17 (2010).
17. Hassenkam, T. *et al.* The low salinity effect observed on sandstone model surfaces. *Colloids Surf., A* **403**, 79–86 (2012).
18. Berner, R. A. The role of magnesium in the crystal growth of calcite and aragonite from sea water. *Geochimica et Cosmochimica Acta* **39**, 489–504 (1974).
19. Freij, S. J., Godelitsas, A. & Putnis, A. Crystal growth and dissolution processes at the calcite-water interface in the presence of zinc ions. *Journal of Crystal Growth* **273**, 535–545 (2004).
20. De Yoreo, J. J. *et al.* Rethinking Classical Crystal Growth Models through Molecular Scale Insights: Consequences of Kink-Limited Kinetics. *Crystal Growth & Design* **9**, 5135–5144 (2009).
21. Arvidson, R. S. *et al.* Magnesium inhibition of calcite dissolution kinetics. *Geochimica et Cosmochimica Acta* **70**, 583–594 (2005).
22. Davis, K. J., Dove, P. M. & De Yoreo, J. J. The role of Mg²⁺ as an impurity in calcite growth.

-
- Science* **290**, 1134–1137 (2000).
23. Harstad, A. O. & Stipp, S. L. S. Calcite dissolution: Effects of trace cations naturally present in Iceland spar calcites. *Geochimica et Cosmochimica Acta* **71**, 56–70 (2007).
 24. Agudo, E. R. & Putnis, C. V. Direct observations of mineral fluid reactions using atomic force microscopy: the specific example of calcite. *Mineral. Mag.* **76**, 227–253 (2012).
 25. Finneran, D. W. & Morse, J. W. Calcite dissolution kinetics in saline waters. *Chemical Geology* **268**, 137–146 (2009).
 26. Gratz, A. J. & Hillner, P. E. Poisoning of calcite growth viewed in the atomic force microscope (AFM). *Journal of Crystal Growth* **129**, 789–793 (1993).
 27. Gutjahr, A., Dabringhaus, H. & Lacmann, R. Studies of the growth and dissolution kinetics of the CaCO₃ polymorphs calcite and aragonite II. The influence of divalent cation additives on the growth and dissolution rates. *Journal of Crystal Growth* **158**, 310–315 (1996).
 28. Ruiz-Agudo, E., Putnis, C. V., Wang, L. & Putnis, A. Specific effects of background electrolytes on the kinetics of step propagation during calcite growth. *Geochimica et Cosmochimica Acta* **75**, 3803–3814 (2011).
 29. Elhadj, S., De Yoreo, J. J., Hoyer, J. R. & Dove, P. M. Role of molecular charge and hydrophilicity in regulating the kinetics of crystal growth. *Proceedings of the National Academy of Sciences* **103**, 19237–19242 (2006).
 30. Freeman, C., Asteriadis, I., Yang, M. & Harding, J. Interactions of Organic Molecules with Calcite and Magnesite Surfaces. *The Journal of Physical Chemistry C* **113**, 3666–3673 (2009).
 31. Hoch, A. R., Reddy, M. M. & Aiken, G. R. Calcite crystal growth inhibition by humic substances with emphasis on hydrophobic acids from the Florida Everglades. *Geochimica et Cosmochimica Acta* **64**, 61–72 (2000).
 32. Orme, C. A. *et al.* Formation of chiral morphologies through selective binding of amino acids to calcite surface steps. *Nature* **411**, 775–779 (2001).
 33. Ruiz-Agudo, E., Putnis, C. V., Jiménez-López, C. & Rodríguez-Navarro, C. An atomic force microscopy study of calcite dissolution in saline solutions: The role of magnesium ions. *Geochimica et Cosmochimica Acta* **73**, 3201–3217 (2009).
 34. Chukwudeme, E. A. & Hamouda, A. A. Oil recovery from polar components (asphaltene and SA) treated chalk rocks by low salinity water and water containing SO₄²⁻ and Mg²⁺ at different temperatures. *Colloids Surf., A* **336**, 174–182 (2009).
 35. Zullig, J. J. & Morse, J. W. Interaction of organic acids with carbonate mineral surfaces in seawater and related solutions: I. Fatty acid adsorption. *Geochimica et Cosmochimica Acta* **52**, 1667–1678 (1988).
 36. Rezaei Gomari, K. A. & Hamouda, A. A. Effect of fatty acids, water composition and pH on the wettability alteration of calcite surface. *Journal of Petroleum Science and Engineering* **50**, 140–150 (2005).
 37. Osman, M. A. & Suter, U. W. Surface Treatment of Calcite with Fatty Acids: Structure and Properties of the Organic Monolayer. *Chem. Mater.* **14**, 4408–4415 (2002).
 38. Shi, X., Rosa, R. & Lazzeri, A. On the Coating of Precipitated Calcium Carbonate with Stearic Acid in Aqueous Medium. *Langmuir* **26**, 8474–8482 (2010).
 39. Shi, X., Bertóti, I., Pukánszky, B., Rosa, R. & Lazzeri, A. Structure and surface coverage of water-based stearate coatings on calcium carbonate nanoparticles. *Journal of Colloid and Interface Science* **362**, 67–73 (2011).
 40. Mihajlović, S., Sekulić, Ž., Daković, A. & Vučinić, D. Surface properties of natural calcite filler treated with stearic acid. *Ceramics* **53**, 268–275 (2009).
 41. Stipp, S. L. S. Toward a conceptual model of the calcite surface: hydration, hydrolysis, and surface potential. *Geochimica et Cosmochimica Acta* **63**, 3121–3131 (1999).
 42. Heberling, F. *et al.* Structure and reactivity of the calcite–water interface. *Journal of Colloid and Interface Science* **354**, 843–857 (2011).
 43. Fenter, P. & Sturchio, N. C. Structure and growth of stearate monolayers on calcite: first results of an in situ X-ray reflectivity study. *Geochimica et Cosmochimica Acta* **63**, 3145–3152 (1999).
 44. O'Brien, W. J. & Hermann, J. J. The Strength of Liquid Bridges Between Dissimilar Materials. *The Journal of Adhesion* **5**, 91–103 (1973).
 45. Sauthier, G., Segura, J. J., Fraxedas, J. & Verdaguer, A. Hydrophobic coating of mica by stearic acid vapor deposition. *Colloids Surf., A* **443**, 331–337 (2014).
 46. Kumar, N., Wang, L., Siretanu, I., Duits, M. & Mugele, F. Salt Dependent Stability of Stearic Acid Langmuir–Blodgett Films Exposed to Aqueous Electrolytes. *Langmuir* **29**, 5150–5159 (2013).
 47. Mihajlović, S. R., Vučinić, D. R., Sekulić, Ž. T., Milićević, S. Z. & Kolonja, B. M. Mechanism of

-
- stearic acid adsorption to calcite. *Powder Technology* **245**, 208–216 (2013).
48. Aschauer, U., Spagnoli, D., Bowen, P. & Parker, S. C. Growth modification of seeded calcite using carboxylic acids: Atomistic simulations. *Journal of Colloid and Interface Science* **346**, 226–231 (2010).
 49. de Leeuw, N. H. & Cooper, T. G. A Computer Modeling Study of the Inhibiting Effect of Organic Adsorbates on Calcite Crystal Growth. *Crystal Growth & Design* **4**, 123–133 (2004).
 50. Stipp, S. L. S., Gutmannsbauer, W. & Lehmann, T. The dynamic nature of calcite surfaces in air. *American Mineralogist* **81**, 1–8 (1996).
 51. Baltrusaitis, J. & Grassian, V. H. Calcite (1014) surface in humid environments. *Surface Science* **603**, L99–L104 (2009).
 52. Hausner, D. B., Reeder, R. J. & Strongin, D. R. Humidity-induced restructuring of the calcite surface and the effect of divalent heavy metals. *Journal of Colloid and Interface Science* **305**, 101–110 (2007).
 53. Usher, C. R., Baltrusaitis, J. & Grassian, V. H. Spatially Resolved Product Formation in the Reaction of Formic Acid with Calcium Carbonate (1014): The Role of Step Density and Adsorbed Water-Assisted Ion Mobility. *Langmuir* **23**, 7039–7045 (2007).
 54. Cappella, B. & Dietler, G. Force-distance curves by atomic force microscopy. *Surface Science Reports* **34**, 1–104 (1999).
 55. Kobayashi, K., Takaoka, K. & Ochiai, S. Application of X-ray photoelectron spectroscopy and fourier transform IR-reflection absorption spectroscopy to studies of the composition of Langmuir-Blodgett films. *Thin Solid Films* **159**, 267–273 (1988).
 56. Gershevit, O. & Sukenik, C. N. In Situ FTIR-ATR Analysis and Titration of Carboxylic Acid-Terminated SAMs. *J. Am. Chem. Soc.* **126**, 482–483 (2004).
 57. Le Calvez, E., Blaudez, D., Buffeteau, T. & Desbat, B. Effect of Cations on the Dissociation of Arachidic Acid Monolayers on Water Studied by Polarization-Modulated Infrared Reflection–Absorption Spectroscopy. *Langmuir* **17**, 670–674 (2001).
 58. Bloch, J. M. & Yun, W. Condensation of monovalent and divalent metal ions on a Langmuir monolayer. *Phys. Rev. A* **41**, 844–862 (1990).
 59. Hutter, J. L. & Bechhoefer, J. Calibration of atomic-force microscope tips. *Rev. Sci. Instrum.* **64**, 1868–1873 (1993).
 60. Voitchovsky, K. & Ricci, M. High-resolution imaging of solvation structures with amplitude-modulation atomic force microscopy. in (Parak, W. J., Yamamoto, K. & Osinski, M.) **8232**, 82320O–8 (SPIE, 2012).
 61. Melcher, J. *et al.* Origins of phase contrast in the atomic force microscope in liquids. *PNAS* 1–6 (2009). <<http://www.pnas.org/cgi/doi/10.1073/pnas.0902240106>>
 62. Magonov, S. N., Elings, V. & Whangbo, M. H. Phase imaging and stiffness in tapping-mode atomic force microscopy. *Surface Science* **375**, L385–L391 (1997).
 63. Garcia, R. *et al.* Identification of Nanoscale Dissipation Processes by Dynamic Atomic Force Microscopy. *Phys. Rev. Lett.* **97**, 016103 (2006).
 64. Kiracofe, D. & Raman, A. Nonlinear dynamics of the atomic force microscope at the liquid-solid interface. *Phys. Rev. B* **86**, 205405 (2012).

Conclusions and Outlook

Solid-liquid interfaces are extremely important for several biological and colloidal processes. The need to gain a molecular description of the processes occurring at solid-liquid interfaces has been shown to be essential for the proper description of several systems. The standard macroscopic models cannot fully capture the varieties of molecular specific interactions that take place in the very proximity of the solid surface. In this thesis, it has been shown how high-resolution AM-AFM can be used to characterize, at the atomic/molecular level, solid-liquid interfaces. The key components to obtaining the desired sub-nanometric resolution are the solvation forces. In particular, the dissipative component of the tip-sample interaction force, due to the finite extension of the interface in the liquid region, allows obtaining a sub-nanometer imaging contrast in the case of AM-AFM.

Solvation forces are even responsible for single ion imaging with small amplitude AM-AFM. In this case, special care has to be taken in the interpretation of the data. The presence of the AFM tip, in fact, introduces some complications in the imaging process. This is particularly important if the properties of the single sample-liquid interface are inferred from the experimental images. In the case of Rb^+ ions absorbed on negatively charged mica surfaces, the effect of the tip can be accounted, for example, by introducing two extra energy components (mechanical and electrostatic) in the absorption model that relates the experimentally measured ionic coverage to the bulk ionic concentration. This correction efficiently explains the deviations of the measured from the unperturbed ionic coverage on the surface. Introducing these extra energy components leads to an estimate on the effect that the AFM tip has on the Stern Layer whilst using the imaging conditions typically employed in the experiments. Special emphasis is put on the surprisingly slow dynamics of the adsorb ions on the surface of mica. In the case of Rb^+ a mean residence time on the order of hundreds of milliseconds has been estimated. This slow dynamics enable the imaging of single ions as protruding objects in topographic images, and as a confined spot of lower phase shift in the phase images. One of the possible explanations of the ions slow dynamics relies on the confinement of the liquid during the tip oscillation.

This deep technical analysis of the high-resolution imaging process is then employed to characterize several solid-liquid interfaces in which an aqueous ionic solution is put in contact with the surface of a solid. The first system examined is the negatively charged mica surface in contact with RbCl , NaCl and KCl aqueous solutions. Given the extensive literature reported on this topic, mica-ionic solutions interface is considered as a model system to characterize the ionic absorption in the Stern Layer. The constant charge and the atomically smooth surface render the interpretation of the AM-AFM results less challenging, if compared to lipid bilayer, for example. The overall picture emerging from AFM measurements and MD-simulations highlights the importance of the interplay between the hydration properties of adsorbed ions and that of the surface. Chaotropic ions such as K^+ or Rb^+ appear mostly located within the first hydration layer with limited effect over the distal layers. This minimal disruption of the mica's interfacial water structure allows the formation of stable ionic structures guided by the hydration landscape of the surface. This effect manifests itself with an attractive ion-ion correlation energy that favours the formation of ionic rows or patches on the surface. We named this newly discovered form of correlation energy within the Stern Layer as the hydration correlation effect. This energy term does not require any specific interaction between the ions and the surface and can, in principle, occur at any interface, which exhibits an appropriate hydration landscape. Although the specific hydration properties of the ions are essential for this phenomenon to manifest, seen in the case of

the cosmotropic Na^+ ions. These, being able to reside on different complexation sites on the surface, are immune from this form of water-induced ordering within the Stern Layer.

Two further systems that have similar hydration properties to mica have been examined to verify the predicted generality of the hydration correlation effect: alcohol-terminated alkane SAMs on gold and two types of lipid bilayers (DPPC and DPPA). In the presence of RbCl aqueous solutions, Rb^+ clusters can be identified at the surface of the SAM, yielding a phase contrast consistent with the results on mica. The clusters are however; less clearly defined because of the relatively weak surface potential of the SAM that limits the adsorptions of ions at the surface. However, the presence of Rb^+ clusters confirms an attractive $\text{Rb}^+\text{-Rb}^+$ correlation energy. These results further support the idea that the surface chemistry of the solid is not critical, nor is the surface potential. The key factor is the surface hydration landscape, which imposes a particular arrangement of the adsorbed ions. In the case of supported lipid bilayer in the gel phase, even if the hydration properties of the self-assembled surface are similar to the ones of the SAM, the headgroups exhibit large thermal fluctuations due to the gap between adjacent molecular groups. This allows the ions present in solution to directly and specifically interact with the lipid headgroups region by penetrating into the surface. On account of this, the interpretation of our experimental data in this case is more challenging and even if in the case of the DPPA lipid bilayer a correlation effect seems to be present, more careful experiments are necessary to draw solid conclusions.

In the second part of this work, the calcite-aqueous ionic solution interface has been explored in detail, both in equilibrium and out-of-equilibrium conditions. This ionic crystal is highly dynamic and restructuring processes happen at the surfaces when in contact with aqueous solutions. This renders the system more complex but at the same time much more interesting, as it is the fundamental ingredient in most of the bio-mineralization processes and oil reservoirs. The interface between the flat terraces of calcite ($10\bar{1}4$) surface and NaCl, RbCl and CaCl solutions in equilibrium conditions have been explored combining high-resolution AFM and MD-simulations. The surface of calcite is strongly hydrated and the approaching ions have to pay a substantial energy penalty, incurred by the loss or restructuring of the hydration shell, when traversing calcite's hydration layers. Monovalent ions like Rb^+ and on some extent Na^+ , are able to interact with the calcite surface, while strongly hydrated Ca^{2+} divalent cations reside mainly as outer-sphere complexes on top of the hydrations layers of the surface. The situation is completely different at the step edges of the surface. Here the water molecules have properties that significantly deviate from that on the flat areas. Moreover different types of steps show different interactions with the surrounding water molecules suggesting that the morphology of the surface plays an important role in the establishment of the final equilibrium between the ionic species composing the crystal and the solution. At step edges even strongly hydrate divalent ions can directly interact with the surface, being incorporated or released from the crystal. These processes are fundamental during the growth and dissolution of the calcite crystal. In particular by investigating the topographical changes of the ($10\bar{1}4$) surface exposed to brines with different ionic compositions and concentration, the specific effects of foreign ions, like Mg^{2+} and Sr^{2+} , on the growth process have been investigated.

By increasing the degree of complexity, the heterogeneous interface between the calcite surface covered with organic fatty acid molecules and several ionic solutions with varying compositions and concentrations has been presented. Fatty acids are known to be the main polar component of crude oil and have been shown to strongly interact with the calcite surface. Long chain fatty acids, like stearic acids, are particularly stable on the mineral surface. Therefore they are expected to be the more resistant component when external physiochemical conditions are changed as in the case of ionic strength variation happening during low salinity water flooding processes. Our results show that the stearic acid layers rearrange to minimize the contact between the hydrophobic groups of the molecules and the aqueous solution. They form bilayers or multilayers, even at low organic coverage, when a complete monolayer is not obtained yet. The calcite restructuring around the organic patches causes them to be trapped in a well, formed by the crystal during the growth process. At higher organic coverage, the growth process concentrates the SA in a confined area

where big multilayer patches appear on the surface. Subsequent dilution of the contacting brine removes the freshly grown calcite and exposes the previously incorporated organic layers back to the solution. The presence of the organic patches on the calcite surface slows down both the growth and dilution processes. Stearic acid patches act as pinning points for receding calcite steps. Significantly, we show that the restructuring of the calcite surface in the presence of low and high salt concentrations does not cause desorption of the adsorbed organic molecules. These observations could contribute to explaining the high variability observed in imbibition experiments performed by petrol companies and may even provide a molecular-level insight into different bio-mineralization processes in which the growth of calcite is happening in the presence of organic material.

Finally, an AFM method to obtain information on the affinity between a specific chemical group and a surface is presented. By functionalizing the AFM tip with relevant molecules, the tip-surface adhesion force is obtained as a function of the variable external conditions. The interpretation of the results can be a bit challenging and special care has to be taken by doing several control experiments. In the case of calcite and a carboxylic acid-functionalized tip, the functionalization process is extremely important. In fact it can influence the stability of the molecules grafted on the AFM tip, which upon repetitive contact with the surface can detach from the tip's apex. If comparative measurements are performed by changing external parameters (ionic strength and pH in our experiment) while maintaining the same tip and surface, this effect can induce a systematic error into the measurement. The effect of the roughness has to also be considered, particularly if it is evolving like in the case of the dynamic calcite surface in different ionic solutions. Our results do not show a significant variation of adhesion force between the carboxylated tips and the calcite's surface as a function of the progressively reduced ionic strength of the solution. The variability of the measurements does not allow for drawing significant conclusions. On the hand, an effect at lower pH and low ionic strength is detected: the adhesion force is increased when the carboxylated molecules are immersed in acidic brine at low ionic concentration. More experiments are necessary to confirm this result but, if true, it suggests that the protonation state of the carboxylic acid is extremely important in the interaction mechanism with the calcite surface.

The general picture emerging from this thesis is that the specific phenomena that take place in the Stern Layer of solid-liquid interfaces are essential for understanding the physicochemical interactions between solid surfaces immersed in liquid media. Without a molecular description of the systems the interpretation of the experimental results in the framework of the classical continuum theories can become challenging or even misleading. The hydration correlation effect, for example, can be extremely important in systems where the local arrangement of ions in the Stern Layer can lead to molecular recognition like in the case of cell membranes. These types of phenomena though, are not considered in the standard continuum models and only a deep look in the Stern Layer with suitable techniques can reveal their existence. The other important conclusion is that ions are not all the same and by interacting in different manners with the water molecules around them can show different behavior in the Stern Layer. The first example is given by Na^+ ions at the surface of mica, unlikely K^+ and Rb^+ -ions, they are not affected by the hydration correlation effect. Even in the case of calcite, depending on the ions' hydration properties, they can penetrate or not the ordered hydration layers that cover the flat areas of the crystal or interact selectively with different steps.

The main open question is the effect that the tip has on the isolated interface. Our model gives an estimation on the electrostatic and mechanical effects of the tip apex but cannot give an answer to the eventual confinement-induced slow ion dynamic. The mobility of ions in the Stern Layer, in the case of single interface or under confinement, is still unknown. The gap between the typical time-scales of the phenomena explored by MD-simulations and AFM cannot help to clarify this effect, so possible other approaches will have to be explored. Moreover complex interfaces like in the case of lipid bilayers have to be characterized by other experimental techniques that can help to discriminate between the different ionic complexation sites and mobility. In particular possible other experimental techniques that can provide this information are electrochemical impedance

Conclusions and Outlook

spectroscopy in nanochannels. This thesis is just the beginning of a long story that can in principle reveal countless interesting phenomena and will pave the way for a deeper and more conscious understanding of interfacial phenomena and colloidal properties of materials.

Appendix

Correction for the effective ionic concentration at the surface of mica in the isotherm models

In Chapter 3 I presented the results obtained when analyzing the coverage of the Rb^+ ions on the mica surface at different bulk concentrations. The values of the ionic coverage were obtained from the AFM images and fitted with the different isotherm models (Langmuir, Frumkin and Frumkin with tip perturbation). To obtain the significant parameters of the isotherms the coverage was plotted as a function of the ionic bulk concentration of the Rb^+ ions and the fit was performed. In reality, the ionic concentrations at the surface are deviating significantly from the bulk values due to the charged mica surface. The correct values can be obtained by knowing the surface charge and applying the Poisson-Boltzmann equation to the system. Since, especially at low ionic concentration, the surface charge is significantly high, an ionic enrichment is expected for both Rb^+ and H_3O^+ at the surface. In this section this effect will be taken into account and a correction for the significant parameters of the isotherm models (binding constant of H_3O^+ , correlation energy and AFM mechanical perturbation) will be presented.

8.1 Effective ionic concentration at the surface of mica

To obtain the Rb^+ coverage at the surface of mica in Chapter 3 we used the following Frumkin model:

$$\theta_{\text{Rb}^+} = \frac{K_{\text{Rb}^+} e^{-\frac{E_c \theta_{\text{Rb}^+}}{T k_B}} c_{\text{Rb}^+}^0}{1 + K_{\text{Rb}^+} e^{-\frac{E_c \theta_{\text{Rb}^+}}{T k_B}} c_{\text{Rb}^+}^0 + K_{\text{H}_3\text{O}^+} c_{\text{H}_3\text{O}^+}^0} \quad (8.1)$$

where θ_{Rb^+} is the Rb^+ coverage at the surface, E_c is the correlation energy between the Rb^+ ions in the Stern Layer, K_{Rb^+} and $K_{\text{H}_3\text{O}^+}$ respectively the Rb^+ and H_3O^+ binding constants and $T k_B$ the product between the temperature and the Boltzmann constant. Similarly for the coverage of hydronium we have:

$$\theta_{\text{H}_3\text{O}^+} = \frac{K_{\text{H}_3\text{O}^+} c_{\text{H}_3\text{O}^+}^0}{1 + K_{\text{Rb}^+} e^{-\frac{E_c \theta_{\text{Rb}^+}}{T k_B}} c_{\text{Rb}^+}^0 + K_{\text{H}_3\text{O}^+} c_{\text{H}_3\text{O}^+}^0} \quad (8.2)$$

with now $\theta_{\text{H}_3\text{O}^+}$, the hydronium coverage. The concentrations $c_{\text{Rb}^+}^0$ and $c_{\text{H}_3\text{O}^+}^0$ used in Eq. 8.1 and Eq. 8.2 should not be considered as the bulk concentrations c_{Rb^+} and $c_{\text{H}_3\text{O}^+}$ of the ions in solution as assumed in the model presented in Chapter 3 and generally implied in the Langmuir adsorption models. This model intrinsically assumes that the concentration of the ionic species is constant everywhere except for the surface. In this region the Langmuir isotherm gives the equilibrium concentration of the species adsorbed determining its effective surface charge. In the real system, as we have seen in Chapter 4, the ionic concentration is not uniform at the aqueous-solid interface. A more reliable approach should consider at the same time the Langmuir/Frumkin adsorption isotherms and the Gouy-Chapman theory. In this case the concentration used for the adsorption model should be equal to the effective ion concentrations at the surface of mica where the competitive adsorption between the different ionic species takes place. According to the Poisson-Boltzmann distribution these values can be obtained as:

$$c_{\text{Rb}^+}^0 = c_{\text{Rb}^+} e^{\frac{-e\psi_0}{k_B T}} \quad (8.3)$$

$$c_{\text{H}_3\text{O}^+}^0 = c_{\text{H}_3\text{O}^+} e^{\frac{-e\psi_0}{k_B T}} \quad (8.4)$$

where ψ_0 is the electrostatic potential at the surface of the solid. We have neglected the corrections for the ionic activity coefficient and we will assume no extra potential drop ($\psi_d - \psi_0$, where ψ_d is the potential at the OHP) across the Stern Layer.¹ In reality $c_{\text{Rb}^+}^0$ and $c_{\text{H}_3\text{O}^+}^0$ correspond the ionic concentration at the OHP where the diffuse Layer of the ions starts. In this diffuse layer the continuum assumptions of the PB are considered to be valid. The OHP in the Stern model do not coincide with the surface plane but it is shifted to take into account the finite size of the hydrated ions on the surface. In our system the OHP should be placed at roughly 0.3 nm from the surface, accordingly to the results of our MD-simulations. In this 0.3 nm gap (d) if only water molecules can adsorb, there will develop a potential drop that, assuming the Stern Layer to be a plane capacitor, depends on the surface charge and the capacitance C_S of the Stern Layer:

$$C_S = \frac{\epsilon_{\text{H}_2\text{O surf}} \epsilon_0 A}{d} \quad (8.5)$$

$$\psi_d - \psi_0 = \frac{Q}{C_S} = \frac{Qd}{\epsilon_{\text{H}_2\text{O surf}} \epsilon_0 A} = \frac{\sigma d}{\epsilon_{\text{H}_2\text{O surf}} \epsilon_0} \quad (8.6)$$

where Q is the charge, and $\varepsilon_{H_2O_{surf}}$ is the relative permittivity of surface water, normally to be considered less than 80 (bulk water permittivity). Of course in our situation between the OHP and the mica surface there are the adsorbed ions so the simple stern treatment is not valid. In our situation an extra plane, the inner Helmholtz plane (IHP) passing through the center of the “specifically adsorbed” ions has to be considered. This plane is inside the Stern Layer being placed between the surface plane and the OHP. This more complex model is called by Hiemstra *et al.*² the three planes model and would imply the addition of an extra potential drop between surface-IHP and IHP-OHP.²

In this section we are interested in determining a first correction to the bulk concentration of the ions and thus estimate the effect of the surface ion enrichment on the significant parameters of the isotherm models. To do so we will neglect the Stern Layer contribution to the potential drop. This implies that ψ_0 in Eq. 8.3 and Eq. 8.4 is the surface potential, the Stern Layer is absent and the effect of the ions is simply to change the effective surface charge of mica by adsorbing onto it. The estimated effect found is going to be the biggest one in terms of ion enrichment at the surface so the worst scenario that we can conceive.

In both PB and GCS models it is possible to obtain a value for the surface charge of the solid and this value has to consistently coincide between the two approaches. Accordingly to the Isotherm model the surface charge of mica, upon ion absorption can be directly calculated:

$$\begin{aligned}\sigma = \sigma_{H_2O} = \sigma_{TOT} + \frac{e \theta_{Rb^+}}{A_{UC}} + \frac{e \theta_{H_3O^+}}{A_{UC}} &= \frac{-e}{A_{UC}} + \frac{e \theta_{Rb^+}}{A_{UC}} + \frac{e \theta_{H_3O^+}}{A_{UC}} \\ &= \frac{-e}{A_{UC}} (1 - \theta_{Rb^+} - \theta_{H_3O^+})\end{aligned}\quad (8.7)$$

Where A_{UC} is the area of a unit cell of mica ($A_{UC} = 46.72 \text{ \AA}^2$) that correspond to one negative $-e$ binding site³ and $\sigma_{TOT} = -e/A_{UC} = -3.43 \cdot 10^{-19} \text{ C nm}^{-2} = -0.343 \text{ C m}^{-2}$ is the mica charge density supposing no adsorbed ions on the surface.

At the same time the surface charge is related to the surface potential though the PB distribution. From PB we have that:

$$\frac{d^2\psi}{dz^2} = -\frac{\rho(z)}{\varepsilon\varepsilon_0}\quad (8.8)$$

where the charge density $\rho(z)$ (C m^{-3}) is:

$$\begin{aligned}\rho(z) &= \sum_i z_i e n_i(z) = \sum_i z_i e n_i^\infty e^{-\frac{z_i e \psi}{k_B T}} \\ &= \sum_i z_i e N_A 10^3 c_i e^{-\frac{z_i e \psi}{k_B T}}\end{aligned}\quad (8.9)$$

where z_i is the ion valence $n_i(z)$ numeric density of ions (m^{-3}) as a function of the distance z from the surface ($z = 0$ is the surface), n_i^∞ is the numeric density of ions in the bulk and N_A the Avogadro number. If we suppose symmetric monovalent electrolyte Eq. 8.8 reduces to:

$$\frac{d^2\psi}{dz^2} = \frac{2 e n^\infty}{\varepsilon \varepsilon_0} \sinh \frac{e \psi}{k_B T}\quad (8.10)$$

By calling:

$$\frac{e \psi}{k_B T} = \Psi\quad (8.11)$$

it is possible to rewrite Eq. 8.10 as:

$$\frac{d^2\Psi}{dz^2} = \frac{2 e^2 n^\infty}{k_B T \varepsilon \varepsilon_0} \sinh \Psi = \kappa^2 \sinh \Psi \quad (8.12)$$

where

$$\kappa = \sqrt{\frac{2 e^2 n^\infty}{k_B T \varepsilon \varepsilon_0}} = \sqrt{\frac{2 e^2 N_A 10^3 c_i}{k_B T \varepsilon \varepsilon_0}} \quad (8.13)$$

is called Debye parameter.

An analytical solution of Eq. 8.12 can be found by imposing $d\Psi/dz(\infty) = 0$ and that $d\Psi/dz(0) = \Psi_0$:

$$\Psi(z) = 4 \operatorname{atanh}(\tanh(\Psi_0) e^{-\kappa z}) \quad (8.14)$$

where Ψ_0 is calculated at the surface.

Generally it is possible to obtain a simplified expression for both potential and concentration dependence on z by supposing Ψ small (the famous Debye-Hückel limit). In the specific case of mica, though, in the approximation of small potential Ψ and assuming no RbCl in solution (at pH 5.5) the estimated Ψ_0 is -15.5. The Debye-Hückel approximation is thus inconsistent in our case at small ion concentration. To proceed further it is necessary to use Eq. 8.14 and impose the electroneutrality condition to the system. This condition implies that the excess of charge in the diffuse layer correspond to the surface charge:

$$e \int_0^\infty dz (n_+(z) - n_-(z)) = e \int_0^\infty dz (n^\infty e^{-\Psi} - n^\infty e^{\Psi}) = -\sigma \quad (8.15)$$

By using Eq. 8.15 and combing the form of $\Psi(z)$ of Eq. 8.14 it is possible to obtain an expression that relates the surface charge to the reduced surface potential Ψ_0 :

$$\frac{e 8 \tanh(\Psi_0) n^\infty}{\kappa - (\tanh(\Psi_0))^2 \kappa} = -\sigma \quad (8.16)$$

Finally Eq. 8.16 relates the reduced surface potential Ψ_0 to the surface charge σ . If we are able to calculate the surface charge σ it is possible to obtain the reduced surface potential Ψ_0 and so estimate the ionic concentration of Rb^+ and H_3O^+ at the surface accordingly to Eq. 8.3 and Eq. 8.4. To estimate the surface charge we used Eq. 8.1 and Eq. 8.2 imposing θ_{Rb^+} and $\theta_{\text{H}_3\text{O}^+}$ to be the values obtained from the old Frumkin isotherms without the effect of the AFM tip. This is a first approximation that does not take into account the surface ion enrichment but was anyway already able to describe in a good way our experimental data as well as the one of Park *et al.*⁴. At this point we do not care about the ionic enrichment at the surface but we simply need a good model that can describe the actual concentration of the ionic species at the surface and determine the effective surface charge. $K_{\text{H}_3\text{O}^+}$, K_{Rb^+} and E_c in Eq. 8.1 and Eq. 8.2 are the old uncorrected values used in Chapter 3. The values of $K_{\text{H}_3\text{O}^+}$ in this case is such that at zero Rb^+ concentration the coverage of $\theta_{\text{H}_3\text{O}^+}$ is 0.28 exactly as in the case of Park *et al.*⁴. Combing the values of θ_{Rb^+} , the $\theta_{\text{H}_3\text{O}^+}$ estimated from the old Eq. 8.1 and Eq. 8.2 into the Eq. 8.7 and finally combining this last equation with Eq. 8.16 it is possible to find the values of reduced surface potential and effective ion concentration as a function of the Rb^+ bulk concentration:

c_{Rb^+} (mM)	σ (C/m)	Ψ_0	$c_{Rb^+}^0$ (mM)	$c_{H_3O^+}^0$ (mM)
0	-0.245	-3.88	0	0.153
0.01	-0.219	-3.46	0.319	0.101
0.1	$-0.520 \cdot 10^{-1}$	-2.23	0.930	$0.294 \cdot 10^{-1}$
1	$-0.201 \cdot 10^{-2}$	$-2.57 \cdot 10^{-1}$	1.29	$0.409 \cdot 10^{-2}$
2	$-0.889 \cdot 10^{-3}$	$-8.35 \cdot 10^{-2}$	2.17	$0.344 \cdot 10^{-2}$
3	$-0.567 \cdot 10^{-3}$	$-4.36 \cdot 10^{-2}$	3.13	$0.330 \cdot 10^{-2}$
4	$-0.416 \cdot 10^{-3}$	$-2.77 \cdot 10^{-2}$	4.11	$0.325 \cdot 10^{-2}$
5	$-0.3279 \cdot 10^{-3}$	$-1.96 \cdot 10^{-2}$	5.10	$0.322 \cdot 10^{-2}$
10	$-0.159 \cdot 10^{-3}$	$-6.73 \cdot 10^{-3}$	10.1	$0.318 \cdot 10^{-2}$
100	$-0.155 \cdot 10^{-3}$	$-2.07 \cdot 10^{-4}$	100	$0.316 \cdot 10^{-2}$

Table 8.1: Values of Rb^+ bulk concentration, surface charge, reduced surface potential, Rb^+ corrected surface concentration and H_3O^+ surface concentration (H_3O^+ bulk concentration constant at 0.003mM at pH 5.5).

Lower the ionic content bigger the deviation between the surface concentration and the bulk values. This is expected given the bigger surface charge at low ionic concentration.

8.2 New fitting coefficients of the isotherm models

With the corrected values of Rb^+ surface concentrations we performed again the fitting of the isotherms for the two experiments with soft and stiff AFM cantilevers. In this case though the values of the coefficient $K_{H_3O^+}$ and K_{Rb^+} had to be left free to vary during the fitting procedure. In the previous case, in fact, those values were constrained to be the same as the one reported by Park *et al.*⁴. To increase the consistency of the fitting procedure, due to the limited number of data points we decided to do a global fitting (inbuilt function in Igor pro) imposing the two set of data to be fitted at the same time with the same values of $K_{H_3O^+}$, K_{Rb^+} , E_c but a different mechanical perturbation E_m^{AFM} :

$$\begin{aligned} \theta_{Rb^+} &= \frac{K_{Rb^+} e^{-\frac{E_c \theta_{Rb^+}}{RT}} e^{-\frac{E_m^{AFM} + E_e^{AFM}}{RT}} c_{Rb^+}^0}{1 + K_{Rb^+} e^{-\frac{E_c \theta_{Rb^+}}{RT}} e^{-\frac{E_m^{AFM} + E_e^{AFM}}{RT}} c_{Rb^+}^0 + K_{H_3O^+} c_{H_3O^+}^0} \\ &= \frac{A e^{-\frac{E_c \theta_{Rb^+}}{RT}} c_{Rb^+}^0}{1 + A e^{-\frac{E_c \theta_{Rb^+}}{RT}} c_{Rb^+}^0 + K_{H_3O^+} c_{H_3O^+}^0} \end{aligned} \quad (8.17)$$

where

$$A = K_{Rb^+} e^{-\frac{E_m^{AFM} + E_e^{AFM}}{RT}} \quad (8.18)$$

We used Eq. 8.17 to fit our AFM experimental data combining the following constrains between the two experiments (soft and stiff AFM tip):

$$\frac{E_c^{stiff}}{RT} = \frac{E_c^{soft}}{RT} = \gamma \quad (8.19)$$

$$K_{H_3O^+}^{stiff} = K_{H_3O^+}^{soft} \quad (8.20)$$

$$K_{Rb^+}^{stiff} = K_{Rb^+}^{soft} \quad (8.21)$$

$$A^{stiff} \neq A^{soft} \quad (8.22)$$

The different values of the constant A between the two types of lever arise from the different mechanical perturbation E_m^{AFM} . θ_{Rb^+} appearing in the exponent was expressed as obtained in the uncorrelated case, when the Frumkin isotherm simplify back to the Langmuir case (first term in the approximation of small correlation energy):

$$\theta_{Rb^+} \text{ in the exponent} = \frac{A c_{Rb^+}^0}{1 + A c_{Rb^+}^0 + K_{H_3O^+} c_{H_3O^+}^0} \quad (8.23)$$

At the same time now the function θ_{Rb^+} is in principle a multivariable function depending on both $c_{Rb^+}^0$ and $c_{H_3O^+}^0$ that now varies as a function of $c_{Rb^+}^0$. To do a global fitting with multivariable functions it is quite complicated so we decided to fix the values of $c_{H_3O^+}^0$ to its mean value that for the data set presented in Table 8.1 ($3.06 \cdot 10^{-5} \text{ mol L}^{-1}$). The final fitting function is so:

$$\theta_{Rb^+} = \frac{A e^{-\gamma \frac{A c_{Rb^+}^0}{1 + A c_{Rb^+}^0 + K_{H_3O^+} \cdot 3.06 \cdot 10^{-5}}} c_{Rb^+}^0}{1 + A e^{-\gamma \frac{A c_{Rb^+}^0}{1 + A c_{Rb^+}^0 + K_{H_3O^+} \cdot 3.06 \cdot 10^{-5}}} c_{Rb^+}^0 + K_{H_3O^+} \cdot 3.06 \cdot 10^{-5}} \quad (8.24)$$

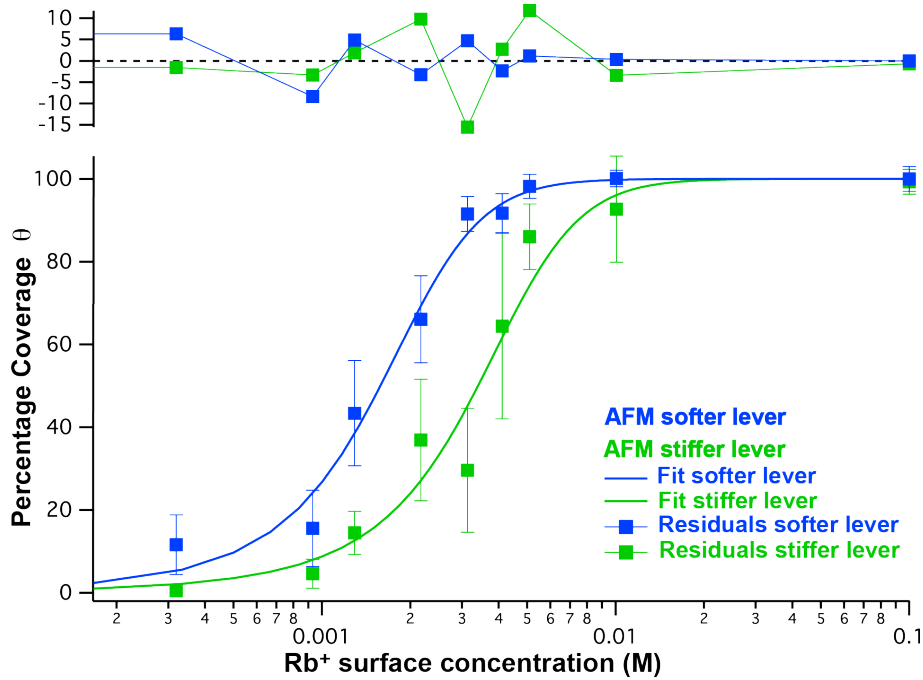


Fig. 8.1: New fitting results of the data presented in Chapter 3.

The new results of the fitting are presented in Fig. 8.1. The parameters obtained from the fittings are the following:

$$A^{stiff} = 415 \pm 9478 \quad (8.25)$$

$$A^{soft} = 892 \pm 20378 \quad (8.26)$$

$$K_{H_3O^+} = 164310 \pm 4326530 \quad (8.27)$$

$$\gamma = -10.63 \pm 0.064 \quad (8.28)$$

Beside the big uncertainty of the coefficients, the actual attractive correlation energy is confirmed by the negative value of γ even in the case of corrected surface concentration of Rb^+ ions. The value of the correlation energy is in this case:

$$E_c = \gamma RT \sim 24 \text{ kJ mol}^{-1} \quad (8.29)$$

This value is 3.4 times bigger than the one found in Chapter 3. The surface enrichment is thus enhancing the effect of the attractive correlation in our experimental data.

Unfortunately, in this case, it is not possible to obtain the actual value of K_{Rb^+} and E_e^{AFM} . In fact the electrostatic contribution to the tip perturbation cannot be decoupled from the constant A without doing further assumptions on K_{Rb^+} that in this case is better to not do. By taking the ratio between A^{stiff} and A^{soft} we can obtain an information on the mechanical perturbation of the system:

$$\frac{A^{\text{stiff}}}{A^{\text{soft}}} = \frac{K_{\text{Rb}^+} e^{-\frac{E_m^{\text{stiff}} + E_e^{\text{AFM}}}{RT}}}{K_{\text{Rb}^+} e^{-\frac{E_m^{\text{soft}} + E_e^{\text{AFM}}}{RT}}} = e^{-\frac{E_m^{\text{stiff}} - E_m^{\text{soft}}}{RT}} \quad (8.30)$$

We know even, from the discussion in Chapter 3 that $E_m^{\text{stiff}}/E_m^{\text{soft}}$ can be even calculated experimentally and the values is roughly 12.

$$\frac{A^{\text{stiff}}}{A^{\text{soft}}} = e^{-\frac{12 E_m^{\text{soft}} - E_m^{\text{soft}}}{RT}} = e^{-\frac{11 E_m^{\text{soft}}}{RT}} \quad (8.31)$$

So we can finally obtain:

$$E_m^{\text{soft}} = -\frac{RT}{11} \ln \frac{A^{\text{stiff}}}{A^{\text{soft}}} \sim 172.4 \text{ J mol}^{-1} \quad (8.32)$$

The value obtained is 3 times lower than in the previous case (330 J mol^{-1}).

In conclusion, the implementation of a correction that takes into account the effective ionic concentration at the surface of mica by combing the isotherm adsorption models with the PB equation confirms the presence of an attractive ion-ion correlation in the Stern Layer. The new value obtained is 3.4 higher than in the case of the uncorrected treatment.

Bibliography Appendix

1. Behrens, S. H. & Borkovec, M. Electrostatic Interaction of Colloidal Surfaces with Variable Charge. *The Journal of Physical Chemistry B* **103**, 2918–2928 (1999).
2. Hiemstra, T. & Van Riemsdijk, W. H. A Surface Structural Approach to Ion Adsorption: The Charge Distribution (CD) Model. *Journal of Colloid and Interface Science* **179**, 488–508 (1996).
3. Lee, S. S., Nagy, K. L. & Fenter, P. Distribution of barium and fulvic acid at the mica–solution interface using in-situ X-ray reflectivity. *Geochimica et Cosmochimica Acta* **71**, 5763–5781 (2007).
4. Park, C., Fenter, P. A., Sturchio, N. C. & Nagy, K. L. Thermodynamics, Interfacial Structure, and pH Hysteresis of Rb^+ and Sr^{2+} Adsorption at the Muscovite (001)–Solution Interface. *Langmuir* **24**, 13993–14004 (2008).

Acknowledgments

That's it! It's finally over.

I'm kind of happy and sad at the same time. Mostly happy.

I guess for each one of us, going through the intense and challenging steps of a PhD, the feelings and states of mind are diverse and personal. For me, it has been a very difficult time, especially during the writing. At the same time, though, I had the overwhelming support of all my colleagues, friends and relatives around me. They have believed in my abilities and strength much more than I do and this is the main reason why today, I can finally write these last two pages.

First of all I have to thank the members of the jury of my private defense. They have been kind enough to read the entire thesis and gave me valuable new insights in the science, I have been thinking and overthinking throughout the past four years. I really appreciated both their comments and their incredible support in such an important moment of my career.

Then I have to thank my two advisors: Francesco and Kislou. They have both been extremely supportive and helpful in all of the different moments of my PhD. Francesco, apart from being an incredible scientist, is one of the most motivating people I have ever met in my life. His optimism and positivity, both from a scientific and human perspective, are astonishing. I can really say that I am proud to have been part of his research group. Kislou, the little boss, has been an advisor, an incredible friend and sometimes almost family to me. In addition to the high esteem I have for his way of conducting research and approaching scientific problems, he has also been able to pass on to me his passion for science and life in general. I couldn't have asked for better advisors.

Of course a big thanks to all of the external collaborators I have worked with during my PhD. Good science is teamwork and the teams I was part of have been amazing! Especially I'd like to thank Reid and Peter, the two "simulations guys". They have been extremely patient with me and my experimental approach :-)

To the people of SuNMIL group, I don't know if calling them colleagues is appropriate. They are friends. Everyone in the group, in his/her own way, has been a part of my life bringing positivity and good memories in addition to new high-level scientific inputs. I have to thank the old fellows: Javier, Randy, Mauro, Tam and Marta. We had incredible scientific and many non-work related adventures together. Particularly, the fabulous MTM team. You girls are just amazing. I don't think I can express properly the affection and esteem I have for you. You actually almost made me cry. Then, maintaining the fundamental hierarchical division of postdocs and PhD students, I have to thank Gigio, Sam (*tank you for individuating all the mistakes!*), Ben, Kellen, Quy and Yun. Not forgetting Stefan who I want to thank personally. He has helped me a lot during this last period, despite us not getting off to the best of starts. Now the PhD students, my pack. Here the list is long so I divide it by geographical origins, since we like to make fun of each other using stupid stereotypes. The Greeks: Evi and Nik. The Turkish: Elif, Ahmet, Pelin and Özgün. The German: Marie. The Brazilians: Paulo and Paulette. The Chinese: Shun and Zhi. Then of course Allegri, my big friend, my personal trainer and my motivational coach. Thank you all. I'd also like to thank the girls of the Milan-side of the group, especially Patrizia and Barbara and our secretary Chiara.

I have to say a special thanks to the LMOM and of course to the Sforzini groups. They have all been really nice neighbors. We have had great times together both in the lab and the real world.

A big thank you to my old friends. The people of my master thesis' lab, especially Loredana and Pietro. My close friends of the physics department of Trieste: Agnese, Lori, Marco,

Schizz, Tanja, Fonda, Blanco and Prio. I want to thank a lot my friends from Muggia and the climbers. Mostly for reminding me that until I build a proper laser sword or the teleportation or a super cool new sail, I'm not done yet!

A big thank to my big crazy family. Voglio ringraziare tutti quanti. I nonni, gli zii e gli innumerevoli cugini. Mi sono stati sempre vicini, e mi hanno aiutato a diventare la persona che sono oggi, anche e soprattutto dal punto vista professionale. Ovviamente il contributo maggiore viene dai miei genitori. Cristina e Mauro mi hanno sempre supportato (soprattutto sopportato), aiutato psicologicamente e materialmente. Hanno creduto in me ricordandomi, ognuno a suo modo, quanto fossero fieri di quello che stavo facendo. Poi c'è mio fratello Pietro, l'altra metà dei geni. Lui è sempre stato il mio più grande sostenitore ed io la sua più grande fan. Penso che senza il suo supporto e il suo modo differente di vedere le cose non sarei mai arrivata (sana di mente) fino a questo punto.

Last but not least, Sergio. Oltre ad essere il mio compagno di avventure e disavventure, lui è il mio punto fisso. Sicuramente lui è il first implicit co-author di questa tesi e dei miei risultati in generale.

Finally to Henry, thanks for always listening (R. Carney thesis, 2013). To Scarfi for showing me that sometimes a smile can help to get you what you want better than any complaint, and to Dick for his important suggestions on fashion.

Lausanne, 16th of March 2015

Maria Ricci

Curriculum Vitae - Maria Ricci

École Polytechnique Fédérale de Lausanne
EPFL STI IMX SUNMIL
MXH 130 (Bâtiment MXH)
Station 12
CH-1015 Lausanne, Switzerland

Mobile Phone: +41 79 8398308
mail: maria.ricci@epfl.ch

CURRENT POSITION

• **Ph.D. student at the Material Science department** November 2010 – April 2015
École Polytechnique Fédérale de Lausanne, Switzerland.
Thesis title: Characterization of Solid-Liquid Interfaces with High-Resolution Atomic Force Microscopy.
Supervisors: Prof. Francesco Stellacci (francesco.stellacci@epfl.ch) and Dr. Kislou Voitchovsky (kislou.voitchovsky@durham.ac.uk)

EDUCATION

• **Master degree in Physics** September 2010
University of Trieste, Trieste, Italy.
Thesis title: Hybrid Carbon/Quartz Nanoelectrodes: an Innovative Tool for Electropysiological Understanding of Neuronal Network communication.
Supervisor: Prof. Renzo Rosei (renzo.rosei@elettra.trieste.it) in collaboration with Dr. Loredana Casalis (loredana.casalis@elettra.trieste.it) at Elettra (synchrotron of Trieste).
Mark: 110/110 with full honors.

• **Bachelor degree in Physics** September 2008
University of Trieste, Trieste, Italy.
Thesis title: Study of retinal photoisomerization efficiency dependence from wavelength excitation.
Supervisor: Prof. Fulvio Parmigiani (fulvio.parmigiani@elettra.trieste.it).
Mark: 110/110 with full honors.

RESEARCH EXPERIENCE

École Polytechnique Fédérale de Lausanne, Lausanne, Switzerland 2010 - 2015

- Imaging of solid/liquid interfaces with atomic/molecular resolution by means of Atomic Force Microscopy (AFM) (examples: supported lipid bilayers, mica, calcite, self-assembled monolayers on gold, aluminum oxide, silicon oxide).
- Experimental characterization (AFM) and theoretical model developments of ionic effects at the interface between charged surfaces and water-based ionic solutions.

- Characterization of mechanical properties of organic layers, including lipid bilayers, deposited on solid surfaces with force spectroscopy.
- Preparation of supported lipid bilayer (vesicles deposition and Langmuir-Blodgett deposition) and characterization (AFM in liquid and Quartz Crystal Microbalance).
- Functionalization of gold and silicon oxide surfaces.
- Imaging and mechanical mapping of living cells with AFM.
- Trained to work in a chemical laboratory and responsible of the AFM instrumentation laboratory.
- Development of procedures for automatized data analysis with Igor Pro.
- Synchrotron experience: Small Angle X-ray Scattering at synchrotron Dasy (Hamburg, Germany).

University of Trieste, Trieste, Italy

2005-2010

- Chemical Vapor Deposition of carbon-based material at high temperature.
- Basic knowledge of a Patch Clamp measurement.
- Basic knowledge of Scanning Tunneling Microscopy and Scanning Tunneling Spectroscopy.
- X-Ray Photoemission Spectroscopy and Low Energy Electron Diffraction studies of Ru(0001) surface in ultra-high vacuum environment.
- Synchrotron experience: X-Ray Photoemission Spectroscopy at synchrotron Elettra (Trieste).

PUBLICATIONS

1. Van Lehn, R. C.,* **Ricci, M.**,* Silva, P., Andreozzi, P., Reguera, J., Voitchovsky, K., Stellacci, F. & Alexander-Katz A. Lipid tail protrusions mediate the insertion of nanoparticles into model cell membranes. *Nature Communications* **5** 4482, (2014).
2. **Ricci, M.**, Spijker, P., & Voitchovsky, K. Water-induced correlation between single ions imaged at the solid-liquid interface. *Nature Communications* **5** 4400, (2014).
3. **Ricci, M.**, Spijker, P., Stellacci, F., Molinari, J. F. & Voitchovsky, K. Direct Visualization of Single Ions in the Stern Layer of Calcite. *Langmuir* **29**, 2207–2216 (2013).
4. Voitchovsky, K. & **Ricci, M.** High-resolution imaging of solvation structures with amplitude-modulation atomic force microscopy. *Proceedings of SPIE* (Parak, W. J., Yamamoto, K. & Osinski, M.) **8232**, 82320O–8 (SPIE, 2012).
5. Ferrari, E., Galli, L., Miniussi, E., Morri, M., Panighel, M., **Ricci, M.**, Lacovig, P., Lizzit, S. & Baraldi, A. Layer-dependent Debye temperature and thermal expansion of Ru(0001) by means of high-energy resolution core-level photoelectron spectroscopy. *Physical Review B* **82**, 195420 (2010).
6. Zgrablić, G., **Ricci, M.**, Novello, A. M. & Parmigiani, F. Dependence of Photochemical Reactivity of the All-trans Retinal Protonated Schiff Base on the Solvent and the Excitation Wavelength. *Photochemistry and Photobiology* **86**, 507–512 (2010).

*Authors contributed equally.

PUBLICATIONS IN PREPARATION OR SUBMITTED

1. **Ricci, M.**, Segura, J. J., Erickson, B., Fantner, G., Stellacci, F., Voitchovsky, K. Growth and dissolution of calcite in the presence of adsorbed stearic acid. *Langmuir*, submitted.
2. **Ricci, M.**, Trewby, W., Voitchovsky, K. Slow ion dynamic in the Stern Layer explored with high-resolution AFM. In preparation.
3. **Ricci, M.**, Stellacci, F., Voitchovsky, K. Review on high-resolution AFM in liquid: physical mechanism behind different imaging modes. In preparation.

CONFERENCE ORAL PRESENTATIONS

- “*Specific ionic effects at aqueous solid-liquid interfaces investigated with high resolution AM-AFM.*” April 2014
Invited talk at 2014 MRS Spring Meeting, Symposium BBB, San Francisco (USA).
- “*Ion absorption at solid-liquid interfaces investigated with high resolution AM-AFM*” October 2014
Invited talk in the group of Prof. Ricardo Garcia, CSIC, Madrid (Spain).

GRANTS

(2005) Awarded the "Luciano Fonda" Scholarship for bachelor student from the University College for Sciences of Trieste.

(2008) Awarded the "Luciano Fonda" Scholarship for master student from the University College for Sciences of Trieste.

TEACHING EXPERIENCE

2010-2015

Teaching assistant for the courses of “Surfaces and interfaces” and “Thermodynamics for material science” in the Bachelor program of Material Science at the École Polytechnique Fédérale de Lausanne.

Supervision of bachelor student for the Bachelor Semester Project (3 months period).

COMPUTER SKILLS

Windows | MacOS | Mathematica | IgorPro | SPIP image analysis | ImageJ | Gwyddion | Adobe Illustrator | VMD (basic)

LANGUAGES

Italian (Native) | English (Fluent)

